^{31}CL β-DELAYED PROTON DECAY AND CLASSICAL NOVA NUCLEOSYNTHESIS

By

Tamas Aleksei Budner

A DISSERTATION

Submitted to
Michigan State University
in partial fulfillment of the requirements
for the degree of

Physics – Doctor of Philosophy

2022

ABSTRACT

Classical novae occur in binary star systems involving a compact white dwarf and a low-mass stellar companion. In these events, material siphoned from the donor star forms an accretion disk around the white dwarf. This hydrogen-rich fuel is compressed, heated, and mixed with the outer layers of the underlying white dwarf until it eventually ignites in a thermonuclear runaway. These violent explosions eject freshly synthesized nuclear material into the interstellar medium, contributing to the chemical evolution of the galaxy.

Nova sensitivity studies involving the most massive oxygen-neon (ONe) white dwarfs have identified the thermonuclear rate of the $^{30}\mathrm{P}(p,\gamma)^{31}\mathrm{S}$ reaction to be the largest remaining source of nuclear physics uncertainty associated with modeling nucleosynthesis for intermediate-mass elements in these highly energetic events. Over the past two decades, considerable experimental effort has been devoted to determining the rate of this proton-capture reaction, but until now, it has remained essentially unconstrained. A recent ^{31}Cl β-delayed γ experiment revealed the existence of a crucial low-energy, $\ell = 0$ resonance that could potentially dominate the total $^{30}\mathrm{P}(p,\gamma)^{31}\mathrm{S}$ rate. At the National Superconducting Cyclotron Laboratory (NSCL), on the campus of Michigan State University, we developed the Gaseous Detector with Germanium Tagging (GADGET) system in order to measure the weak, low-energy, β-delayed proton decay of ^{31}Cl through this astrophysically important resonance. In GADGET's first dedicated science experiment, we measured the weakest β-delayed charged-particle decay ever reported for resonances below 400 keV. Combining our experimentally determined proton branching ratio with shell-model calculations of the state's lifetime and with past work on other resonances, we computed the total thermonuclear rate for the $^{30}\mathrm{P}(p,\gamma)^{31}\mathrm{S}$ reaction across peak classical nova temperatures. Our new, recommended rate was used in fully hydrodynamic nova model simulations to predict the elemental and isotopic abundances in ONe nova ejecta.

In this dissertation, we will discuss the experimental methods and analysis employed to achieve our scientific results and investigate their astrophysical impact by comparing to observations from astronomy. Furthermore, we present the first-ever detailed look at the $^{31}\mathrm{Cl}(\beta p\gamma)^{30}\mathrm{P}$ decay scheme,

reporting preliminary energies and intensities for previously unobserved β-delayed proton transitions to ^{30}P excited states.

ACKNOWLEDGEMENTS

I would like to acknowledge everyone in my research group at Michigan State University with whom I have had the pleasure of collaborating over the past six years. Specifically, I would like to thank my Ph.D. advisor, Prof. Christopher Wrede, for his patient guidance and support throughout my graduate career. He has been working on the astrophysical problem motivating this research for the better part of two decades and was the principal investigator of the Department of Energy (DOE) grant proposal that funded this thesis project. I would also like to thank our former postdoctoral research associate, Prof. Moshe Friedman, who was essential in the technical development of the GADGET system. Furthermore, I want to acknowledge fellow graduate students Jason Surbrook and Tyler Wheeler, as well as postdoctoral researcher Lijie Sun, for their specific contributions to necessary simulations and data analysis for this project.

In addition, I would like to credit other members of our collaboration, including Prof. Alex Brown and Prof. Jordi José for their theoretical calculations, David Pérez-Loureiro and Emmanuel Pollacco for their contributions to detector development, as well as everyone who participated in NSCL experiment 17024 to ensure that it was a success. I want to also extend this appreciation to all the NSCL staff for their administrative and technical support; none of the experimental research at the lab would be possible without their diligent efforts. Lastly, I want to give thanks to all the friends I have made during my time in Michigan, whose love and support have kept me somewhat sane throughout graduate school.

TABLE OF CONTENTS

CHAPTER 1

INTRODUCTION AND BACKGROUND

The central component of the doctoral thesis project discussed in this dissertation revolves around the quantification of one property, of a single quantum state, within a particular atomic nucleus, which is relevant to a specific astrophysical environment. More specifically, the purpose of this research is to determine the probability that an excited and unstable sulfur (S) nucleus will emit a proton, in order to calculate the rate at which radioactive phosphorus (P) nuclei will capture protons in the thermonuclear explosions that occur on the surface of certain dead stars. In this first chapter, we will provide a short primer on some basic nuclear physics and define terminology that will be used throughout. In addition, we wish to contextualize the scientific motivation for this research within the broader field of modern nuclear astrophysics.

1.1 A Brief Overview of Nuclear Structure and Radiation

The Atom and Nuclear Notation

Almost all matter with which we interact on a daily basis is comprised of atoms. Every atom contains a nucleus and at least one *electron* (e^-), which are held together by the electrostatic attraction between the negatively charged electrons and the positively charged nucleus. Figure 1.1, although not drawn to scale, offers a comparison between the diameters of the atom and its nucleus. While the region in which electrons orbit around the nucleus makes up most of an atom's volume, over 99.9% percent of the atomic mass is contained within its nucleus. The nucleus itself is composed of positively-charged *protons* (p) and electrically neutral *neutrons* (n). The number of protons in a nucleus is given by the *atomic number* Z and determines the chemical properties of that particular element. Atomic nuclei of the same chemical element with different *neutron numbers* N are the various *isotopes* of that element. The total number of *nucleons* in a given nucleus is its *mass number* $A = Z + N$. Standard nuclear notation will sometimes refer to a specific nucleus using the

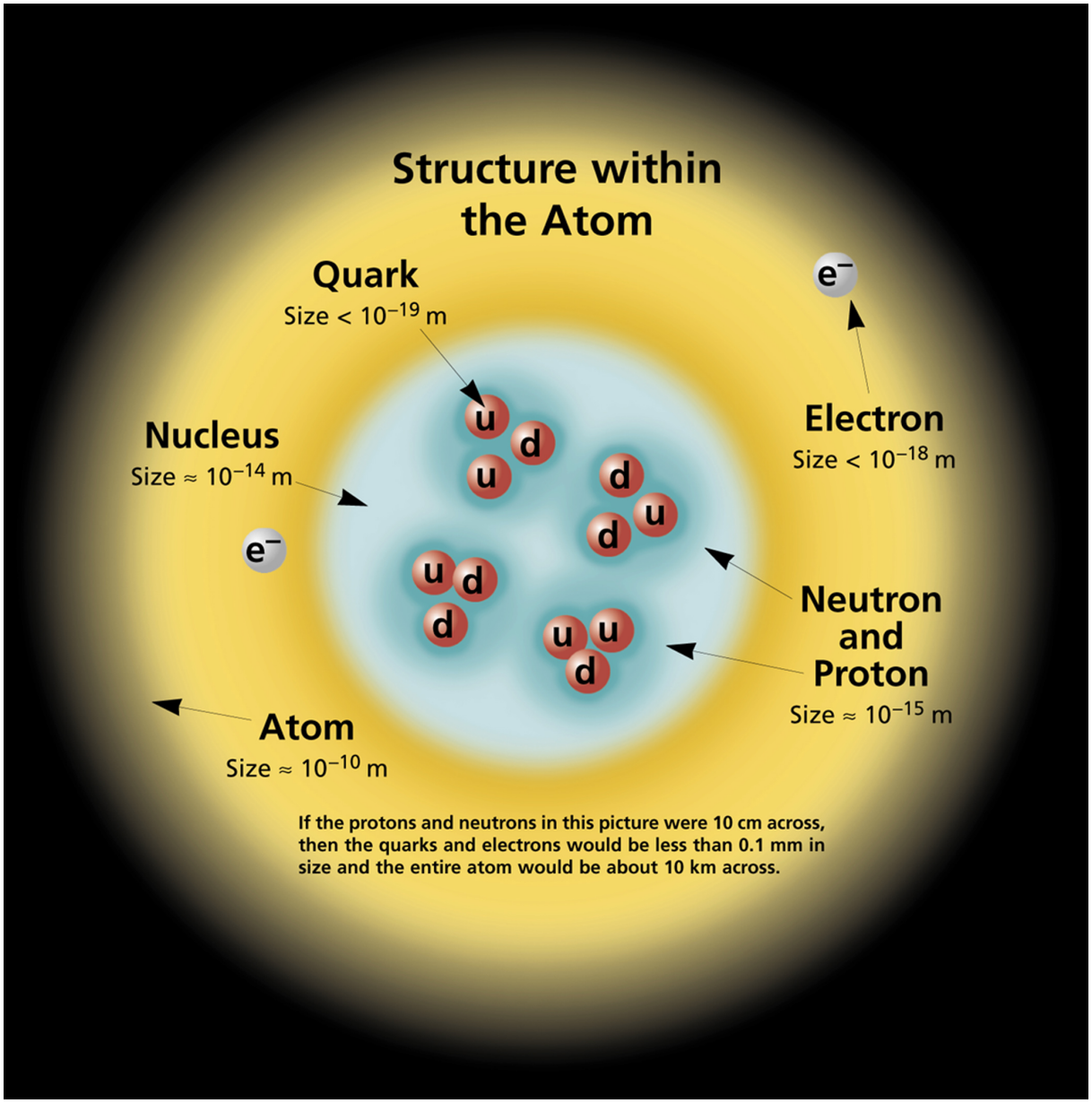

Figure 1.1: Cartoon diagram of a helium (He) atom. Nucleons are bound systems of three fundamental particles called *quarks*; protons have two "up" quarks and one "down" quark, while neutrons have one up and two down quarks. Figure credit: Contemporary Physics Education Project, Lawrence Berkeley National Laboratory.

shorthand ${}^{A}_{Z}X$, where X is the chemical symbol for a given element, but usually the redundant Z subscript is omitted.

Stable and Unstable Nuclei

Nucleons are tightly bound by the residual effects of the *strong interaction*, which describes the behavior of the elementary particles within each nucleon over very small distances and is the strongest of the four fundamental forces in nature. Stable nuclei are less massive than the sum of their individual nucleons alone, and their *nuclear binding energy* is defined as the energy required to break up a given nucleus into its constituent protons and neutrons. Using perhaps the most famous equation in all of physics, $E = mc^2$, which relates the energy of an object to its mass at rest, we can express the binding energy of a particular nucleus with mass $m(N, Z)$ as

$$\mathrm{BE}(N, Z) = Zm_p c^2 + Nm_n c^2 - m(N, Z)c^2, \tag{1.1}$$

where $c^2 = 8.98755179 \times 10^{16}$ m^2/s^2 is the speed of light squared, $m_p = 938.27203(8)$ MeV/c^2 is the mass of the proton, and $m_n = 939.56536(8)$ MeV/c^2 is the mass of the neutron [1]. In the energy regime relevant for nuclear physics, it is often convenient to express energies in units of mega- (MeV) or kiloelectron-volts (keV), where 1 MeV = 10^3 keV = 10^6 eV.

Similar to how the periodic table organizes chemical elements by increasing order in Z, the *chart of nuclides* shown in Figure 1.2 plots Z versus N for every known nucleus; rows and columns are outlined at the so-called *magic numbers*, which correspond to the "closure" of *nuclear shells*. Similar to, although distinctly different from, how electrons fill atomic orbitals, individual protons and neutrons will occupy the lowest-energy configuration available, following the *Pauli exclusion principle*. Despite the fact that vast majority of atoms on Earth are stable, Figure 1.2 clearly shows that most known nuclei are not, and the stability of an atomic nucleus is determined by its relative number of protons and neutrons. Only isotopes with the largest binding energy per nucleon (BE/A) are to be found in the so-called *valley of stability*.

Unstable nuclei are said to be *radioactive* and undergo *nuclear decay* by emitting *radiation*, of which there are a variety of types. Nuclear decay is a fundamentally random process, but it follows a simple, exponential trend. The number of radioactive nuclei N at time t is given by

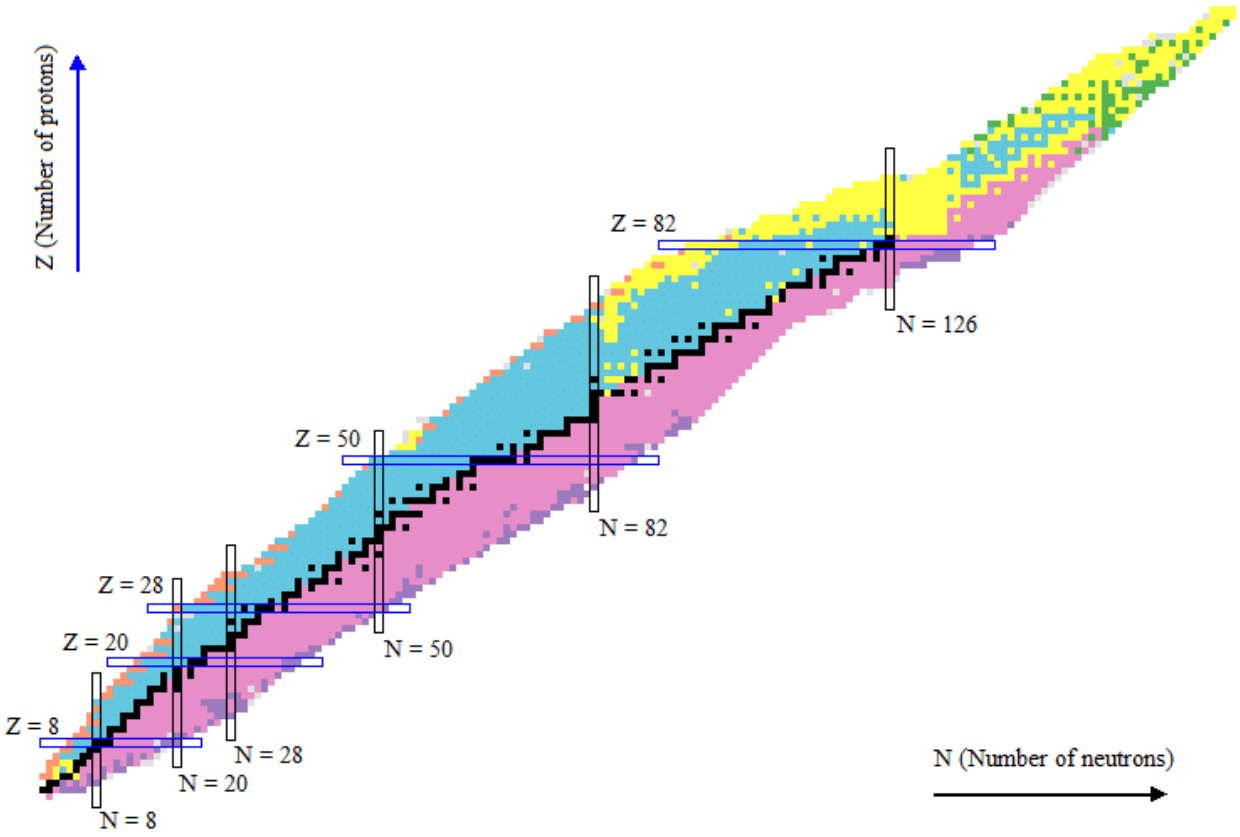

Figure 1.2: The chart of nuclides. Stable nuclei are represented by black squares, while radioactive nuclei are color-coded by their primary decay modes: β^+ or electron capture (blue), β^- (pink), α (yellow), fission (green), and spontaneous proton (orange) or neutron (purple) emission. Figure credit: National Nuclear Data Center (NNDC), Brookhaven National Laboratory.

$$N(t) = N_0 e^{-t/\tau}, \tag{1.2}$$

where $N_0 = N(t = 0)$ is the number of radioactive nuclei present when they are first counted, and τ is the *lifetime* of the radioactive nucleus. The lifetime is simply the average time that a nucleus takes to decay. Typically, when discussing how radioactive a nucleus is, we quote its *half-life* $t_{1/2} = \ln 2\tau$, which is the time required for half of the radioactive nuclei within an isotopically pure sample decay [$N(t_{1/2}) = N_0/2$].

Weak Decays

Radioactive nuclei located below this valley in Figure 1.2 are *neutron-rich* and typically undergo β^- *decay*, whereby a neutron turns into a proton, emitting an electron and *antineutrino* ($\overline{\nu}$) in the process:

$$ {}^{A}_{Z}X \rightarrow {}^{A}_{Z+1}X' + e^- + \overline{\nu} \tag{1.3} $$

Electrons and *neutrinos* (ν) are both fundamental particles called *leptons* and have a *lepton number* of $L = 1$, while their antiparticles have $L = -1$. Thus, emission of the antineutrino during β^- decay conserves this quantity ($\Delta L = 0$). Similarly, on the *proton-rich*, or *neutron-deficient*, side of the chart, nuclei typically undergo β^+ decay, in which a proton turns into a neutron:

$$ {}^{A}_{Z}X \rightarrow {}^{A}_{Z-1}X' + e^+ + \nu \tag{1.4} $$

In this case, the electron's antiparticle the *positron* (e^+) is emitted instead, along with a neutrino this time, again conserving lepton number. A related decay process is *electron capture*, in which a proton-rich nucleus captures one of its innermost electrons and converts a proton into a neutron:

$$ {}^{A}_{Z}X + e^- \rightarrow {}^{A}_{Z-1}X' + \nu \tag{1.5} $$

These three decay processes are all caused by the other short-range nuclear force, appropriately named the *weak interaction*, due to its relatively weak strength compared to the to the strong nuclear and electromagnetic forces.

Alpha Decay and Nuclear Fission

Not all decay modes are mediated by the weak interaction. For example, α *decay* typically occurs in heavy nuclei and is governed by competition between the two stronger forces. Even though the attractive nuclear force is generally much more intense over short ranges than the electric repulsion between the protons, the strength of the former drops quickly over the distance of $\approx 10^{-15}$ m, while

the latter increases in proportion to Z^2 and has an unlimited range. Thus, $A > 210$ nuclei have such large radii that the strong nuclear force can barely counterbalance the proton-proton repulsion [2]. Qualitatively, the emission of a tightly bound ^{4}He nucleus, or α particle, can be thought to occur as a means of increasing the stability and reducing the size of the nucleus:

$$ {}^{A}_{Z}X \rightarrow {}^{A-4}_{Z-2}X' + \alpha \tag{1.6} $$

While it is energetically possible for a heavy nucleus to reduce the amount of energy stored in its mass via α decay, the kinetic energy dissipated by this disintegration is quite small compared to the large potential energy barrier it must overcome in order to escape the nucleus. This is only possible due to a phenomenon called *quantum tunneling*, which we will discuss further in Chapter 2. A similar process is responsible for the effect of *nuclear fission*, in which a very heavy nucleus splits into two smaller, more tightly bound nuclei.

Nuclear Reactions and Nucleon Emission

As seen in Figure 1.3, the binding energy per nucleon begins to decline with increasing mass number beyond iron (Fe) and nickel (Ni), which are the most tightly bound nuclei. This means a *nuclear reaction* that fuses two light nuclei with a combined mass of $A < 58$ can result in the release of energy. In fact, it is this *nuclear fusion* process that drives the energy production of stars like our Sun. Nuclear processes, such as fusion reactions and radioactive decay, cause a change in the amount of energy that stored in the nuclear masses. The difference between the final binding energies and the initial binding energies of the nuclei involved in these processes is called the *Q-value*:

$$ Q = \sum_f \mathrm{BE}(N_f, Z_f) - \sum_i \mathrm{BE}(N_i, Z_i) = \sum_i m_i(N_i, Z_i)c^2 - \sum_f m_f(N_f, Z_f)c^2 \tag{1.7} $$

Spontaneous decays always have a positive Q-value, otherwise the nucleus would be stable and remain unchanged. The Q-value of a nuclear reaction can be positive or negative. Reactions for

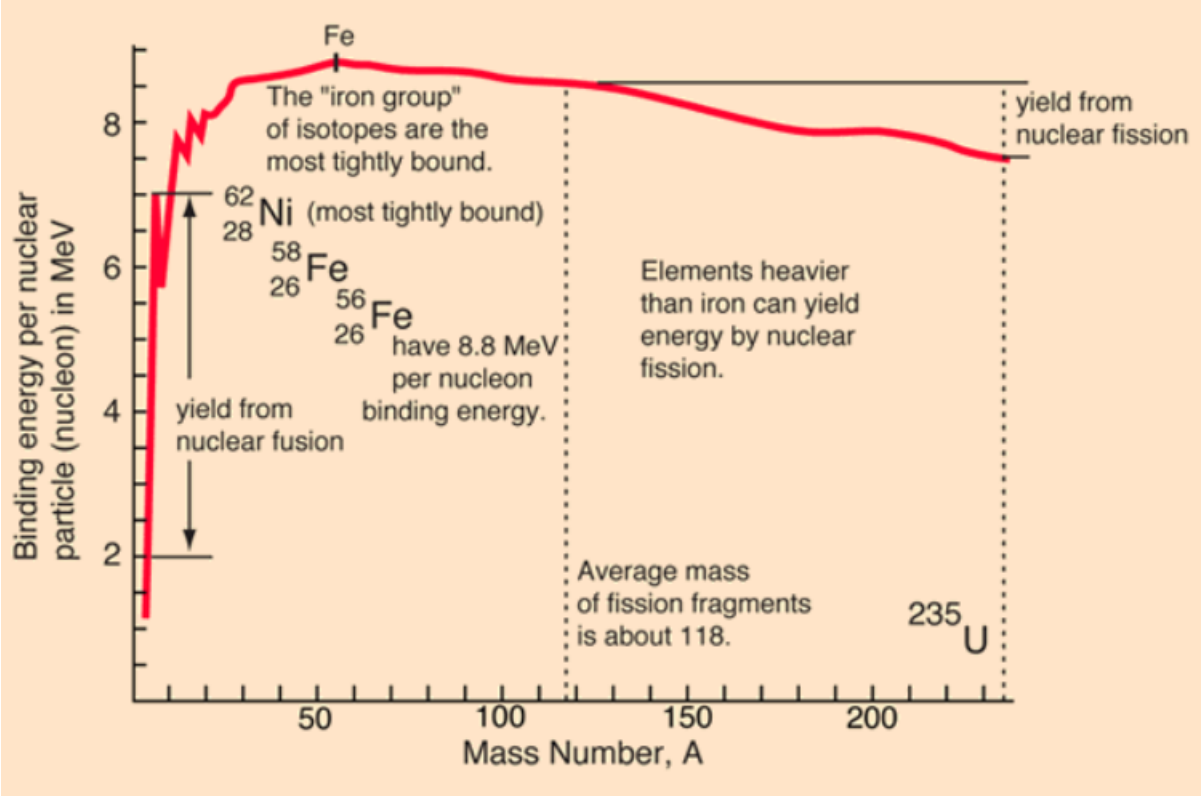

Figure 1.3: Binding energy per nucleon plotted over mass number. Nuclear processes that result in nuclei becoming more stable tend to release energy. Figure credit: HyperPhysics, Carl Rod Nave.

which $Q > 0$ release energy and are said to be *exothermic*, while *endothermic* reactions ($Q < 0$) require energy from the environment to be added into the nuclear system in order to proceed. The energy required to remove a single nucleon from the nucleus is called the one-nucleon *separation energy*. The proton separation energy is simply defined as

$$S_p = -Q_p = \mathrm{BE}(N, Z) - \mathrm{BE}(N, Z-1), \tag{1.8}$$

and the neutron separation energy is

$$S_n = -Q_n = \mathrm{BE}(N, Z) - \mathrm{BE}(N-1, Z). \tag{1.9}$$

Extremely proton-rich nuclei for which $S_p < 0$ are said to be *proton unbound*; extremely neutron-rich nuclei for which $S_n < 0$ are said to be *neutron unbound*. Exotic nuclei of this kind are only

found far away from stability at the *nuclear drip lines*, beyond which the addition of an extra neutron or proton would simply "drip" away, not forming a bound nucleus.

Nuclear Levels and Gamma Decay

This brings us to arguably the last piece of introductory knowledge necessary for understanding a majority of the nuclear physics discussed throughout this dissertation: the concept of *excited states*. So far, we have implicitly assumed that the nucleus in question is occupying its *ground state*, the lowest possible energy configuration of its nucleons. However, just as the electrons in an atom can be excited to higher atomic energy levels, so too can the nucleus be excited. Moreover, driving a current through a chemically pure gas at low pressure, like in a neon (Ne) light fixture, results in electronic excitations, which upon their decay, result in the emission of *photons* of visible light, whose characteristic color is indicative of the energy they radiate away as the atom descends the discrete levels. Usually, these atomic states decay within 10 ns to 10 ms ($10^{-9} - 10^{-4}$ s) [3].

Analogously, a nucleus that is the product of a reaction, the *daughter* of radioactive decay, or simply participates in a sufficiently energetic scattering interaction, will initially populate a nuclear configuration with a discrete energy level well above its ground state. However, the *excitation energies* required to populated these various nuclear levels are on the order of $10^5 - 10^6$ times higher than that of atomic energy levels. Thus, the photons they emit, known as γ *rays*, are well outside the visible spectrum and are usually given in keV or MeV units. Furthermore, their lifetimes are frequently $\lesssim 10^{-12}$ s. By convention, nuclear levels are usually referenced by their lifetime compared to the half-lives quoted for charged-particle decays.

The lifetime of a nuclear level will often depend on its total *angular momentum* $J = L+S$, where L, or ℓ, is the *orbital angular momentum* and S is the *spin*. These are conserved, discrete quantities for which the analog in classical physics is not particularly useful in understanding their quantum interpretation. Nuclear levels also have either even or odd *parity* ($\pi = \pm 1$). If the wave function corresponding to a particular nucleon configuration is identical under coordinate transformation, it is said to have even parity ($\pi = +$), but if it is a mirror image under reflection then it has odd

parity ($\pi = -$). The total parity of the quantum state of a nucleus is the product of over all nucleons $\pi = \Pi_i(-1)^{\ell_i}$.

Lighter nuclei have fewer possible nuclear configurations and thus have sparse and relatively simple level structures. However, massive nuclei with many nucleons often have a high density of nuclear levels and very complicated decay schemes, where highly excited states will emit multiple γ rays in a cascade of transitions between levels of decreasing energy until they reach the ground state. If an nuclear level is populated such that its excitation energy is greater than the nucleon separation energy for that nucleus ($E_x > S_{p,n}$), there is some probability that this level will decay by spontaneous nucleon emission instead. This is particularly relevant for understanding the research topic of this dissertation specifically, as well as nuclear reactions in stars more broadly.

1.2 On the Origin of Elements

Nuclear astrophysics is an interdisciplinary field which includes areas of study in computational astrophysics, observational astronomy, as well as both experimental and theoretical nuclear physics. Each of these different academic disciplines provide unique insights that further our understanding of the universe on the largest and smallest of scales. Because of the diversity of research interests between these fields, collaboration and open exchange is extremely important in order to determine what information is needed from its individual contributors to best serve the scientific interests of the community as a whole.

Ultimately, the goal of the nuclear astrophysics community is to address fundamental questions about the universe which include, but are not limited to the following: Where did the chemical elements that constitute the natural world originate? What are the individual contributions of various astrophysical environments? How do the properties of nuclei affect the life cycles of stars? How might we utilize radioactive nuclei in the cosmos to better understand the evolution of our galaxy? What is the underlying structure of neutron stars, and what is the nature of dense nuclear matter? The astrophysical motivation for the original research contained in this thesis dissertation pertains to the chemical and isotopic abundances produced in certain stellar explosions. Thus, in this section, we will focus primarily on the first two questions, in order to contextualize our current

understanding of the universe's chemical evolution.

In the Beginning

The process of *nucleosynthesis* refers to the nuclear mechanisms by which the chemical elements and their various isotopes were forged. Nearly all of the complex chemistry that permeates our nearly 14-billion-year-old universe was made possible due to the nucleosynthesis occurring in stars. Immediately following the Big Bang, the universe was too hot for any nuclei to form and was instead likely filled with a hot, dense mixture of electrons, *quark-gluon plasma*, and potentially other elementary particles. As the universe rapidly expanded and cooled, the first protons, or hydrogen (H) nuclei, were able to condense, colliding with the high-electrons to form neutrons once the universe reached a balmy ~10 billion degrees (K) [4]. By the time it cooled to a temperature of ~1 billion K, the first nucleosynthesis occurred between ^{1}H and free neutrons to form *deuterium* nuclei (^{2}H), also known as *deuterons* (d). These quickly fused to form the extremely stable ^{4}He. Some other reactions participating in early Big Bang nucleosynthesis involved p, n, ^{3}He, and ^{4}He produced trace amounts of the first lithium (Li) nuclei. However, given that the half-life of the neutron is only about 15 minutes [5; 6], all the unreacted neutrons quickly decayed away, leaving only the remaining H and He nuclei to form the first stars. As shown in Figure 1.4, basically all the H and He we observe in our Solar System today were produced shortly after the Big Bang. Since then, about 2% of those primordial nuclei have been processed into the all the heavier chemical elements we observe today [7; 8].

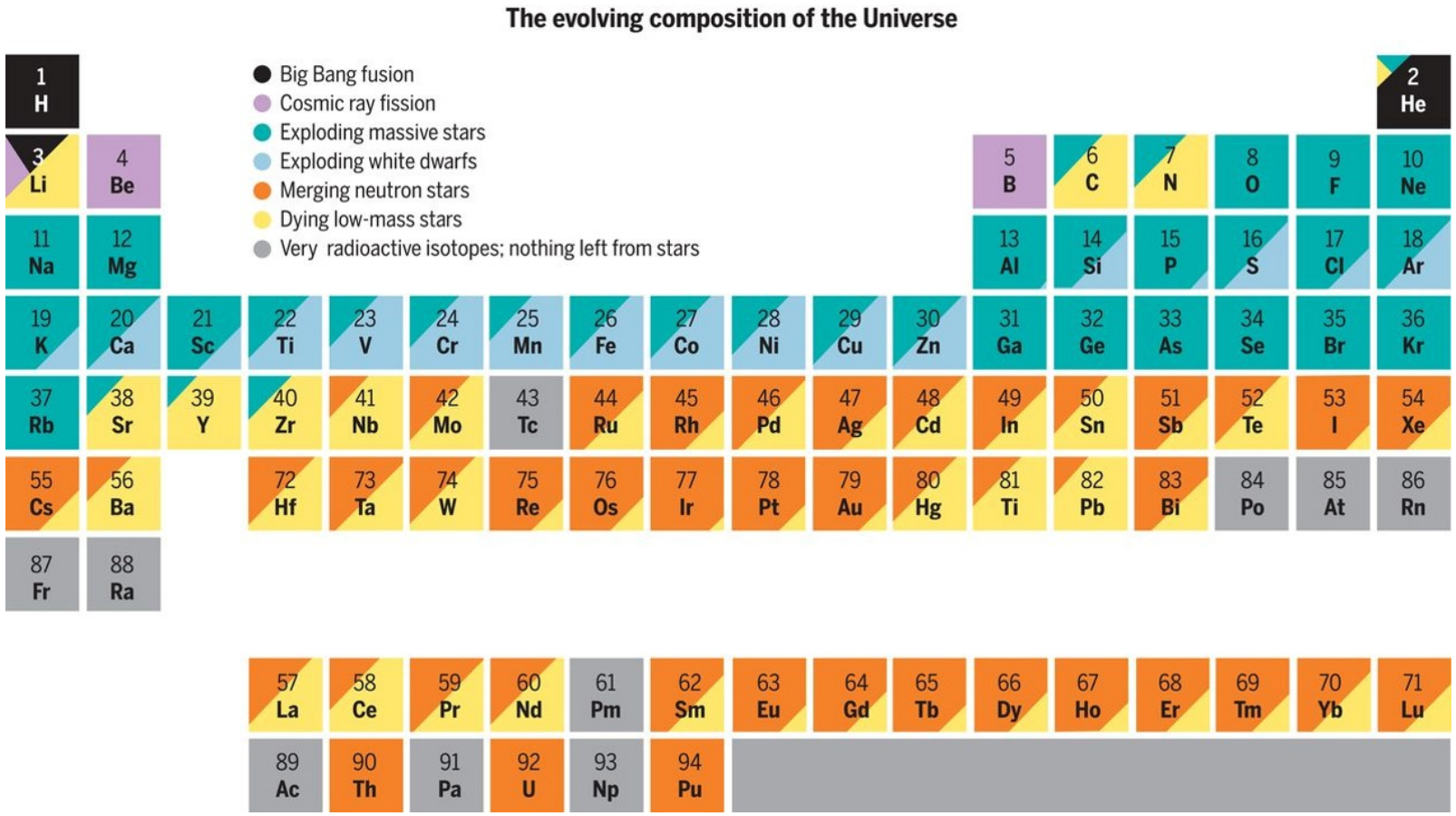

Figure 1.4: The periodic table. Chemical elements are color-coded to indicate the relative contribution from each nucleosynthesis site. Figure credit: Ref. [9].

The Life of Stars

The first stars did not for some ~100 million years after the inception of the universe. The average temperature of the gas was too high for gravity, the weakest of the four fundamental forces of nature, to overcome the thermal pressure of the gas. At first, this prevented gas clouds from clumping together and collapsing to form stars, but eventually, once the universe reached ~100 K, the first generations of stars were able to form. This is was the only time period in our universe's history in which star formation favored stellar masses greater than that of our Sun. This is because the diversity of heavier chemical elements in our modern universe, with their higher degrees of freedom in atomic and molecular transitions, allow kinetic energy that would otherwise be conserved in the random motion of simpler atoms to be radiated away, cooling down the gas clouds more rapidly. This meant that in the early universe, more material was needed to clump together in order for the gravitational force to be strong enough to collapse a gas cloud into a star.

Eventually, when the first star did form, only H and He were available for nucleosynthesis, which proceeded quite slowly. Essentially the only reaction available was $p + p \rightarrow d + e^+ + \nu_e$, which requires the weak interaction to turn a proton into a neutron and is extremely unlikely to occur. Since this p-p fusion does not produce enough energy to power the star, the star begins to collapse in on itself [10]. However, in the process of stellar contraction, the nuclear fuel heats up, causing any He produced via H fusion process to be converted relatively quickly to carbon (C) through the triple-α reaction [11]. Once C was present, this kicked off the *carbon-nitrogen-oxygen* (CNO) *cycle*, acting as a catalyst for the processing of ^{1}H into ^{4}He, as shown in Figure 1.5. The CNO cycle prevents stellar collapse and begins producing more N and O as well [12].

The core of a star will continue to fuse H into He until all of the H fuel has been exhausted. This happens much more quickly in high-mass stars because, despite having more H nuclei to fuse than low-mass stars, their stronger gravity produces higher temperatures in their interior, accelerating the rate at which these *thermonuclear reactions* occur. This makes high-mass stars more luminous and shorter-lived than low-mass stars. H-burning in a star with the mass of our Sun ($M_\odot$) lasts for 10 billion years, while a star with ten times that of a *solar mass* will exhaust its H reserves in 25

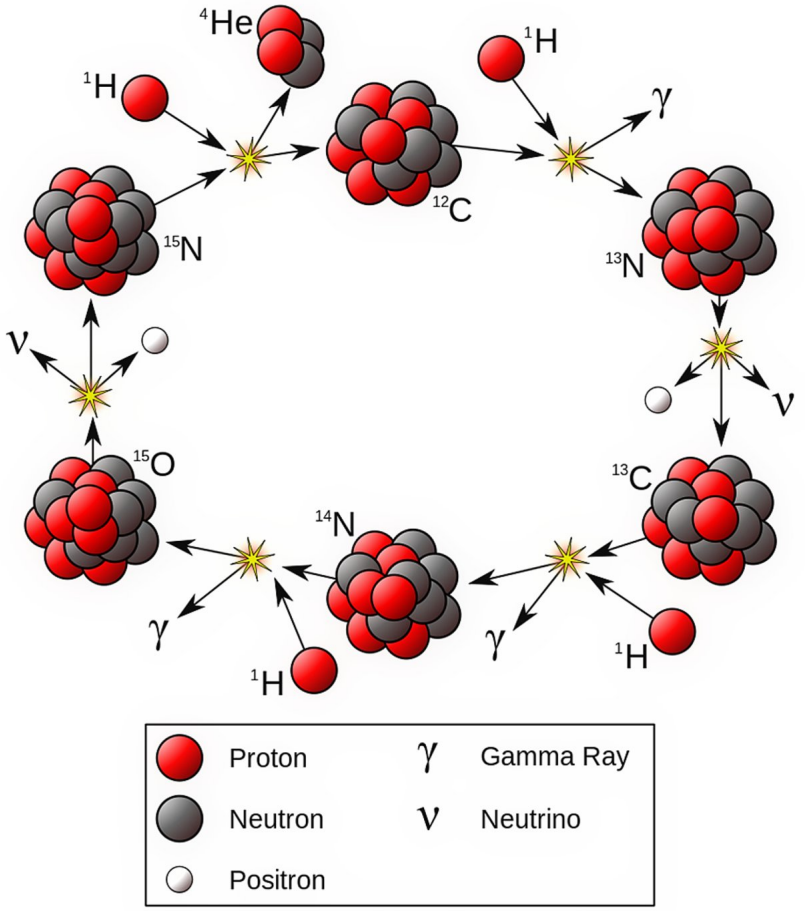

Figure 1.5: The CNO cycle. Figure credit: Borb.

million years; a 30-$M_\odot$ star will complete the H-burning stage in only 6 million years [13]. Once H burning in the core ceases, the star can not longer support its own weight and begins to contract, causing the core to heat up and increasing the probability for He fusion reactions to take place. At ~10 K, He burning ignites to synthesize C and O; the star stops contracting once the outward thermal radiation pressure and the inward force of gravity reach equilibrium [9].

The Death of Stars: With a Bang

Provided that the star is massive enough ($\gtrsim 8\ M_\odot$), this cycle of nuclear burning in the core until fuel is exhausted, followed by stellar contraction, and the ignition of a new source of nucleosynthesis, can

repeat for progressively heavier elements. All the while, lighter elements in the shells surrounding the core can continue to burn as well. Once ^{12}C nuclei start fusing together, the nuclear reactions become more varied, forming not only ^{24}Mg, but also ^{23}Na+p and ^{20}Ne+α, among others [14]. At the next stage, highly energetic photons can begin to break apart Ne nuclei via *photodisintegration*, which facilitates the α-capture reaction $^{20}\mathrm{Ne}(\alpha,\gamma)^{24}\mathrm{Mg}$. During the phase of C and Ne burning, leftover O from the He-burning stage remains inert, but once the stellar interior reaches temperatures $\gtrsim$1 billion K, it too ignites [10; 14].

Once the last of the O fuel has been exhausted, what is left in the core is mainly silicon (Si). The star contracts once again, bringing the core to a temperature of 3 billion K, but even at these extreme temperatures, the electrostatic repulsion from the $Z = 14$ nuclei prevents the Si nuclei from fusing together. The photodisintegration reactions (γ, p) and (γ, α) involving intermediate-mass nuclei within the stellar interior produce p and α particles, which are then able to overcome the *Coulomb barrier* of Si and other intermediate-mass elements, like sulfur (S). These (p, γ) and (α, γ) reactions drive the Si-burning stage towards the *iron peak* elements, including Fe and Ni [15]. In order of increasing binding energy per nucleon, ^{56}Fe, ^{58}Fe, and ^{62}Ni are the mostly tightly bound nuclei in nature [16]; beyond this mass region, nucleosynthesis is endothermic.

Each successive burning stage takes less time to complete than the previous. This is because nuclear reactions become less exothermic, and more of the energy that is released will be carried away from the core by neutrinos. The thermonuclear reactions that produce the thermal radiation pressure necessary to the support the star under the crushing weight of its own gravity, increasingly consume more nuclear fuel. In the case of a 15-$M_\odot$ star, core H burning lasts on the order of millions of years, while C burning lasts only a few thousand years. By the time the star reaches the stage of O burning, it ends within a few weeks, and the Si burning that follows only lasts several days [17]. Near the end of its life, the massive star has accumulated a 1.4-$M_\odot$ Si-burning core, surrounded by a series intermittent burning shells: O, Ne, C, He, and H, listed in order of increasing radial distance from the core. Most of these shells contain at least half a Sun's worth ($\gtrsim$0.5 $M_\odot$) of processed, nucleosynthetic material ready to be injected into the cosmos [9].

As the Si-burning stage terminates near the end of a massive star's life cycle, the stellar core can no longer produce enough energy from nuclear reactions to oppose its collective gravity; the collapse is inevitable. The core contracts slowly at first, but as the iron-peak nuclei photodisintegrate and the temperature reaches that of the early universe, protons and high-energy electrons can start synthesizing neutrons again. These processes dissipate energy from the core, accelerating its collapse. The details surrounding the physical processes governing these extremely massive, energetic, and complicated events called *core-collapse supernovae* (CCSNe) are an ongoing subject of research in computational astrophysics [18; 19; 20]. Nevertheless, it is believed the rapid change in density causes a shock wave to propagate out through the outer shells, driving one last burst of nucleosynthetic activity in the final moments of the massive star's violent death [21] and ejecting all that enriched nuclear material processed over a stellar lifetime into space.

What remains of the core depends on its mass at the time of the explosion. Most stars with initial masses >30 $M_\odot$ should lead to *black holes* [22], localized regions of spacetime so dense that their immense gravity prevents any matter or light from escaping [23]. Black holes do not directly contribute to the chemical evolution of galaxy but actively delete nuclear matter from existence. However, only about ~10% of supernovae come from stars with initial masses >20 $M_\odot$ [24]. The consensus is that the majority of stars in the mass range $8M_\odot < M < 20M_\odot$ will result in a supernova that leaves behind an ultradense remnant of the collapsed core called a *neutron star* [22], which likely play a prominent role in the nucleosynthesis of the heaviest elements found in nature called the *rapid neutron-capture process*, or *r-process*.

The Death of Stars: With a Whimper

In stars with masses $\lesssim 8\ M_\odot$, the nucleosynthesis reactions powering their evolution typically cease after the production of C and O, or perhaps Mg and Ne, in slightly more massive stars; these elements are tightly bound gravitationally to the stellar core [9]. Since energy is no longer being generated in the core to oppose the inward pull of gravity, the core contracts, but the temperature never gets high enough to ignite the next stage of nuclear burning. Eventually, this contraction

is halted by the *degeneracy pressure*. The stellar core becomes so compressed that the fermions cannot be packed any more tightly without violating the Pauli exclusion principle. Having shrunk to a fraction of its original size, its gravitational hold on the outer layers of the star gradually weakens. As this happens, the stellar envelope is slowly ejected over the course of >100 thousand years, along with the He, C, and N synthesized in its shell burnings [9], leaving behind a hot, dense remnant of the stellar core; these objects are called *white dwarfs*.

This is the ultimate fate of stars like our Sun. Without nuclear reactions to power their evolution or energetic particles to dissipate their energy, white dwarfs remain dormant indefinitely. Although not active, they are still very hot and will cool extremely slowly, emitting their thermal energy via emission of *black-body radiation*. This process will take longer than the current age of the universe, but eventually, once a white dwarf radiates away the last of its energy, it will reach thermal equilibrium with whatever still remains of the interstellar medium and become invisible within the void of space: a *black dwarf*.

While low-mass stars do not undergo such dramatic deaths as their more massive counterparts, they still play an important role in processing nuclear material. For one, they live much longer than massive stars do, and they are much more common in our modern universe [25]. In fact, they are responsible for synthesizing a substantial fraction of the heavier elements in the universe. This is possible because temperatures only need to be high enough for nuclear reactions that release neutrons, not for nuclei with large numbers of charged particles to merge [9]. Neutrons in low-mass stars are not produced by high-energy collisions between protons and electrons, but dying low-mass stars can produce free neutrons in their He-burning shells under certain circumstances [25]. Through the process of convection, fresh material from the unreacted, H-rich envelope can be mixed into the He-burning shell, and the combination of ^{4}He, ^{1}H, and ^{12}C enables a series of nuclear reactions that produce ^{16}O, releasing a neutron in the process.

These free neutrons readily fuse with Fe and other seed nuclei forged by the generation of stars that preceded them. A seed nucleus typically captures a neutron every few weeks to months [26]. If a neutron-capture results in a product nucleus that is radioactive, it will almost certainly undergo

β^- decay before it can capture another nucleon, thus slowly synthesizing heavier nuclei close to the valley of stability. Due to the long timescales over which this process occurs, it is called the *slow neutron-capture process*, or *s-process.* However, this tedious mechanism is not the only way that low-mass stars can contribute to the chemical enrichment of the galaxy. In fact, even their white-dwarf corpses can play an important role in explosive nucleosynthesis, provided that they are found in a *binary star*.

Classical Novae

Depicted in Figure 1.6, a *classical nova* is a luminous eruption that occurs in a binary system that includes a white dwarf and a nondegenerate stellar companion, which orbit around a common center of mass. As the active companion star evolves, its radius swells, and as it begins to overflow its *Roche lobe*, the white dwarf can begin to siphon material from the H-rich donor to form an *accretion disk* around its surface [27]. As this accreted layer builds up on the surface of the compact white dwarf, the density and temperature of the compressed material rise, increasing the rate of nuclear burning. The stability of this nuclear burning process is very sensitive to the mass of the underlying white dwarf as well as the rate of accretion. Once a critical mass is reached, the layer becomes unstable, triggering a *thermonuclear runaway* event [28; 29; 30]. The energy released causes the H-rich envelope to expand tremendously, leading to its ejection and often dredging up dense nuclear material from deeper layers of white dwarf in the process [31].

The standard paradigm of classical nova models is one driven exclusively by thermal emission from the hot white dwarf. After the thermonuclear runaway, the ejected shell of gas expands into the surrounding environment at $\sim 10^2 - 10^3$ km/s [31]. They are most identifiable as *optical transients*, where the intensity of their visible light is observed to rise rapidly to a maximum and then decay over the timescale of days or months [32]. However, as their ejecta expand and dilute, they become increasingly transparent to radiation of shorter wavelengths, and their spectral energy distribution shifts to the predominantly ultraviolet (UV) part of the spectrum [33]. Eventually the photosphere recedes sufficiently inward that the white dwarf is visible in the low-energy part of

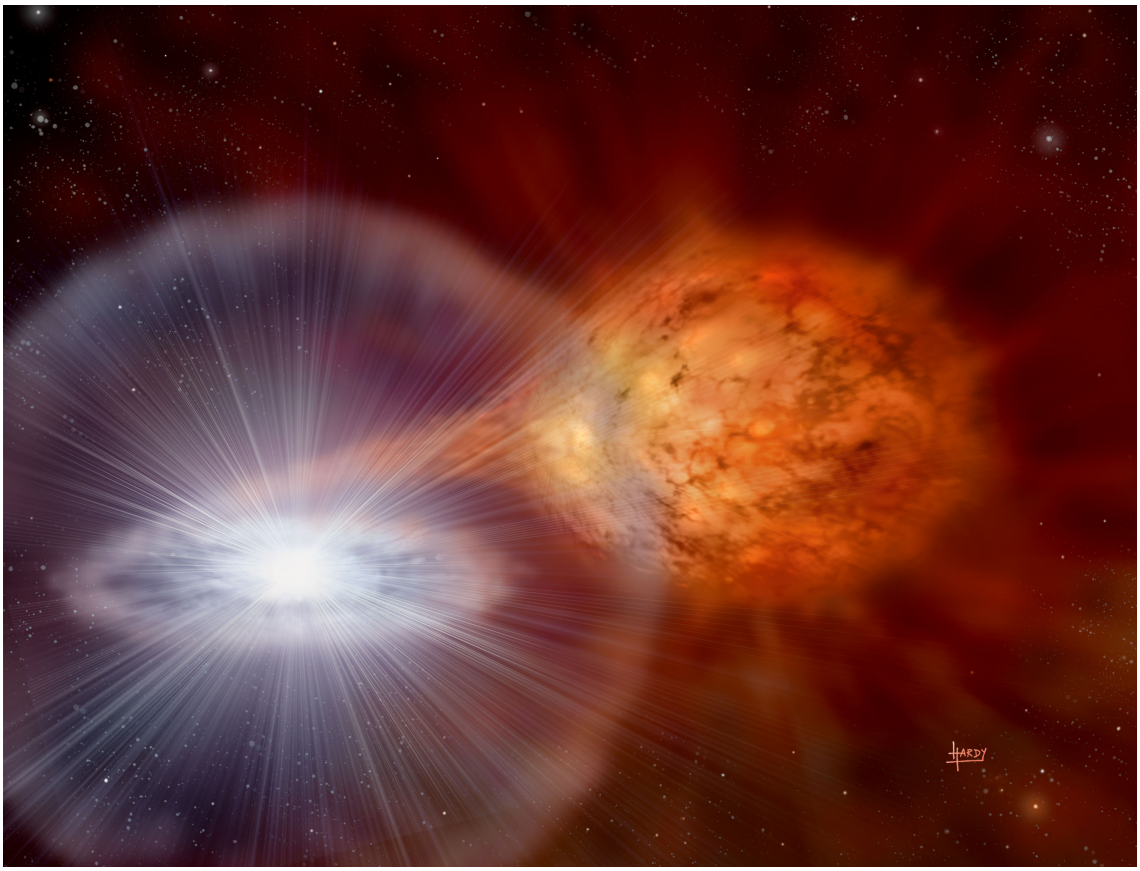

Figure 1.6: Artist's depiction of a classical nova. Figure credit: astroart.org, David A. Hardy.

the X-ray spectrum, sustained by residual nuclear burning for weeks or potentially even years [34]. Many novae also form dust grains in their ejecta, which are revealed by sudden increases in their infrared (IR) emission [35]. This dust formation occurs rapidly and nova grains grow to large sizes ($\sim$1 μs) compared to dust from the intersteller medium [36; 37].

Derived from the Latin *stella nova*, meaning "new star," the misnomer originates from Danish astronomer Tycho Brahe's 1573 book entitled *De nova stella*, in which he reports the observation of what appeared to be a new star in the night sky; this stellar event has since been identified as a supernova, named B Cassiopeiae (SN 1572) [38]. Unlike supernovae, which typically result in the destruction of their stellar host, nova events will often recur on the timescale of years or decades. Although estimates of the galactic nova rate have varied widely over the years [39; 40], by all accounts, these events are common. Their frequency is $\approx 20 - 70$ eruptions per year in the Milky

Way, with about a dozen observed annually [41]. This detection rate has increased in recent years and is likely to continue to do so with more time dedicated to finding them using state-of-the-art telescopes [42]. Still, many of these observations are reported by amateur astronomers as classical novae are among the brightest transients in the night sky.

Despite their storied role in the history of astronomy, the abundance of observational nova data, and significant progress in computational ability, many open questions surrounding classical novae remain. We cannot begin to address them all here, but in this dissertation, we will provide meaningful constraints on nuclear uncertainties associated with modeling explosive nucleosynthesis in the thermonuclear runaway of classical novae.

CHAPTER 2

THE ^{30}P$(p,\gamma)^{31}$S REACTION

2.1 Effects on Astronomical Observables

Nova Nucleosynthesis

Classical novae are the second-most common type of thermonuclear eruptions in the galaxy, following Type I X-ray bursts which occur in stellar binaries involving a neutron star instead of a white dwarf [43]. In spite of this, they only process a small fraction of the interstellar matter throughout the Milky Way, contributing very little in the way of galactic dust condensed from stellar outflows [44]. Nevertheless, simulations and observational evidence both suggest that novae are responsible for the overproduction of certain nuclei such as ^{7}Li [45; 46], ^{13}C, ^{15}N, and ^{17}O [29; 47; 48; 49; 50; 51], perhaps accounting for a significant fraction of their galactic content [52]. Radioactive γ emitters are also produced in novae [53; 54; 55; 49; 56; 51]. For example, most novae are thought to produce the long-lived radionuclide ^{26}Al and could be responsible for up to 30% of its presence in the Milky Way [57]. Some novae are also expected to produce ^{22}Na, whose shorter half-life might enable the detection of nova sites via this radionuclide's unique γ-decay signature, depending on how much of it survives explosive nucleosynthesis [58]. Even heavier species like ^{31}P, ^{32}S, ^{33}S, and ^{35}Cl have been reported to originate in novae as well [49; 51], but the accuracy and precision of modeling the chemical composition of their ejecta is constrained by uncertainties in the thermonuclear rates of the nuclear reactions that participate in nova nucleosynthesis.

Hydrodynamic simulations are used to model explosive nucleosynthesis in classical novae. During the thermonuclear runaway, nuclei participate in a complex reaction network of competing weak interactions, such as β^{+} decay and electron capture, versus proton- and α-capture reactions, as shown in Figure 2.1. The rates at which these nuclear processes occur affect the path of nucleosynthesis in classical novae, which is close enough to stability such that many of these decay

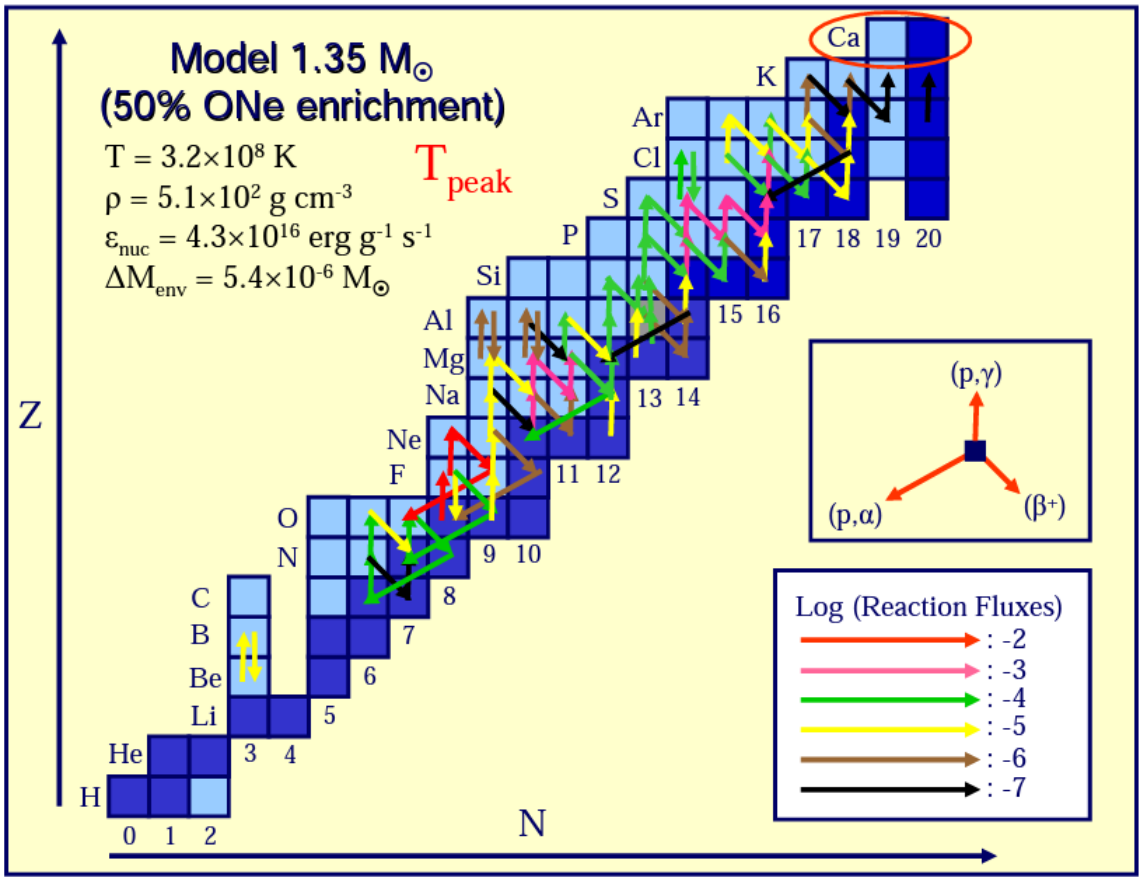

Figure 2.1: Path of nucleosynthesis in an ONe nova involving a 1.35-$M_{\odot}$ white dwarf, assuming a 50% mixing ratio between the H-rich envelope and the underlying white dwarf material. Nuclides shown in dark blue are stable, while light blue squares correspond to radioactive nuclei. Figure credit: Ref. [59].

and reaction rates can be determined experimentally. For this reason, many of the relevant nuclear reactions in novae have been sufficiently constrained for modeling the chemical composition of their ejecta. However, sensitivity studies of ONe novae involving the most massive white dwarfs indicate that ^{30}P$(p,\gamma)^{31}$S is the largest remaining source of nuclear uncertainty for the synthesis of intermediate-mass elements [60; 61].

The 2.5-minute half-life of ^{30}P is on the order of the thermonuclear runaway event, making it a waiting-point nucleus. Thus, the ^{30}P$(p,\gamma)^{31}$S reaction serves as a bottleneck to the production of $A > 30$ in ONe novae. Furthermore, its thermonuclear rate affects the chemical and isotopic abundances of the processed nuclear material that ONe novae contribute to the galaxy. These

observables can also inform our understanding of individual novae and their properties.

Presolar Grains

Perhaps the most interesting effect of the $^{30}\mathrm{P}(p,\gamma)^{31}\mathrm{S}$ reaction on the isotopic ratios of nova ejecta is related to the classification of a handful of unidentified *presolar grains* recovered from certain meteorites; an example is depicted in Figure 2.2. These are tiny bits of stardust, often only a few microns in length, that were ejected as hot plasma from their original astrophysical source into interstellar space before cooling and condensing into crystalline granules. These grains were then incorporated into the *molecular cloud* and mixed with the surrounding material, which eventually condensed to form the Solar System [62]. Thus, they are said to be "presolar" because they were forged before the formation of the Solar System and can be identified by isotopic ratios that are well outside the expected range for terrestrial rocks and meteoroids formed in the early Solar System. The discovery and detailed analysis of these grains has opened up a new field within astronomy, providing unique insights into the formation of the Solar System as well as the chemical evolution of the Milky Way [63; 64; 65]. Several different types of presolar grains have been identified, including silicon carbide (SiC), graphite (C), diamond (C), silicon nitride (Si_3N_4), and various silicate and oxide compounds [66], but to date, none have been confirmed originating in classical novae.

SiC grains are among the most well-studied presolar grains and can be classified into distinct populations according to their stellar birthplace [67]. Almost all of these grains come from the outflows of *asymptotic giant branch* (AGB) stars, with the 93% "mainstream" population originating in low-mass stars of this variety [68; 69; 70]. Another 4 – 5% are classified as AB grains, characterized by low $^{12}\mathrm{C}$:$^{13}\mathrm{C}$ ratios, and while several types of stars have been proposed as progenitors of AB grains, the majority likely originated in C-rich, so-called *J-type* stars [71]. Y and Z grains make up about 1% each, whose origins are linked to low-metallicity AGB stars [72; 73; 74], while X grains account for the remaining 1% and are distinguished by their large excesses in $^{44}\mathrm{Ca}$ and $^{28}\mathrm{Si}$, evidence they formed in the ejecta of supernovae [75; 76]. However, ion

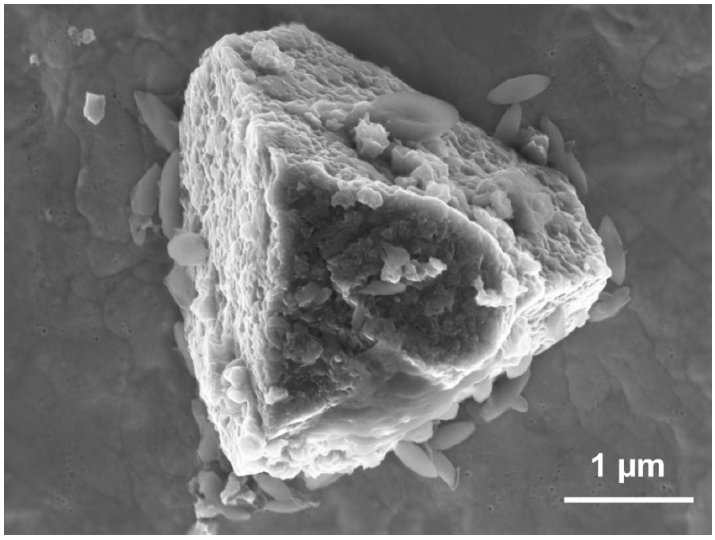

Figure 2.2: Electron microscope image of a SiC presolar. Photo credit: J. Huth, A. Besmehn, and J. Kodolányi, Max Planck Institute for Chemistry.

microprobe isotopic analysis of several rare SiC grains, as well as a few anamolous graphite grains, has revealed isotopic signatures indicative of potential nova origins [77; 78].

Classical novae have previously been implicated in some of the isotopic anomalies found in meteorites, despite the fact that they are not major contributors to the chemical evolution of the galaxy. Although about $30 - 40\%$ of novae are known to produce dust some $20 - 100$ days after their initial outburst [79], the argument for the existence of nova grains has relied primarily on low ^{20}Ne:^{22}Ne ratios in certain graphite grains, which could be attributed to the decay ^{22}Na, potentially indicative of nova nucleosynthesis [80; 81; 82]. In contrast, these unusual grains have low ^{12}C:^{13}C ratios, extremely low ^{14}N:^{15}N ratios, and high ^{26}Al:^{27}Al ratios, all qualitatively consistent with theoretical predictions for both CO and ONe nova models [77]. The C and N ratios are plotted in Figure 4.20 for grain data taken from the Presolar Database at Washington Unviersity in St. Louis [83; 84].

These candidate nova grains also exhibit large excesses in ^{30}Si. The Si isotopic ratios of various presolar grains are shown in Figure 2.4. Generally speaking, ^{29}Si:^{28}Si and ^{30}Si:^{28}Si ratios of nova ejecta increase with white dwarf mass. Thus, all CO nova models predict close-to or lower-than solar ^{29}Si:^{28}Si ratios as well as close-to solar ^{30}Si:^{28}Si ratios. While nucleosynthesis is mostly

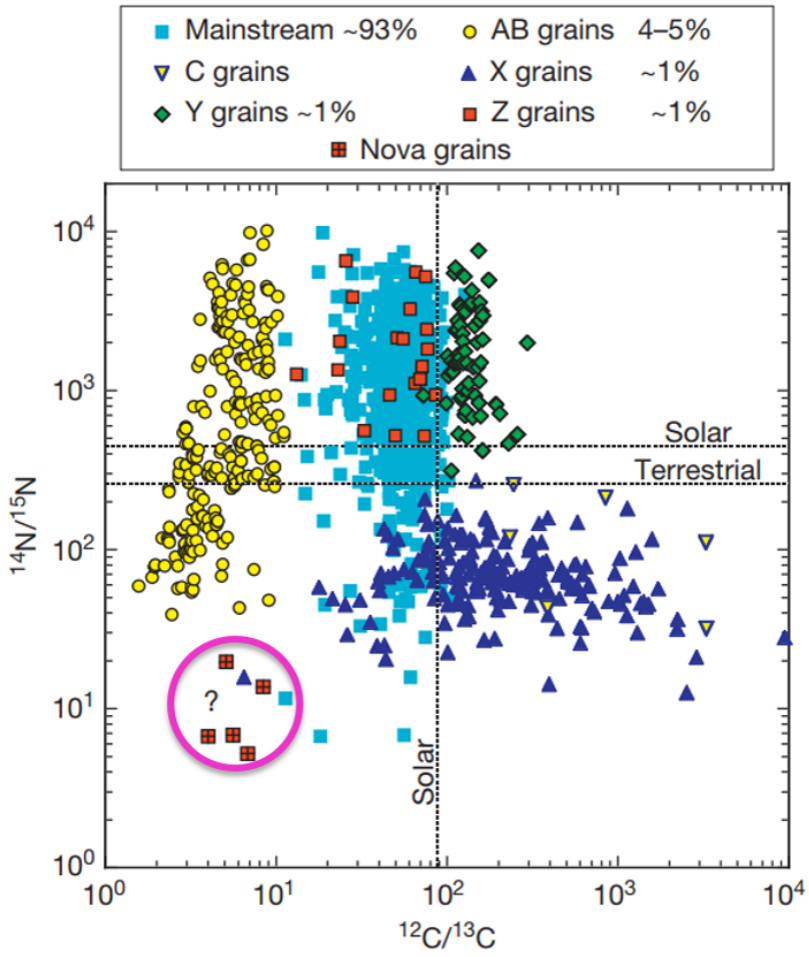

Figure 2.3: Isotopic ratios for plotted for C and N. Candidate nova grains are circled in magenta. Figure credit: Ref. [85].

constrained to the CNO mass region for CO novae, the higher peak temperatures in ONe novae and the more abundant "seed" nuclei from beyond the CNO mass region lead to the synthesis of intermediate-mass elements. So while all ONe nova models predict close-to or lower-than solar ^{29}Si:^{28}Si ratios and models for white dwarf masses $\leq$1.15 predict close-to or lower-than solar ^{30}Si:^{28}Si ratios, ONe nova models for white dwarf masses $\geq$1.25 $M_\odot$ predict large excesses in ^{30}Si [60].

The conclusion that these unidentified grains are from ONe novae ejecta, however, is controversial for two main reasons. First, not only are ONe novae less common than CO novae, they are also less prolific dust producers. Second, the isotopic abundance of ^{30}Si in ONe nova ejecta is vastly

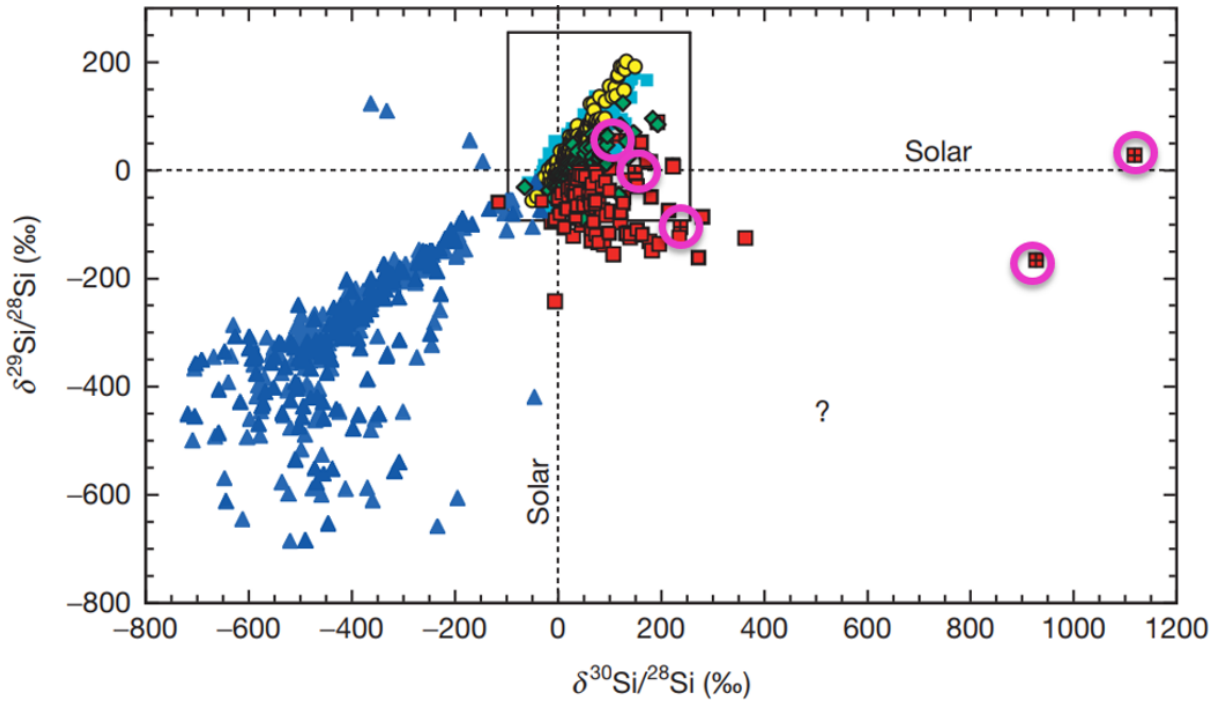

Figure 2.4: Isotopic ratios for plotted for Si. Candidate nova grains are circled in magenta. Figure credit: Ref. [85].

over-predicted by simulations compared to grain data. To quantitatively reproduce the observed ^{30}Si:^{28}Si ratios, one must assume some unknown mixing process between the freshly synthesized, ^{30}Si-enriched material and over 10 times as much unprocessed, isotopically close-to-solar material before the grains formed [60]. Because of these complications, in recent years, there have been efforts to explain SiC grain formation in the ejecta of CO novae without invoking this dilution process [79; 86]. While one-dimensional (1D), hydrodynamic simulations represent the current state-of-the-art capabilities of nova modeling and generally agree with astronomical observations of elemental abundances, large systematic uncertainties remain [60]. For one, the parameter space of all relevant input variables is quite large and includes factors such as the composition of the white dwarf, the peak temperature and density, the explosive timescales, any possible dilution of ejecta after the outburst, as well as potentially the biggest unknown, how the accreted material from the donor star mixes with the outer layers of the WD [79]. So far, multidimensional investigations into this mixing problem have not been successful in reproducing the gross properties of nova outbursts

[77], and to make matters worse, the lack of convective mixing in these parameterized calculations leads to overestimating the influence of nuclear uncertainties [60]. These theoretical challenges cannot be directly eliminated by nuclear physics experiments, but these measurements can be employed to reduce uncertainties associated with reaction rates that confound model predictions.

Currently, most theoretical models rely on the *Hauser-Feshbach statistical method* for evaluating the ^{30}P$(p,\gamma)^{31}$S rate. When estimating the effect of nuclear uncertainties on their predictions, modelers will often vary this rate by arbitrary factors of 10. Tightening the error bars on this rate could substantially constrain the range of predicted ^{30}Si:^{28}Si ratios for candidate nova grains. If proton-capture on ^{30}P is particularly rapid in ONe novae, this will enable increased nucleosynthesis of $A > 30$ nuclides. However, if this reaction proceeds relatively slowly on the timescales of the thermonuclear runaway, the radioactive ^{30}P will primarily β^+ decay to stable ^{30}Si, leading to excesses in ONe nova ejecta.

Nuclear Thermometers and Mixing Meters

Observational studies using IR, UV, and optical spectroscopy are able to identify elemental abundances within the ejecta shells surrounding nova sites [44; 87; 88]. The ejected gas and dust from nova outbursts consist of white dwarf matter and the accreted material from the companion star, which have been processed by explosive H-burning. The chemical makeup of this ejecta provides information about the composition of the underlying white dwarf as well as the thermonuclear runaway event, including the peak temperature achieved and the expansion rate of the accreted envelope. Thus, chemical abundances can be used to constrain models of stellar explosions [89]. Hydrodynamic simulations using the 1D code SHIVA were performed for a range of white dwarf masses suggest that several abundance ratios are quite sensitive to temperature and may be useful *nuclear thermometers* for constraining the peak temperatures achieved in novae [52]. The hydrodynamic models were used to calculate temperature-density profiles across all mass zones of the envelope. This profile served as input for Monte Carlo post-processing nuclear reaction network calculations to assess the impact of thermonuclear rate uncertainties.

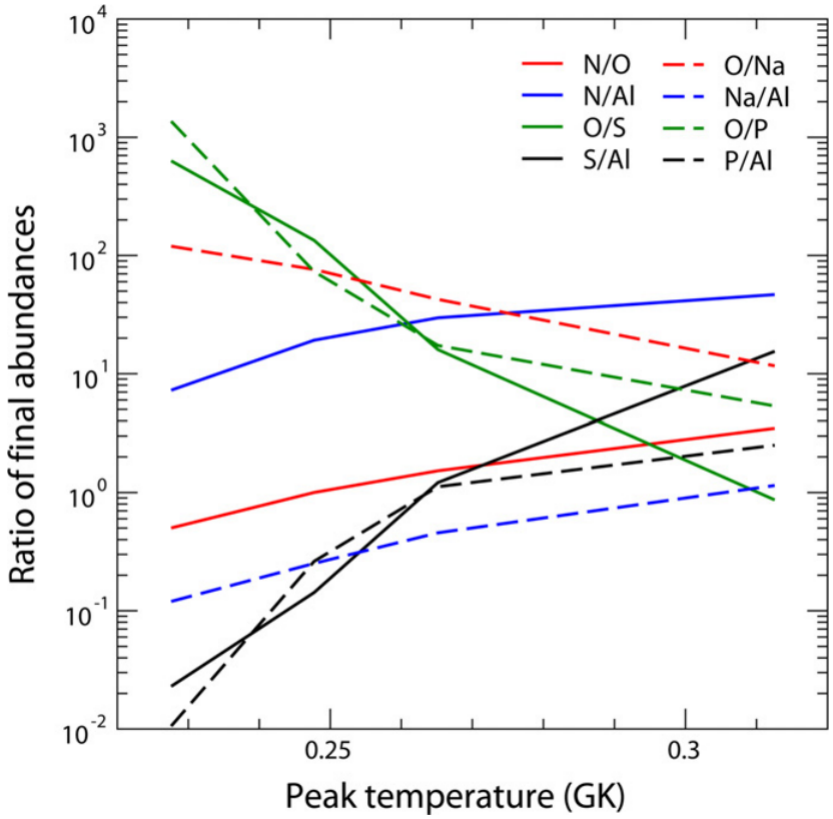

Figure 2.5: Ratios of elemental abundances, given in terms of their mass fractions, plotted as function of peak temperature achieved in hydrodynamic nova model simulations. Figure credit: Ref. [90].

The best candidate thermometers exhibit steep, monotonic dependence on peak temperature and include N:O, N:Al, S:Al, O:Na, Na:Al, O:P, and P:Al. These are plotted in Figure 2.5. The sensitivity of these thermometers to variation in thermonuclear rates has been investigated using post-processing nucleosynthesis calculations, and while N:O, N:Al, O:Na, and Na:Al are robust to these uncertainties, O:S, S:Al, O:P, and P:Al strongly influenced by the poorly constrained rate of the $^{30}\mathrm{P}(p,\gamma)^{31}\mathrm{S}$ reaction. Thus, determining this thermonuclear rate would reduce uncertainties associated with these nuclear thermometers and allow a more precise, accurate determination of peak nova temperatures.

The peak temperature achieved in a nova strongly depends on the mass of the underlying white dwarf and its initial luminosity. It also is influenced by the mass, metallicity, and accretion rate of the disk [90]. The fact that both the processed, H-rich fuel and material from the outer layers

of the white dwarf can be observed in nova ejecta suggests that there must be mixing between the two stellar sources before the thermonuclear runaway, but the mechanism by which this occurs is not well-understood [91; 92; 93]. However, the extent to which the envelope mixes with the outer layers of the dense white dwarf affects the chemical abundances of the observed nova ejecta. Thus, like thermometers, certain elemental abundances can be used as *nuclear mixing meters* if there is a steep, monotonic relationship between the abundance ratio and the *mixing fraction*, which is defined as mass of the outer white dwarf matter that has been mixed as a fraction of the envelope [94].

Nova simulations have been performed for three different mixing fractions $25 - 75\%$ at four different white dwarf masses ($1.15 - 1.35\ M_{\odot}$) with a fixed initial luminosity and accretion rate. Just as in the studies investigating nuclear thermometers, hydrodynamic simulations were used to evaluate the temperature-density across the active burning regions in the nova. Nuclear reaction network calculations were used to quantify the affect of reaction rate uncertainties on the final ejecta abundances. The results of these calculations, as shown in Figure 2.6, identified several useful mixing meters for ONe novae, including ΣCNO:H, Ne:H, Mg:H, Al:H, and Si:H. While most of these ratios were found to be robust with respect to thermonuclear rate uncertainties, again the $^{30}\mathrm{P}(p,\gamma)^{31}\mathrm{S}$ reaction was implicated in the uncertainty of Si:H ratios. The error bars on each elemental abundance are largely unchanged between the top and bottom panels in Figure 2.6, with the exception of Si, since it is highly sensitive to the rate of proton capture on ^{30}P. This further motivates the experimental determination of this critical thermonuclear rate for constraining ONe nova models.

2.2 Thermonuclear Reaction Rate Formalism

Here, we follow a derivation provided in Christian Iliadis's *Nuclear Physics of Stars* [15] to arrive at a general formula for the total thermonuclear rate of a non-specific nuclear reaction. A more detailed description of reaction theory and its applications to nucleosynthesis can be found there, as well as in *Nuclear Reactions for Astrophysics* by Thompson and Nunes [95].

In nuclear physics, often the most fundamental quantity used to describe the probability that

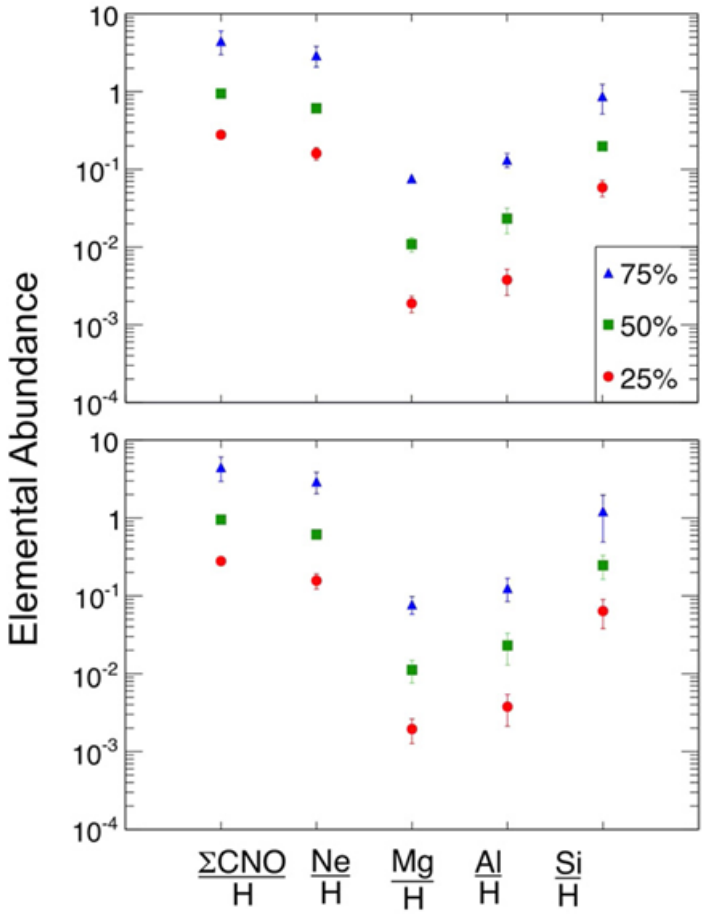

Figure 2.6: Elemental abundances, given in terms of their mass fraction relative to H, predicted in hydrodynamic nova model simulations. The three different marker shapes/colors represent the mixing ratios between the underlying white dwarf material and the H-rich envelope. Top panel: Error bars only include variation due to changes in peak temperature. Bottom panel: Error bars include variation due to changes in peak temperature as well as uncertainties in thermonuclear reaction rates. Figure credit: [94].

two nuclei will participate in a reaction is the *cross section* σ. Consider the simple case of beam particles impinging on a target area A at a constant rate N_b/t. The cross section is defined as the ratio between the number of reactions per unit time N_r/t and the product of the number of nonoverlapping target nuclei N_t times the beam flux:

$$\sigma \equiv \frac{N_r/t}{N_t \cdot N_b/(tA)}. \tag{2.1}$$

Thus, we can write the rate at which nuclear reactions occur within some volume V in terms of the cross section and the relative velocity between the beam particle and the target nucleus:

$$\frac{N_r}{t \cdot V} = \sigma \cdot \frac{N_t N_b}{tA \cdot V} = \sigma v \frac{N_t}{V} \frac{N_b}{V}. \tag{2.2}$$

In a stellar environment, neither the target nor the projectile particles are ever truly at rest, and the nuclear reaction cross section depends on the relative velocity between the two nuclei. For a reaction involving four species $1 + 2 \rightarrow 3 + 4$, we can define our *reaction rate* $r_{12} \equiv N_r/(Vt)$ and write it in terms of the number densities for the target nucleus ($N_1 \equiv N_t/V$) and projectile nucleus ($N_2 \equiv N_t/V$) as

$$r_{12} = N_1 N_2 v \sigma(v). \tag{2.3}$$

In principle, the relative velocity between projectile and target nuclei can be any positive real number, which we can represent as an arbitrary probability distribution $f(v)$, where $\int_0^\infty f(v)dv = 1$. Generalizing Equation (2.3) over this velocity distribution, we can define the *reaction rate per particle pair* as

$$r_{12} = N_1 N_2 \int_0^\infty v f(v) \sigma(v) dv \equiv N_1 N_2 \langle \sigma v \rangle_{12}. \tag{2.4}$$

However, in practice, the most useful quantity for describing the frequency of nuclear reactions in stellar environments is the *thermonuclear reaction rate* $N_A \langle \sigma v \rangle_{12}$, whose units are cm^3/mol/s and where N_A is Avogadro's number.

In most astrophysical cases, particles within a stellar plasma are not degenerate and move at nonrelativistic speeds [96]. Thus, their motion in thermal equilibrium can be described using the *Maxwell-Boltzmann velocity distribution*

$$f(v)dv = \left(\frac{\mu}{2\pi kT}\right)^{3/2} e^{-\mu v^2/(2kT)} 4\pi v^2 dv, \tag{2.5}$$

where $\mu = m_1 m_2/(m_1 + m_2)$ is the *reduced mass* of the two-body system, $k = 8.6173 \times 10^{-5}$ eV/K is the Boltzmann constant, and T is the temperature of the stellar plasma. It can be shown that if the velocity distributions of both species of interacting particles are Maxwellian, then the relative velocities between the two species must also follow this distribution [14]. In the nonrelativistic limit, $E = \mu^2/2$, and thus $dE/dv = \mu v$, allowing us to write the energy distribution as1

$$\begin{aligned} f(E)dE &= \left(\frac{\mu}{2\pi kT}\right)^{3/2} e^{-E/kT} 4\pi \frac{2E}{\mu}\frac{dE}{\mu}\sqrt{\frac{\mu}{2E}} \\ &= \frac{2}{\sqrt{\pi}}\frac{1}{(kT)^{3/2}}\sqrt{E}e^{-E/kT}dE, \end{aligned} \tag{2.6}$$

which we can then plug back into Equation 2.4. After multiplying by our normalization constant N_A, we arrive at a generalized thermonuclear rate for particle-induced reactions:

$$N_A\langle\sigma v\rangle_{12} = \sqrt{\frac{8}{\pi\mu}}\frac{N_A}{(kT)^{3/2}}\int_0^\infty E\sigma(E)e^{-E/kT}dE. \tag{2.7}$$

The Gamow Window

Consider a beam of protons impinging on a target of ^{30}P. According to Equation 2.1, if the beam rate, target area, and total number of target nuclei are known, an experiment measuring the number of induced ^{30}P$(p,\gamma)^{31}$S reactions over a fixed period of time could be performed to determine the total cross section, and the total thermonuclear rate could be calculated using Equation 2.7. However, the 2.5-min half-life of unstable ^{30}P means using it as a target in a stable beam experiment is nearly impossible. Inverse kinematics experiments involving a radioactive beam of ^{30}P incident on a hydrogen target are also problematic because, due to their refractory chemical nature, ^{30}P beams

are difficult to produce with sufficient intensity at the relevant energies using either fragmentation or *isotope separation on-line* (ISOL) techniques. Due to the energy dependence of the nuclear cross section and the statistical velocity distribution of the stellar plasma, there is a relatively small range of energies that are relevant for determining a thermonuclear rate; this is known as the *Gamow window*.

The *transmission coefficient* $\hat{T}$ describes the probability of a quantum particle tunneling through a potential barrier and can be determined by solving the Schrödinger equation. For the simple case of an s-wave ($\ell = 0$) scattering on a time-independent potential, the radial equation becomes

$$\frac{d^2u(r)}{dr^2} + \frac{2m}{\hbar^2}[E - V(r)]u(r) = 0. \tag{2.8}$$

In the case of charged-particle reactions, over short distances, the attractive nuclear force between the target and projectile can be described as a square-well with some width R_0 and depth V_0, but for $r > R_0$, there exists a repulsive Coulomb potential as shown in Figure 2.7. Using this potential to solve Equation 2.8 in the low-energy limit, the leading order term for the s-wave transmission coefficient is known as the *Gamow factor*

$$\hat{T} \approx \exp\left(-\frac{2\pi}{\hbar}\sqrt{\frac{\mu}{2E}}Z_0Z_1e^2\right) \equiv e^{-2\pi\eta}, \tag{2.9}$$

where we define the Sommerfeld parameter η. The Gamow window describes the overlap between this probability density function and the Maxwell-Boltzmann distribution as shown in Figure 2.8. The *Gamow peak* is the energy at which the thermonuclear reactions are most likely to occur and can be determined by taking the derivative of the product of these two functions:

$$\begin{aligned}\frac{d}{dE}\left[\exp\left(-\frac{2\pi}{\hbar}\sqrt{\frac{\mu}{2E}}Z_0Z_1e^2 - \frac{E}{kT}\right)\right]_{E=E_0} &= 0 \\ =\exp\left(-\frac{2\pi}{\hbar}\sqrt{\frac{\mu}{2E_0}}Z_0Z_1e^2 - \frac{E_0}{kT}\right)&\left(\frac{\pi}{\hbar}\sqrt{\frac{\mu}{2}}Z_0Z_1e^2E_0^{-3/2} - \frac{1}{kT}\right).\end{aligned} \tag{2.10}$$

Thus, the peak of the Gamow window occurs at

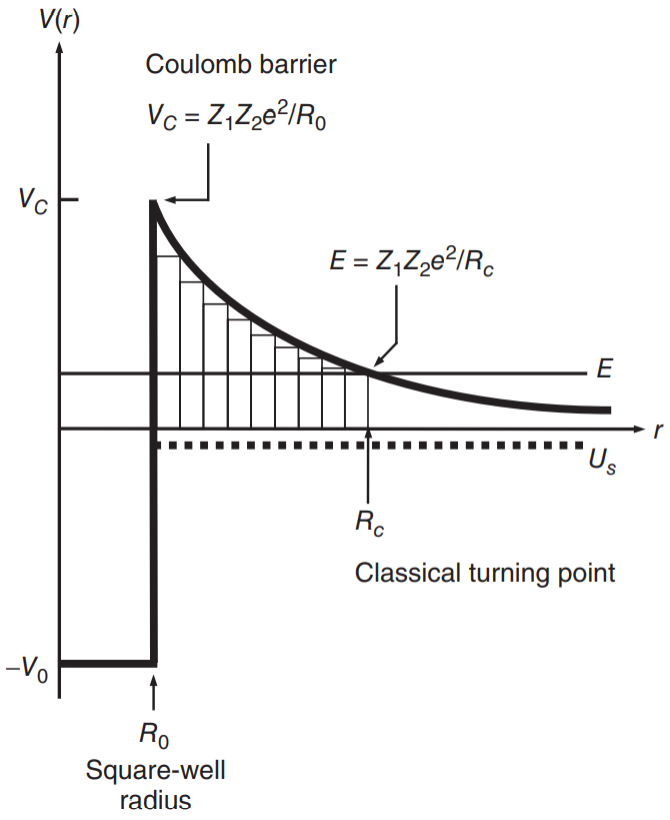

Figure 2.7: Diagram of the potential energy diagram for a charged particle with energy E approaching a nucleus as a function of radial distance $V(r)$. At long ranges ($r > R_0$), the projectile experiences repulsive Coulomb force, while over short ranges ($r < R_0$), the residual nuclear force dominates and results in an attractive potential. A projectile need not have energy $E > V_C$ to overcome the Coulomb barrier given the possibility of quantum tunneling. Figure credit: Ref. [15]

$$\begin{aligned} E_0 &= \left[\left(\frac{\pi}{\hbar}\right)(Z_0Z_1e^2)^2\left(\frac{\mu}{2}\right)(kT)^2\right]^{1/3} \\ &= 0.1220\left(Z_0^2Z_1^2\frac{m_0m_1}{m_0+m_1}T_9^2\right)^{1/3} \quad \text{[MeV]}. \end{aligned} \tag{2.11}$$

Given a temperature T_9 in units of gigakelvin (GK), this numerical expression returns the resonance energy in units of MeV at which the Gamow distribution is at a maximum for a given thermonuclear reaction.

While this distribution is asymmetric, it can be approximated with a Gaussian function of the same maximum amplitude. Rewriting the Gamow distribution in terms of E_0,

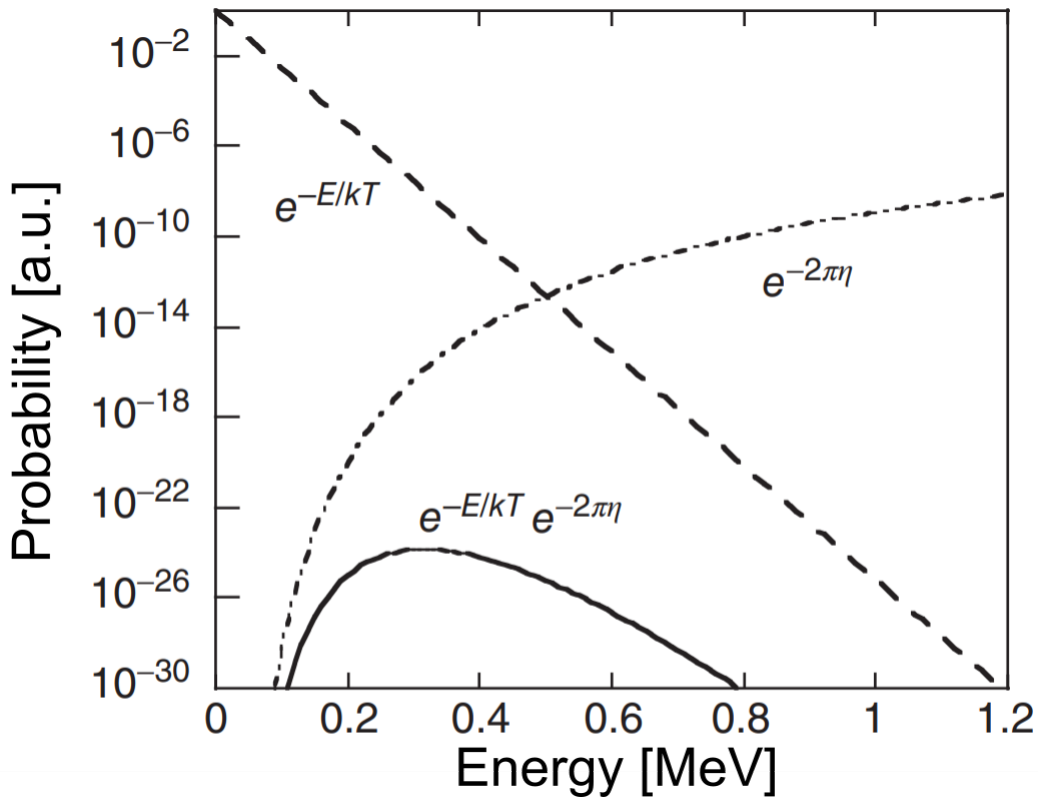

Figure 2.8: Arbitrary Gamow window. Dashed curves correspond to the Maxwell-Boltzmann distribution and the probability density for penetrating the Coulomb barrier. The Gamow window, plotted as a solid black curve, represents a product of these two probability distributions. Figure credit: Ref. [15].

$$\begin{aligned} \exp\left(-\frac{2\pi}{\hbar}\sqrt{\frac{\mu}{2E}}Z_0Z_1e^2-\frac{E}{kt}\right) &= \exp\left(-\frac{2E_0^{3/2}}{\sqrt{E}kT}-\frac{E}{kT}\right) \\ &\approx \exp\left(-\frac{3E_0}{kt}\right)\exp\left[-\left(\frac{E-E_0}{\Delta/2}\right)^2\right], \end{aligned} \tag{2.12}$$

and enforcing the condition that the curvatures must agree at $E = E_0$,

$$\begin{aligned} \frac{d^2}{dE^2}\left(\frac{2E_0^{3/2}}{\sqrt{E}kT}+\frac{E}{kT}\right)_{E=E_0} &= \frac{3}{2E_0kT} \\ = \frac{d^2}{dE^2}\left(\frac{E-E_0}{\Delta/2}\right)^2_{E=E_0} &= \frac{8}{\Delta}. \end{aligned} \tag{2.13}$$

Solving for the width of the Gamow window peak, we find

$$\Delta = 4\sqrt{\frac{E_0 kT}{3}}$$
$$\Delta = 0.2368(Z_0^2 Z_1^2 \frac{m_0 m_1}{m_0 + m_1} T_9^5)^{1/6} \quad \text{[MeV]}. \tag{2.14}$$

The peak temperature range for ONe classical novae is often reported to be $T_{\text{peak}} = 0.1 - 0.4$ GK [97], so even across a wide range of temperatures, the Gamow peak for $^{30}\text{P}(p,\gamma)^{31}\text{S}$ lies within a relatively small range at low resonance energies: $159 - 399$ keV. Still, even for $T = 0.4$ GK, this resonance energy is much higher than $kT = 34$ keV, which suggests most of the particles participating in this reaction have relative velocities sampled from the high-energy tail of Maxwell-Boltzmann distribution.

However, the Gamow window is only a rough guide for identifying the energy regime most likely to be important for constraining a nuclear reaction rate. This is because nuclear reactions can proceed in various ways, and the existence of a resonance state may greatly enhance the total thermonuclear rate, even if the resonance energy lies outside the Gamow window.

Radiative Proton Capture

The process of *radiative proton capture* involves some target nucleus ^{A}Z capturing a proton to form a $^{A+1}(Z+1)^*$ product nucleus in an excited state. That excitation energy promptly radiates away via a cascade of one or more γ ray emissions, leaving behind the $^{A+1}(Z+1)$ nucleus in its ground state configuration. Radiative proton capture reactions occur when the projectile and target nuclei get close enough such that they can interact via the attractive nuclear potential shown in Figure 2.7. In a stellar plasma, this typically happens when the center-of-mass energy of the two bodies is within the Gamow window. A nonresonant, *direct capture* reaction occurs when the target nucleus captures a proton into a bound state of the product nucleus. If a nonresonant reaction does occur, a photon is simultaneously emitted, with a γ energy equal to the difference between the excitation energy of the newly-formed $^{A+1}(Z+1)^*$ bound state and the summed kinetic energy of both the projectile and target nucleus prior to the reaction. In general, the cross section for this direct capture

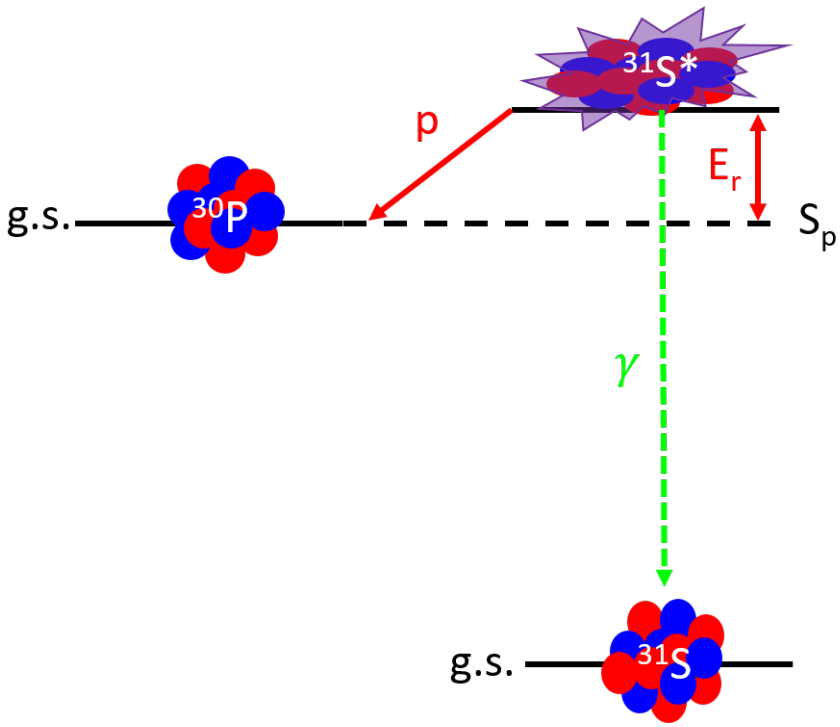

Figure 2.9: Cartoon diagram of resonant proton capture for the $^{30}\mathrm{P}(p,\gamma)^{31}\mathrm{S}$ reaction.

process varies smoothly as a function of energy across the Gamow window, but cross sections may sharply increase at particular energies due to *resonant capture*.

In this context, *resonances* correspond to nuclear levels with excitation energies above the proton separation energy ($E_x > S_p$), such that they are proton unbound. The presence of these resonances states can enhance the synthesis or facilitate the destruction of certain nuclei more efficiently, depending our their properties and the stellar environment. Each resonance state has a characteristic mean energy and width. The resonance energy is defined by the difference between the excitation energy of the proton-unbound state and the proton separation energy ($E_r = E_x - S_p$). Due to the Coulomb barrier, as resonance energy increases, so does the proton decay *partial width* Γ_p relative to the partial γ decay width Γ_γ. These quantities are proportional to the probability of a proton-unbound state decaying via proton emission or γ emission, respectively. The sum over all decay channels is the *total decay width* of the state $\Gamma = \sum_i \Gamma_i$ and is inversely proportional to the lifetime $\Gamma = \hbar/\tau$.

When the combined center-of-mass energy of a free proton and nearby ^{A}Z nucleus are close

to the resonance energy of a $^{A+1}(Z+1)^*$ state, the nuclear reaction cross section is significantly enhanced. In this case, as shown in Figure 2.9, the proton and target nucleus form a *compound nucleus* which can either re-emit the proton or γ decay to lower energy levels of the product nucleus, having undergone radiative capture. If there are other decay modes available, it is also possible for the nucleus to proceed through those channels instead. Using the one-level, Breit-Wigner formalism to describe narrow, isolated resonances, we can express the resonant reaction cross section as

$$\sigma_{\mathrm{BW}}(E) = \frac{\lambda^2}{4\pi}\frac{(2J_r+1)}{(2J_p+1)(2J_t+1)}\frac{\Gamma_p\Gamma_\gamma}{(E_r-E)^2+\Gamma^2/4}, \tag{2.15}$$

where $\lambda = 2\pi\hbar/\sqrt{2\mu E}$ is the de Broglie wavelength, J_r is the spin of the resonance, J_p is the spin of the projectile, and J_t is the spin of the target nucleus. For the sake of brevity, we can define $\omega = (2J_r+1)/[(2J_p+1)(2J_t+1)]$. This Breit-Wigner model is only valid for narrow, isolated resonances. Resonances are said to be "narrow" if their partial widths are approximately constant across the total width of the resonance, and they must be "isolated" in the sense that their amplitudes cannot overlap significantly with any nearby resonances. Since both the nuclear level density and average resonance width tend to increase as a function of excitation energy, this model is most useful for relatively low-energy resonances just above the proton separation energy.

Plugging the Breit-Wigner cross section from Equation 2.15 into Equation 2.7 for the total thermonuclear reaction rate and simplifying,

$$N_A\langle\sigma v\rangle_{12} = \frac{\sqrt{2\pi}\hbar^2}{(\mu kT)^{3/2}}\omega\int_0^\infty \frac{\Gamma_p\Gamma_\gamma}{(E_r-E)^2+\Gamma^2/4}e^{-E/kT}dE. \tag{2.16}$$

Assuming the resonance is sufficiently narrow, the Maxwell-Boltzmann factor should be constant over the total width of the state. Thus, it can be pulled out of the integrand with the approximation $E = E_r$, allowing us to evaluate the remaining integral analytically:

$$
\begin{aligned}
N_A\langle\sigma v\rangle_{12} &= \frac{\sqrt{2\pi}\hbar^2}{(\mu kT)^{3/2}} e^{-E_r/kT}\omega\Gamma_p\Gamma_\gamma\frac{2}{\Gamma}\int_0^\infty \frac{\Gamma/2}{(E_r-E)^2+\Gamma^2/4} \\
&= \frac{\sqrt{2\pi}\hbar^2}{(\mu kT)^{3/2}}\omega e^{-E_r/kT}\omega\frac{\Gamma_p\Gamma_\gamma}{\Gamma}2\pi \\
&= \left(\frac{2\pi}{\mu kT}\right)^{3/2}\hbar^2 e^{-E_r/kT}\omega\gamma.
\end{aligned}
\tag{2.17}
$$

Defining the quantity $\gamma \equiv \Gamma_p\Gamma_\gamma/\Gamma$, we can now express the thermonuclear reaction rate in terms of the *resonance strength* $\omega\gamma$ for a single level. The contributions of multiple narrow resonances can be summed incoherently to yield the total thermonuclear rate:

$$
N_A\langle\sigma v\rangle_{12} = \left(\frac{2\pi}{\mu kT}\right)^{3/2}\hbar^2\sum_r(\omega\gamma)_r e^{-E_r/kT}. \tag{2.18}
$$

Due to relatively low level density of ^{31}S and limited peak temperatures achieved in classical novae, the thermonuclear rate of the ^{30}P$(p,\gamma)^{31}$S reaction is expected to be dominated by radiative proton captures into a small number of low-energy resonances. For this reason, over the past two decades, significant experimental and theoretical effort has been dedicated to identifying these resonances and constraining their properties.

2.3 Indirect Methods for Reaction Studies

Because it is not possible to measure ^{30}P$(p,\gamma)^{31}$S directly at present, many experimental attempts to determine the thermonuclear rate have employed clever, indirect techniques for constraining the properties of ^{31}S levels within the relevant energy regime near the Gamow window. In the years since this reaction was first identified as being particularly important for modeling nova nucleosynthesis, numerous experimental investigations have been performed, and it is likely that all of the most important resonances have been observed. Some have been sufficiently constrained for utilization in a resonant reaction rate calculation. The current status of all relevant ^{31}S excited states is discussed in Chapter 4. Here we will introduce some of the indirect methods employed in to study the ^{30}P$(p,\gamma)^{31}$S reaction.

Single-Nucleon Transfer Reactions

As the name suggests, this type of reaction involves the transfer of a single nucleon between the light, projectile nucleus and the heavy, target nucleus such that the ejectile emitted from the compound nucleus differs in mass number from the incoming projectile by $\Delta A = \pm 1$. For example, in the case of ^{31}S, excited states have been populated using the forward reactions ^{32}S$(p, d)^{31}$S [98; 99; 100], ^{32}S$(^3$He,$\alpha)^{31}$S [101], and ^{32}S$(d, t)^{31}$S [102; 103].

The resulting spectra from the charged ejectiles correspond to the energy transferred between the reactants in the formation of the compound nucleus, allowing the excitation energies of the levels populated in the ^{31}S* to be deduced. The energies of these ejectiles can be measured by a Si detector array, like in the cases of Refs. [98; 100], or with the use of *magnetic spectrographs*, which measure the kinetic energy of the charged particles by the magnitude of their deflection through a strong magnetic field, as employed in Refs. [101; 102; 103; 99; 100]. By performing these reaction measurements at many different angles, the relative intensity of the observed peaks reveal an angular distribution. To investigate the spin and parity assignments of the final state in the recoil nucleus, *Distorted-wave Born approximation* (DWBA) calculations are often utilized to fit the data for multiple values of orbital angular momentum ℓ, constraining possible values of J^π for a given level.

Single-nucleon transfer reaction measurements can also be employed using *inverse kinematics*, by impinging a heavy beam on a light target. The reaction ^{30}P$(d, n)^{31}$S was used to measure the angle-integrated cross sections for levels above the proton emission threshold and deduce spectroscopic factors of these states [104].

Charge-Exchange Reactions

Charge-exchange reactions are similar to single-nucleon transfer reactions in that both the incoming projectile and outgoing ejectile are slightly different light nuclei. However, instead of the total mass number of the reacting nuclei changing, protons and neutrons are effectively swapped in the process. This occurs in the reaction ^{31}P$(^3$He,$t)^{31}$S, which has been measured to probe some of the same

resonances of astrophysical interest [105; 102; 106; 107]. The angular distribution of the ejected triton, t in this case, as well as angular momentum selection rules can be used to constrain the spin and parity of resonance states populated through charge exchange.

In-Beam Gamma-Ray Spectroscopy

Experiments utilizing γ-ray spectroscopy involve populating highly excited states in the nucleus of interest and observing as many γ rays as possible that are emitted during the cascade of γ decay transitions between different energy levels before reaching the ground state. This requires a high detection efficiency in order to collect as many statistics as possible, as well as a precise detector resolution in both energy and time. This is important for the purposes of differentiating γ rays of similar energies as well as accurate identification of coincidences between γ events.

Experiments performed at the same accelerator facility using the same Gammasphere array employed two different reactions, ^{12}C(^{20}Ne, n)^{31}S [108; 109] and ^{28}Si(α, n)^{31}S [110; 111], to populate high-spin states in ^{31}S. Both double- (γ-γ) and triple-coincidences (γ-γ-γ) were used to construct detailed decay schemes, which were then compared to the level structure of the mirror nucleus ^{31}P for the purpose of constraining spin and parity assignments.

Beta Decay Spectroscopy

As discussed in Chapter 1, β decay is a form of radioactivity mitigated by the weak interaction that results in the emission of either an $\overline{\nu}_e$-e^- or ν_e-e^+ pair. It also follows the selection rules for Fermi and Gamow-Teller transitions [14; 112; 113]. The emission of two spin-1/2 particles may cause a change in angular momentum of $\Delta J = 0, \pm 1$ between the final and initial state; larger changes in angular momentum are said to be "forbidden" and, although technically not impossible, are highly suppressed. In the case of ^{31}Cl, which has a $J^\pi = 3/2^+$ ground state, its β^+ decay almost exclusively populates $J^\pi = 1/2^+, 3/2^+, 5/2^+$ levels in ^{31}S. This is useful for placing strong spin-parity constraints on newly observed states and is particularly relevant for the astrophysically

important ^{30}P$(p,\gamma)^{31}$S reaction, since these form the $\ell = 0, 1$ resonances expected to dominate the total thermonuclear rate in ONe classical novae.

The process of β-delayed particle emission occurs when a radioactive nucleus undergoes β decay and populates an excited state in the daughter nucleus with an excitation energy above the particle-emission threshold, which can then spontaneously decay via particle emission. The first observation of ^{31}Cl β-delayed proton decay was reported over 40 years ago [114], the implications of which were presented in further detail by Refs. [115; 116]. However, it was not until 2006 that ^{31}Cl β^+ decay was investigated on the basis of astrophysical motivations [117]. Using three double-sided Si strip detectors (DSSDs) to measure proton energies in the laboratory frame, Kankainen *et al.* observed all of the same β-delayed proton decays reported by Ref. [116], including several more. In addition, inclusion of a high-purity Ge detector (HPGe) allowed for the conclusive identification of the ^{31}Cl ground state's isobaric analog in ^{31}S through measurement of its γ decay. Another experiment, also using solid-state Si detectors, measured the intensities and lab-frame energies of ^{31}Cl β-delayed proton decays; these results were reported in a 2011 doctoral thesis dissertation but were never published in a peer-reviewed journal [118]. However, this measurement has provided the best-resolution, highest-statistics spectrum of the ^{31}Cl$(\beta p)^{30}$P decay sequence yet, and its reported intensities and energies (converted to the center-of-mass frame) were essentially adopted unaltered in the latest evaluation of recommended literature values for β-delayed charged-particle decays [119].

Prior to the original research contained within this dissertation, the most recent investigation into the ^{30}P$(p,\gamma)^{31}$S reaction using β^+ decay spectroscopy involved a β-delayed γ ray measurement performed at NSCL. A radioactive beam of ^{31}Cl was implanted into a plastic scintillator, surrounded by the Cloversharе Array, which consisted of nine HPGe detectors. Subsequent analysis of the data collected during this experiment resulted in the most comprehensive study of the ^{31}Cl$(\beta\gamma)^{31}$S decay scheme to date [120]. In addition to the discovery of many new ^{31}S levels and previously unobserved γ transitions, Bennett *et al.* crucially identified the existence of a proton-unbound state with spin-parity $J^\pi = 3/2^+$ and an excitation energy of $E_x = 6390.2(7)$ keV [121].

The most recent atomic mass evaluation reports that the proton emission threshold for ^{31}S to be S_p = 6130.65(24) keV [16], which means that the resonance energy is E_r = 6390.2(7) − 6130.65(24) keV = 259.6(7) keV, placing this resonance in close proximity to the Gamow peak for ONe nova temperatures during thermonuclear runaway. In addition, since the ground state of ^{30}P is $J^\pi = 1^+$ [122], proton capture to a $J^\pi = 3/2^+$ level forms an $\ell = 0$ resonance, which means $^{30}\mathrm{P}(p,\gamma)^{31}\mathrm{S}$ is be unimpeded by a *centrifugal barrier* through this channel. For these reasons, we hypothesize that the $\ell = 0$, 260-keV resonance will dominate the thermonuclear rate for this reaction of interest in ONe novae. However, in order to calculate the strength of this resonance and, by extension, its contribution to the total rate, we need to determine its proton branching ratio Γ_p/Γ.

The reason why ^{31}Cl β-delayed proton decays through this resonance have not been observed in the previous measurements is likely due to their use of off-the-shelf Si diodes. Solid-state detectors made of semiconducting material are plagued by the large β^+ backgrounds that are especially prominent at low energies. This has motivated the development of a new detector for measuring weak, low-energy, β-delayed protons decays. This experimental system and its application to the scientific problem at hand is the topic of the next chapter.

CHAPTER 3

EXPERIMENTAL INVESTIGATION

3.1 GADGET: Gaseous Detector with Germanium Tagging

The GADGET system was specifically developed to measure weak, low-energy, β-delayed, charged-particle decays for the purpose of constraining thermonuclear reaction rates relevant to the study of explosive nucleosynthesis. It was designed for conducting radioactive beam experiments using the exotic ion beams provided by the Coupled Cyclotron Facility at NSCL. GADGET's namesake refers to the coupling of the existing Segmented Germanium Array (SeGA) at NSCL to the new Proton Detector, a gaseous, proportional counter. The former consists of an array of high-resolution, high-efficiency γ ray detectors. The latter was designed, built, tested, and commissioned at NSCL as part of Phase I of the GADGET system.

Micro-Pattern Gaseous Detectors

Since the invention of the Geiger-Müller counter in 1928, for almost a century, gas-filled radiation detectors have been employed in a wide variety of applications. The MICRO-MEsh GAs Structure (MICROMEGAS) was developed for high-rate experiments and proved to be a cost-effective solution to the spatial-resolution problem encountered by the multi-wire proportional chambers (MWPC) that preceded them. MICROMEGAS detectors were also able to provide higher signal amplification than the micro-strip gas chambers (MSGC) built to solve the same problem [123]. The interactions of charged particles with matter are quite complicated, but the semi-classical Bethe-Bloch expression is often used to approximate the stopping power of charged particles in a gas. Qualitatively, we can express the differential energy loss per unit distance as

$$\frac{\Delta E}{\Delta x} \propto -\frac{Z}{\beta^2}, \tag{3.1}$$

where Z is the charge of the particle, and β is its velocity as a fraction of the speed of light [124]. This can be calculated using the relation

$$\beta = \sqrt{1 - \frac{1}{\gamma^2}}, \tag{3.2}$$

where the relativistic γ can be written in terms of a particle's kinetic energy E_k and its rest mass m_0:

$$\gamma = \frac{E_k}{m_0 c^2} + 1. \tag{3.3}$$

For *minimum ionizing* radiation such as muons or β particles, a kinetic energy of 1 MeV implies a speed of 94% the speed of light, while for the much heavier proton of the same energy $\beta \approx 0.046$. This implies that faster, lighter β particles hardly deposit any energy in the gas at all over short distances and have much longer tracks, compared to the slower, heavier protons and α particles. Because fast-moving β particles do not deposit their full energy in the volume of a gas-filled proportional counter, their contribution to the background is suppressed in β-delayed proton decay experiments that utilize such devices. Furthermore, a high-gain, gaseous amplifier based on the MICROMEGAS design results in high detection efficiency for low-energy protons, while maintaining good resolution. This was demonstrated in the measurement of ^{23}Al β-delayed proton decays at $\approx$ 200 keV with a full width at half maximum (FWHM) resolution of 7% using the AstroBox instrument at Texas A&M University's Cyclotron Insitute [125]. The Proton Detector at NSCL was designed in collaboration with the developers of AstroBox in order to replicate its technical performance as well as to adapt the gaseous detection system such that it fits snugly inside the existing SeGA structure. The ability of GADGET to acquire high statistics particle-γ coincidences is useful for determining which states in ^{30}P are populated by ^{31}Cl β-delayed proton decay, which is important for understanding nova nucleosynthesis.

Principle of Operation

The schematic drawing in Figure 3.1 depicts the basic operating principles of the Proton Detector. Once the radioactive beam particles have been produced from the accelerator facility and delivered to the experimental setup, they exit the beam line and implant inside the Proton Detector. After stopping in the fill gas, they quickly thermalize, diffusing via Brownian motion until they decay from essentially at rest. Usually, β decay is promptly followed by one or more γ decays, which can be detected by SeGA, as the daughter nucleus deexcites to its ground state. However, if the β decay populates a proton-unbound state in the daughter nucleus, a proton may be emitted. The decay proton and the recoil nucleus deposit almost all their kinetic energy into the fill gas by colliding with neutral atoms to create electron-ion pairs. Under the influence of a uniform electric field, these primary ionization electrons drift at a constant velocity towards the amplification region, where they encounter an electric field on the order of 100 times stronger than the field in the drift region. This causes a *Townsend avalanche* of secondary electrons which induce a detectable signal on the detector pads [126; 127]. Thus, the size of the readout voltage is proportional to the center-of-mass energy of the proton decay. The fast-moving β particles have long tracks and deposit only some of their energy within the detector's active volume, suppressing their contribution to background in the final β-delayed proton spectrum.

Proton Detector Design

Figure 3.2 contains a partially labeled diagram of the Proton Detector. Most of the detector volume is contained within a cylindrical tube made of stainless steel. The chamber is $\approx$ 49 mm long and 16.5 cm in diameter. On the upstream end of the detector, relative to the direction of the incoming beam, a 1.5-μm-thick Kapton® window with a 50.8-mm diameter allows the beam particles to enter the drift tube. Also attached to that end cap are four outlet lines, which allow gas to flow out of the detector, as well as a high-voltage electrical feedthrough, which is used to apply a negative bias to the *cathode*. The Proton Detector's cathode provides the large voltage needed to create an electric field along the length of the drift tube. The uniformity of the electric field is preserved by a *field*

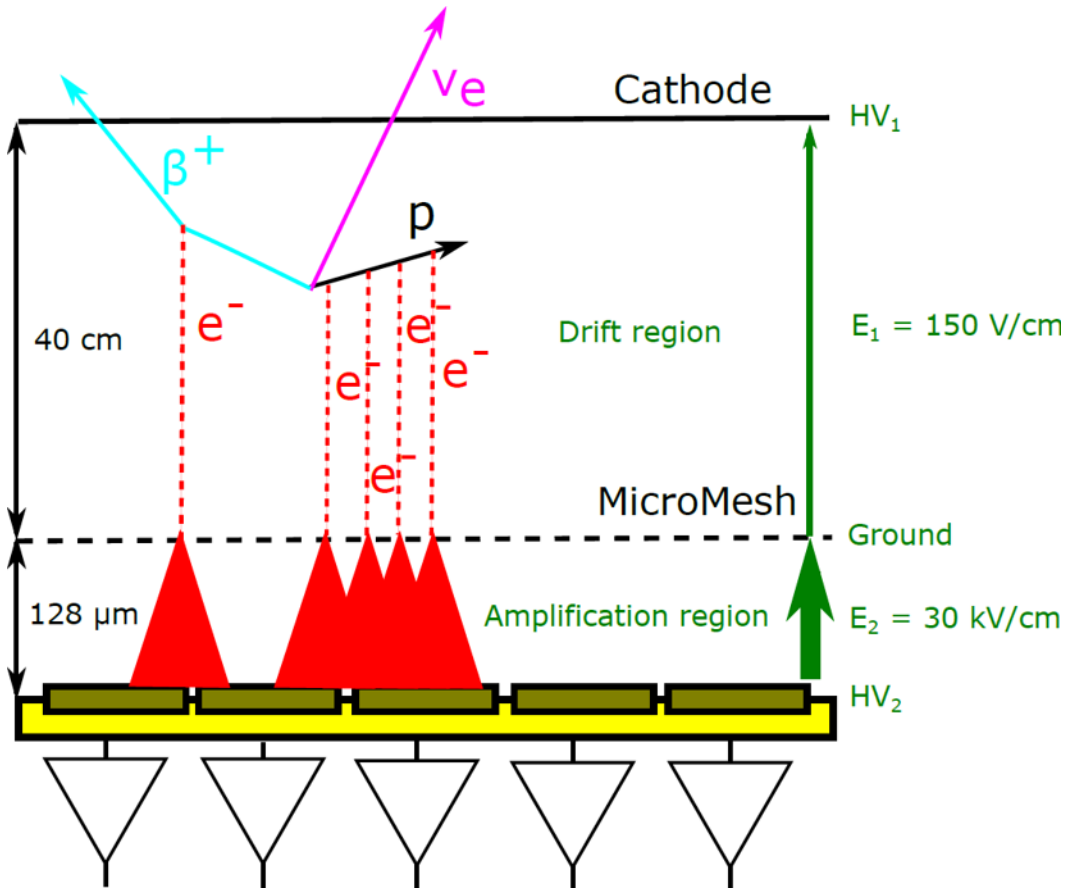

Figure 3.1: Diagram of the Proton Detector's principle of operation.

cage.

The field cage consists of a thin, flexible polyimide film wrapped into a cylinder, onto which 101 equipotential copper rings have been printed along the inside. The first, most-upstream ring is in electrical contact with the cathode, and the electric potential is stepped down over the length of the cage through a series of resistors. The field cage is surrounded by an insulating polyether ether ketone (PEEK) material, with cutouts allowing space for the resistors. At the downstream end of the field cage, there is an electronic *gating grid* that protects sensitive electrical components from the large charges produced during beam implantation. Between the gating grid and the MICROMEGAS detector pad plane, there is a pair of copper rings separated by insulating PEEK spacers. The ring closer to the gating grid is in electrical contact with the last ring of the field cage on the low-voltage end, while the downstream ring is grounded. This preserves the electric

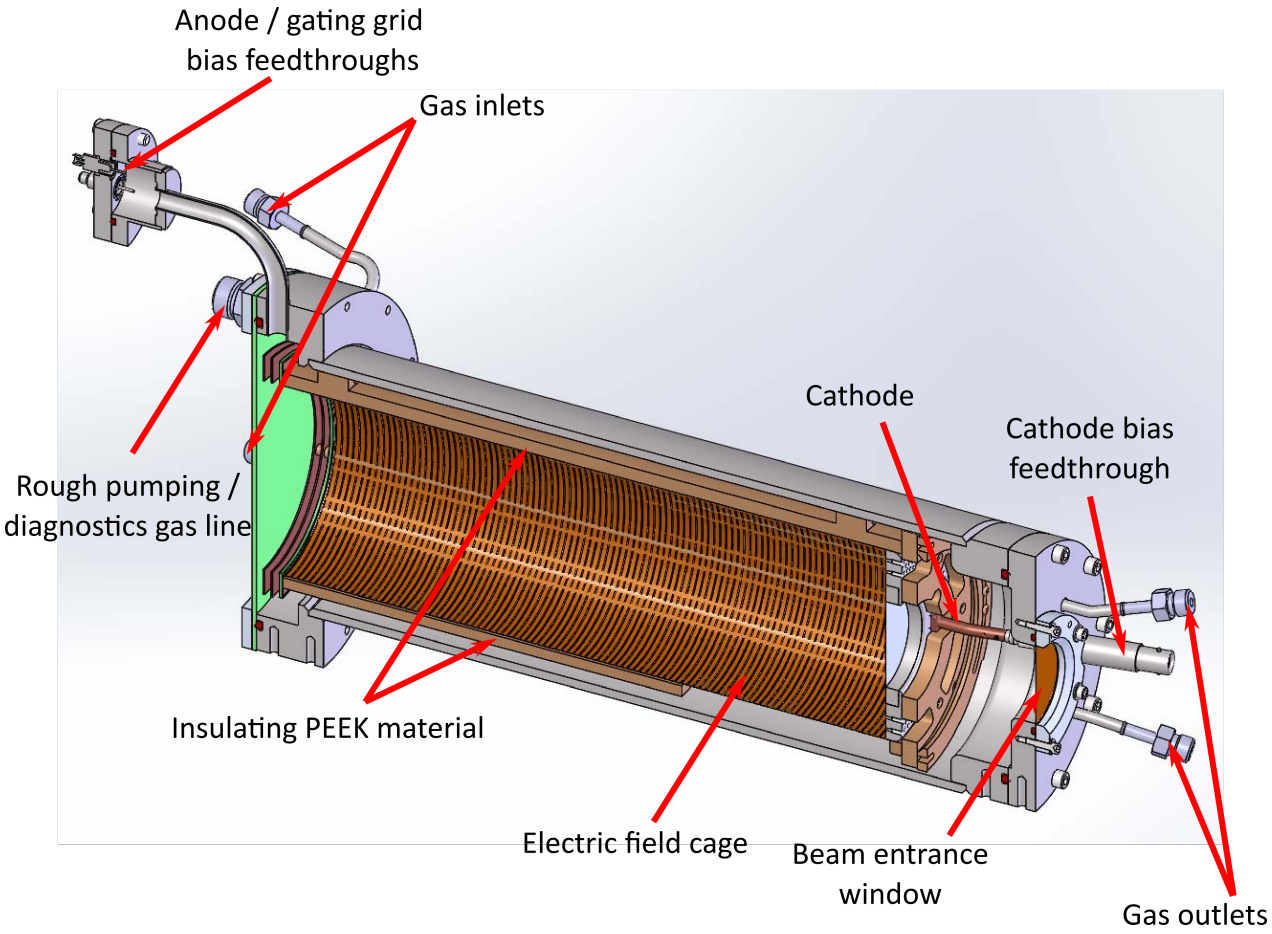

Figure 3.2: Mechanical design drawing of the Proton Detector.

drift field between the gating grid and the MICROMEGAS, which is responsible for amplifying the detector signal.

On the downstream end of the detector, there is a flange with a 22.9-cm diameter to which the other end cap connects. Similar to the upstream end, this flange has four, thin tubes connected to it which allow for filling the detector with gas. In addition to the gas inlets, a single, thick tube is connected to the downstream flange for more efficient vacuum pumping as well as for diagnostic and safety purposes. An additional flange is attached to this end which contains the electrical feedthroughs necessary for biasing the positive anode and the gating grid. The end cap that seals the downstream end of the detector is the printed circuit board for routing electronic signals and the MICROMEGAS.

Designed and manufactured at CERN, the MICROMEGAS consists of a stainless steel, mi-

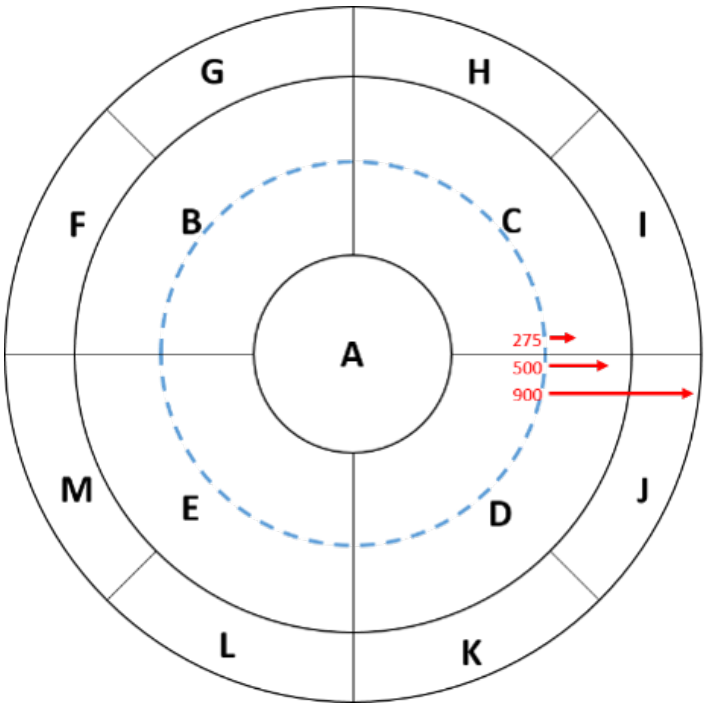

Figure 3.3: Diagram of the detector pad plane. The MICROMEGAS is segmented into 13 charge-sensitive pads labeled A-M. The dashed blue circle represents the projection of the beam entrance window onto the pad plane, and the red arrows correspond to proton tracks. The size of the arrows, labeled by their energies in units of keV, are scaled in proportion to their calculated ranges in P10 gas at a pressure of 800 Torr.

croscopic mesh structure, which is electrically grounded, and is supported by insulating pillars of PEEK material that separate it from the positively biased *anode* plane. This 128-μm gap is the amplification region that provides the detector with adjustable gain. A schematic drawing of the pad plane is shown in Figure 3.3. The anode itself is segmented into 13 gold-plated, copper electrodes. The five inner pads measure the energy of charged-particle decays, while the eight outer pads are used to veto events whose full energy is not measured by the active, inner pads.

The gating grid was installed in the Proton Detector between the field cage and the MICROMEGAS structure, covering the entire area of the charge-sensitive pad plane. The grid is made of an insulating ring, on which 60 gold-plated, copper wires have been soldered, each 20 μm in diameter and spaced in 2-mm increments. When the grid is operated in the transparent mode, the wires are held at the same potential (-225 V) as the final copper ring in the field cage before the MICROMEGAS, allowing ionization electrons to enter the amplification region. In the opaque

Figure 3.4: The MICROMEGAS being operated in "pancake" mode. By shortening the active volume of the gas, we were able to use an ^{55}Fe X-ray source to characterize the performance of individual detector pads.

mode, the wires are held at a positive potential (+150 V) relative to the micro-mesh, which reverses the direction of the drift field between the gating grid and the MICROMEGAS. This prevents the large ionization currents created during beam implantation from damaging the channels in the preamplifier, which is necessary for signal processing. When running experiments, the gating grid is operated in cycles synchronized with beam delivery, alternating between opaque mode during beam implantation, and transparent mode, when beam is not being implanted.

Gas Handling System

A used gas handling system, provided by the NSCL detector lab, was initially utilized during the testing stages of the Proton Detector development. This was necessary in order to characterize the individual MICROMEGAS pads using a "pancake" version of the detector, depicted in Figure 3.4. We also used this gas handling system during the the GADGET commissioning experiment. However, gas purity affects the quality of the detector response and, by extension, the resolution of the final proton spectrum. Before the first dedicated science experiment, a new, customized gas

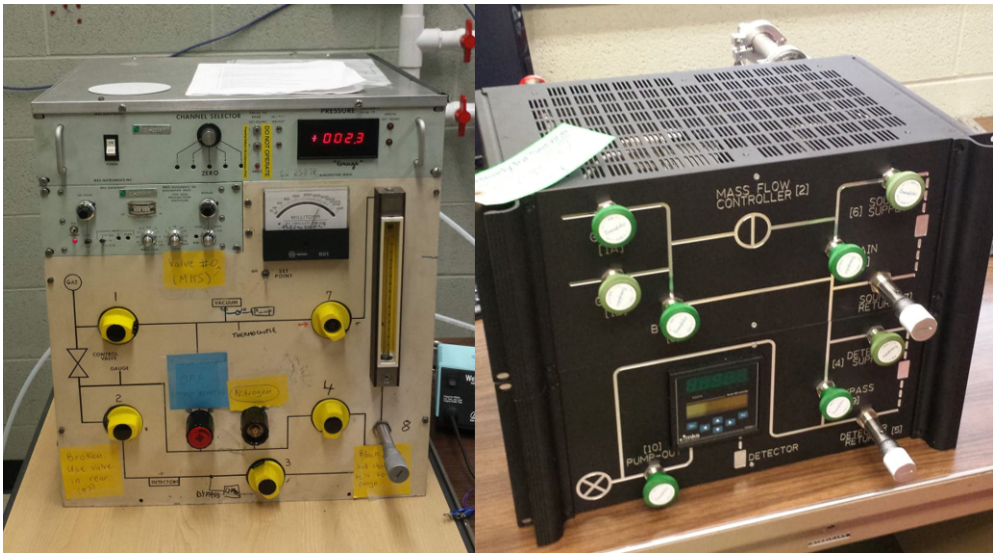

Figure 3.5: Gas handling systems used to operating the Proton Detector. Left: Older version of the gas handling system borrowed from the NSCL detector lab. Right: Custom-built gas handling system for GADGET.

handling system was constructed to be used in the ^{31}Cl β-delayed proton decay measurement as well as all subsequent GADGET experiments. It was designed to fit on the same portable rack used to house the electronics modules and remote controls system for GADGET. A comparison between the old and new gas handling systems is shown in Figure 3.5.

In collaboration with the mechanical engineering department at NSCL, this new gas handling system was developed for functionality during radioactive beam experiments as well as during offline systematic tests. Figure 3.6 provides a detailed schematic drawing of the gas handling system. While GADGET does not operate by mixing gases *in situ*, two gas sources can be connected to the gas handling system simultaneously. Typically, one gas line is connected to a bottle containing P10, a mixture of 90% Ar and 10% CH_4, which is commonly used to fill gaseous amplification detectors. Another gas line containing N_2 is usually connected to the detector; this feature was included in order to flush the detector and gas handling system with an inexpensive, inert gas. This was both for safety purposes when operating the systems with marginally flammable gases as well as for keeping the detector clean and pressurizing the system when it is not in use.

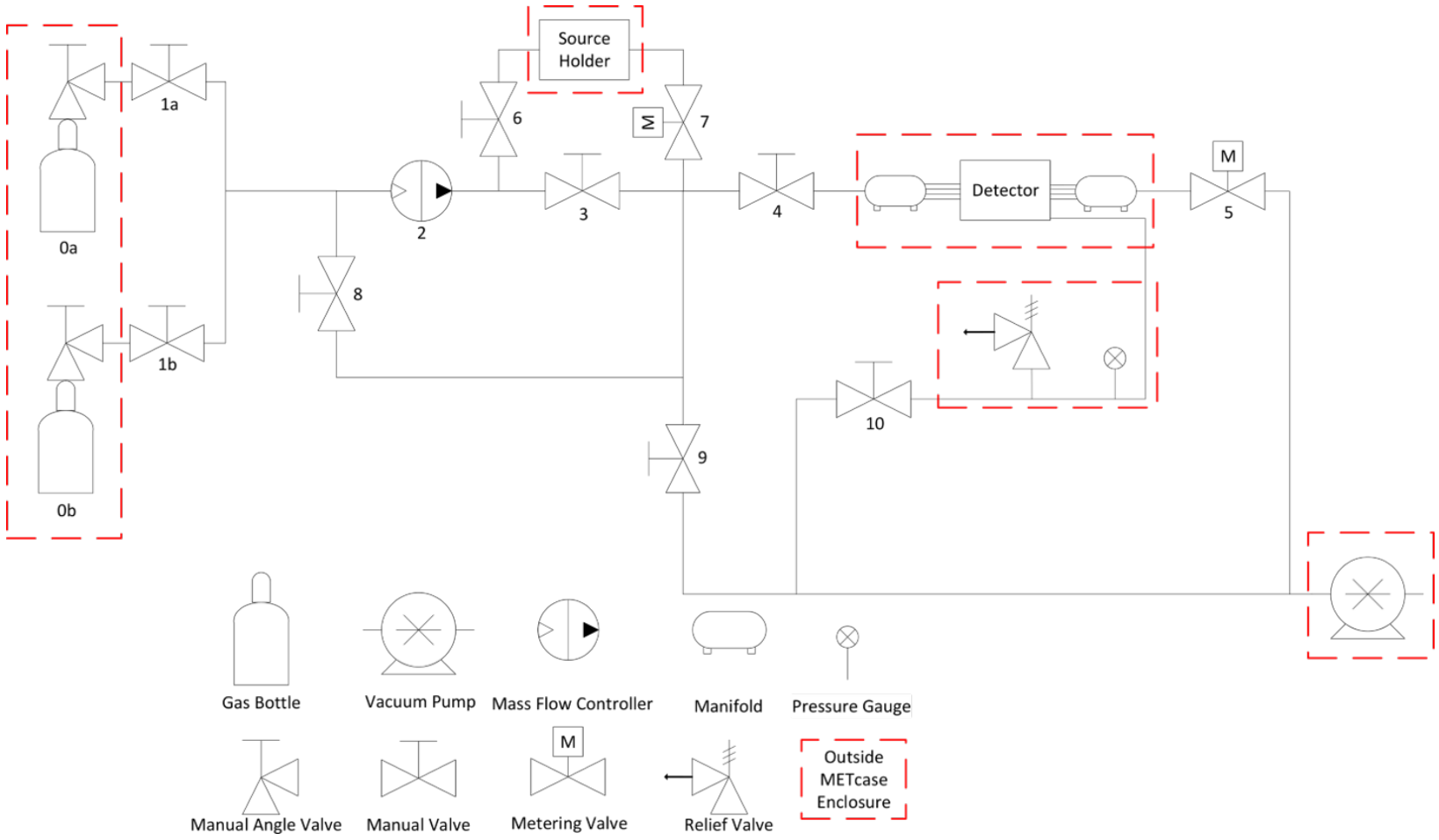

Figure 3.6: Schematic drawing of the custom-built gas handling system for GADGET.

The gas pressure inside the detector chamber is regulated by a πPC PC99 integrated downstream pressure controller with a mass flow meter from MKS Instruments. The current operating procedure for controlling this device involves communicating with the mass flow controller over Ethernet connection through an Internet Explorer session on a Windows laptop. The MKS Instruments software interface was used to set and record the gas pressure as well as for monitoring the rate of gas flowing through the meter. The flow rate can only be changed by manually adjusting a metering value, which is physically attached to the gas handling system. At the end opposite to the gas sources, an electric vacuum pump causes gas to flow through through the system and disposes of the spent gas into the experimental vault's exhaust line, which is then vented to an outdoor area.

A rough pumping line is connected to the downstream flange of the Proton Detector. This allows for more efficient pumping of the detector when placing the system under vacuum. Connected to this rough pumping line is a pressure gauge which gives an independent reading of the pressure closer to the detector chamber. There is also a safety relief value that will vent over-pressured gas into the experimental vault. The valve is set manually at a nominal pressure above the operating pressure of the Proton Detector. For the commissioning and first dedicated science experiment with GADGET, we chose to operate the system above atmospheric pressure at 800 Torr. Thus, any small leaks in the experimental setup would cause gas to flow out of the system and prevent air in the atmosphere from contaminating the vessel.

Additionally, a radioactive source-holder is connected to an isolated loop in the plumbing of the gas handling system. By inserting a radioactive sample, such as ^{232}U or ^{228}Th, which contain ^{220}Rn gas in their decay chains, the α-emitting isotope can diffuse out of the source holder and into the Proton Detector. Detecting these charged-particle decays has been useful in testing the experimental setup without the use of a radioactive beam. A more detailed discussion of the design, testing, and commissioning of the Proton Detector and the GADGET system can be found in Ref. [128].

SeGA: Segmented Germanium Array

SeGA is a high-resolution, γ-ray detection system with good geometric efficiency. The array consists of 18 segmented, coaxial high-purity germanium (HPGe) crystals. Ge is a semiconductor, meaning its atomic structure causes the bulk material to have an electrical conductivity somewhere between that of a true, metallic conductor and a non-metallic insulator. It has a small *band gap*, meaning less energy is required to excite valence electrons to the *conduction band*, and a large atomic number, which increases the probability of a radiation interacting with the crystal. An energetic photon like a γ ray can ionize atoms in the crystal lattice, creating an *electron-hole pair*. In the presence of an external electric field, this causes a pulse of current to flow through the Ge.

The SeGA detectors are coaxial in the sense that the semiconducting Ge material is cylindrical in shape with a smaller cylindrical cavity inside along the same axis. The central hole bores through almost the entire length of the crystal, making these *close-ended coaxial* HPGe detectors. An electrical contact in the central hole, as well as all along the outer surface of the of the HPGe cylinder, provides the requisite bias voltage to allow charge carriers to flow through the semiconducting material. The end of the central contact is also rounded, or *bulletized*, to eliminate low-field regions in the crystal [126]. The amount of current measured in the central contact is proportional to the amount of energy deposited in the detector by the γ ray. Unlike conductors, whose electrical conductivity increases as the metal is cooled, conductivity in a semiconductor increases with warmer temperatures. Thermal excitations can cause electrons to cross the band gap and produce leakage currents. This results in noisy electronic signals and degrades the resolving power of the detector. For this reason, the HPGe crystals must be kept cool at all times using liquid N_2, which has a temperature $\leq$ 77 K at atmospheric pressure.

The HPGe crystals are segmented into eight discs, which are each further subdivided into four, planar quadrants [129]. This segmentation allows for determining the point of initial interaction between a γ ray and the detector as well as increased angular resolution. For GADGET experiments, we do not need to not collect data from the individual segments of the HPGe crystals, and instead only measure the current on the central contacts. We have implemented 16 of the SeGA detectors

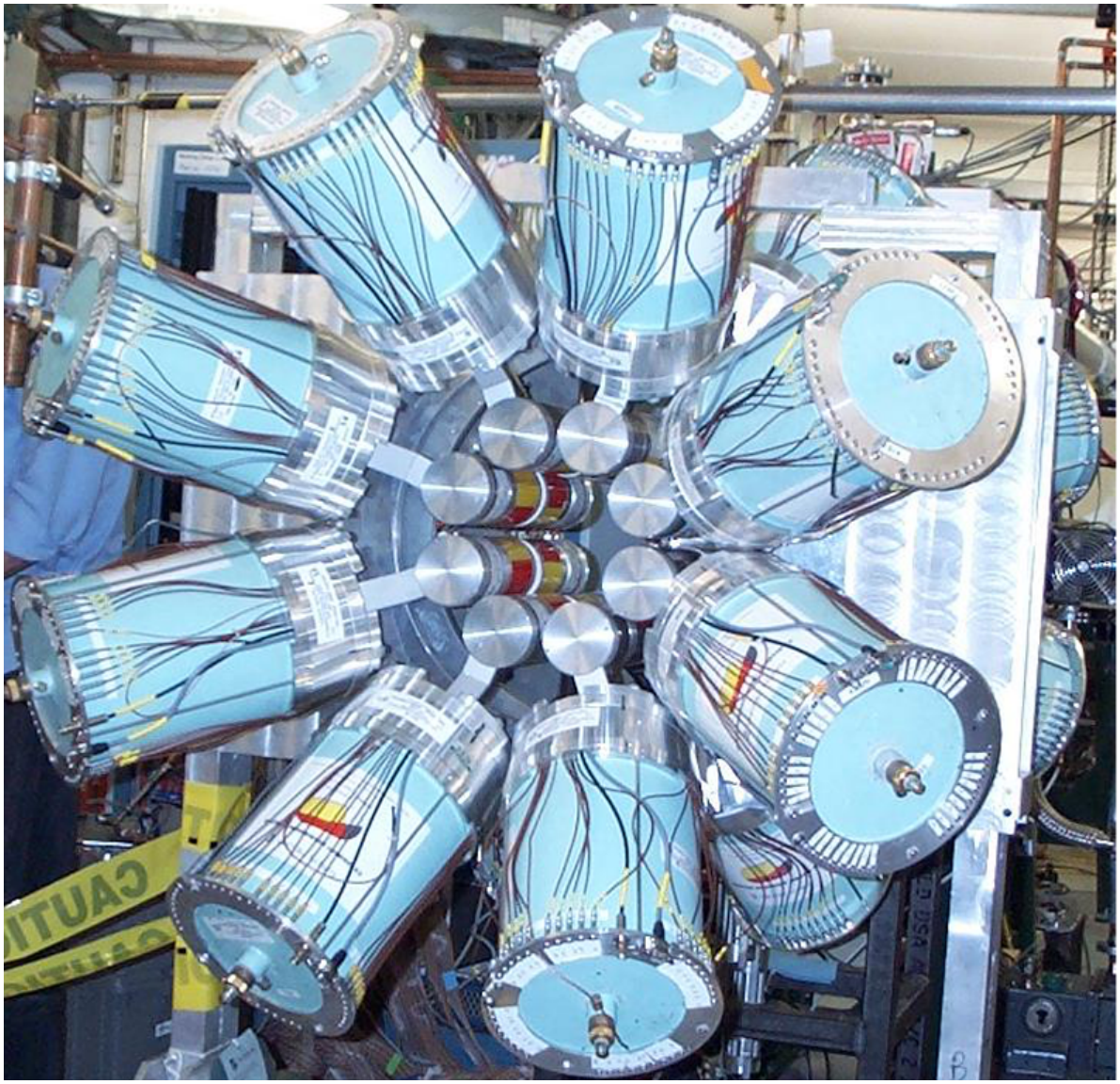

Figure 3.7: The betaSeGA, or "barrel," configuration of the Segmented Germanium Array set up in the experimental vault. This employs 16 HPGe detectors in two rings around the beam line with a diameter of 17.3 cm. The large, blue-green containers are cryogenic storage dewars that hold the liquid N_2 for cooling the HPGe crystals located in the center of the array. Photo credit: National Superconducting Cyclotron Facility / Facility for Rare Isotope Beams, Dirk Weisshaar, Alexandra Gade.

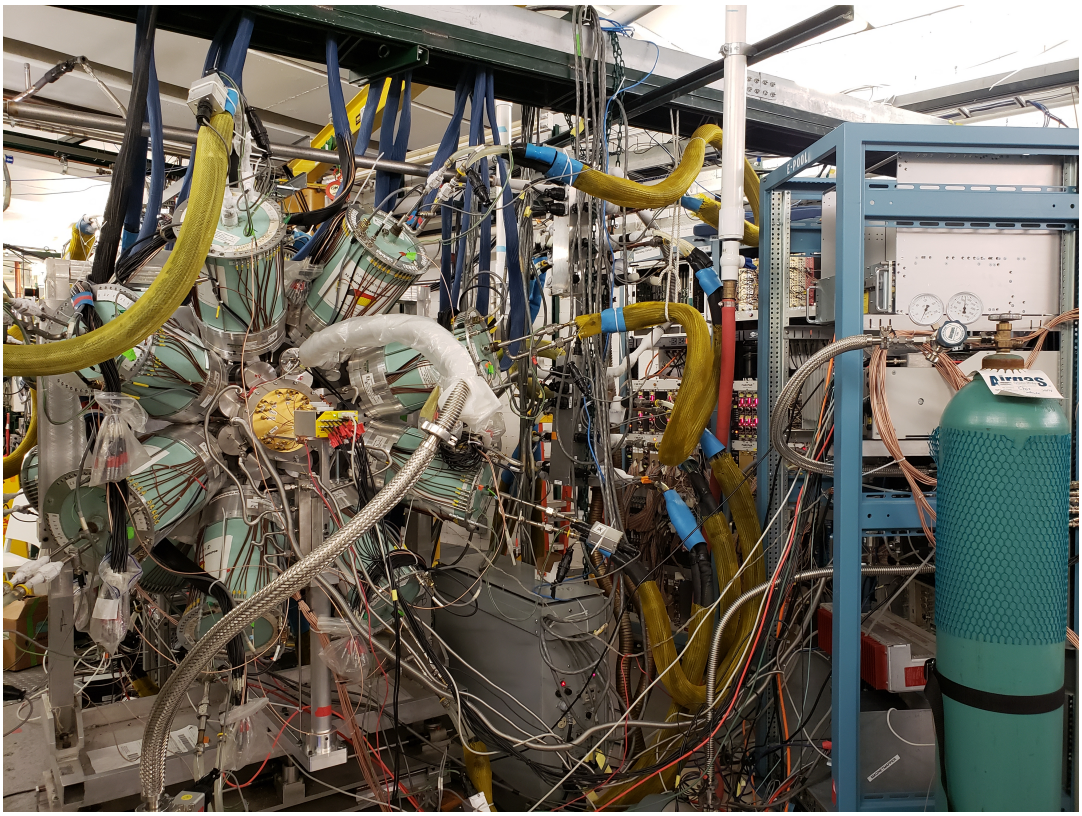

Figure 3.8: The fully assembled GADGET system in the S2 vault.

in their "barrel" configuration, as shown in Figure 3.7, inside which the Proton Detector was designed to fit. The angular distribution of γ emission is irrelevant for the purposes of our scientific measurement, and we prefer to maximize geometrical detection efficiency for this measurement.

3.2 NSCL Experiment 17024: β-Delayed Proton Decay of ^{31}Cl

A radioactive beam experiment (e17024) at NSCL was performed in November 2018 to measure the β-delayed proton decay of ^{31}Cl. The primary goal of this measurement was to determine the proton branching ratio of the $J^\pi = 3/2^+$, 6390-keV excited state in ^{31}S. This is the same resonance state that had been identified in a previous ^{31}Cl β-delayed γ-ray experiment at NSCL. In preparation for e17024, the GADGET system was assembled in the S2 experimental vault, as pictured in Figure 3.8. Meanwhile, data collection and monitoring of the system was performed remotely in the NSCL Data-U. Here, we discuss the supporting infrastructure and operating procedure during the first dedicated scientific experiment using GADGET.

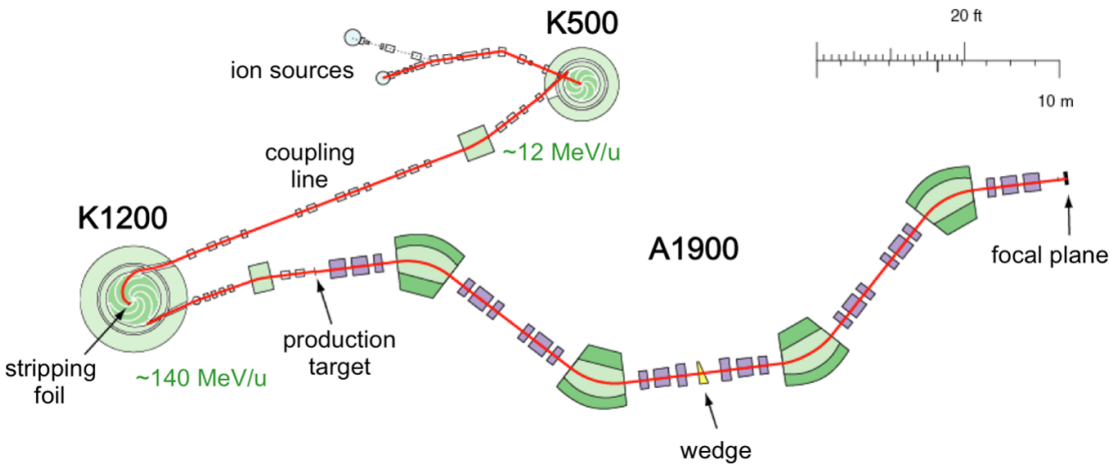

Figure 3.9: Diagram of the Coupled Cyclotron Facility and A1900 fragment separator at NSCL. Figure credit: Ref. [130].

Beam Delivery

A radioactive ion beam of ^{31}Cl was produced via fragmentation at the Coupled Cylcotron Facility by accelerating a stable beam of ^{36}Ar up to 150 MeV/u and impinging it on a 1645-mg/cm^2 Be production target. The A1900 fragment separator, depicted in Figure 3.9, removed most of the undesirable nuclear species from the cocktail beam using magnetic rigidity and a 150-mg/cm^2 Al wedge. *Magnetic rigidity* causes the higher-energy beam particles to pass through the thicker end of the wedge, slowing them down closer to the speed of the lower-energy beam particles which interact with less Al material on the thinner end.

The secondary beam was further purified using the Radio Frequency Fragment Separator (RFFS), which applied an oscillating electric field to deflect the ^{31}Cl ions through a set of collimating slits, meanwhile deflecting all other nuclear fragments such that they do not pass through the collimator. Ultimately, we were delivered a 65% pure beam of ^{31}Cl at 6375 pps. In decreasing order of intensity, the main beam contaminants were ^{28}Si, ^{30}S, and ^{29}P, but fortunately, none of these nuclide are β-delayed particle emitters.

The Diagnostics Cross

In preparation for radioactive beam experiments, a six-way, ConFlat® cross, supported by an Al stand, is installed at the end of the beam line in the S2 vault. The cross structure is used for housing Si detectors as well as a rotatable Al degrader foil and is physically connected to the beam line using an ultrahigh vacuum seal and a series of hand-tightened clamps. From the reference point of the beam, the flange on the left side of the cross is connected to an electric turbo pump, which is backed by an oil roughing pump. Prior to operating diagnostic tools in the cross, the oil pump removes most of the air in the cross, and only after the pressure in the cavity reaches $\lesssim 1$ Torr, the turbo pump is switched on to reach the highest vacuum possible. Attached to the flange on one of the faces parallel to the beam axis is a manual valve for venting the cross when bringing the cavity back up to atmospheric pressure as well as a pressure sensor. Connected to the downstream flange of the cross is a short beam line extension with a thin beam exit window. This limits the distance the beam particles travel through the air to ≈ 15 cm after leaving the beam line but before entering the Proton Detector.

PIN Detector

The top flange of the cross is connected to a pneumatic drive which, when connected to a source of pressurized air in the vault, can control the position of a 300-μm-thick PIN detector, shown in Figure 3.10. A *p-i-n (PIN) detector* is a commonly used semiconductor diode, named for its three distinct doping regions. The *i-type* region in the middle of the detector refers to a chemically pure, undoped *intrinsic* semiconductor material, which in this case is Si. This intrinsic region is sandwiched between *p-type doping* and *n-type doping* regions. The p-type region is doped with elemental impurities that have a higher electron affinity (e.g. P, As, and Sb), and are thus more likely to accept electrons. Conversely, dopants with a lower electron affinity (e.g. B, Al, Ga) are used in the n-type region, which serve as electron donors.

At the beginning of and periodically throughout the experiment, diagnostic runs were taken for the purposes of particle identification. During these diagnostic measurements, the beam current

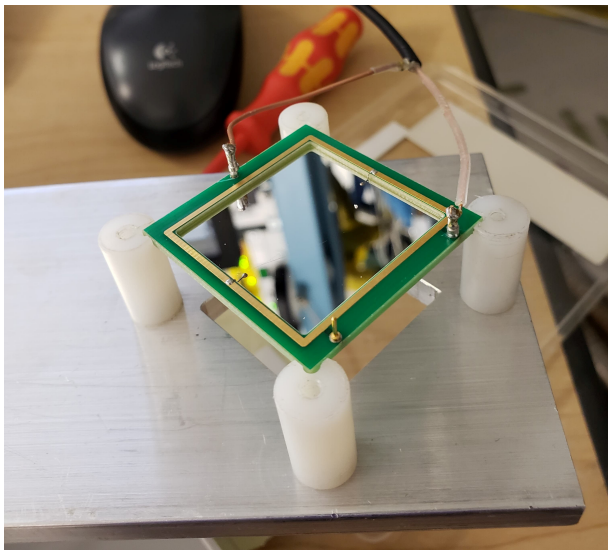

Figure 3.10: Si PIN detector mounted on PEEK spacers before being inserted into the six-way cross chamber.

from the accelerator was attenuated and the PIN detector was inserted into the path of the ion beam in order to measure its energy loss ΔE in the detector. To protect the Proton Detector electronics during PID runs, the bias voltage on the MICROMEGAS anode was turned off, such that beam need not be cycled on and off, allowing a constant beam intensity be impinged on the PIN detector for several minutes. As beam particles pass through the PIN detector, their ΔE is measured, as shown in Figure 3.11. This was compared to the expected energy loss of beam particles passing through 300 μm of Si using version 1.2 of the ATIMA program in LISE++. This allowed us to verify that ^{31}Cl and ^{28}Si were the two primary nuclear fragments being delivered to GADGET. After a diagnostic run was completed, the beam is stopped; the pneumatic drive retracts the PIN detector from the path of the ion beam; beam pulsing resumes, and only then can the MICROMEGAS voltages be reapplied before beginning a new measurement run.

Beam Energy Degrader

Attached to the bottom flange of the cross is a second pneumatic drive as well as a stepper motor for controlling the position and angular orientation of the beam energy degrader, respectively. During a data production run, when beam is being implanted in the gaseous detector chamber and

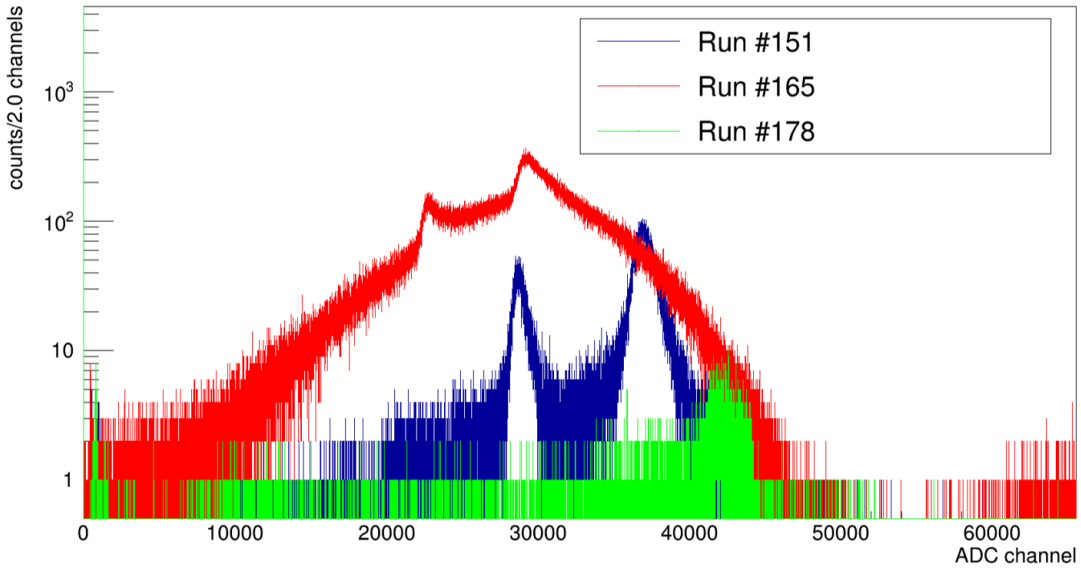

Figure 3.11: Energy loss ΔE spectrum measured in the PIN detector during particle identification runs. The ratio between the peak positions is consistent with the ratio between calculated energy losses in the equivalent thickness of Si.

β-delayed proton decays are being measured, a thin, highly pure Al plate is inserted into the beam path to degrade the energy of incoming ions before they reach the Proton Detector. Detailed beam calculations were performed with LISE++ to determine 0.75 mm as the ideal degrader thickness for slowing the $\approx$ 50-MeV/u ^{31}Cl ions leaving the RFFS such that they stop in the middle of the Proton Detector's drift region.

By rotating the degrader foil from between 0°, when the beam is perpendicular to the broad side of the Al plate, and 90°, when the beam is parallel with the plane of the thin foil, the effective thickness of the degrader can be adjusted. At 0°, beam particles pass through the minimum amount of Al possible without removing the degrader entirely, but with increasing degrader angle, ions must traverse more material in the degrader plate, further slowing down the beam particles and shortening their implantation range in the Proton Detector.

In principle, the stepper motor allows for remote control of the degrader plate's angular orientation inside the cross. However, in preparation for the ^{31}Cl β^+ decay measurement, utilizing the stepper motor induced substantial electronic noise in the Proton Detector. While this technical challenge was later resolved, for the duration of e17024, the Al degrader plate was removed from

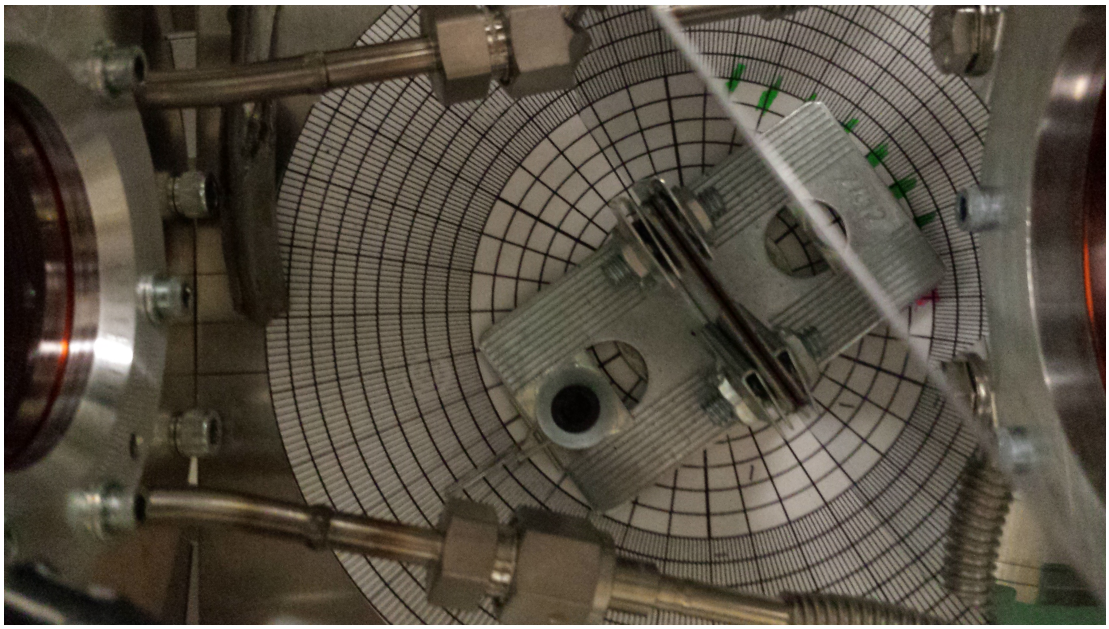

Figure 3.12: Overhead view of the Al degrader foil mounted on a circular protractor between the entrance window to the Proton Detector (on the left side of the image) and the exit window from the beam line (on the right side of the image). The degrader angle was set manually and could be determined to within 1° precision.

the vacuum cross and positioned in air, directly in front of the Proton Detector's beam entrance window. Thus, in between beam implantation runs, the angle of the degrader plate was adjusted manually in the experimental vault until an operating angle was determined. Figure 3.12 depicts how the degrader angle was measured over the course of the experiment.

Online analysis of scalars from the upstream and downstream SeGA rings allowed us to estimate the relative, longitudinal position of the origin for β-delayed γ decays occurring in the Proton Detector. These scalars are proportional to the the number of γ ray counts detected in either the eight upstream or the eight downstream SeGA detectors; we assumed that when the scalar readings from both SeGA rings were approximately equal, the ^{31}Cl beam distribution should be roughly centered within GADGET longitudinally. Offline analysis using β-γ coincidences allowed a more precise determination of the longitudinal beam distribution.

The constant drift velocity for electrons within the field cage implies the total drift time in the Proton Detector is proportional to the distance between the MICROMEGAS pad plane and

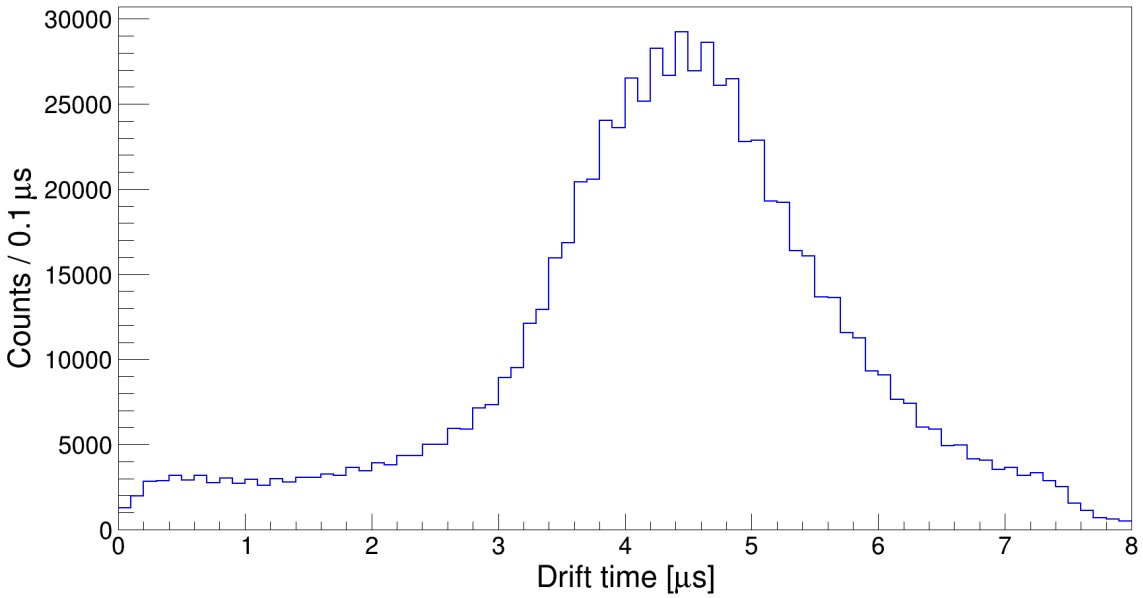

Figure 3.13: Drift times recorded for Proton Detector events observed in coincidence with γ ray events detected by SeGA. This plot allows us to visualize the longitudinal beam distribution within the drift chamber.

the position where β^+ decay occurred along the beam axis. The maximum possible drift time for primary ionization electrons in a 40-cm drift region is about $\approx$ 8 μs, assuming an 800-Torr P10 fill gas and a 150-V/cm drift field. This defines the length of our time window for proton-γ coincidences, since β-delayed γ events will be detected in SeGA almost immediately, while charged-particle events resulting from the same decay will take several microseconds to be detected by the MICROMEGAS. The measured difference in time between when the γ and charged-particle events are detected yields drift times of the ioniziation electrons, plotted in Figure 3.13.

Electronics

A detailed electronics diagram for e17024 is presented in Figure 3.14. In summary, two modules were used to provide all biases for the Proton Detector system as well as the PIN detector. Setting voltages can be done remotely over the lab network via a Linux terminal, and the currents in all preamplifier channels can be monitored through the same terminal. The bias voltages applied to the HPGe crystals are set and controlled by designated SeGA electronics, which are maintained by

the Gamma Group at NSCL.

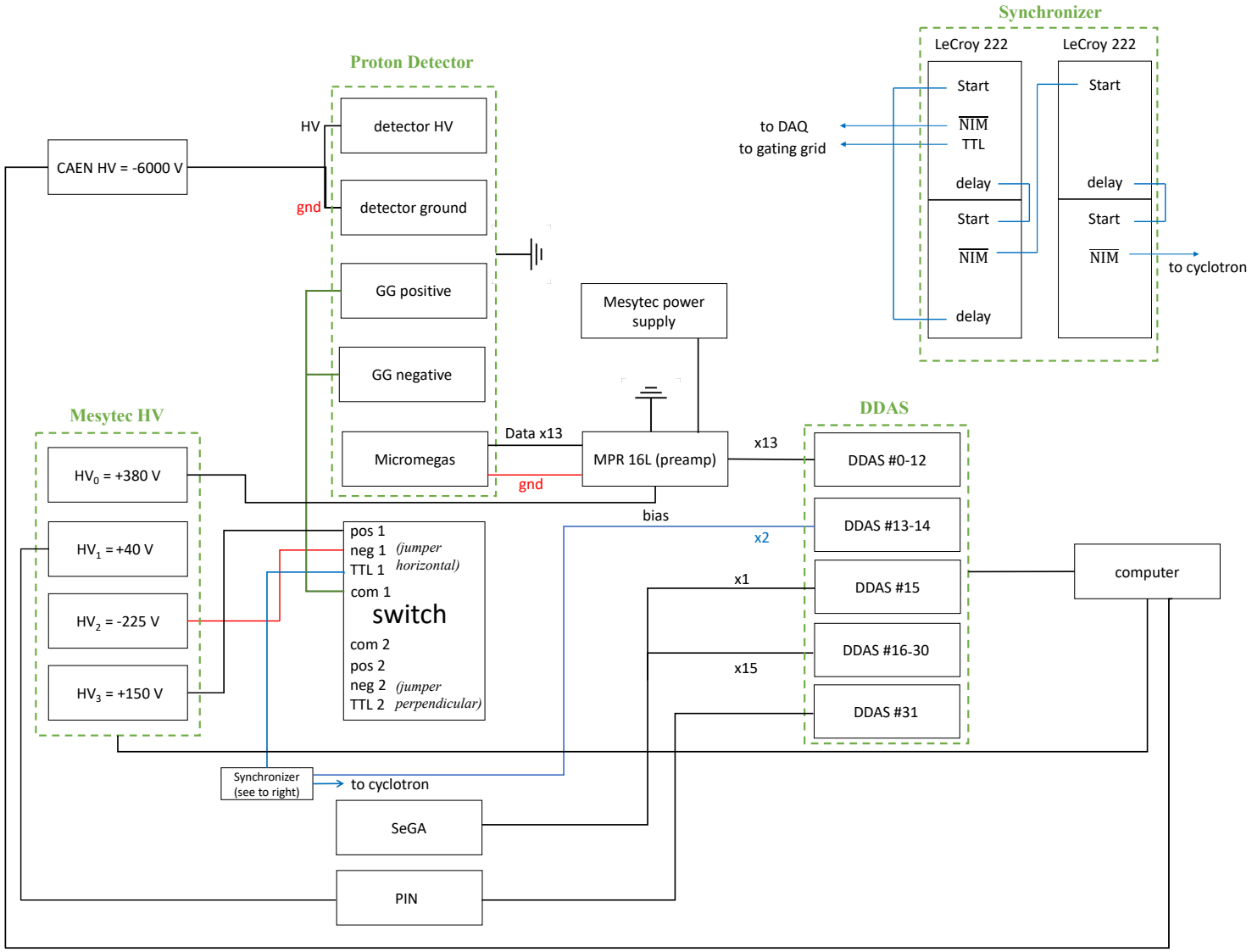

Figure 3.14: Diagram of GADGET electronics configuration for NSCL experiment 17024.

Drift Field

An N1470B programmable high voltage power supply from CAEN is used to bias the Proton Detector cathode through a safe high voltage (SHV) cable connection. In order to generate the 150-V/cm electric field in the drift region, a large, negative voltage (-6 kV) is required. Once the Proton Detector is filled to its operating pressure with P10 gas, the bias is slowly ramped to the set-point voltage, where it remains for the duration of the measurement. It is important to avoid applying high voltages to electrical components when the surrounding gas has not yet reached operating pressure because this can induce sparking in the detector. The relationship between the breakdown voltage and gas pressure is described by *Paschen's law* [131]. Qualitatively, it implies that the voltage required to cause electric discharge in near-vacuum or near-atmospheric pressures is very high, but around pressures of $1 - 10$ Torr, the breakdown voltage is only on the order of 100 V, depending on the chemistry of the gas.

Detector Gain

The other high voltage power supply is the MHV-4 module from Mesytec. The first of its four channels supplies the positive voltage necessary for inducing a strong electric field in the amplification region. This 380-V bias is applied through the preamplifier, which is directly connected to the 13 charge-sensitive anode pad plane. The MPR-16-L is a 16-channel, charge-integrating preamplifier, which acts as a charge-to-voltage converter before the electronic detector signals can be digitized and saved to memory on a lab network computer. The second channel in the MHV-4 unit applies a 40-V bias to the PIN detector via another another preamplifier borrowed from the NSCL electronics pool. Both preamps are powered by an MNV-4. This multi-channel NIM power distribution and control module, as well as the two preamps, were all manufactured by Mesytec. The two remaining channels in the MHV-4 module are used to bias the gating grid.

Gating Grid

The electronic gating grid was designed to protect the preamplifier during beam implantation. When beam is implanted in the gaseous Proton Detector, large quantities of ionization electrons are liberated, which can induce strong currents on the MICROMEGAS anode plane. This rapid charge deposition can saturate the preamp and damage individual channels, preventing signals induced on the corresponding detector pad from being recorded in data. To avoid charge saturation, beam experiments using GADGET run in two-step cycles of beam implantation followed by decay measurement, with which the gating grid is synchronized. When beam is implanting in the Proton Detector, a positive voltage is applied to the gating grid, causing it to appear "opaque" to free electrons. Systematic tests of the gating grid were performed before e17024, and a 150-V bias was found to be most effective.

After beam implantation stops, the voltage on the gating grid switches to a negative bias at equipotential with the last copper ring in the field cage, which was calculated to be -225 V. This causes the gating grid to appear "transparent" to primary electrons, allowing ionization created from β-delayed, charged-particle decays to enter the amplification region and produce detectable signals. In order to utilize beam time as efficiently as possible, the length of these implant-decay cycles is chosen with respect to the half-life of the nuclear species being studied. Considering the 190-ms half-life of ^{31}Cl, the length of the implantation time per cycle was set to be $\approx$300 ms, while the optimal measurement time per cycle was about 200 ms.

It is important that the electronics connected to the MICROMEGAS are protected by the gating grid over the entire beam implantation period. For this reason, the gating grid is switched to opaque mode slightly before the beam restarts implantation, and it only switches back to transparent mode once the beam implantation period has ended, as depicted in Figure 3.15. These two timing signals need to be sent to the beam operators and the gating grid to ensure synchronization. The logic signals used to communicate this information were constructed using the two LeCroy Model 222 Dual Gate and Delay Generators in Figure 3.16.

The gating grid logic signal must be sent to a CGC Instruments NIM-AMX500-3 switch, shown

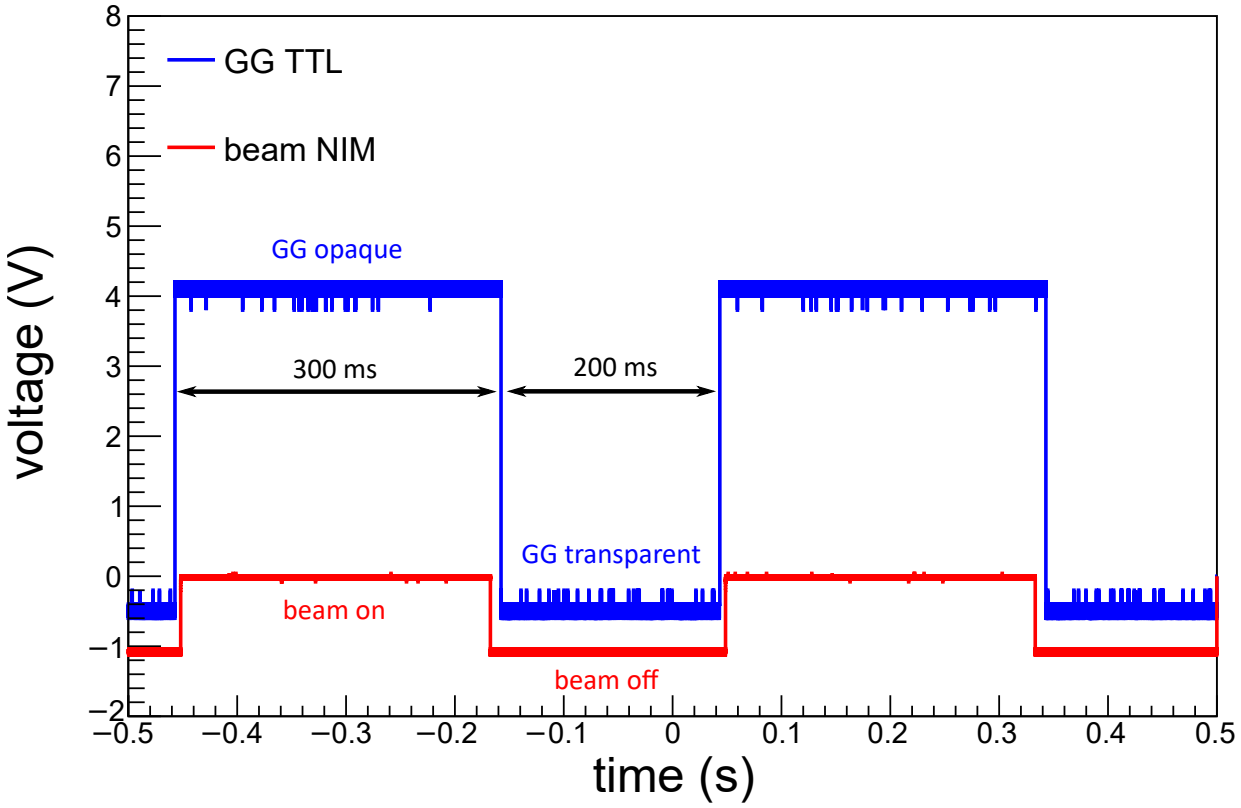

Figure 3.15: Logic signals represented as voltage over time for the gating grid (blue) and the ion beam (red). The amplitude of the voltages are related to differences in logic signal families. The dual gate/delay generator sends a transistor-transistor logic (TTL) signal to the switch, communicating which bias voltage should be applied to the gating grid. When a TTL signal has a voltage amplitude of 1.5 – 5 V, this corresponds to a digital signal of "1," while a signal voltage of 0 – 0.7 V logically implies "0." Similar timing information is communicated via a Nuclear Instrumentation Module (NIM) signal, which is sent to the beam operators and the digital data acquisition system. When a NIM signal voltage is exactly 0 V, this implies a digital "0," but a NIM signal voltage between -0.8 and -1 V corresponds to a binary value of "1."

in Figure 3.17, which is responsible for alternating the source bias between the negative and positive voltages. SHV cables connect the third and fourth channels in the MHV-4 module to the switch's "Neg1" and "Pos1" feedthroughs, respectively. A T-shaped, SHV connector is attached to the switch's "Com1" feedthrough, to which two SHV cables directly connect the switch and the gating grid via the electrical feedthroughs in one of the Proton Detector's downstream flanges. The same timing signal is also sent directly to the digital data acquisition system to record the gating grid status over the course of the entire experiment.

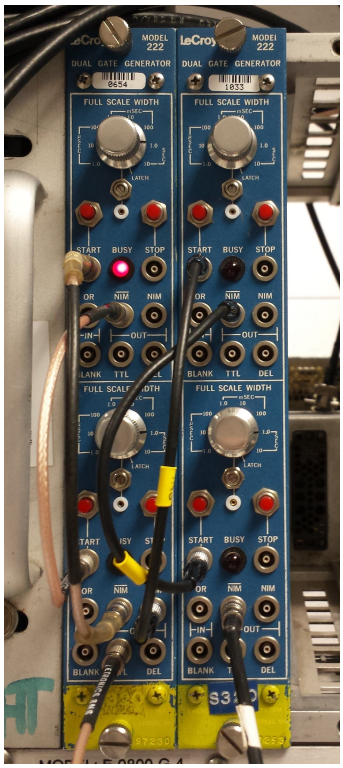

Figure 3.16: Dual gate/delay generators in the Data-U electronics rack. These modules produced the TTL and NIM timing signals sent to the gating grid and beam operators, respectively.

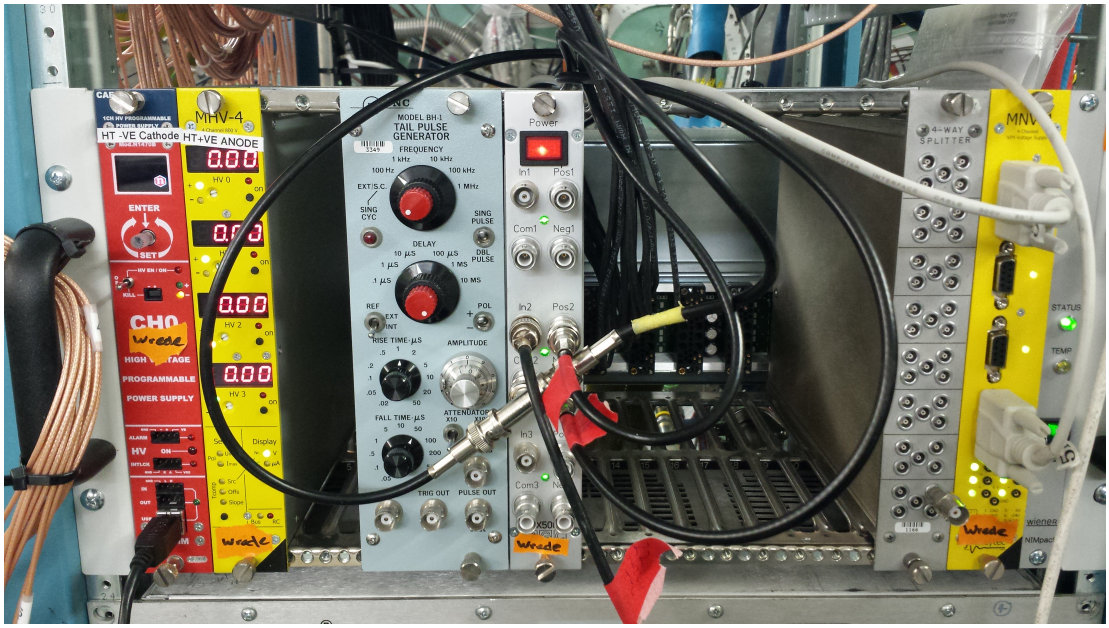

Figure 3.17: All electronics modules utilized on the rack in the S2 vault during NSCL experiment e17024.

Digital Data Acquisition System

All experimental data measured with GADGET was obtained using NSCL's digital data acquisition system (DDAS). Traditionally, data acquisition systems for experimental nuclear physics involved passing detector signals through a series of analog NIM modules, which are designed to shape electronic pulses, as well as correct for any timing discrepancies between signals that should arrive in coincidence but are misaligned in time due to small differences in delay between channels. Once signals are well-shaped and synchronized, they can then be digitized and read into a computer or written directly to magnetic tape. In contrast, DDAS eliminates the need for many of the analog signal-processing modules in its pulse-shape analysis of digitized signals.

Primarily, DDAS was developed to work in conjunction with SeGA for the purposes of in-beam studies that combine γ-ray detection with identification of reaction residues [132]. This streamlined, digitized system was implemented in SeGA for determining the first interaction position of a γ ray in one of the segmented crystals and subsequent γ-ray tracking in the detector. This has significantly improved the ability to measure the angular distribution of γ emission and has allowed for more precise Doppler corrections in fast beam experiments. For stopped-beam measurements involving beam implantation followed by charged-particle decay, like NSCL experiment 17024, DDAS allows for zero dead time measurements of rare decays [133].

For NSCL experiment 17024, we utilized two 250-MHz, 16-channel PXI Digital Pulse Processors in a PXIE-CRATE-P16X14 from XIA, which was connected to one of the lab network's data acquisition computers. DDAS employs a pair of trapezoidal filters for leading-edge triggering and pulse-amplitude measurements as well as a constant-fraction discriminator (CFD) algorithm to determine the timestamp and energy of detector signals [134]. As depicted in Figure 3.14, the first 13 DDAS channels were connected to all the MICROMEGAS detector pads through the MPR-16-L preamp. Another channel was dedicated to measuring the $\overline{\text{NIM}}$ signal from the dual gate/delay generator modules for recording the status of the gating grid mode throughout the experiment. Each of the 16 individual SeGA detectors were connected to their own DDAS channel in the XIA crate, and a single channel was used to record events from the PIN detector in the cross. A more complete

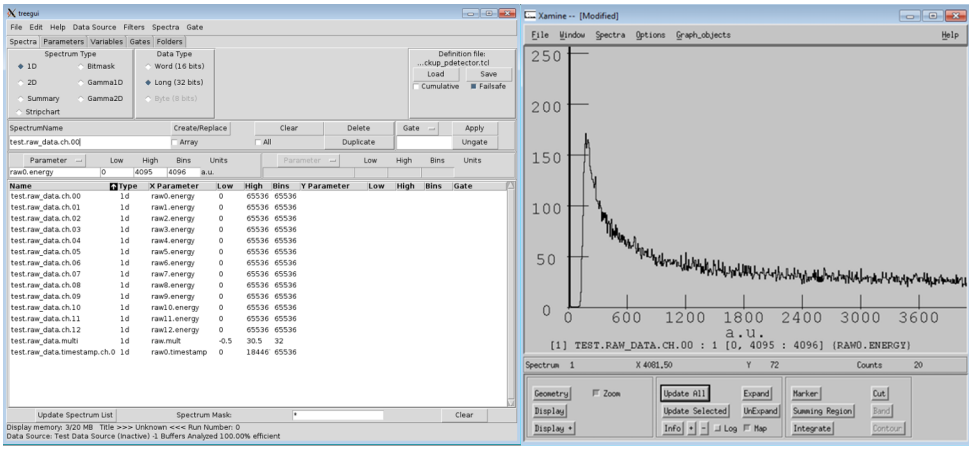

Figure 3.18: Example of the visualization windows used during online analysis using SpecTcl.

description of hardware implementation for DDAS in experimental applications at NSCL is given by Ref. [134].

Operating Procedure and Online Analysis

Detailed documentation on the architecture of the NSCL data acquisition software is provided in the user guide [135], but in short, each detector signal triggered in DDAS is assigned a timestamp and written to the *ring buffer* by the Readout program. The ring buffer is divided into *events* with a characteristic time window, which we set to 4 μs for this experiment. Data in the ring buffer can be saved by writing to a binary event file (".evt"), accessed for online analysis, or both simultaneously. The ReadoutShell program was used for collecting and saving GADGET events. Experimental data were generally procured in hour-long measurement runs. The purpose of relatively short runs was to reduce the probability of the Readout program from crashing in the middle of a measurement, which would result in the loss of all data from a single run.

Before beginning of a standard measurement run, the gas flow and pressure inside the Proton Detector was ensured to be stable. We verified that the beam was off, that the timing between the gating grid and the beam cycling was appropriately synchronized, and that the PIN detector was in the retracted position. Then, detector biases were slowly ramped until they reached the set-point voltage. Once beam was allowed to start entering the Proton Detector again, data collection could

resume, and all the diagnostic information about the present status of the experimental setup would be recorded. At the end of the hour, the ReadoutShell program was halted to prevent further data collection. During a diagnostic run for particle identification, which were performed aperiodically multiple times per day, we would typically attenuate the beam, remove the amplification bias on the anode, and turn off the beam pulse cycling. The Si detector would then be inserted into the path of the beam via the pneumatic drive, which is controlled remotely, and a new Readout session would be used for the PIN detector. All GADGET data was visualized during the experiment using the SpecTcl program, as depicted in Figure 3.18.

After a measurement run was terminated and all events were written to file, the "ddasdumper" program was used to convert ".evt" files to ".root" files. A sorting code was used to extract the relevant information from each DDAS channel and fill histograms corresponding to each detector channel in the GADGET system. A second sorting code was used to apply the veto conditions on the individual Proton Detector pads and build all the histograms storing particle-γ coincidence information. The time window for building coincidence histograms was extended to 8 μs because this is the maximum possible drift for ioniziation electrons created by decays near the cathode. These processed ".root" files could then be analyzed using the ROOT analysis framework to provide a more detailed understanding of dataset during the experiment.

CHAPTER 4

DATA ANALYSIS AND SCIENTIFIC RESULTS

4.1 The Proton Branching Ratio

The primary scientific goal for the analysis of the ^{31}Cl β-delayed proton decay data obtained during NSCL experiment 17024 was to determine the proton branching ratio Γ_p/Γ of the 6390-keV level in ^{31}S. This information is needed to evaluate the equation for the resonance strength:

$$\omega\gamma = \frac{(2J_r+1)}{(2J_p+1)(2J_t+1)}\frac{\Gamma_p\Gamma_\gamma}{\Gamma}. \tag{4.1}$$

From a previous ^{31}Cl β^+ decay measurement, Bennett *et al.* determined the β-delayed γ decay intensity through this state to be $I_\gamma(\text{abs.}) = 3.38(16)\%$ [121]. In the case of this resonance state, γ and proton emission are the only two open decay channels. Therefore, the sum of the branching ratios is simply $(\Gamma_\gamma + \Gamma_p)/\Gamma = 1$. This allows us to express the proton branching ratio in terms of the β-delayed radiation intensities through the 6390-keV level as

$$\frac{\Gamma_p}{\Gamma} = \frac{I_p}{I_\gamma + I_p}. \tag{4.2}$$

Gain Matching and Sorting

The spectra referenced in this dissertation contain data from over 86 hours of on-target beam time. Each hour-long run was automatically divided into a number of sub-runs, determined by how much data was acquired in a particular acquisition session. After completing a measurement run, the raw event files of the recently acquired data were converted to a file format that allowed for more detailed offline analysis using the ROOT framework [136]. An automated analysis script was used to provide a preliminary gain-matching of the five inner MICROMEGAS pads. This involved fitting the largest proton peak in the spectrum to extract the mean analog-to-digital converter (ADC) channel of the intense 1-MeV β-delayed proton transition, modeling the proton distribution as a

Gaussian function. Because the statistics for any one particular acquisition run were quite low, especially at the beginning of the experiment, only the 1-MeV proton peak could be consistently fit automatically. For the sake of expediting our analysis while still collecting data, our zeroth-order calibration procedure assumed a linear mapping between ADC channel and center-of-mass decay energy with no offset, estimating the gain of a single detector pad as the ratio between the 1-MeV decay energy and the mean ADC channel. After applying this rough gain-matching procedure for each of the active detector pads, we were able to combine statistics from all inner pads to observe the presence of the weak, low-energy β-delayed proton decay near 260 keV before the end of NSCL experiment 17024.

The sorting routine used to accomplish this task applied veto conditions to remove Proton Detector events with long tracks which deposited energy across multiple detector pads. By applying these anti-coincidence cuts, histograms were generated for each of the five, inner detector pads labeled A-E in Figure 3.3. The procedure is as follows: If all ionization electrons generated from a single proton event are detected in only one MICROMEGAS channel, the energy of this event is added to the one-dimensional histogram spectrum for that detector pad. The β-delayed proton spectra for all individual pads A-E are plotted in Figure 4.1. However, if a proton decay deposits all of its energy within the active region of the detector, but this charge is shared among multiple inner pads, this event will not be recorded in any single detector channel's histogram. Instead, this decay energy is added to the event-level combined spectrum as shown in Figure 4.2. Events that deposit all their energy in only one of the five inner pads are also included in this cumulative proton spectrum as well. A more detailed gain-matching procedure was performed for each individual pad on a run-by-run basis after the experiment during offline analysis. This utilized the two strongest proton peaks in the spectrum to determine a linear mapping, instead of just using the single 1-MeV peak and assuming zero offset.

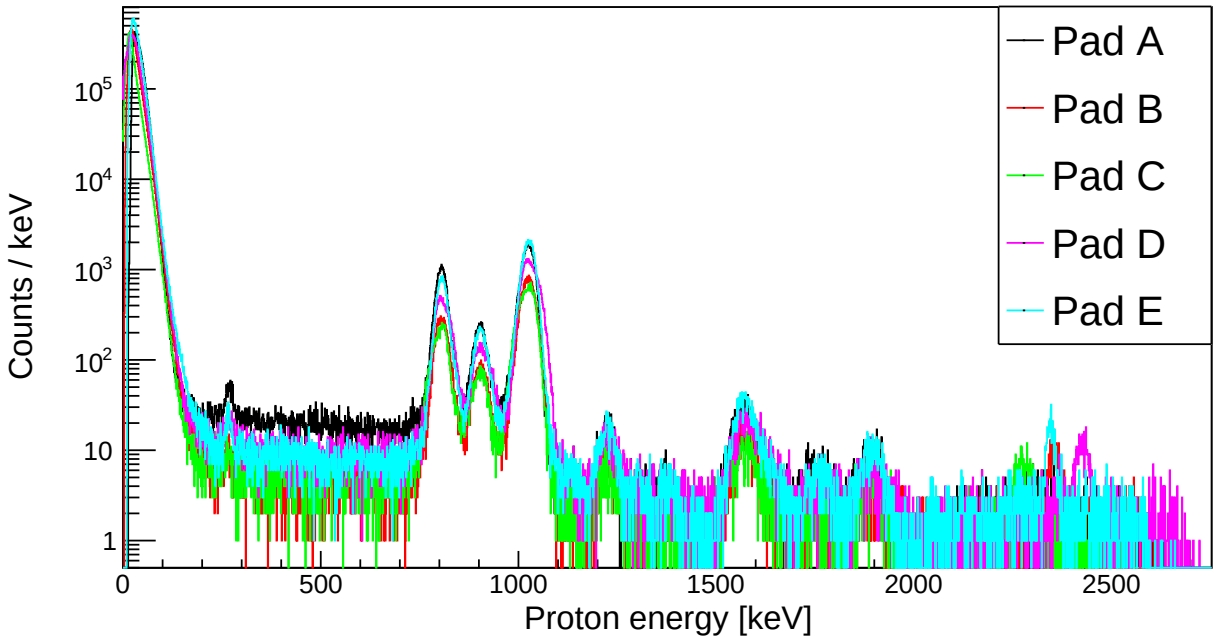

Figure 4.1: ^{31}Cl β-delayed proton spectra as measured by each of the five inner pads individually.

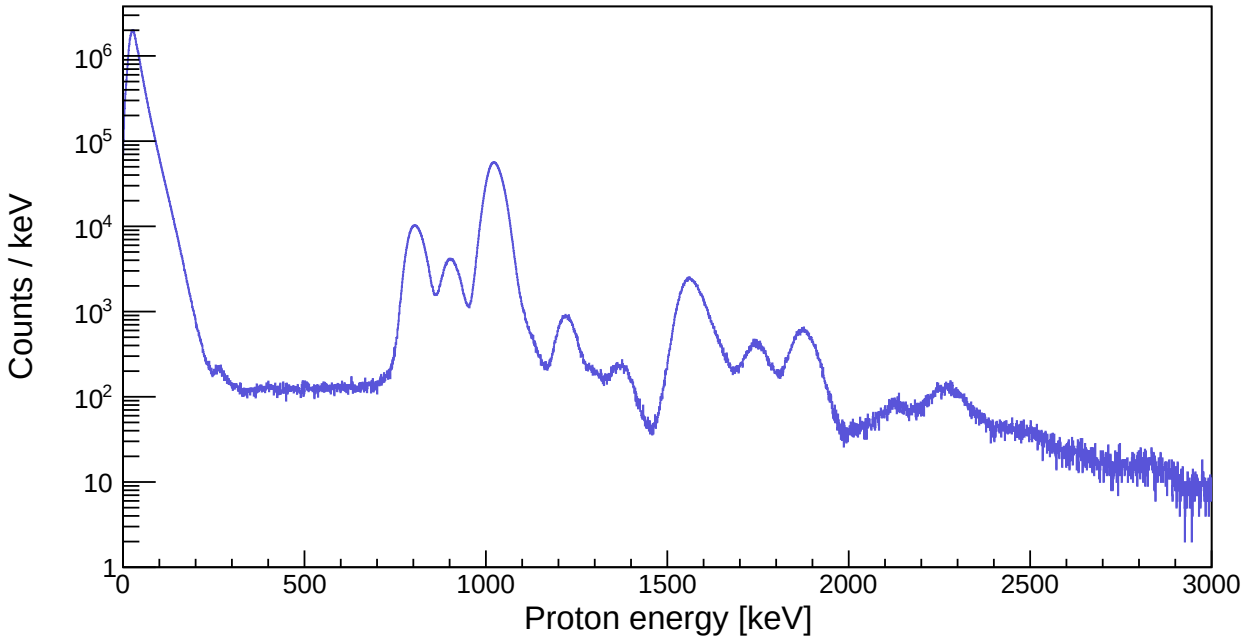

Figure 4.2: Combined energy spectrum for ^{31}Cl β-delayed proton decays with event-level summing over all pads.

Preliminary Energy Calibration with Central Pad

All previous reports of ^{31}Cl β-delayed proton decays assumed that particles emitted from proton-unbound states in ^{31}S populated the ground state of ^{30}P. If this is also the case for the only visible proton peak below 300 keV in Figs. 4.1 and 4.2, it should be obvious that these protons were emitted from the astrophysically important 6390-keV level; no other states within 100 keV have been observed to be populated by ^{31}Cl β^+ decay. However, in order to say for sure that we have observed proton decays from the 260-keV resonance of interest, we must demonstrate that decay energy we measure is consistent with Ref. [121].

It did not take long in the process of analyzing the ^{31}Cl β-delayed proton data to realize that the spectrum above 700 keV is much more complicated than had previously been assumed. For this reason, we did not feel comfortable using all high-energy proton peaks and their reported literature energies in our initial energy calibration procedure. Instead, we only used the decay energies of the three strongest β-delayed proton decays as our calibration standards. We confirmed that these are ground-state transitions since they are not observed in coincidence with any ^{30}P γ rays. Their decay energies as measured in previous ^{31}Cl β-delayed proton experiments [117; 118] are in agreement with the well-known ^{31}S excitation energies measured in many reaction experiments [137; 138; 101; 105; 102; 103; 99]. They also have the added benefit of being the decay energies closest to our 260-keV resonance of interest. For our first attempt at an energy calibration, we adopted the evaluated center-of-mass energies E_p(c.m.) = 806, 906, and 1026 keV, each with an associated 2-keV uncertainty [119].

We chose to use the pad A proton spectrum, comprised of events only measured by the central MICROMEGAS pad, for our first calibration attempt when reporting the energy of the low-energy peak. Its location in the detector means that pad A has relatively high statistics compared to the other four inner pads, but it is also has a smaller area than all other active pads. This limits the amount of energy β^+ particles can deposit in this pad before being vetoed, pushing the β^+ background to lower energies and reducing the effect of summing with energy from proton decays. Thus, the resulting proton peaks are the sharpest in the central pad spectrum and allow for a more

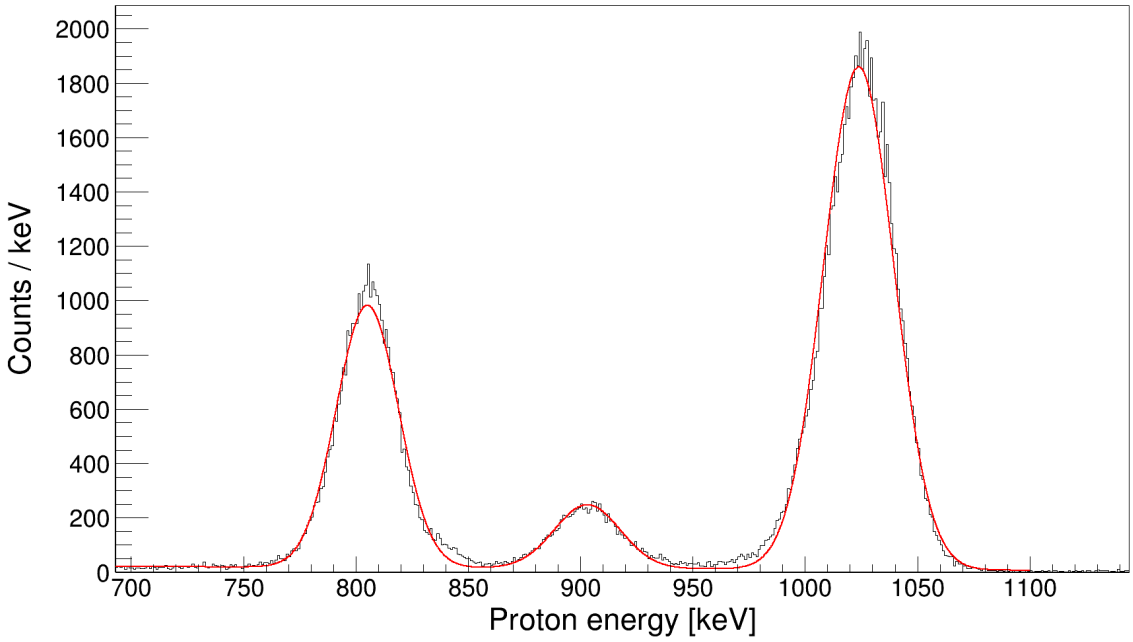

Figure 4.3: A χ^2-minimized fit of the calibration peaks as measured by the central pad of the Proton Detector. The three proton peak distributions were modeled as Gaussian and the background as linear.

precise energy calibration. The calibration peaks and the low-energy resonance peak of interest were all fit with Gaussian distributions and a first-order polynomial function to describe the mostly flat background in the energy range 300 - 700 keV, as shown in Figs. 4.3 and 4.4, respectively.

The fraction of the proton's kinetic energy that goes into ionizing the fill gas varies as a function of decay energy. The discrepancy between the measured amount of ionization in the detector and the total energy of the resonance center-of-mass decay energy is known as the *pulse height defect*. This was calculated for the protons and recoils associated with each of the calibration peaks as well as for resonances up to 2 MeV using TRIM [139]. Since the 806- and 1026-keV proton peaks were used to gain match all proton spectra, calibrating relative to the three peaks in this energy region should already account for the effect of any small pulse height defect; the difference between their center-of-mass decay energies and the amount of ionization they created in an 800-Torr P10 gas is 6-8 keV. However, extrapolating this defect down to lower energies may cause the low-energy proton peak to appear shifted in the spectrum.

To account for this, we plotted the means of three calibration peak's fitted Gaussian distributions

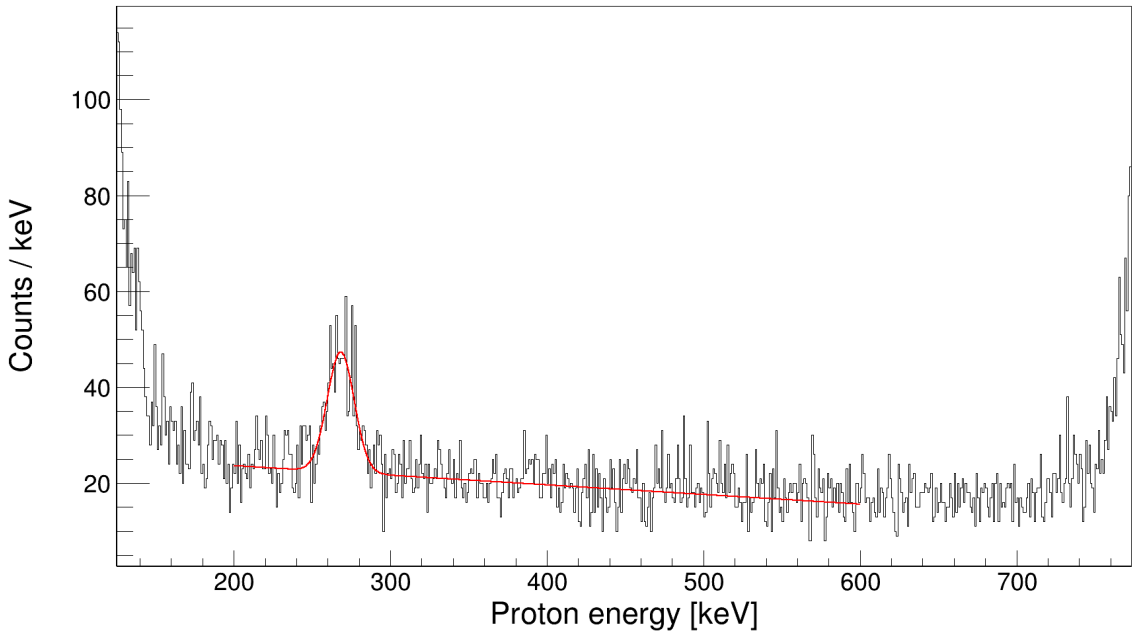

Figure 4.4: Fit of the weak, low-energy proton peak and background region in the pad A spectrum.

as the independent variable and the calculated total ionization in the gas as the dependent variable. Figure 4.5 shows this data fit with a line and the associated uncertainty band. We then used this calibration function to evaluate the amount of ionization the low-energy proton decay should have produced [268.2(8.5) keV] and then calculated its resonance energy to be E_p(c.m.) = 273(10) keV based on what the decay's pulse height defect should be in order to produce the observed amount of ionization in the detector. The total uncertainty in the resonance energy comes from summing in quadrature the 8.5-keV uncertainty associated with extrapolating the energy calibration down to low energies, the uncertainty associated with the 5-keV pulse height defect, and the 1-keV statistical error from fitting the small peak. While not expected to be as accurate or precise as other methods for determining the resonance energy, we are consistent with Ref. [121] to within 1.4 standard deviations. For this reason, we refer to this resonance as the 260-keV decay throughout this document. A more robust energy calibration of the proton spectrum over all energies is provided in Chapter 5 of this dissertation.

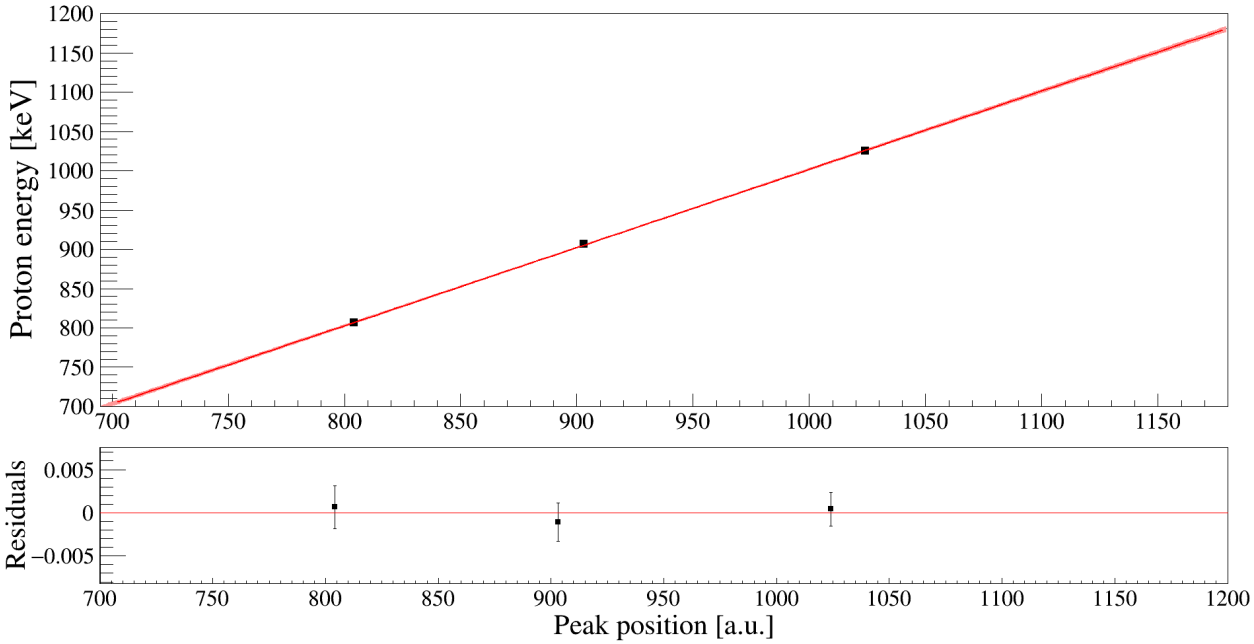

Figure 4.5: Central detector pad energy calibration. Top panel: Linear fit mapping positions of three calibration peaks in Pad A spectrum to known decay energies. Bottom panel: Plotting residuals between data and linear fit model.

Proton-γ Coincidences

In addition to the ^{31}Cl β-delayed proton decay data, we simultaneously collected substantial β-delayed γ ray statistics with SeGA over the course of e17024. This information was extremely useful for diagnostic purposes and ultimately for constructing the most detailed $^{31}\mathrm{Cl}(\beta p\gamma)^{30}\mathrm{P}$ decay scheme to date, as will be discussed in Chapter 5. However, the primary astrophysical importance of the γ rays from this experiment was the use of coincidence analysis to conclusively determine the initial and final states of the 260-keV proton transition. In order to visualize this γ data, we produced a variety of different histograms.

Ungated γ ray events were detected by all 16 of SeGA's HPGe crystals. We produced a gain-matched energy spectrum histogram for each detector channel using the energies of well-known sources of background radiation as calibration points. This included γ rays emitted in the decays of naturally occuring ^{214}Bi, ^{228}Ac, ^{40}K, and ^{208}Tl in the environment [140]. We also utilized the ^{31}Cl β-delayed γ at 6279 keV in order to extrapolate our linear gain-matching function to higher

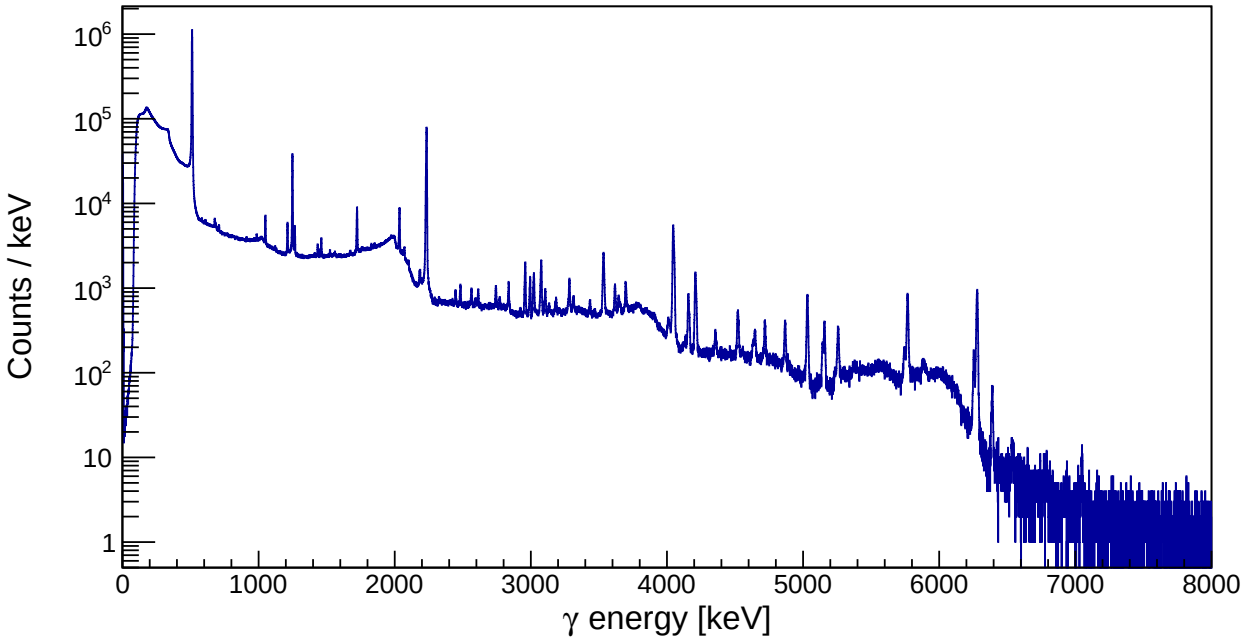

Figure 4.6: ^{31}Cl β-delayed γ ray singles spectrum including all events from 15 of the 16 SeGA detectors observed to be in coincidence with non-vetoed, charged-particle radiation in the Proton Detector.

energies. Not unlike the proton spectra, each SeGA detector's energy spectrum was gain-matched on a run-by-run basis by fitting these calibration peaks with Gaussian functions, recording the mean ADC channel of the χ^2-minimized distributions, plotting known the γ ray energies as a function of these means, and fitting the data with a linear calibration function. Combining histograms from 15 of the 16 HPGe detectors produced a "singles" spectrum with maximum γ ray statistics; one of the SeGA detectors exhibited poor energy resolution and was excluded from subsequent analysis.

However, without enforcing any gating conditions, we cannot be sure that the decays measured by SeGA occurred within the active region of the detector. This makes it challenging to compare the intensities of β-delayed proton and γ emissions. For this reason, we set an 8-μs time window to record proton-γ coincidences since this is the maximum possible drift time for primary ionization electrons originating from decays near the cathode. Thus, every γ ray detected in SeGA that occurs within the 8 μs prior to a recorded Proton Detector event is added to the one-dimensional proton-gated γ ray spectrum shown in Figure 4.6. In addition to this proton-gated γ singles spectrum, we

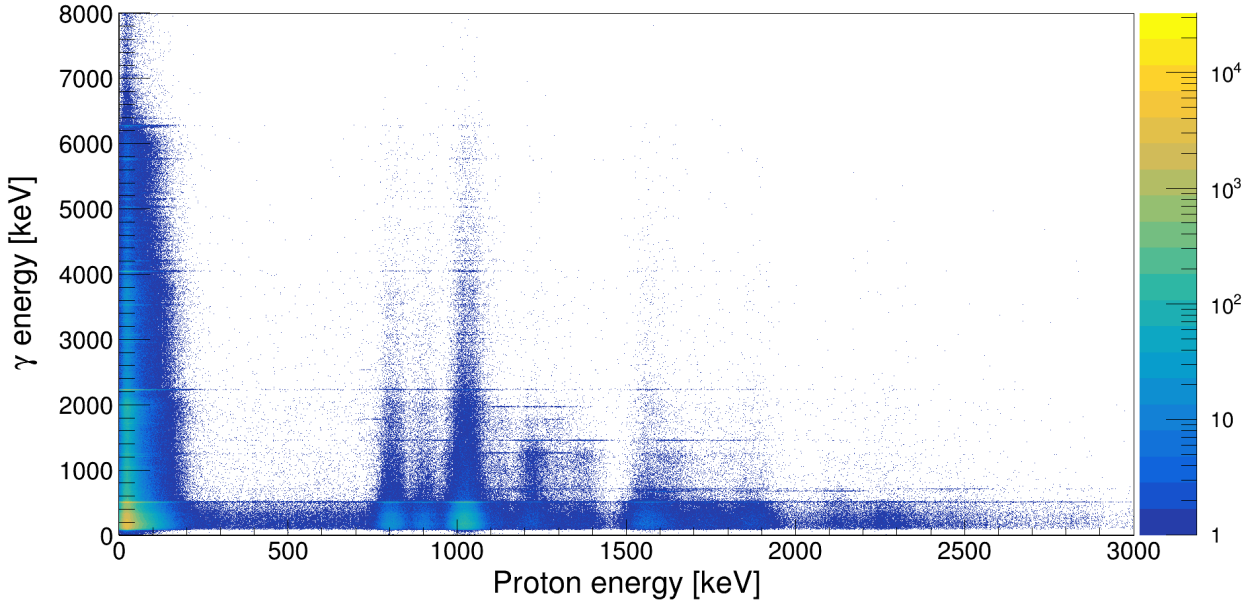

Figure 4.7: Two-dimensional coincidence matrix between γ rays detected in SeGA and charged-particle events in the Proton Detector.

also generated two-dimensional histograms that plot γ energy versus proton energy for all proton-γ coincidences, as depicted in Figure 4.7. Similarly for multiple γ rays detected in coincidence with each other, assuming their detection in SeGA precedes a non-vetoed Proton Detector event, these events are added to another coincidence matrix, shown in Figure 4.8, where both axes correspond to γ energy.

By applying a coincidence cut on 260-keV proton events and plotting all the detected γ rays in that are observed within that same 8-μs time window, we can check to see if this low-energy, β-delayed proton decay is truly populating the ground state of ^{30}P. This is relevant because only proton captures on the ground state of ^{30}P are relevant for $^{30}\mathrm{P}(p,\gamma)^{31}\mathrm{S}$ in ONe nova nucleosynthesis. For comparison, we can place another coincidence gate on a featureless background region of the Proton Detector data over the energy range 350 – 700 keV. This roughly linear background contribution decreases gradually across the entire spectrum and likely originates from higher-energy proton events that do not deposit their full energy in the active region. This continuum should be a reasonable representation of the background under the 260-keV peak.

To ensure a proportional comparison between the two regions, the background-gated γ ray

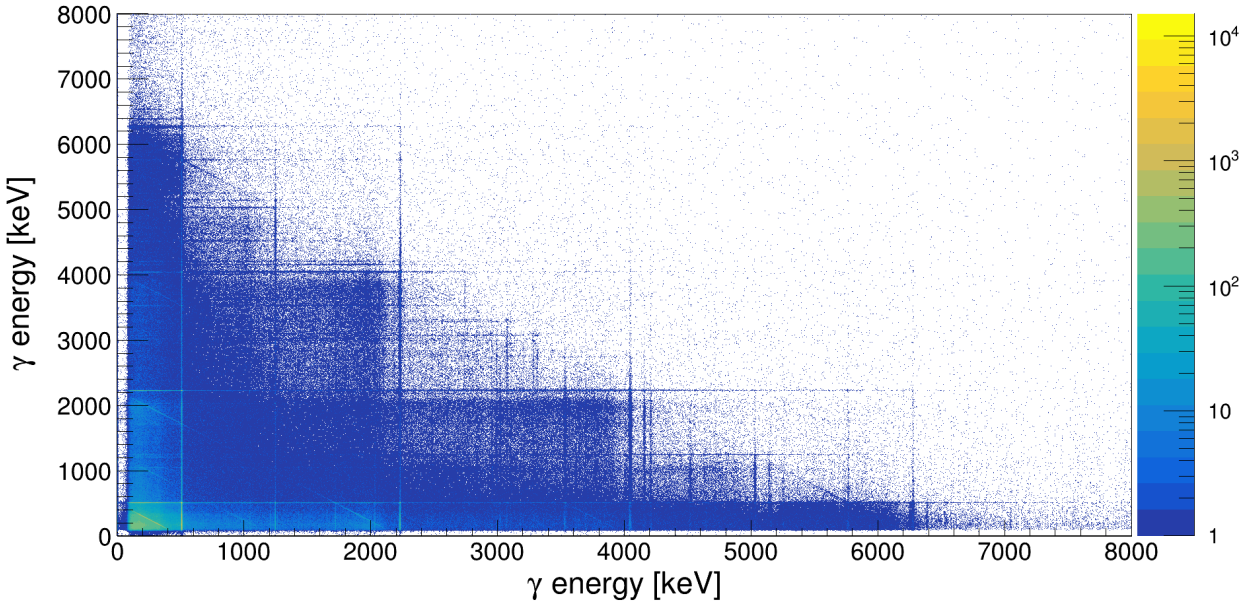

Figure 4.8: Two-dimensional γ-γ coincidence matrix for events occurring within the same 8-μs window preceding charged-particle radiation observed in the Proton Detector.

spectrum should be scaled down by the ratio of counts in each region of the proton singles spectrum. We can see in Figure 4.9 that there is no evidence of γ emissions in coincidence with the 260-keV protons above background level. The fact that there are slight excesses across most bins in the 260-keV-proton-gated spectrum likely reflects the fact that some of the background under the peak is the result of β^+ particles, which we know are likely to populate γ-emitting states in ^{31}S. Meanwhile, sampling from the background region 350 – 700 keV almost exclusively includes proton events, so any coincidence γ rays must be either accidental or true coincidences from higher-energy protons populating ^{30}P excited states. Still, there is no statistically significant difference in the number of the photopeak between the two particle-gated histograms, suggesting that we are, in fact, observing β-delayed proton decay through the 260-keV resonance of interest.

Combined Pads Detector Response

The random, statistical variation associated with measuring some quantity with a particular central value can usually be described by a Gaussian distribution, assuming the number of observed events is large. Since the Proton Detector and SeGA are designed to measure the charge or

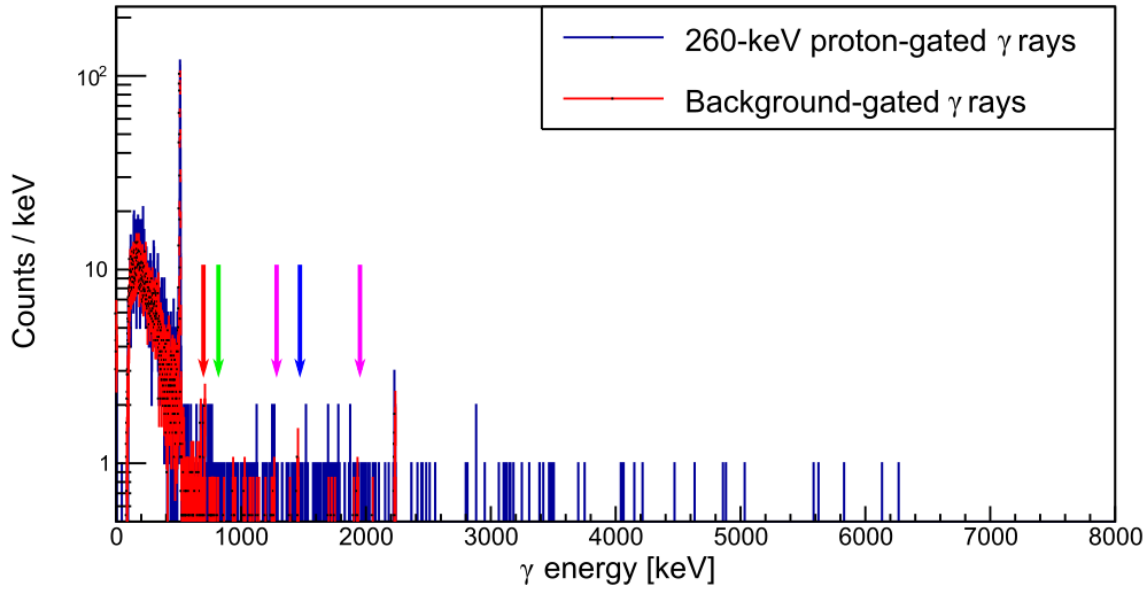

Figure 4.9: Comparison between 260-keV proton-gated γ rays and background-gated γ ray spectrum. The γ rays in coincidence with background are sampled from the energy range 350 – 700 keV in the Proton Detector spectrum and have been scaled down by the ratio of counts in the two gating regions in the proton singles spectrum. The arrows point to the energies where γ events would be observed if the 260-keV β-delayed proton decays populate excited states in ^{30}P; their colors correspond to the energy levels from which the γ rays are emitted.

current induced by stochastic processes, which are proportional to the energies of discrete nuclear transitions, the corresponding spectral peaks exhibit shapes that can be represented by Gaussian functions. However, the complicated physical interactions between radiation and the detection medium degrade the symmetry of a normal statistical distribution.

In the case of the Proton Detector, β-delayed proton decays result in the emission of three ionizing, charged particles: the β^+ particle, the proton, and the recoil nucleus. Because the proton and recoil nucleus decay back-to-back over a relatively short range, moving in opposite directions due to conservation of linear momentum, depositing comparable fractions of their energy into ionizing the detector's fill gas, the peak shape associated with the center-of-mass energy of the proton decay alone is basically symmetric. However, the β^+ particles inevitably deposit some of their energy in the gas as well, resulting in an observed decay energy which is slightly higher than the proton-emitting resonance energy. This β^+ summing effect causes the β-delayed proton decay

peaks to be slightly skewed to the right. The shape of the large β^+ background that exists at low energies (<200 keV) is well fit with a decaying exponential function, and peaks corresponding to β-delayed proton decays can be understood as a sum of these energies. For this reason, we model the detector response of each Proton Detector pad as an *exponentially modified Gaussian* (EMG) function with a high-energy tail. In terms of the independent variable x, which is proportional to energy in our spectra, the shape can be expressed using the equation

$$f(x;\mu,\sigma,\lambda) = A\frac{\lambda}{2}e^{\frac{\lambda}{2}(2\mu+\lambda\sigma^2-2x)}\mathbf{erfc}\left(\frac{\mu+\lambda\sigma^2-x}{\sqrt{2}\sigma}\right), \tag{4.3}$$

where μ represents the centroid of the function's symmetric Gaussian component, σ is proportional to the width of the peak, λ determines how asymmetrically skewed the distribution is, and the normalization constant A represents the area under the curve [141]. The *complementary error function* (erfc) is defined in terms of the *error function* (erf) as

$$\begin{aligned}\mathbf{erfc}(x) &= 1-\mathbf{erf}(x)\\ &= \frac{2}{\sqrt{\pi}}\int_x^\infty e^{-t^2}dt.\end{aligned} \tag{4.4}$$

The proton peaks in the individual pad's histograms have a unique shape and resolution. The extent to which proton peaks are skewed in each pad is primarily due to the relationship between detector pad surface area and the transverse distribution of the radioactive beam. Detector pads with a larger surface area can collect more charge from β^+ particles, resulting in a more right-skewed distribution function. Similarly, the beam distribution in the detector affects how likely the β^+ particles are to deposit their maximal energy into ionizing the fill gas. Furthermore, event-level summing over all five inner pads also results in a unique detector response, which although having worse energy resolution, has the benefit of much higher statistics and a better, more precise detection efficiency.

Many of the peaks in the ^{31}Cl β-delayed proton spectra are quite close together at higher proton energies since the level density of proton-emitting states increases with excitation energy. To accurately quantify the number of counts in any single peak using an analytical fit function, it is

often necessary to fit multiple peaks in the spectrum over a range of several hundred keV using a sum of several EMG distributions. We refer to the ratio between a spectral peak's *full width at half maximum* (FWHM = $2\sqrt{2\ln 2}\sigma \approx 2.355\sigma$) and its corresponding decay energy as the *relative resolution*, which should, in principle, decrease as a function of energy. However, the absolute value of the FWHM is likely to increase both due to detector physics and because the total decay width of quantum states tends to increase as a function of energy, and some of these levels are likely to be intrinsically broad. The observed peak widths over a relatively small energy range ($\approx$ 300 keV) are basically constant, but they tend to increase slightly from 700 keV up to 2.5 MeV. For this reason, when fitting multiple proton peaks, we assume the width varies smoothly as a function of energy and thus parameterize the shape of our EMG distributions by the relation $\sigma(\mu) = b + m\mu$. This constrains the peak width to be a linear function of decay energy, the slope and intercept of which we determine via χ^2-minimization. Similarly, we assume the skew parameter λ to vary smoothly as a function of energy and let this parameter be constant for each EMG distribution over a given fit range.

The mostly featureless region over $\approx 300 - 700$ keV in the event-level combined spectrum is extremely flat. We suspect this background results from higher-energy decays near the upstream end of the detector chamber, whose decay protons are emitted in the direction of the cathode. This "wall effect" likely causes protons to deposit some fraction of their energy in the active detection region before being absorbed by the cathode and are thus not rejected by the veto pads. This hypothesis agrees with the observation that the individual pad spectra have slightly steeper slopes in this background region since increasing proton energy heightens the probability of triggering the veto condition more sensitively when the effective pad detection area is smaller. While much of the spectra are populated with many features at decay energies above 700 keV, in the regions between obvious peaks, the background level clearly decreases with energy, which also agrees with the presented explanation for this effect. Thus, we believe it is reasonable to assume a linear model to describe our background, while fitting the β-delayed proton peaks with EMG functions. We estimated the systematic uncertainty in our detector response model by fixing and varying all

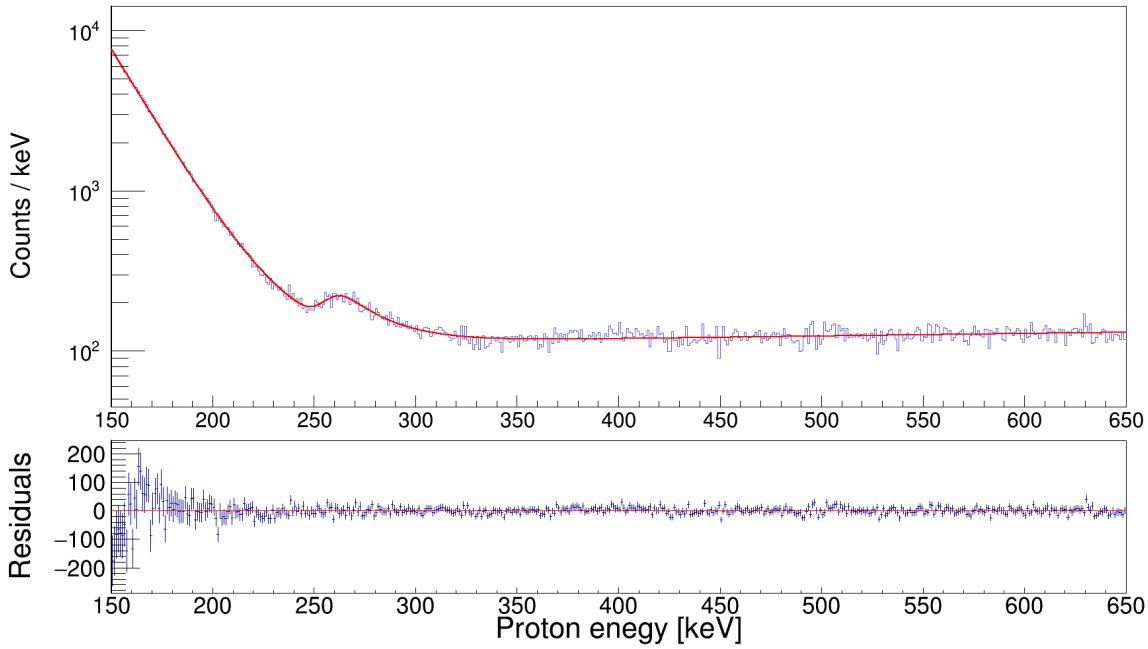

Figure 4.10: Fit of the 260-keV resonance peak summing proton events over all active detector pads.

parameters given in Equation 4.3 and applying these fits over various energy ranges across the entire proton spectrum.

Normalization Procedure

Having parameterized our detector response function at higher proton energies background, we determined the observed number of protons emitted from the 6390-keV level in ^{31}S to be $N_{\beta p}$ = 2731(203). As shown in Figure 4.10, this was accomplished by fitting the small, low-energy protons in the event-level combined spectrum with the sum of an EMG distribution for the peak; a linear function was used to describe the flat background region above the resonance energy and an exponential function for the β^+ background below the resonance energy. The total uncertainty in the number of counts was determined by adding the statistical error of the fit $\Delta N_{\text{stat.}} = \pm 200$ in quadrature with the systematic uncertainty $\Delta N_{\text{sys.}} = \pm 36$ associated with varying the fit range and constraints on the response function parameters. However, in order to determine the proton branching ratio of interest, we must normalize this β-delayed proton decay intensity to some known

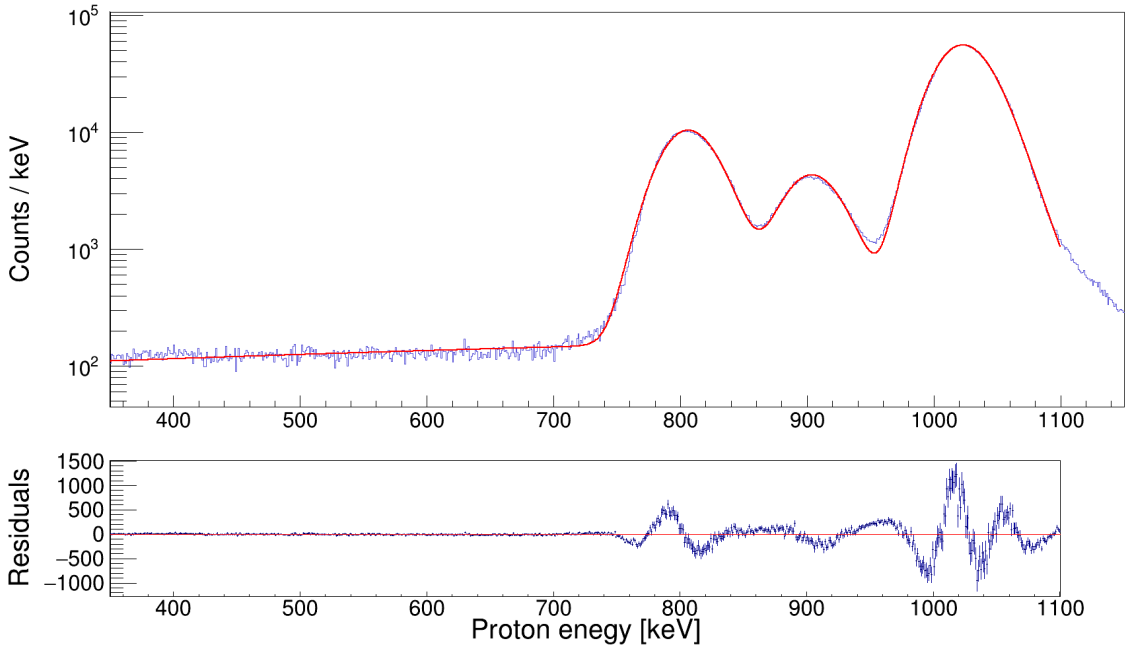

Figure 4.11: Fit of the three calibration peaks in the all-pads-combined spectrum. We do not extend the fit above 1.1 MeV in this case because we determined that there are previously unobserved β-delayed proton decays in this region. These transitions had not been considered when evaluating the intensity of the 1-MeV proton peak, and thus for the purposes of normalizing the literature values, we exclude them as well.

value.

We considered a variety of different normalization strategies, including normalizing to known β-delayed γ decay intensities, counting individual ^{31}Cl ions by measuring their energy deposition in the detector without the amplification field, as well as using proton-γ coincidences that indicate population of ^{30}P excited states. However, each of these methods had their own unique challenges that prevented us from achieving an unambiguous normalization standard. Ultimately, we chose to adopt the evaluated literature intensity [I_p(abs) = 1.31(2)%] of a strong, β-delayed proton emission with the center-of-mass decay energy E_p(c.m.) = 1026 keV [119]. We determined the number of 1-MeV proton counts to be $N_p^{1026} = 3.16(2) \times 10^6$ by fitting the spectrum from 350 to 1100 keV with three EMG distributions to model proton peaks at 806, 906, and 1026 keV on top of a linear background as shown in Figure 4.11.

By taking the ratio between the number of counts in the small, 260-keV resonance peak of

interest and the total counts in the large, 1-MeV normalization peak, we can determine the β-delayed proton intensity needed to evaluate Equation 4.23. However, we must also take into account the effect of proton detection efficiency ϵ_p at the relevant energies. This relationship can be expressed as

$$I_p^{260} = \frac{N_p^{260}/\epsilon_p^{260}}{N_p^{1026}/\epsilon_p^{1026}} I_p^{1026}. \tag{4.5}$$

Proton Detector Efficiency Simulations

In the process of designing the Proton Detector, Monte Carlo simulations were used to model detector response and evaluate the detection efficiency as a function of proton energy. These initial simulations were performed using the GEometry ANd Tracking (GEANT4) framework, which is a detailed, object-oriented platform designed at CERN to simulate the passage of particles through matter and their interactions with variety of detection media [142; 143; 144]. The exact geometry of the Proton Detector was specified in code as well as the chemistry of the gas and the specific energies of known proton decays. The only experimental input to the GEANT4 simulations was the three-dimensional distribution of the ^{31}Cl gas inside the detector chamber. Assuming the beam spot on the detector pad plane is well-described by a two-dimensional Gaussian function, the transverse distribution of the radioactive source was deduced from the observed hit pattern over the course of the measurement.

Using the multiplicity of proton events above 700 keV detected by each of the five inner pads, a χ^2-minimization procedure was implemented to approximate the x- and y-coordinates of the beam spot's origin as well as the radial width for the transverse component of the beam distribution. In the initial GEANT4 calculations, we also enforced the condition that the beam spot be truncated at a radial distance of 25.4 cm from the center of the pad plane, since this corresponds to the size of the window through which the beam enters the Proton Detector; Figure 4.12 shows the transverse beam distribution after allowing for one half-life of radial beam diffusion. The longitudinal distribution

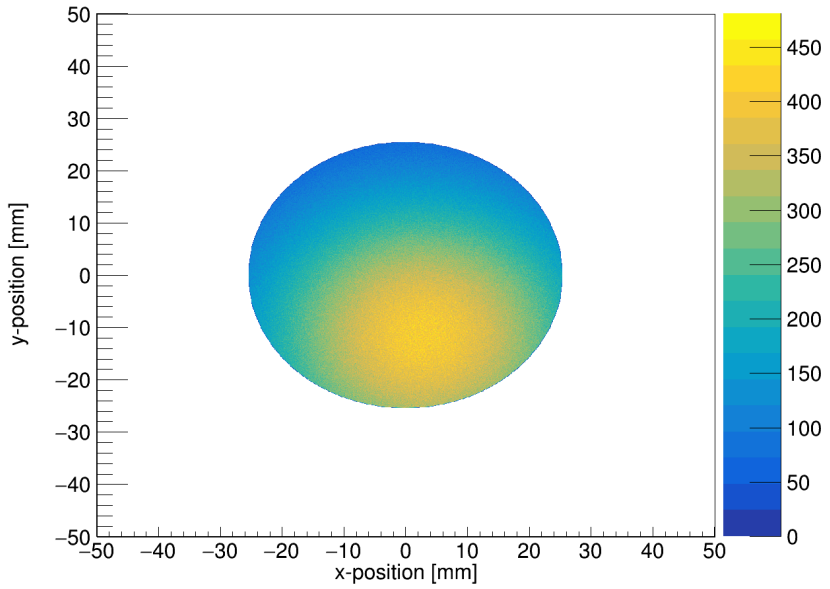

Figure 4.12: Beam spot used to represent the transverse distribution of ^{31}Cl β-delayed proton decays in the Monte Carlo efficiency simulations.

in the efficiency simulation was specified in terms of the observed drifted times, plotted in Figure 3.13, for Proton Detector events observed in the 8-μs window following the detection of a γ ray in SeGA. However, this model did not take into account the effect of electron diffusion in the P10 fill gas.

The GADGET system has recently been upgraded to operate as a time projection chamber (TPC), resulting in a need for improved spacial granularity. The number of detection channels has been increased from 13 to 1024, contained within basically the same pad plane area. This means that each detector pad is now much smaller, and the effect of ionization electrons spreading out radially in time as they drift toward the anode is readily apparent. Upon further investigation, this effect was actually found to be much larger than originally anticipated, which motivated us to incorporate this electron diffusion into our efficiency calculations. In the interest of time, we developed a simple, geometrical model of the efficiency first to estimate the size of this effect. When neglecting electron diffusion, this Monte Carlo method with simplified physics was able to reproduce the proton detection efficiency from the GEANT4's much more detailed simulation of physical interactions to within 3% for proton energies up to 1.4 MeV, as shown in Figure **??**.

Ultimately, we decided to use this simplified geometric model to calculate our final proton detection efficiencies after adding in the diffusion of ionization electrons.

The simplified, geometric Monte Carlo model assumes the same transverse and longitudinal beam distributions as described for the GEANT4 simulations. The x- and y-position coordinates at which a ^{31}Cl beam particle undergoes β-delayed proton decay are randomly sampled from the beam spot histogram. The z-coordinate of the decay is generated by converting a randomly selected drift time to its analogous spatial location, since the average z-component of the ionization electrons' drift velocity is constant under a uniform electric field. A total of 10^4 proton decay events were simulated for every proton energy corresponding to a decay peak in our spectrum, resulting in a 1% statistical uncertainty. The proton stopping power dE/dr was calculated for a range of energies using SRIM for a 808-Torr gaseous medium of 90% Ar and 10% CH_4.

In the simulation, components of the emitted proton's direction are generated isotropically in all three spatial dimensions. The deposition of proton energy in the fill gas is iteratively calculated as

$$\Delta E = \frac{dE}{dr}\Delta r \tag{4.6}$$

for step sizes of $\Delta r = 0.01$ mm over the entire length of the track. Because the recoiling ^{30}P nuclei have such short ranges in the gas, we only consider the energy carried away by the proton in the laboratory frame, just like in the GEANT4 simulations. At each 0.01-mm step along the proton track, we generate a cloud of ionization by randomly sampling the x- and y-positions of electrons from a two-dimensional Gaussian distribution, whose width is proportional to the drift time of the decay event

$$\sigma(t) = \sqrt{2nD_e t}, \tag{4.7}$$

where $n = 2$ dimensions, since only diffusion in the transverse plane affects detection efficiency [127]. The electron diffusion coefficient $D_e = 9116(273)$ cm^2/s was calculated using MAGBOLTZ [145], and the primary component of the uncertainty in D_e comes from the gas pressure, while the

uncertainty from the drift field is negligible. The number of electrons simulated on each iterative step is proportional to the energy loss of the proton in the gaseous volume

$$N_e \approx \Delta E/W, \tag{4.8}$$

where $W = 26$ eV/ion pair is the energy required to form a single electron-ion pair in P10 gas [126; 146]. If the number of electrons sampled from outside the active region of the detector, that is for which $\sqrt{x^2 + y^2} > 4$ cm, exceeds some trigger threshold, the corresponding proton decay event is vetoed. The veto threshold is set in software to be the same for all pads in units of ADC channels. However, the five active pads all have slightly different gains, corresponding to an energy threshold range of $5 - 20$ keV. The number of electrons was calculated using Equation 4.8 for 5-, 10-, and 20-keV thresholds, and simulations were performed at each trigger sensitivity level in order to quantify the systematic uncertainty associated with the veto condition. The electron veto trigger threshold accounts for a $3-4\%$ uncertainty on both the upper and lower limits of the relative detection efficiency $\epsilon_{1026}/\epsilon_{260}$.

The other sources of systematic uncertainty associated with modeling the ratio of detection efficiencies are related to the initial spatial distribution of the beam particles when they decay as well as the ranges of the protons in the gas. The latter is a small effect, for which SRIM documentation quotes a 4% uncertainty in the stopping powers for protons in gas [139]; this translates to a 1% uncertainty in the lower limit of $\epsilon_{1026}/\epsilon_{260}$ and a 2% effect on the upper limit. The former uncertainty related to the distribution of ^{31}Cl in the gaseous volume is a bit more complicated. Using the χ^2-minimization procedure to determine the x- and y-components of the beam spot's centroid as well as the width of the distribution, we estimate that these parameters can be realized to within ±6 mm. Varying each of these parameters by 6 mm in simulation produces a 2% uncertainty on the lower limit and a 5% uncertainty on the upper limit of the relative detection efficiency.

Because the beam enters the Proton Detector through a thin window with a 25.4-mm radius, the initial efficiency model assumed a hard cutoff at this boundary, meaning no ^{31}Cl decays were simulated further than 25.4 mm away from the origin of the pad plane. However, it is possible for

beam particles to diffuse under Brownian motion before undergoing β-delayed proton decay. The amount of outward radial diffusion from the entrance aperture was calculated using Equation 4.7 for zero, one, and two ^{31}Cl half-lives to evaluate the upper limit, central value, and lower limit of $\epsilon_{1026}/\epsilon_{260}$, respectively. The diffusion constant for ^{31}Cl in Ar gas was calculated using the equation

$$D_a = \frac{AT^{3/2}}{p\sigma_{12}\Omega}\sqrt{\frac{1}{M_1}+\frac{1}{M_2}}, \tag{4.9}$$

where M_1 and M_2 are the molar masses (g/mol) of the ^{31}Cl and Ar, p is the pressure (atm) inside the chamber, T is room temperature (K), and A is just an empirical coefficient [147]. Values for the dimensionless, temperature-dependent collision integral Ω are tabulated in Ref. [148] but are usually on the order of unity, which we adopt. The average collision diameter (Å) is simply $\sigma_{12} = (\sigma_1 + \sigma_2)/2$, where σ_1 and σ_2 are twice the Van der Waals atomic radii for Cl and Ar, adopted from Ref. [149]. The calculated value of D_a for ^{31}Cl in Ar gas agrees well with the empirical self-diffusion coefficient for Ar as reported in Ref. [148]. Ultimately, like the uncertainty associated with parameterizing the transverse beam distribution, the systematic error from beam particle diffusion from the aperture is 2% for the lower limit of $\epsilon_{1026}/\epsilon_{260}$ and 5% for the upper limit. After performing numerous Monte Carlo simulations over a variety of input parameters and having tested all the systematic effects in our efficiency model, we determined that the ratio of proton detection in efficiencies in our experiment was $\epsilon_{1026}/\epsilon_{260} = 0.73^{+0.09}_{-0.05}$.

Since originally reporting this number in literature [150], we have updated the efficiency simulation to include the wall effect and improved the sampling procedure. The latest version yields consistent, albeit slightly different numerical results. The preliminary numbers reported in Chapter 5 for all ^{31}Cl β-delayed proton intensities reflect these changes. The Monte Carlo results of the simplified, geometric model and the GEANT4 simulations are compared in Figure 4.13.

Final Result

Substituting the results from relative detection efficiency simulations into Equation 4.5 along with the adopted literature intensity of the 1-MeV normalization peak and the observed counts in both

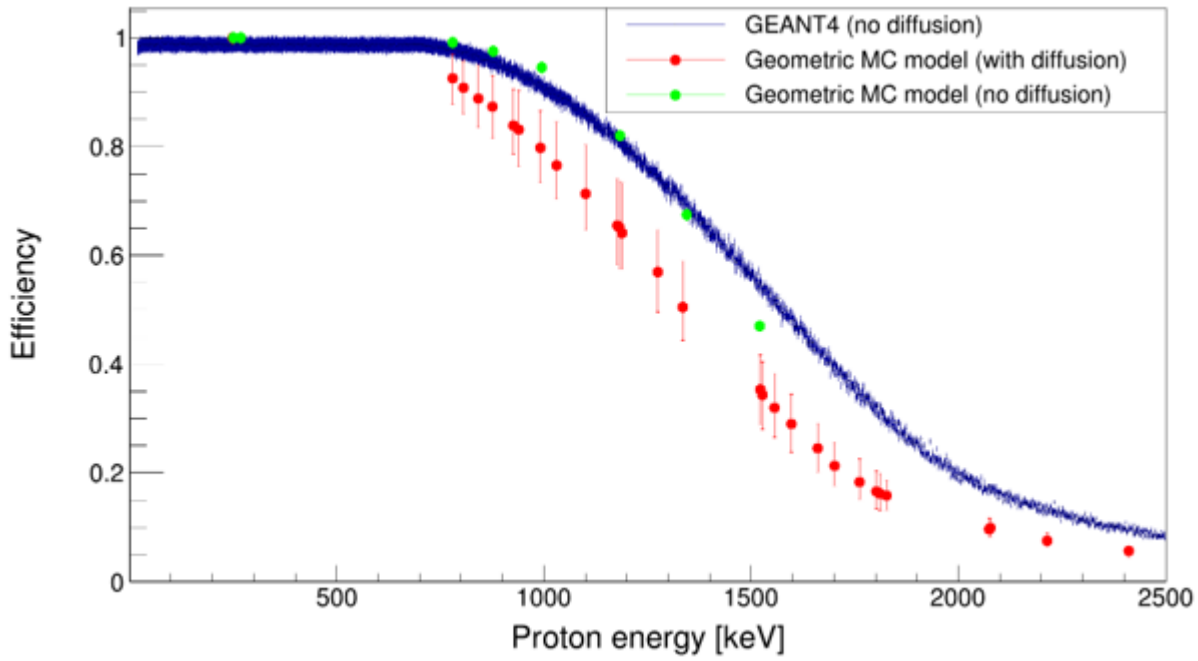

Figure 4.13: Efficiency to detect protons with GADGET as calculated by GEANT4 simulations assuming no electron diffusion (blue), the simplified, geometric model without electron diffusion (green), and the simplified, geometric model including the electron diffusion effect (red).

spectral peaks, we determined that the β-delayed proton decay intensity through the low-energy resonance of interest was $I_p^{260} = 8.3^{+1.2}_{-0.9} \times 10^{-6}$. After perusing the most recent literature evaluation of β-delayed charged-particle decays [119], we determined that our result represents the weakest β-delayed proton decay ever measured for resonances below 400 keV. Using Equation 4.23, we have calculated the desired proton branching ratio to be $\Gamma_p/\Gamma = 2.5^{+0.4}_{-0.3} \times 10^{-4}$.

4.2 Calculating the Total Thermonuclear Rate

Having determined the crucial proton branching ratio, the only remaining piece of information needed to evaluate Equation 4.21 for the 260-keV, $J^\pi = 3/2^+$ resonance is the γ partial width Γ_γ. Since $I_p \ll I_\gamma$ for the ^{31}S excited state at 6390 keV, we can make the approximation $\Gamma_\gamma/\Gamma \approx 1 \implies \Gamma_\gamma \approx \Gamma$. Because the total width of the nuclear level is inversely proportional to its lifetime $\Gamma = \hbar/\tau$, there have been several attempts to measure the lifetime τ of this short-lived state, but so far, a finite value has eluded experimental determination. Thus, we must rely on theory to calculate this value in collaboration with Prof. Alex Brown at Michigan State University. Discussion of the nuclear

shell model in this section also borrows heavily from his lecture notes [1].

In addition, the 6390-keV level discussed extensively in this dissertation is not the only resonance state that contributes to the $^{30}\mathrm{P}(p,\gamma)^{31}\mathrm{S}$ reaction, although it is expected to dominate the total thermonuclear rate. Here, we will also evaluate past work on other resonances in literature, calculate a new recommended rate, and compare the resonant reaction formalism to Hauser-Feshbach statstical model calculations.

The Nuclear Shell Model

The nuclear shell model was first developed by Eugene Paul Wigner, Maria Goeppert Mayer, and Johannes Hans Daniel Jensen, for which they earned the 1963 Nobel Prize. As fermions, protons and neutrons follow the Pauli principle and fill their respective orbitals independently. The shell model assumes that a given nucleon moves in an effective attractive potential created by the presence of all other nucleons in the nucleus. Although realistically, due to the short-range nature of this interaction, the potential can be approximated by the mean field produced by only the nearest neighboring nucleons. Protons and neutrons are almost identical in term of their nuclear interactions, but the net positive charge of the proton means introduces an electrostatic interaction as well, as illustrated in Figure 4.14.

Woods-Saxon Potential

While the negatively-charged electrons in an atom are bound to the positively-charged nucleus exclusively by an attractive, long-range Coulomb potential $V_c(r)$, the *Woods-Saxon potential* describes the interaction for a single nucleon with the mean field produced by the nucleus and can be written as

$$V(r) = V_{ws}(r) + V_{so}(r)\vec{\ell}\cdot\vec{s} + V_c(r), \tag{4.10}$$

where $V_{ws}(r) = V_{ws}f_{ws}(r)$ is the spin-independent, central Woods-Saxon potential. The average proton-neutron potential is stronger than the average proton-proton or neutron-neutron potential.

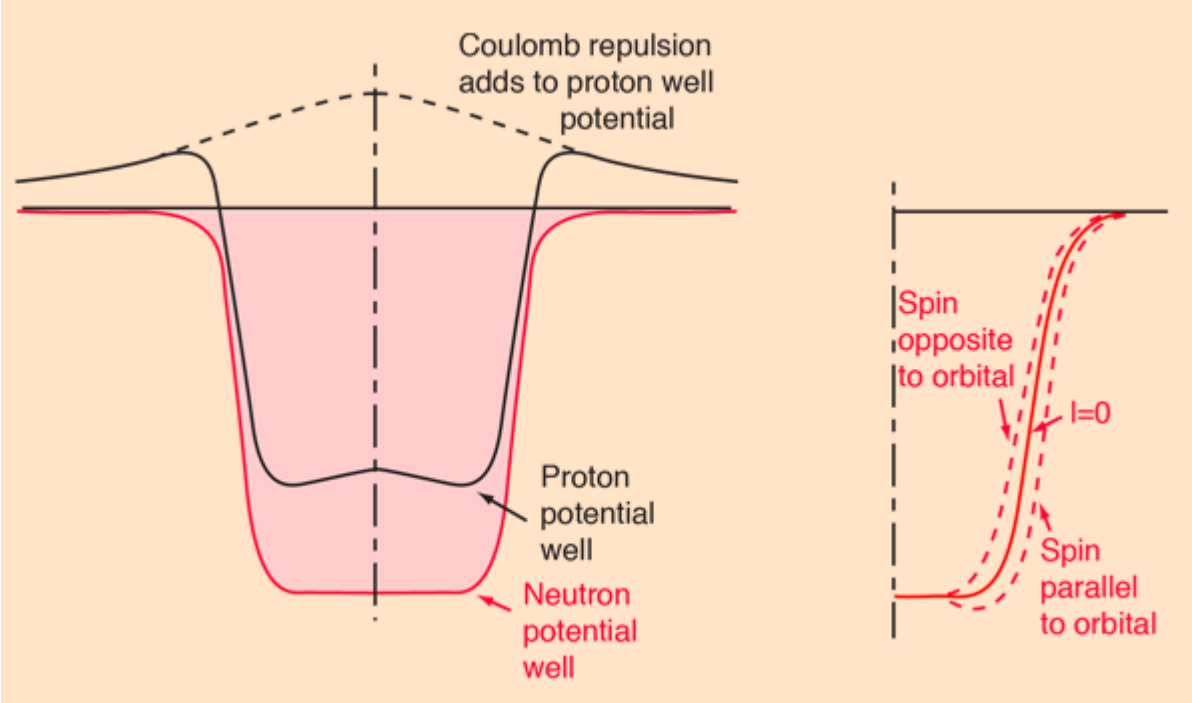

Figure 4.14: Effective interaction potentials seen by the proton and neutron as a function of the distance between the nucleon and the nucleus. The effect of alignment between spin and orbital angular momentum on the potential is also shown. Figure credit: HyperPhysics, Georgia State University, Carl Rod Nave.

Thus, for protons

$$V_p = V_{ws} + \frac{(N-Z)}{A} V_1, \tag{4.11}$$

and for neutrons

$$V_n = V_{ws} - \frac{(N-Z)}{A} V_1. \tag{4.12}$$

The spin-orbit component of the potential V_{so} describes the coupling between the spin of the nucleon and its orbital angular momentum:

$$V_{so}(r) = V_{so} \frac{1}{r} \frac{df_{so}(r)}{dr}. \tag{4.13}$$

In both cases, the Fermi component of these functions have the form

$$f_i(r) = \frac{1}{1 + e^{(r-R_i/a_i)}}, \tag{4.14}$$

while the Coulomb term in the Woods-Saxon potential describes the electrostatic interaction over two different ranges with the boundary conditions

$$V_c(r) = \begin{cases} \frac{Ze^2}{r}, & r \geq R_c \\ \frac{Ze^2}{2R_c}\left(3 - \frac{r^2}{R_c^2}\right), & r \leq R_c \end{cases}.$$

The radii R_{ws}, R_{so}, and R_c are often expressed in terms of the mass number $R_i = r_i A^{1/3}$. One can usually assume $r_{ws} = r_{so} = 1.25$ fm and similarly for the "surface thickness" of the nucleus $a_{ws} = a_{so} = 0.65$ fm. However, the Coulomb radius $r_c = 1.20$ fm is a bit smaller. The interaction strengths V_0, V_1, and V_{so} determine the depth of the potential well, and as with all the other numerical constants, they can vary depending on the region of the nuclear chart.

Nuclear Orbitals and Shell Structure

Solving the Schrödinger equation for the Woods-Saxon potential with the addition of spin-orbit coupling results in a set of quantized energy levels as depicted in Figure 4.15, which compares this more realistic model to the relatively simple solution for the isotropic harmonic oscillator potential $V(r) = \mu\omega^2 r^2/2$. These nuclear orbitals are denoted by the combination of quantum numbers $n\ell_j$ that define a state. The principle quantum number n specifies the number of nodes in the wave function, ℓ is the orbital angular momentum, and j is the total angular momentum. Thus, the $1s$ orbital, for example, has $\ell = 0$ and can only contain two nucleons of the same type. Since the total angular momentum is $j = 1/2$, within a pair of identical fermions, if one is spin-up ($j_z = +1/2$), the other must be spin-down ($j_z = -1/2$). Furthermore, the $1p$ orbital, with its $\ell = 1$, can hold up to six identical particles: two in the $1p_{1/2}$ state ($j = 1/2; j_z = \pm 1/2$) and four in the $1p_{3/2}$ state ($j = 3/2; j_z = \pm 3/2, \pm 1/2$).

Unlike in atomic theory, nuclear shells do not strictly correspond to the specific quantum numbers of their orbitals. Instead, shells represent clusters of nuclear orbitals which are separated

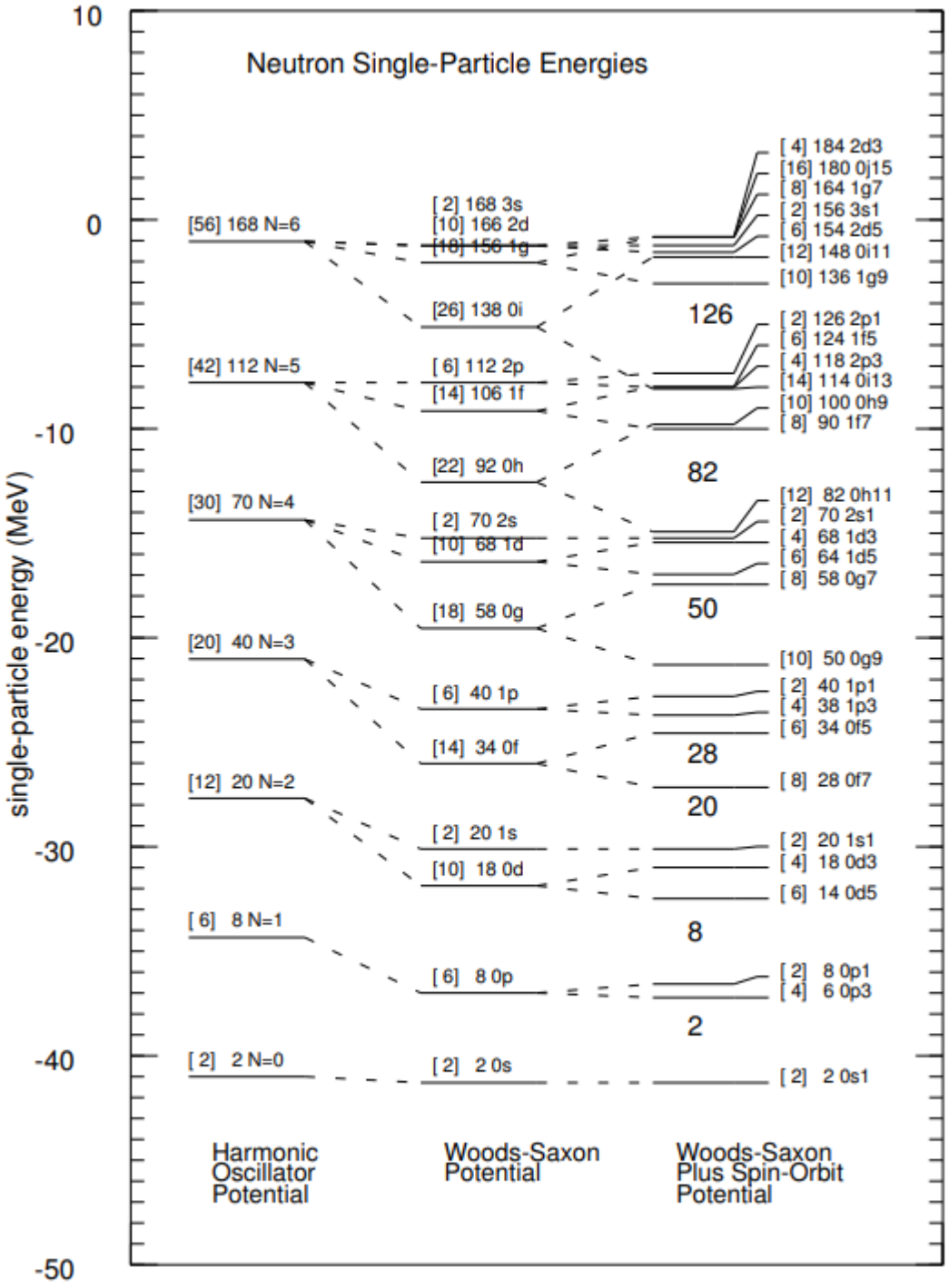

Figure 4.15: Neutron single-particles states in ^{208}Pb using three different potentials. The addition of each term further breaks the level degeneracy. Bracketed numbers indicate the number of neutrons contained in each orbital, while the following number is the running sum total. Figure credit: Ref. [1].

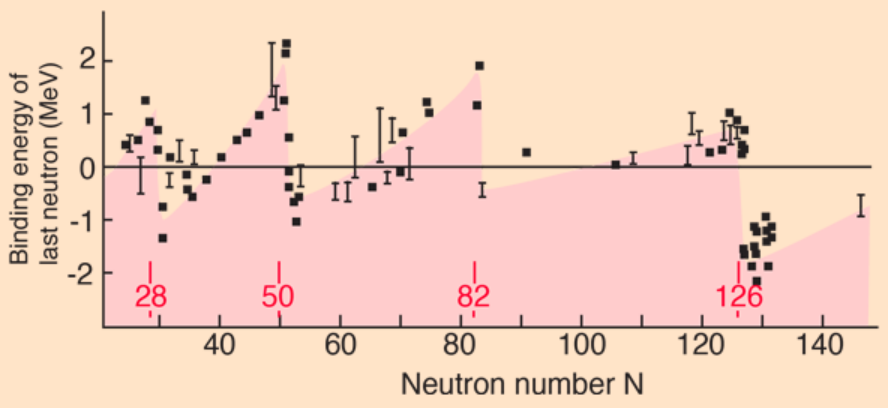

Figure 4.16: Deviation in neutron separation energy plotted as a function of neutron number, where the line at zero represents expected binding energy according to the semi-empirical mass formula. Figure credit: HyperPhysics, Georgia State University, Carl Rod Nave.

by large gaps in energy as shown in Figure 4.15. While the s-shell is just the $1s_{1/2}$ orbital and the p-shell only contains the $1p_{3/2}$ and $1p_{1/2}$ orbitals, the sd-shell is comprised of the $1d_{5/2}$, $2s_{1/2}$, and $1d_{3/2}$ orbitals; the clustering of orbitals with different quantum numbers only becomes more complicated as the number of nucleons increases. The magic numbers correspond to the total number of nucleons needed to fill the nuclear shells. As depicted in Figure 4.16, the fact that the energy required to remove a neutron from the nucleus peaks at shell closures then drops off dramatically with the addition of extra neutron, provides strong experimental evidence for shell model theory.

In addition to this, the shell model can predict the spin and parity of the ground state for a given nucleus. For example, in the case of ^{30}P, both its 15 protons and its 15 neutrons fill their respective $1s$, $1p$, and $1d$ orbitals. This leaves the remaining proton and neutron in their $2s$ orbitals. Thus, we can think of the ^{30}P nucleus as an *inert core* consisting of 14 protons and 14 neutrons with two extra *valence nucleons*, each with spin $j = 1/2$. The inert core has a total angular momentum of $j = 0$ since it fills the $1d_{5/2}$ orbital, and the sum total angular momentum of the valence nucleons is $j = 1$. Because the $2s$ orbital is an $\ell = 0$ level and since $\Pi = (-1)^{\ell}$, this means the parity of the ^{30}P ground state is positive, which agrees with the observation that $J^{\pi} = 1^{+}$.

While the shell model allows us to infer ground state spin-parity from the properties of individual

valence nucleons, this is not trivial for excited states. However, the existence of *mirror nuclei* allows us to deduce information about the level structure of a nucleus with mass number A, proton number Z_1, and neutron number N_1 from a different nuclide with mass number A but for which the proton number is $Z_2 = N_1$ and the neutron number is $N_2 = Z_1$. Due to their symmetry, the excited states in one mirror nucleus can often be matched to an analogous state in the other mirror nucleus, and assuming we know the properties of one mirror state, we can assign spin and parity to the other mirror state. This reflects a useful property of the nucleus called *isospin*.

Isospin Mixing

The isospin model proposes that because the proton and neutron are nearly identical, instead of treating them as distinct nucleons, they can be understood as projections in isospin space of a single nucleonic particle. This *isospin doublet* still has spin $j = 1/2$, but in addition, it also possesses isospin $T = 1/2$, the projections of which correspond to $T_z = +1/2$ for the neutron and $T_z = -1/2$ for the proton. The total isospin projection of a particular nuclide can be expressed as $T_z = (N - Z)/2$, which is the same across all excited states of that nucleus. However, each nuclear level will not have the same total isospin T. The isospin model is formulated similarly to angular momentum in the sense that for a given total isospin T there will be $2T + 1$ projections spanning $-T < T_z < T$. Thus, the analogous levels in mirror nuclei can be thought of as nearly identical states with the same spin-parity and quantum number T but with different projections in isospin space; these are called *isobaric analog states* (IAS).

Of course, protons and neutrons are not identical particles, and the difference in the strength of the Coulomb interaction between mirror nuclei perturbs the energy level spacing between the nuclides. In addition to this, Coulombic perturbations can result in *isospin mixing* between nearby states of the same spin and parity. In the simple case of two-level mixing, the quantum states $|\psi_1\rangle$ and $|\psi_2\rangle$ can be written as a linear combination of isospin basis states:

$$|\psi_1\rangle = \cos\theta\,|T_1\rangle + \sin\theta\,|T_2\rangle \tag{4.15}$$

$$|\psi_2\rangle = -\sin\theta\,|T_1\rangle + \cos\theta\,|T_2\rangle \tag{4.16}$$

If the energy difference between two levels is large, the amount of mixing between then will be negligible. The *mixing angle* θ is given by the relation

$$\tan 2\theta = \frac{2V}{D}, \tag{4.17}$$

where V is the mixing matrix element and D is the unperturbed energy difference between the original states. The relationship between these two quantities and the observed (perturbed) level spacing is given by $E = \sqrt{D^2 + 4V^2}$.

Using β decay measurements, the extent of this mixing can sometimes be determined from experimental observables. If the β decay proceeds via a *Fermi transition*, the emitted e^--$\bar{\nu}_e$ or e^+-ν_e pair will have antiparallel spins, such that the total angular momentum of the nucleus is unchanged ($\Delta j = 0$), and similarly, parity is also conserved ($\Delta\pi = 0$). Typically, Fermi decays of a radioactive parent nucleus will only populate its IAS in the daughter nucleus, but if isospin mixing occurs between its IAS and another state, the Fermi *transition strength* $B(F)$ to the nearby level will be nonzero. The transition strengths of two states (B_1 and B_2) can be deduced from the β-feeding intensities, and their ratio is related to the mixing angle:

$$R = \tan\theta = \sqrt{\frac{B_2}{B_1}}. \tag{4.18}$$

This allows us to write the unperturbed energy spacing as

$$D = E\frac{1 - R^2}{1 + R^2}, \tag{4.19}$$

and the unperturbed mixing matrix element becomes

$$V = E\frac{R}{1 + R^2}. \tag{4.20}$$

USDC Model Calculations

In Mayer and Jensen's original formulation, they assumed each nuclear level corresponded to a single valence nucleon in a single-particle orbit around an inert core at shell closure. We now know that the nucleus is much more complicated than this and that the collective behavior of quantum many-body interactions is necessary to accurately described the properties of nuclear excitations. Modern shell-model calculations must incorporate many multinucleon configurations as a consequence of the fact that valence nucleons can occupy multiple, partially filled, single-particle states simultaneously [151]. This requires extensive numerical computation in order to predict experimental observables, and even still, the valence space must often be truncated simply due to the sheer number of possible configuration-interactions. Nevertheless, the shell model remains an extremely useful tool for predicting excitation energies, spin-parity assignment, multipole moments, and matrix elements between nuclear levels.

In order to perform these calculations, a Hamiltonian is needed to describe the configuration-interactions within the valence space. Nearly 40 years ago, the "universal *sd*-shell" (USD) Hamiltonian was proposed to account for the wide variety of observed phenomena in the level structure of nuclides with mass numbers $A = 17 - 39$ and has since provided realistic *sd*-shell wave functions for this region of the nuclear chart [152]. In 2006, its successors USDA and USDB were introduced using an updated and expanded set of nuclear levels [153; 154]. Recently, several new isospin-breaking, USD-type Hamiltonians have been developed, including USDC [155], which we used to evaluate the γ decay width Γ_γ for the 6390-keV level in ^{31}S.

For the USDC Hamiltonian, the strongest isospin mixing with the IAS for the ^{31}Cl ground state comes from a $T = 1/2$ level in ^{31}S, which the shell model predicts to be 300 keV below the $T = 3/2$ IAS. The isospin-mixing matrix element for these levels $V_{\text{theory}} = 36$ keV is in good agreement with the experimental value $V_{\text{exp}} = 41(1)$ keV [155]. Theory predicts γ-decay widths of 190 meV for the $T = 1/2$ state and 920 meV for the $T = 3/2$ state. However, the observed $T = 1/2$ state, corresponding to the 6390-keV level in ^{31}S, lies above the $T = 3/2$ IAS at 6279 keV. The mixing of these two states depends on the energy difference between them, which is determined by the strong

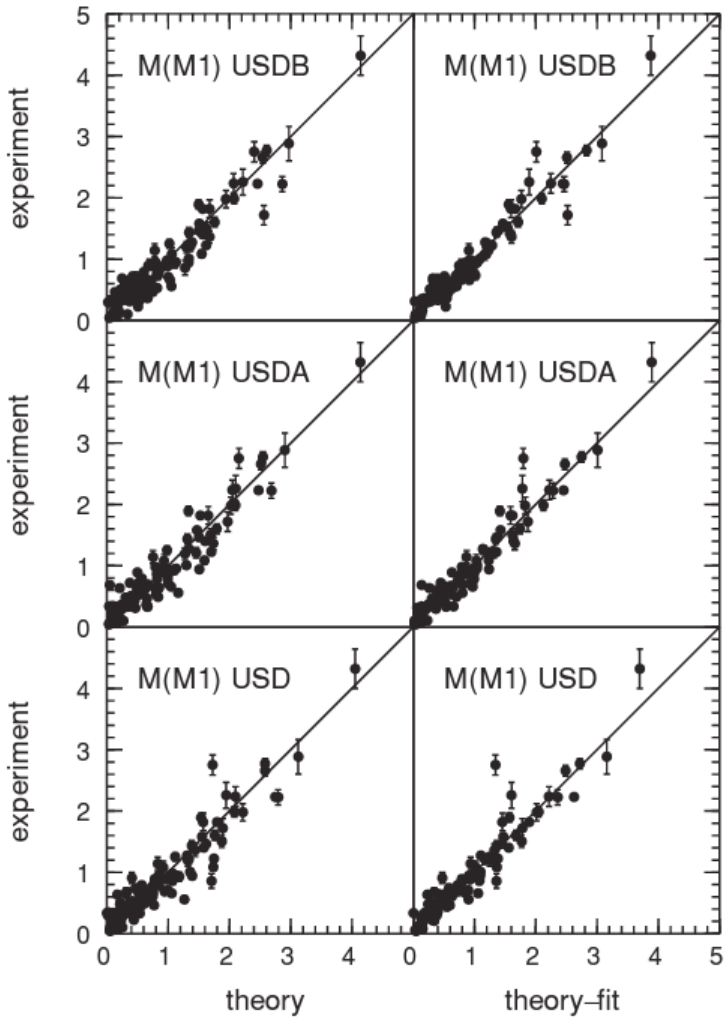

Figure 4.17: A comparison of experimental and theoretical values of the M1 matrix elements for magnetic dipole transitions. Figure credit: Ref. [154].

interaction. Adding a term in the Hamiltonian, which is proportional to the $\hat{T}^2$ operator, moves the $T = 1/2$ state up by 410 keV. After this shift, the new partial widths are $\Gamma_\gamma^{6390} = 490$ meV and $\Gamma_\gamma^{\mathrm{IAS}} = 430$ meV. The sum of these two widths is not exactly the same due to interference from other $T = 1/2$ states that do not demonstrate strong isospin mixing.

There are two primary sources of systematic uncertainty associated with calculating Γ_γ theoretically. The first comes from the choice of the USD Hamiltonian. By comparing results from the four different Hamiltonians derived in Ref. [155], we assume this uncertainty in Γ_γ between the models is relatively small, at about 50 meV. The second source of error in this calculation arises

from the uncertainty in the matrix element of the magnetic dipole (M1) transition. γ decay of the $T = 1/2$ state is dominated by a 66% branch to the lowest $J^\pi = 5/2^+$ state with an M1 transition strength of $B(M1) = 0.48\mu_N^2$, where $\mu_N = e\hbar/2m_p$ is the *nuclear magneton*. The M1 decay matrix element is $M = \sqrt{(2J_i + 1)B(\mathrm{M1})} = 1.38\mu_N$. Comparing to other experimental values of M, as shown in Figure 4.17 taken from Ref. [154], we adopt a systematic uncertainty of $\approx 0.4\mu_N$. This ultimately leads to a total uncertainty of 280 meV. Thus, we can combine Prof. Alex Brown's shell-model calculations for $\Gamma_\gamma = 490(280)$ meV and our experimentally determined proton branching ratio $\Gamma_p/\Gamma = 2.5^{+0.4}_{-0.3} \times 10^{-4}$ with the known angular momentum information $J_r = 3/2$, $J_p = 1/2$, and $J_t = 1$ for the resonance, proton, and target nucleus, respectively. Using our definition of the resonance strength

$$\omega\gamma \equiv \frac{(2J_r + 1)}{(2J_p + 1)(2J_t + 1)} \frac{\Gamma_p \Gamma_\gamma}{\Gamma}, \tag{4.21}$$

we computed a final value of $\omega\gamma = 80(48)$ μeV for the crucial 260-keV resonance of interest.

Resonant Contributions

The most important resonances that contribute to the total thermonuclear rate typically fall within $\pm\Delta/2$ of the Gamow peak as calculated using Eqs. 2.11 and 2.14. For a peak nova temperature of $T = 0.31$ GK, this corresponds to resonance energies $E_0 \pm \Delta/2 = 337 \pm 110$ keV for the $^{30}\mathrm{P}(p,\gamma)^{31}\mathrm{S}$ reaction. There have been many experiments dedicated to the study of proton-unbound states in ^{31}S over this resonance energy range. We believe most of the key resonances within the Gamow window have been experimentally observed, but the nuclear dataset remains incomplete for many of these states. For example, the spin-parity assignments for several high-spin states remain tentative, and certain measurements of spectroscopic factors provide only upper limits. Here, we review the resonance strengths reported in literature as summarized nicely by Kankainen *et al.* [104]. Finally, we are able to calculate a total thermonuclear rate for $^{30}\mathrm{P}(p,\gamma)^{31}\mathrm{S}$ using the individual contributions of nine narrow, isolated resonances based on the available experimental information complemented by theoretical evaluations.

Calculating Proton Partial Widths

For states with known spin-parity and well-constrained spectroscopic factors, it is possible to calculate proton partial widths with reasonable accuracy. The analytical approximation can be expressed as

$$\Gamma_p = 2\frac{\hbar^2}{\mu a_c^2} P_c (C^2S)\theta_{\rm sp}^2, \tag{4.22}$$

where P_c is the penetration factor, C^2S is the spectroscopic factor, and $\theta_{\rm sp}^2$ is the dimensionless single-particle reduced width [15]. The interaction radius is $a_c = 1.25(A_p^{1/3} + A_t^{1/3})$ fm and depends on the mass of the proton A_p and target nucleus A_t in atomic mass units. The penetration factor is the probability that a single proton will penetrate the Coulomb and centrifugal barriers and is given by

$$P = \frac{k_c a_c}{F_c^2 + G_c^2}, \tag{4.23}$$

where $k_c = \sqrt{2\mu E_r}/\hbar$ is the wave number, while F_c and G_c represent the regular and irregular Coulomb wave functions, respectively, evaluated at the interaction boundary [156]. To compute these wave functions, we use the GNU Scientific Library's numerical calculation.

The dimensionless quantity for the single-particle reduced width is related to the probability that the single nucleon, the proton in our case, will appear at the boundary. We calculate this value using the summation

$$\theta_{\rm sp}^2 = \sum_{i,j}^{2} c_{i,j} A_i E_j, \tag{4.24}$$

where here, $c_{i,j}$ are parameters given by Illiadis in Ref. [156], who arrives at these values by fitting angular distribution data as a function of bombardment energy for protons scattered on various target nuclei. More formal values calculated from an R-matrix formula are reported by Ref. [157], but these results agree with Illiadis's values, as well as with shell-model calculations, to within

about 10% on average. Thus, we assign a 10% systematic uncertainty to the single-particle reduced width $\Gamma_{sp} = \Gamma_p / C^2S$.

Lastly, the *spectroscopic factor* C^2S represents the probability that the nucleons involved in the reaction will arrange themselves in a configuration that corresponds to the final compound state. This value can often be measured via single-nucleon transfer reaction experiments, but many times we must rely on shell-model calculations of C^2S, which have their own associated uncertainties.

The 6159-keV Level

Ref. [104] reports a spectroscopic factor $C^2S = 0.036(13)$ for this $J = 7/2^{(-)}$ state. Because this resonance has such an extremely low resonance energy ($E_r = 28$ keV) and a relatively high angular momentum transfer, it does not contribute substantially to the overall rate at peak nova temperatures. However, for completeness, we calculated this state's proton partial width to determine its resonance strength and found that it could be potentially dominant at low temperatures ($T < 0.02$ GK). Any resonances below this excitation energy are excluded from the calculation because their contributions are assumed to be negligible.

The 6255-keV Level

This ^{31}S excited is known to be an $\ell = 0$ resonance state with spin-parity $J^\pi = 1/2^+$ and a resonance energy of 124 keV. Ref. [104] reports an upper limit on the spectroscopic factor for this resonance $C^2S \leq 0.19$ and references Brown *et al.*, whose shell-model calculations predict a value of 1.7×10^{-3} [158]. While this resonance lies just below the Gamow window at $T = 0.4$ GK, this relatively weak resonance could contribute to the total rate at lower temperatures ($T < 0.15$ GK). For this reason, we include it in our total thermonuclear rate calculation, adopting Brown's theoretical resonance strength $\omega\gamma = 9.5 \times 10^{-12}$, with a factor of two uncertainty.

The 6279-keV Level

The nuclear level at 6279 keV in ^{31}S was first definitively identified as the IAS of the ground state in ^{31}Cl in Ref. [117]. Thus, it is strongly populated by ^{31}Cl β^+ decay, but because this state has isospin $T = 3/2$, it should not contribute to the total $^{30}\mathrm{P}(p,\gamma)^{31}\mathrm{S}$ reaction rate due to isospin conservation. However, Ref. [121] provides evidence of isospin mixing between the IAS and the 6390-keV level. Theory predicts the energies of these states should be higher than observed, but by shifting down the excitation energies such that the difference between the levels agrees with experiment, we can use the USDC Hamiltonian to calculate the spectroscopic factor $C^2S = 0.0036^{+0.0036}_{-0.0018}$ for the 6279-keV state. Using Equation 4.22, we can compute the proton partial width Γ_p and thus constrain the resonance strength.

The 6327-keV Level

In the case of this excited state, calculating the resonance strength is straightforward. The spin-parity is known to be $J^\pi = 3/2^-$ [111]. Ref. [104] reports a spectroscopic factor of $C^2S = 0.023(12)$. Thus, we can simply calculate this resonance's contribution to the total thermonuclear rate using our analytical approximation for the proton decay partial width.

The 6357-keV Level

The γ-ray angular distribution data suggests this state has spin $J = 5/2$ [111]. The fact that this state is not populated in β decay indicates negative parity [121], so we adopt $J^\pi = 5/2^{(-)}$. Ref. [104] only reports an upper limit on the level's spectroscopic factor and thus on its resonance strength. For this reason, we exclude it from our total thermonuclear rate calculation.

The 6377-keV Level

Similarly to the 6327-keV level, the spin and parity of resonance are known to be $J^\pi = 9/2^-$ [111]. Its spectroscopic factor was measured to be $C^2S = 0.051(17)$ [104]. We use this information to

calculate a resonance strength.

The 6390-keV Level

The importance of this level has been discussed at length previously and is the central topic of this dissertation. It is noteworthy that Ref. [104] only reports an upper limit on the spectroscopic factor for this state, demonstrating the unique sensitivity of our measurement. Our newly constrained resonance strength is ≈ 3 times larger than the previous theoretical evaluation provided in Ref. [121].

The 6393-keV Level

The 6393-keV level is another relatively simple case because its spectroscopic factor has been measured $C^2S = 0.007(3)$. Ref. [104] reports this as a $J^\pi = 5/2^{(+)}$ state, implying it is an $\ell = 2$ resonance. We calculate its contribution to the total rate.

The 6394-keV Level

Ref. [104] only reports an upper limit on this state's spectroscopic factor $C^2S \leq 0.002$, which is already quite small. This high-spin $J^\pi = 11/2^+$ state [111] is unlikely to contribute to the total thermonuclear rate, so we exclude it from our total rate calculation.

The 6402-keV Level

Evidence of the existence of a 6402-keV excited state from a $^{32}\mathrm{S}(d,t)^{31}\mathrm{S}$ reaction experiment was reported in Ref. [103], which tentatively assigns this state a spin of $J = (7/2)$. Beyond this, there is little experimental information on this candidate state in the literature, and it may not even exist. For this reason, we exclude it from total rate calculation.

The 6542-keV Level

The spin-parity assignment of the 6542-keV level is ambiguous, but Kankainen *et al.* adopts $J^\pi = 7/2^+$ from Ref. [107]. Deuteron angular distribution data is fit well with $\ell = 4, 5, 6$ transfers, and thus, the state is potentially consistent with $J^\pi = (7/2^+, 9/2^-, 11/2^+)$ [99]. Ref. [104] sets an upper limit on the spectroscopic factor and resonance strength. While this resonance is likely not important for ONe nova nucleonsynthesis, it could play a role at higher temperatures.

The 6583-keV Level

This resonance has a tentative spin-parity assignment $J^\pi = (5/2, 7/2)^-$ [111]. Ref. [104] reports an upper limit on the spectroscopic factor and assumes $\ell = 3$ but does not include an upper limit on the resonance strength. Because of the large angular momentum transfer and position in the Gamow window, this resonance is unlikely to contribute substantially to the total thermonuclear rate. For theses reasons, we ignore proton capture on this level.

The 6636-keV Level

Most literature for this state assigns a spin-parity of $J^\pi = 9/2^-$. This is consistent with deuteron angular distribution data from a $^{32}\mathrm{S}(p, d)^{31}\mathrm{S}$ reaction experiment, which are fit reasonably well with $J^\pi = 7/2^+, 9/2^\pm, 11/2^+$ assignments [99]. No spectroscopic information is found in literature other than the arbitrary $C^2S = 0.02$ according to Ref. [105]. Because of the large angular momentum transfer and the unknown spectroscopic factor, we choose to neglect this resonance.

The 6720-keV Level

This level is tentatively a $J = (5/2)$ state. Due to a lack of other experimental information on this level, we refer to Ref. [158] for a theoretical calculation of the resonance strength. Uncertainties associated with this resonance strength are assumed to be a factor of two. Due to its relatively high

energy, this resonance likely does not contribute substantially to the $^{30}\mathrm{P}(p,\gamma)^{31}\mathrm{S}$ rate at peak nova temperatures. However, it could play a role at higher temperatures.

The 6749-keV Level

As with the previous resonance, a spectroscopic factor has not been measured, and its high excitation energy suggests it does not play an important role in the reaction of interest at lower temperatures. Still, it is a $J^\pi = 3/2^+$ state, making the $\ell = 0$ potentially dominant at higher energies $T > 0.4$ GK. Again, we refer to Ref. [158] for a theoretical evaluation. All known states above this level fall well beyond the Gamow window for this reaction at nova temperatures and are assumed to be irrelevant.

Total Rate Summed Over All Resonances

A new thermonuclear rate for $^{30}\mathrm{P}(p,\gamma)^{31}\mathrm{S}$ was computed using Equation 2.18. The resonances' properties, including their adopted strengths for this calculation, are tabulated in 4.1. The total rate and its contributions from each individual resonance are plotted in Figure 4.18; this excludes the very weak, low-energy 28-keV resonance whose contribution to the total rate is not visible on the scale of this plot. Figure 4.18 clearly shows that the 260-keV, $J^\pi = 3/2^+$ resonance at the heart of this work dominates this reaction rate at temperatures $T > 0.15$ GK.

Hauser-Feshbach Statistical Model

In the case of most of the nuclear reactions which are relevant for understanding stellar nucleosynthesis, insufficient experimental information prevents the total thermonuclear rate from being calculated on the basis of individual resonances alone. For this reason, the Hauser-Feshbach statistical model is often employed as an approximation method, and to date, most nova model simulations have relied on it to evaluate the $^{30}\mathrm{P}(p,\gamma)^{31}\mathrm{S}$ rate. Originally developed in 1952 for calculating the total and differential cross sections of inelastic neutron scattering, the model assumes that the compound nucleus in question is sufficiently excited that the nuclear levels can be treated

E_x (keV)	E_r (keV)	J^π	C^2S	$\omega\gamma$ (eV)
6158.5(5)	27.9(6)	$7/2^{(-)}$	0.0036(13) [104]	$1.1(4) \times 10^{-33}$
6255.3(5)	124.7(6)	$1/2^+$	≤ 0.19 [104]	9.5×10^{-12} [158]
6279.0(6)	148.4(6)	$3/2^+$	$0.0036^{+0.0036}_{-0.0018}$	$2.1^{+2.1}_{-1.1} \times 10^{-9}$
6327.0(5)	196.4(6)	$3/2^-$	0.023(12) [104]	$5.1(27) \times 10^{-7}$
6357.3(2)	226.7(3)	$5/2^{(-)}$	≤ 0.011 [104]	$\leq 1.4 \times 10^{-6}$ [104]
6376.9(4)	246.3(5)	$9/2^-$	0.051(17) [104]	$6.1(21) \times 10^{-8}$
6390.2(7)	259.6(7)	$3/2^+$	0.016^{+16}_{-8}	$8.0(48) \times 10^{-5}$
6392.5(2)	261.9(3)	$5/2^{(+)}$	0.007(3) [104]	$5.8(25) \times 10^{-7}$
6394.2(2)	263.6(3)	$11/2^+$	≤ 0.002 [104]	—
6402(2)	271.4(20)	—	—	—
6541.9(4)	411.3(5)	$7/2^+$	$\leq 5.9 \times 10^{-3}$ [104]	$\leq 1.7 \times 10^{-4}$ [104]
6583.1(20)	452.5(20)	(7/2)	≤ 0.007 [104]	—
6636.1(7)	505.5(7)	$9/2^-$	—	—
6720	589	(5/2)	0.081 [158]	$0.072^{+0.072}_{0.036}$ [158]
6749	618	$3/2^+$	4.5×10^{-3} [158]	$0.2^{+0.2}_{-0.1}$ [158]

Table 4.1: All resonances near the Gamow window for ^{30}P$(p,\gamma)^{31}$S at nova temperatures. We adopt all measured values reported in Ref. [104] whenever possible. In the case of insufficient experimental information, we appeal to theoretical evaluation, excluding only resonances for which spectroscopic factors are unknown and likely do not contribute substantially to the total rate due to a large centrifugal barrier.

statistically [159]. Using input parameters such as level density and transmission coefficients, a cross section can be calculated for many resonances and averaged over the whole energy region.

While this method is usually reliable within a factor of 2 – 3 for proton capture reactions, this is only true if the density of states is high enough such that the level structure can be approximated as a continuum. The largest uncertainties associated with this statistical model arise from the nuclear level density and transmission coefficients. For many cases, especially near shell closures and the drip lines, radiative capture into narrow, isolated resonances must be considered individually. The ^{30}P$(p,\gamma)^{31}$S reaction is expected to be near the edge of applicability for the Hauser-Feshbach model

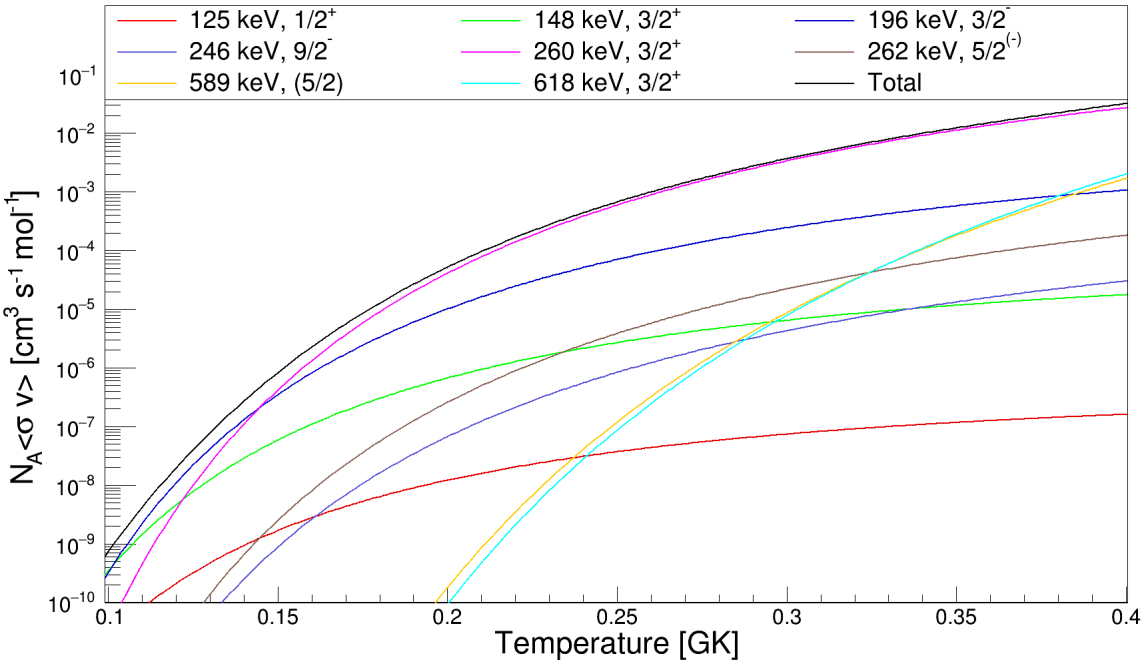

Figure 4.18: Individual resonances contributions and their sum total thermonuclear rate for the ^{30}P$(p,\gamma)^{31}$S over peak nova temperatures.

because the level density within the Gamow window at nova temperatures is relatively low.

Using the NON-SMOKER code [160], Rauscher and Thielemann report their calculations of a variety of reaction types and their inverse reactions for target nuclei with $10 \geq Z \geq 83$ performed over a grid of 24 temperatures $T = 0.1 - 10.0$ GK [161]. For easy evaluation of any astrophysical rate within a given temperature range, the results of the formal theoretical calculations were fit with the highly parameterized numerical formula

$$N_A\langle\sigma v\rangle = \exp(a_0 + a_1 T_9^{-1} + a_2 T_9^{-1/3} + a_3 T_9^{1/3} + a_4 T_9 + a_5 T_9^{5/3} + a_6 \ln T_9), \tag{4.25}$$

where the free parameters $a_0 - a_6$ are tabulated for all reactions of interest and T_9 is the temperature in GK units. Ref. [161] also tabulates partition functions for all nuclei provided, in order to account for the effect of nuclear reactions involving radiative capture to excited states on the total thermonuclear rate. In the case of ^{30}P, this effect only becomes relevant at $T > 1$ GK, well above peak nova temperatures. We used the functional form provided in Equation 4.25 to evaluate the thermonuclear rate of ^{30}P$(p,\gamma)^{31}$S across peak nova temperatures and compared our experimentally

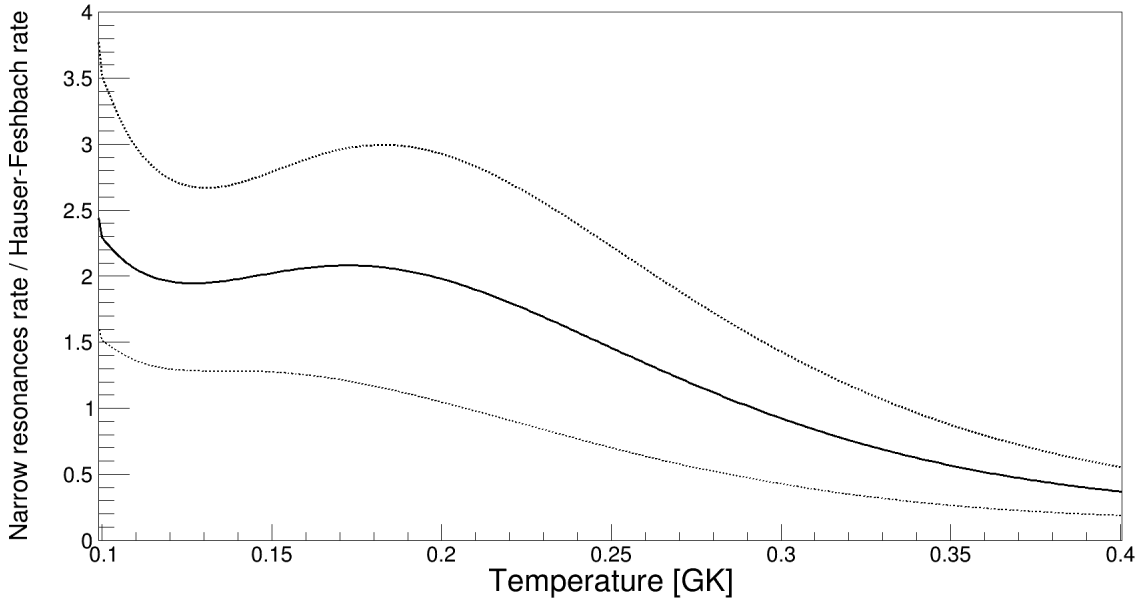

Figure 4.19: Ratio of thermonuclear rates for the ^{30}P$(p,\gamma)^{31}$S reaction comparing the narrow resonances model to the Hauser-Feshbach statistical method. The solid curve represents the recommended central value of the narrow resonance model, while its upper and lower limits are plotted as dashed curves.

constrained resonant reaction calculation to the Hauser-Feshbach statistical method. Figure 4.19 shows the ratio between two thermonuclear rate calculations, where the numerator is calculated from the resonance strengths of individual ^{31}S levels, and the denominator is the evaluated using Equation 4.25. There is relatively good agreement between the two models to within about a factor of 2 for the case of this radiative proton capture reaction at nova temperatures. However, as Figure 4.18 shows, the $J^\pi = 3/2^+$, 260-keV resonance is by far the largest contribution to the total ^{30}P$(p,\gamma)^{31}$S rate, and the Hauser-Feshbach method should not be considered a generally reliable approximation for thermonuclear reactions dominated by a single resonance.

4.3 Astrophysical Impact

Hydrodynamic Nova Simulations

In collaboration with Prof. Jordi José from the Departament de Física Universitat Politècnica de Catalunya and the Institut d'Estudis Espacials de Catalunya, simulations of classical nova explosions

were performed to investigate the effect of the newly constrained ^{30}P$(p,\gamma)^{31}$S rate on the nuclear abundances of nova ejecta. The one-dimensional, hydrodynamic code SHIVA was developed to simulate nova outbursts, starting from the onset of accretion up to the mass ejection stage [47; 162]. The parallelized computer program program solves a set of differential equations for conservation of mass, momentum, and energy, both radiative and convective transport equations, as well as the definition of Lagrangian velocity. The hydrodynamics model has been coupled to a network of 370 nuclear reactions involving 100 nuclear species from ^{1}H to ^{40}Ca. The chemical composition of the envelope and the underlying white dwarf mass are among the most impactful input parameters in the prediction of nova nucleosynthesis [52].

Modeling the chemical composition of the envelope is a complicated problem and requires further investigation. Multi-dimensional simulations have now been employed to study the mixing between the H-rich envelope with the dense outer layers of the underlying white dwarf [91; 92], but due to computational limits, the state-of-the-art, fully hydrodynamic simulations of explosive nucleosynthesis in classical novae are still one-dimensional. A much more detailed discussion of modern computational hydrodynamics for astrophysical simulations can be found in Ref. [163]. The most recent SHIVA calculations using our new recommended rate for proton capture on ^{30}P assumed an *a priori* 50-50 mixing between the H-rich envelope and ONe white dwarf material. This 50% value is based on observations of nova ejecta and is meant to mimic results of the complex mixing process that should occur near the stellar surface. It reflects the mean composition of the ejecta in ONe novae, which is characterized by a "metal" content of around $Z = 0.5$, implying the ejected material is composed of half H/He and half heavier elements.

In addition, because of the relatively high mass number ($A > 19$) for the seed nuclei necessary to activate ^{30}P$(p,\gamma)^{31}$S, the reaction is only expected to be relevant for the heaviest ONe white dwarfs. The nuclear abundances in nova ejecta were predicted for a 1.35-$M_{\odot}$ ONe white dwarf using the upper and lower limits on the constrained reaction rate in addition to the central, recommended value for the thermonuclear rate. Partial results from these simulations are shown in Table 4.2. The chemical elements for which abundances are provided here were chosen because of their relevance

to the aforementioned astrophysical motivation for this research. Namely, this includes identifying the origins of certain presolar grains based on their isotopic ratios as well as the calibration of nuclear thermometers for classical novae.

Isotopic Ratios in Candidate Nova Grains

For reference, we consider the isotopic ratios of SiC and graphite (C) grains with an inferred nova origin tabulated in Ref. [60]. Figure 4.20 plots the ratios ^{12}C:^{13}C and ^{14}N:^{15}N observed in grain data as well as the results from our simulations. The latest computational values for C and N ratios are in agreement with previous 1.35-$M_\odot$ ONe nova models for 50-75% mixing fractions. At $^{12}\mathrm{C}{:}^{13}\mathrm{C} = 2.19^{+0.20}_{-0.06}$, our calculations slightly underestimate measurements of the C isotopic ratios in all candidate nova grains. Again for N, our prediction of $^{14}\mathrm{N}{:}^{15}\mathrm{N} = 0.547^{+0.003}_{-0.029}$ is in agreement with previous evaluations of classical nova explosions under the same conditions. However, our theoretical results underpredict the observed N ratios by at least an order of magnitude in all grains hypothesized to be of nova origin.

With respect to Si isotopic ratios, as shown in Figure 4.21, we are overpredicting ^{29}Si and ^{30}Si abundances by at least an order of magnitude for all samples in this unidentified class of presolar grains. Our results overlap with previous uncertainty bands for both $\delta(^{29}\mathrm{Si}{:}^{28}\mathrm{Si})$ and $\delta(^{30}\mathrm{Si}{:}^{28}\mathrm{Si})$ predictions, which are given in units of permille (‰) deviation from Solar isotopic abundances:

$$\delta\left(\frac{^{29,30}\mathrm{Si}}{^{28}\mathrm{Si}}\right) = \left[\left(\frac{^{29,30}\mathrm{Si}}{^{28}\mathrm{Si}}\right) \div \left(\frac{^{29,30}\mathrm{Si}}{^{28}\mathrm{Si}}\right)_\odot - 1\right] \times 1000. \tag{4.26}$$

The size of our error bars due to nuclear uncertainties are significantly reduced in comparison to past predictions as a result of our experimental constraints on the $^{30}\mathrm{P}(p,\gamma)^{31}\mathrm{S}$ rate. Previous simulations yielded near-Solar isotopic ratios for ^{29}Si:^{28}Si, with either excesses or even slight deficits as likely possibilities. In our ONe nova ejecta, we strictly predict excesses of $\delta(^{29}\mathrm{Si}{:}^{28}\mathrm{Si}) = 471(8)$, which actually brings us out of agreement with observational data on ^{29}Si abundances in candidate nova grains.

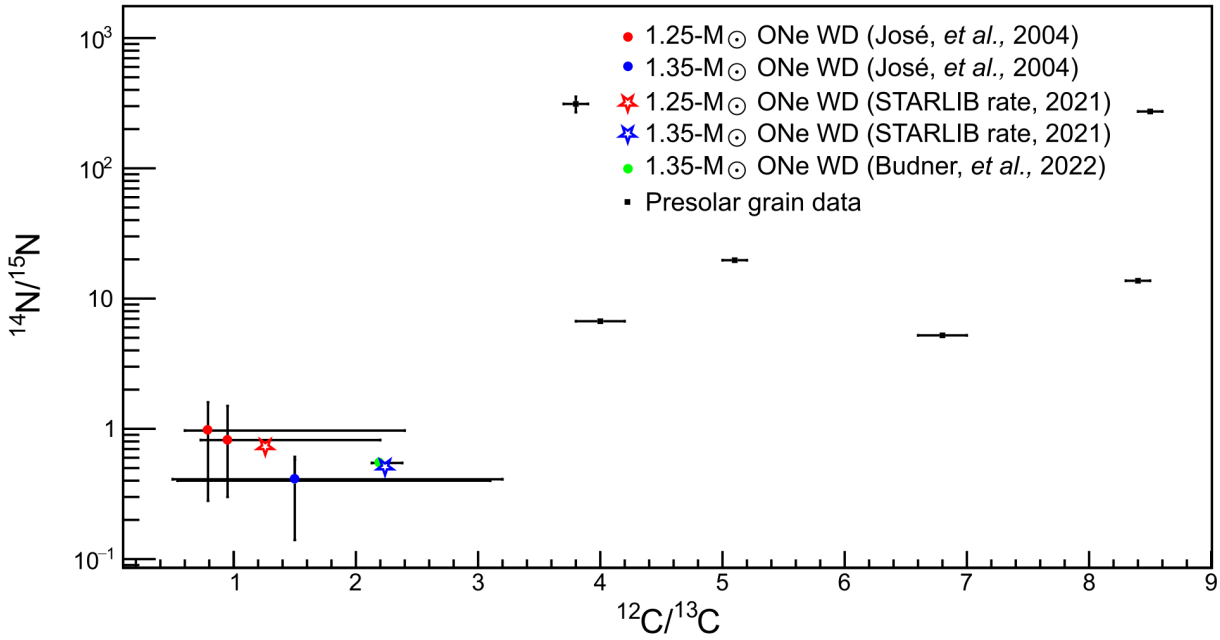

Figure 4.20: C and N isotopic ratios, comparing grain data to previous ONe nova models for different white dwarf (WD) masses as well as the most recent SHIVA calculations using both the nominal STARLIB rate for ^{30}P$(p,\gamma)^{31}$S and our experimentally constrained rate. All simulations assume an intial mixing fraction of 50% between the H-rich envelope and WD material.

Similarly for ^{30}Si, which is among the nuclides most dramatically affected by the rate of proton capture on ^{30}P, previous estimates on its prevalence in nova ejecta had massive uncertainties. Abundances calculated using the lower limit of the ^{30}P$(p,\gamma)^{31}$S rate were a factor of ≈ 6 higher than results produced from the nominal rate, and at the theoretical upper limit of this rate, simulations even predicted slight deficits relative to Solar [60]. At $\delta(^{30}\text{Si}{:}^{28}\text{Si}) = 1.14^{+0.93}_{-0.35} \times 10^4$, we can conclusively say that ONe novae involving the most massive white dwarfs should produce enhanced ^{30}Si:^{28}Si ratios in their ejecta when compared to Solar abundances. While this result qualitatively agrees with all candidate nova grains, whose ^{30}Si:^{28}Si ratios exceed that of the Solar System's, we overpredict this deviation in each case by at least a factor of 10.

To reconcile this discrepancy, some have invoked an *ad hoc* mixing of the processed nucleosynthetic material with some unspecified source of near-Solar material which dilutes the ^{29,30}Si excesses before the grains are able to condense. It is not clear if this can be explained by the

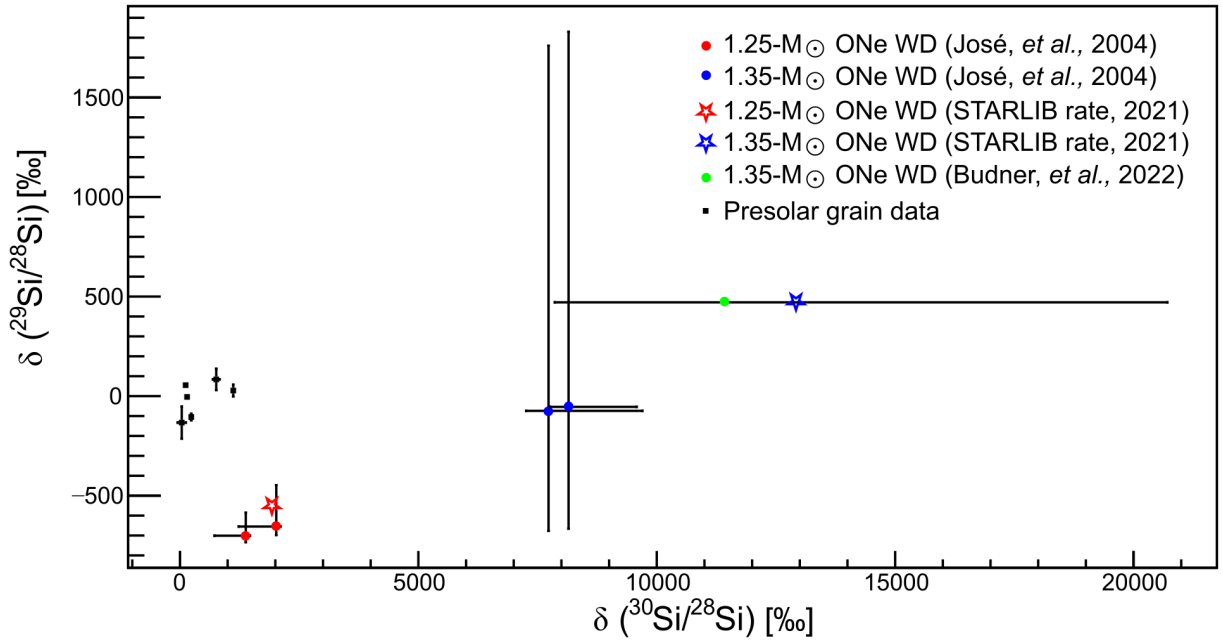

Figure 4.21: Si isotopic abundances in plotted in permille deviations from Solar ratios for ^{29}Si:^{28}Si and ^{30}Si:^{28}Si.

interaction between the ejected shells and the surrounding accretion [66]. It is also possible that ignorance of relevant details in modeling explosive nucleosynthesis, such as the mixing of the accreted material with the outer layers of the white dwarf, prevents an accurate prediction of ejecta composition. Still, others have suggested that these grains did not originate in classical novae at all but came from supernovae instead [164]. Based on our findings and the current state of the literature, we cannot draw any definitive conclusions about the cosmic origins of the presolar grains in question. Nevertheless, from the perspective of experimental nuclear physics, we have done our part by substantially constraining the reaction rate uncertainties related to this issue surrounding Si isotopic ratios.

Elemental Abundances for Nuclear Thermometers

As discussed in Chapter 2, the relative amount of different chemical elements in the ejecta shells from classical nova explosions can be used to constrain the peak temperatures achieved during the

thermonuclear runaway. In contrast to the isotopic ratios discussed in the previous section, which compare the relative number of atomic nuclei, the elemental abundance ratios presented in Ref. [90] are given in terms of their mass fraction relative to H. Thus, all ratios mentioned here should be understood as comparing their proportional contributions to the total mass of the ejecta material.

Among the various abundance ratios, N:O, N:Al, O:S, S:Al, O:Na, Na:Al, O:P, and P:Al have been identified as the most useful thermometers, due to the fact that they all exhibit a steep, monotonic dependence on peak nova temperature. The mass fraction ratios N:O, N:Al, O:Na, and Na:Al are robust to nuclear uncertainties in the sense that they are not particularly sensitive to the effects of unconstrained reaction rates. However, the ratios O:S, S:Al, O:P, and P:Al reveal a strong dependence on both temperature and the thermonuclear rate of $^{30}\mathrm{P}(p,\gamma)^{31}\mathrm{S}$. The ratio between the upper and lower limits on an astronomical value is sometimes called the *variation*. For the N and Na ratios, the variation of final elemental abundance ratios over the range of nova models explored in Ref. [90] spans factors of 5.59 – 13.4, but for S and P ratios, these factors in variation are 216 – 541. Furthermore, the effect of varying the $^{30}\mathrm{P}(p,\gamma)^{31}\mathrm{S}$ rate between its previous upper and lower limits resulted in factors of 3.36 – 6.44 in the uncertainty of predicted S and P ratios; our recently constrained reaction rate reduces these uncertainties.

The peak temperature achieved during thermonuclear runaway is highly correlated with the mass of the underlying white dwarf. Classical novae involving a 1.35-$M_\odot$ ONe white dwarf are expected to reach peak temperatures of $T = 0.312$ GK, according to our model. Thus, the most recent simulation results can be compared to the predicted mass fraction ratios in Ref. [90] for the hottest peak temperatures. Performing more nova simulations that adopt the new recommended rate for $^{30}\mathrm{P}(p,\gamma)^{31}\mathrm{S}$ with smaller white dwarf masses may reduce uncertainties in the expected elemental abundances at lower temperatures. However, any reduction in the variation of predicted abundance ratios at lower temperatures will likely not be as substantial as this effect on modeling the hottest novae, since proton capture on $^{30}\mathrm{P}$ is most important for nucleosynthesis involving very massive ONe white dwarfs.

By summing the ejected mass fractions in Table 4.2 for all isotopes of a given element, we arrive

at the elemental abundance ratios O:S = $0.86^{+0.12}_{-0.04}$, S:Al = $15.7^{+0.9}_{-2.2}$, O:P = $4.9^{+0.5}_{-0.2}$, and P:Al = $2.7^{+0.1}_{-0.3}$. These findings are in good agreement with past abundance predictions and have smaller error bars. Overlaying our simulation results on the original plot from Downen *et al.*, we can clearly see in Figure 4.22 that the uncertainty in the predicted mass fractions has been reduced [90]. For some candidate thermometers, fully hydrodynamic simulations either over- or underpredict elemental abundance ratios when compared to post-processing calculations. The latter have the advantage of being less computationally expensive since they merely adopt the temperature-density profiles produced from hydrodynamic models and use this as input to execute a nuclear reaction network code for each burning zone in the nova event, but ultimately, fully hydrodynamic simulations should provide more realistic results.

By visual inspection at $T_{\text{peak}} = 0.31$ GK, we estimate that the variation in the four ratios, as predicted by the post-processing calculations, were factors of about $2 - 3$ [90]. Meanwhile, our expected variation due to the rate of $^{30}\text{P}(p,\gamma)^{31}\text{S}$ is within factors of $1.1 - 1.2$ for the same peak temperature across all nova thermometers. As a consistency check and for the sake of completeness, we note that the mass fractions O:Na and Na:Al are also in good agreement with the hydrodynamic simulation results. However, the variations in these abundances due to nuclear uncertainties alone, as evaluated by the post-processing calculations, were already quite small and are unaffected when varying the $^{30}\text{P}(p,\gamma)^{31}\text{S}$ rate.

Unfortunately, neither Na nor P have yet been observed in ONe nova ejecta. Thus, the otherwise prime candidates O:Na, Na:Al, O:P, and P:Al are currently useless as thermometers. However, the presence of N, O, Al, and S have all been identified in the shells of ONe novae. In fact, the N:O and O:S abundance ratios observed from the nova event V838 Herculis suggest its peak temperature range is $T_{\text{peak}} = 0.30 - 0.31$ GK, which corresponds to a white dwarf mass of $M_{\text{WD}} = 1.34 - 1.35$ $M_{\odot}$ [90]. Therefore, we are able to directly compare our predicted abundances to the observed mass fractions of the processed nuclear material ejected by V838 Herculis. As shown in Figure 4.23, our results are in agreement with post-processing calculations. Previous simulations slightly overestimate the expected ratios N:Al and N:O for V838 Herculis, and since our constraints on

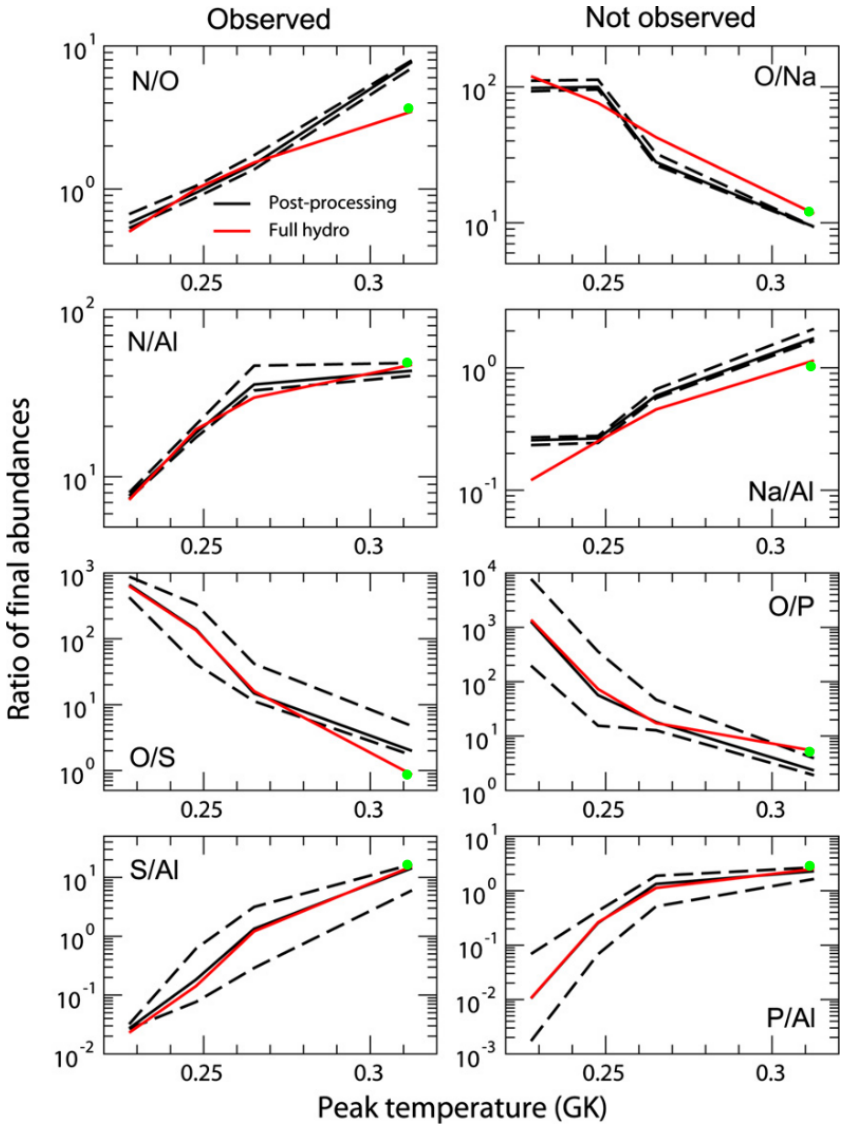

Figure 4.22: Mass fraction ratios plotted as a function of peak nova temperature for all candidate thermometers. The solid black and red lines represent predicted abundance ratios from post-processing calculations and fully hydrodynamic simulations, respectively. The dashed lines form error bands on these predictions as a result of independently varying the rate of relevant nuclear reactions within their uncertainties. Green markers correspond to our simulation results, whose error bars are approximately the size of the data point. Left column: abundance ratios for elements observed in ONe nova shells. Right column: abundance ratios for elements that have not yet been observed in the ejecta of ONe novae. Figure credit: Ref. [90].

^{30}P$(p,\gamma)^{31}$S do not affect these abundances, the latest SHIVA predictions are unable to resolve the discrepancy. However, we do agree with observations of S:Al and O:S from V838 Herculis to the level of one standard deviation and with substantially smaller uncertainties.

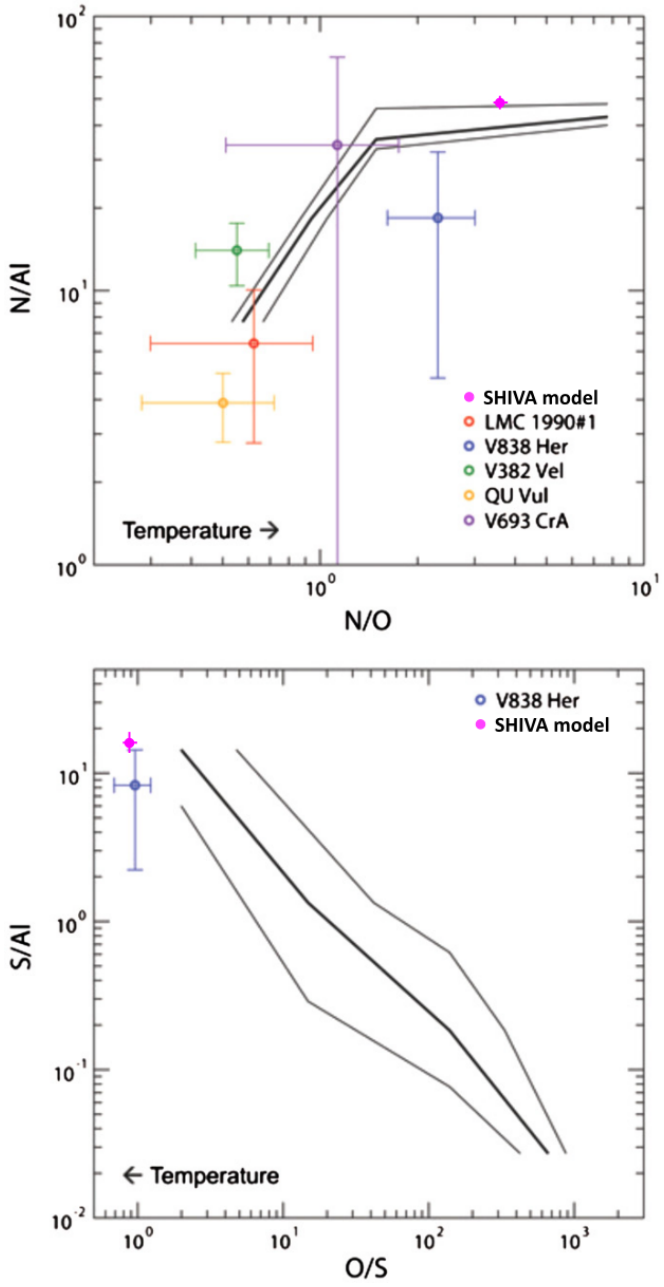

Figure 4.23: Mass fraction ratios comparing observational nova data to theoretical predictions. The black lines represent abundances and their uncertainties according to post-processing calculations, while the magenta data point corresponds to our latest hydrodynamic simulation results using the constrained $^{30}\mathrm{P}(p,\gamma)^{31}\mathrm{S}$ rate. Top panel: Al and O abundances plotted relative to N, where peak nova temperature increases from left to right. Bottom panel: Al and O abundances plotted relative to S, where peak nova temperature increases from right to left. Figure credit: Ref. [90].

	Ejected mass fraction		
Nuclide (^{A}X)	Lower limit	Recommended rate	Upper limit
^{9}C	1.59×10^{-31}	1.96×10^{-28}	5.49×10^{-32}
^{11}C	5.64×10^{-10}	6.14×10^{-10}	5.84×10^{-10}
^{12}C	2.22×10^{-2}	2.22×10^{-2}	2.20×10^{-2}
^{13}C	1.13×10^{-2}	1.01×10^{-2}	1.09×10^{-2}
^{12}N	6.39×10^{-33}	1.88×10^{-30}	$4.27 \times 10–33$
^{13}N	4.33×10^{-3}	4.17×10^{-3}	4.66×10^{-3}
^{14}N	5.49×10^{-2}	5.32×10^{-2}	5.46×10^{-2}
^{15}N	1.07×10^{-1}	1.10×10^{-1}	1.07×10^{-1}
^{13}O	1.30×10^{-34}	1.83×10^{-34}	1.30×10^{-34}
^{14}O	1.13×10^{-6}	3.70×10^{-6}	2.12×10^{-6}
^{15}O	1.48×10^{-4}	2.94×10^{-4}	2.12×10^{-4}
^{16}O	6.06×10^{-3}	5.95×10^{-3}	6.00×10^{-3}
^{17}O	3.98×10^{-2}	4.07×10^{-2}	4.09×10^{-2}
^{18}O	6.63×10^{-6}	6.45×10^{-6}	6.67×10^{-6}
^{23}Al	2.30×10^{-34}	4.90×10^{-30}	2.30×10^{-34}
^{24}Al	2.40×10^{-34}	2.08×10^{-25}	2.40×10^{-34}
^{25}Al	2.10×10^{-31}	5.36×10^{-18}	7.20×10^{-32}
^{26}Al	4.56×10^{-4}	4.57×10^{-4}	4.53×10^{-4}
^{27}Al	3.01×10^{-3}	3.02×10^{-3}	3.02×10^{-3}
^{25}Si	2.50×10^{-34}	3.59×10^{-33}	2.50×10^{-34}
^{26}Si	2.60×10^{-34}	9.44×10^{-25}	2.60×10^{-34}
^{27}Si	8.22×10^{-28}	1.47×10^{-18}	1.48×10^{-28}
^{28}Si	3.04×10^{-2}	3.10×10^{-2}	3.11×10^{-2}
^{29}Si	2.34×10^{-3}	2.40×10^{-3}	2.42×10^{-3}
^{30}Si	2.37×10^{-2}	1.38×10^{-2}	9.89×10^{-3}
^{29}S	2.90×10^{-34}	6.53×10^{-32}	2.90×10^{-34}
^{30}S	3.00×10^{-34}	6.00×10^{-27}	3.00×10^{-34}
^{31}S	1.96×10^{-33}	4.59×10^{-21}	1.16×10^{-33}
^{32}S	4.57×10^{-2}	5.33×10^{-2}	5.63×10^{-2}
^{33}S	6.67×10^{-4}	7.98×10^{-4}	8.52×10^{-4}
^{34}S	3.00×10^{-4}	3.60×10^{-4}	3.86×10^{-4}
^{35}S	3.50×10^{-34}	3.50×10^{-34}	3.50×10^{-34}
^{36}S	3.60×10^{-34}	3.60×10^{-34}	3.60×10^{-34}

Table 4.2: Predicted mass fractions for C, N, O, Al, Si, and S relative to the total mass ejected (9.043×10^{27} g) during a classical nova explosion on a 1.35-$M_{\odot}$ ONe white dwarf. Three different rates for the ^{30}P$(p,\gamma)^{31}$S reaction were used to quantify the effect of this nuclear uncertainty on isotopic and elemental abundances.

CHAPTER 5

THE ^{31}CL($\beta p\gamma$)^{30}P DECAY SCHEME

Having achieved the primary scientific motivation of this research by measuring the proton branching ratio of the key 260-keV, $J^{\pi} = 3/2^{+}$ resonance and interpreting its astrophysical impact, we may now turn our attention to the higher-energy protons in our decay spectrum. Essentially all previous measurements of ^{31}Cl β-delayed proton decay assumed that these charged-particle emissions populate the ground state of ^{30}P. However, using the γ-tagging capabilities of GADGET on the high-statistics dataset acquired during NSCL experiment 17024, we demonstrate conclusively that many of these transitions proceed from proton-unbound states in ^{31}S to excited states of ^{30}P. In addition, we have identified several new β-delayed proton decay transitions and present a preliminary ^{31}Cl($\beta p\gamma$)^{30}P decay scheme for the first time.

5.1 Populating ^{30}P Excited States

Evidence of level population above the ^{30}P ground state was first realized, and is perhaps most obviously illustrated, upon plotting the γ ray spectrum observed in coincidence with protons in the region spanning $1170 - 1280$ keV in our energy spectrum. Figure 5.1 clearly shows that emitted protons are strongly populating all four of the lowest-lying excited states in ^{30}P. For reference, the γ decay scheme for these low-lying levels is shown in Figure 5.2. By placing coincidence gates on these observed γ ray transitions, we have been able to identify previously unobserved proton peaks that, due to their weak intensities, are otherwise obscured in the cumulative singles spectrum.

Background-Subtracted Coincidence Spectra

At least one of the γ ray deexcitations for each of the four lowest excited states in ^{30}P can be observed in the proton-gated γ singles spectrum. By placing a coincidence gate on all γ events that fall within the energy region that contains the photopeak of a ^{30}P transition and plotting the resulting proton spectrum, we can clearly see features emerge that are distinct from the qualitative structure

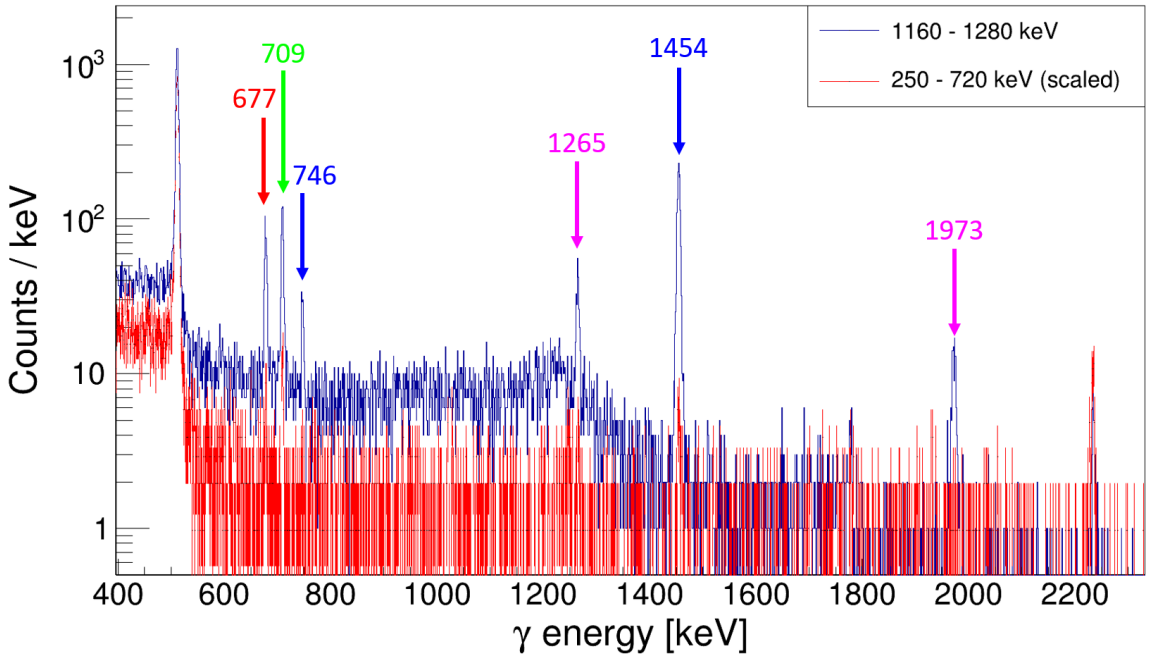

Figure 5.1: Proton-gated γ ray spectra. The legend indicates the energy range over which γ coincidences are sampled for the 1.2-MeV region (blue) and the background region (red), whose statistics have been scaled by the ratio of counts in the proton singles spectrum within the two gating regions. Photopeaks corresponding to ^{30}P transitions are labeled with their γ energy in keV units. Labels of the same color indicate γ transitions from the same excited state.

of the cumulative proton spectrum. In order to determine the decay energies and intensities of these new β-delayed protons, it is necessary to remove the background contribution from strong β-delayed proton decays which are in random coincidence with γ rays of all energies.

The most prominent feature in the ^{31}Cl β-delayed proton spectrum is the massive peak at 1 MeV. As discussed in Chapter 4, this strong proton branch has been observed in previous β^+ decay experiments and was assumed to populate the ^{30}P ground state. Furthermore, the corresponding ^{31}S level from which this proton is emitted has been observed in single-nucleon transfer and charge-exchange reaction experiments as well and has an excitation energy of 7156 keV [101; 105; 102; 99]. By gating on this proton peak in our data and analyzing the coincident γ spectrum, we were able to determine that the 1-MeV β-delayed proton decay is, in fact, a ground-state transition.

We can represent the contribution of random coincidences to the background in our γ-gated proton spectra as a scaled-down version of the cumulative β-delayed proton spectrum in Figure

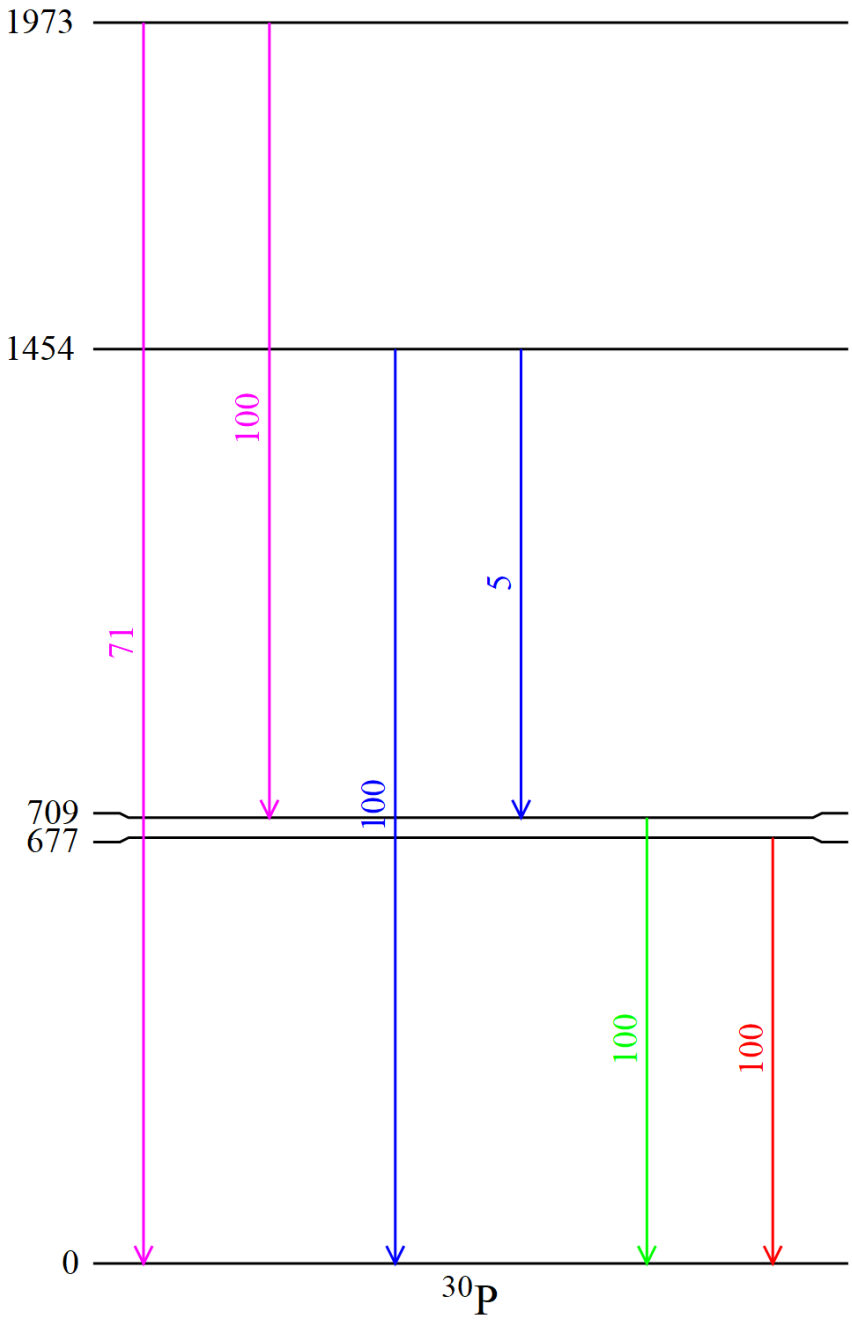

Figure 5.2: Level scheme for the first four excited states in ^{30}P. Level energy labels (black) are given in units of keV, and transition labels (colored) represent relative intensities. All of these transitions are observed in coincidence with β-delayed proton decay events with energies between 1.1 and 1.2 MeV.

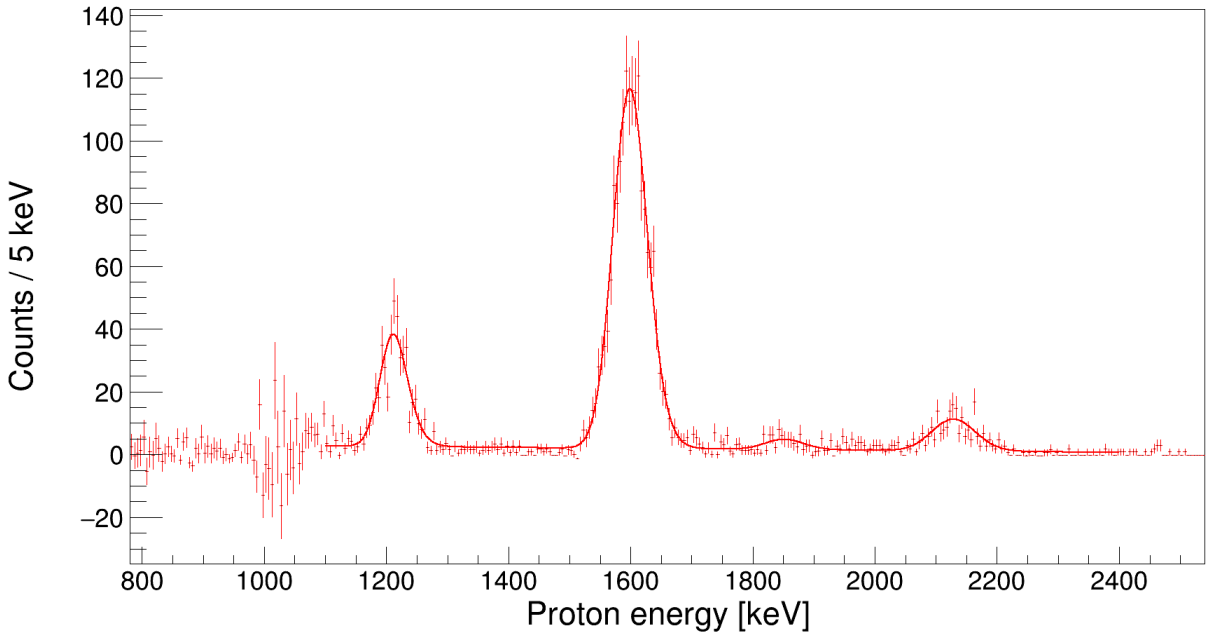

Figure 5.3: Background-subtracted energy spectrum for β-delayed protons in coincidence with 677-keV γ rays emitted from the first excited state. The four peaks were fit with EMG distributions, and the background is modeled as linear. The feature near 1 MeV shows large statistical fluctuations in each bin due to the subtraction of the largest proton peak in the spectrum; the integral over this energy range is consistent with zero.

4.2. The scaling factor is simply the ratio between the number of 1-MeV events in γ-gated proton spectrum and the number of 1-MeV protons in the total, combined spectrum. Taking the difference bin-by-bin between the scaled "background" spectrum and the proton spectrum that results from gating on the γ ray of interest, we can produce a background-subtracted proton spectrum for each ^{30}P transition. These spectra are shown in Figures 5.3, 5.4, 5.5, 5.6, 5.7, and 5.8 for ^{31}Cl β-delayed protons detected in coincidence with 677-, 709-, 1454-, 746-, 1265- and 1973-keV, γ rays, respectively.

This analysis procedure provides a very clean background-subtraction method for eliminating accidental coincidences between protons and random γ rays. However, there are also a number of "real" coincidences that can also contribute to the background of our γ-gated proton spectra. In our γ ray spectra, we can think of the photopeak as corresponding to γ events that deposit their full energy in the detector. However, many more γ rays will scatter off the HPGe crystal, depositing only a fraction of their energy in SeGA. This results in a substantial *Compton background* associated

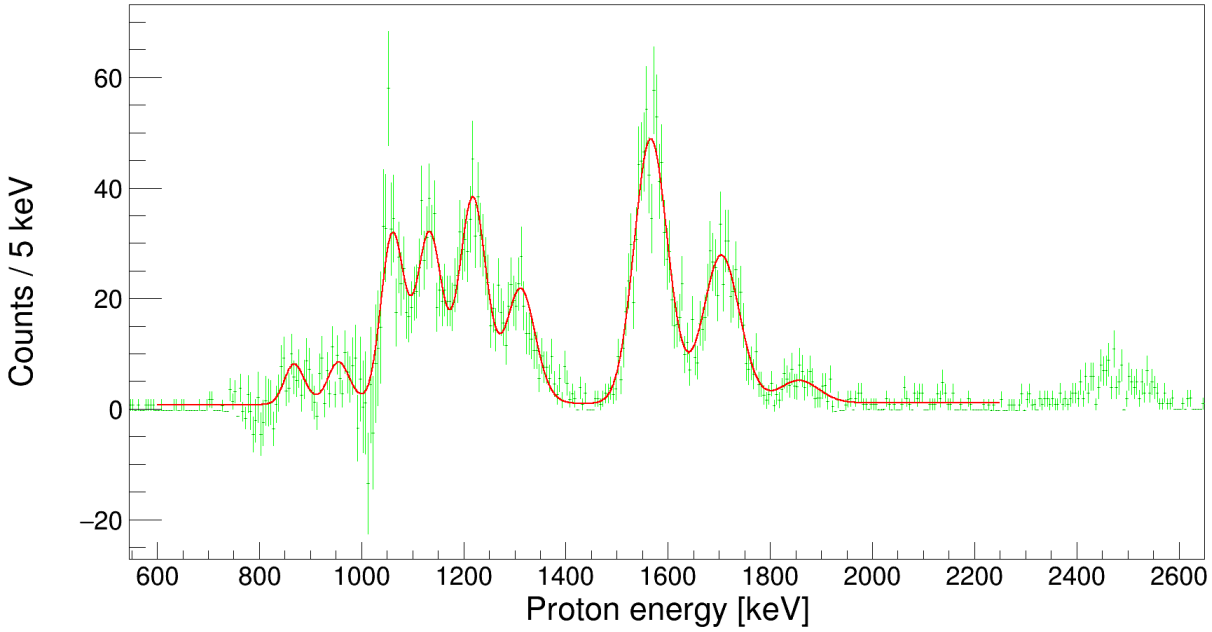

Figure 5.4: Background-subtracted energy spectrum for β-delayed protons in coincidence with 709-keV γ decays from the second ^{30}P excited state to the ground state. The nine peaks were fit with EMG distributions, and the background is assumed to be constant. Several background models were applied to fits of all spectra in order to quantify systematic uncertainty. The proton peak above 2.4 MeV was fit using different constraints over a smaller energy region because it appears to be intrinsically broad.

with each γ ray that spans all energies up to the photopeak. Thus, the contribution from Compton scattering decreases at higher energies since there are fewer γ rays whose partial energies are high enough to populate this region of the spectrum. When placing a coincidence gate on γ ray events within the photopeak of a known transition, we necessarily include Compton-scattered events from higher-energy transitions. Those higher-energy γ transitions that precede the coincidence γ ray of interest in the decay scheme are real coincidences, in the sense that protons could be populating more highly excited states before γ decaying to the lower levels on which we are applying the coincidence gate.

To account for these real coincidences, we set another coincidence gate on a "featureless" background region of the spectrum. The energy range from which we are sampling proton coincidences with background γ events should be higher in energy than the the photopeak of interest. This ensures we avoid the Compton tail of the γ decay on which we are gating. Then, we scale down

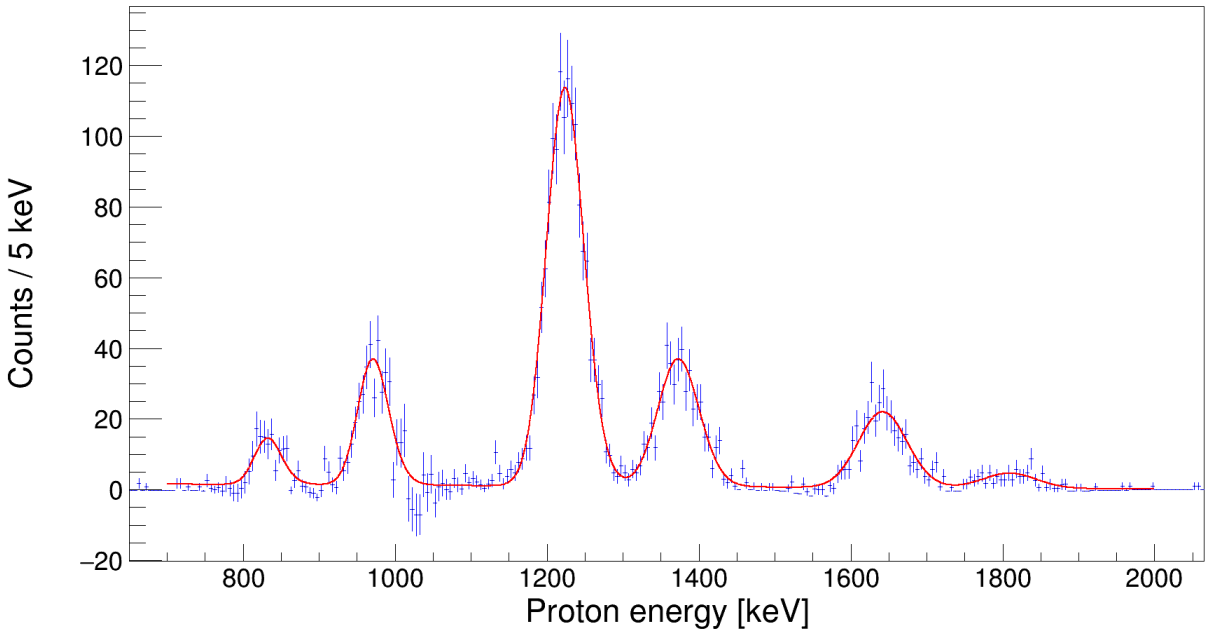

Figure 5.5: Background-subtracted energy spectrum for β-delayed protons in coincidence with 1454-keV γ decays to the ^{30}P ground state from the third excited state. The six peaks were fit with EMG distributions, and the background is modeled as linear.

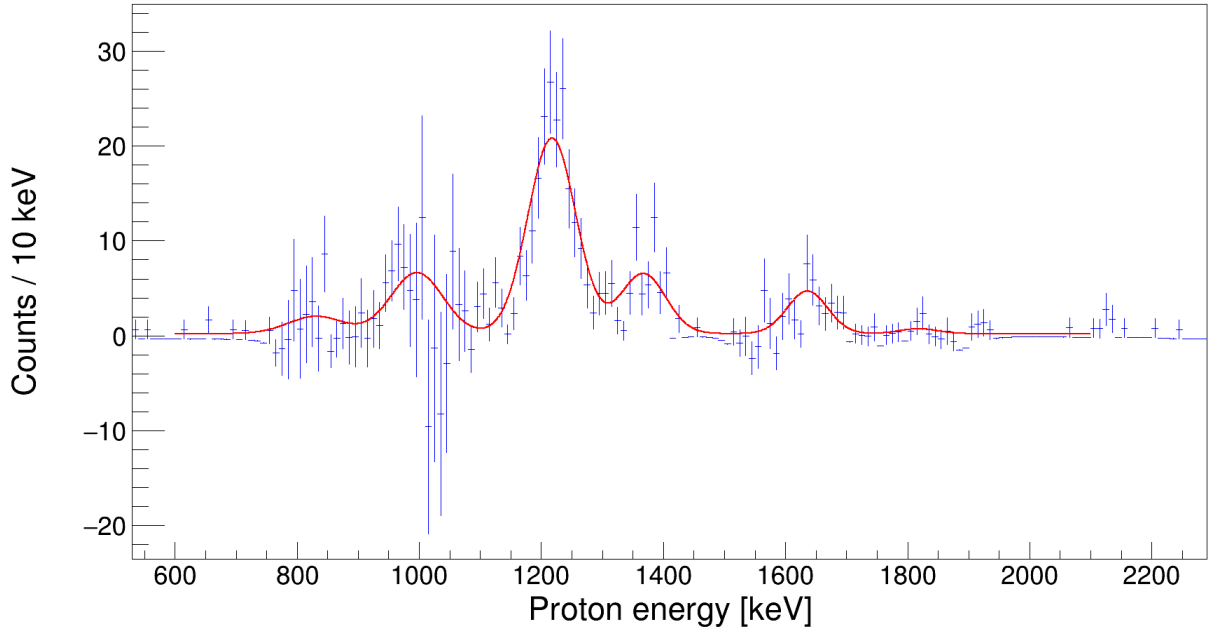

Figure 5.6: Background-subtracted energy spectrum for β-delayed protons in coincidence with 746-keV γ decays from the third excited state in ^{30}P at 1454 keV to the second excited state at 709 keV. This γ branch is much weaker than the 1454-keV transition to the ground state from the same level, and the binning reflects the low statistics. Again, the six peaks were fit with EMG distributions, and the background is constrained to be constant.

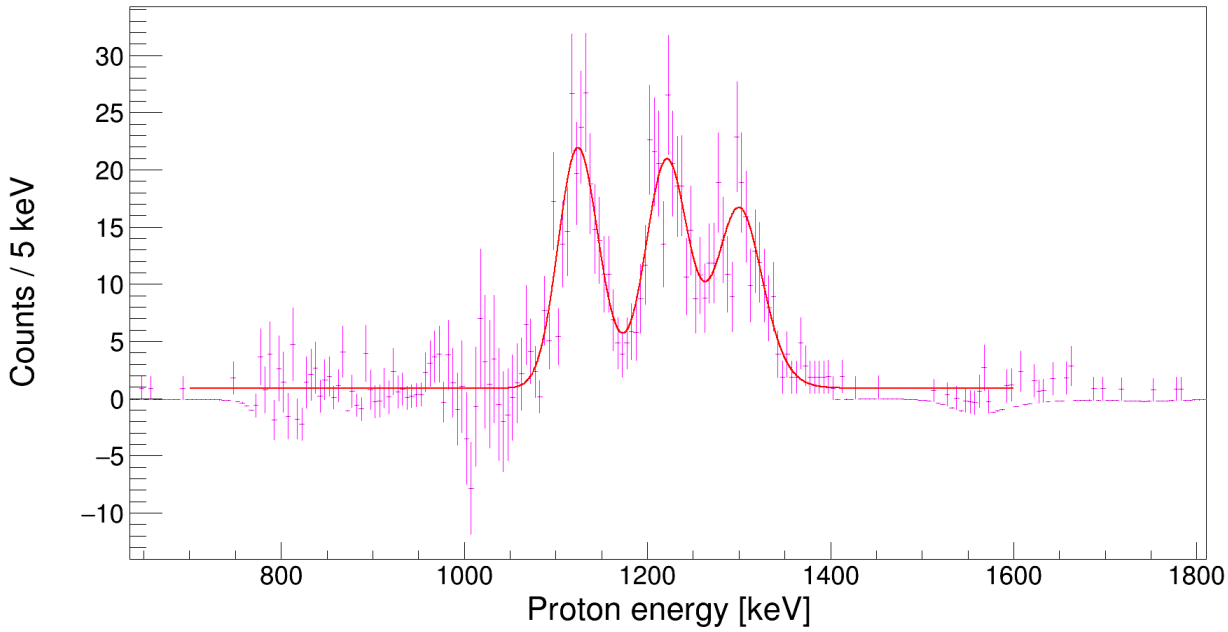

Figure 5.7: Background-subtracted energy spectrum for β-delayed protons in coincidence with 1265-keV γ decays from the fourth excited state in ^{30}P at 1973 keV to the second excited state at 709 keV. This is the stronger of the two γ branches for this level. The three peaks were fit with EMG distributions, and the background is constrained to be constant.

this background γ-gated proton spectrum by the ratio between the number of counts under the photopeak and the total number of background γ counts over their respective energy ranges. We used these two background subtraction methods for the accidental and real coincidences to quantify the systematic uncertainty in the number of β-delayed proton decays to excited states.

Some of the stronger β-delayed proton decays found to be populating excited states of ^{30}P have been observed before and are clearly visible in the cumulative proton spectrum. However, most of the smaller peaks are completely obscured by the much larger peaks that correspond to ground-state transitions. In order to accurately quantify the energy and intensity of the various β-delayed proton decays in the singles spectrum, we need to determine how many of these weaker proton decays we should expect to see in the entire dataset. We can calculate this from the integrals of the γ-gated, background-subtracted proton peak fits if we also know the absolute detection efficiency of SeGA at the appropriate γ ray energies.

5.2 γ-Ray Detection Efficiency with SeGA

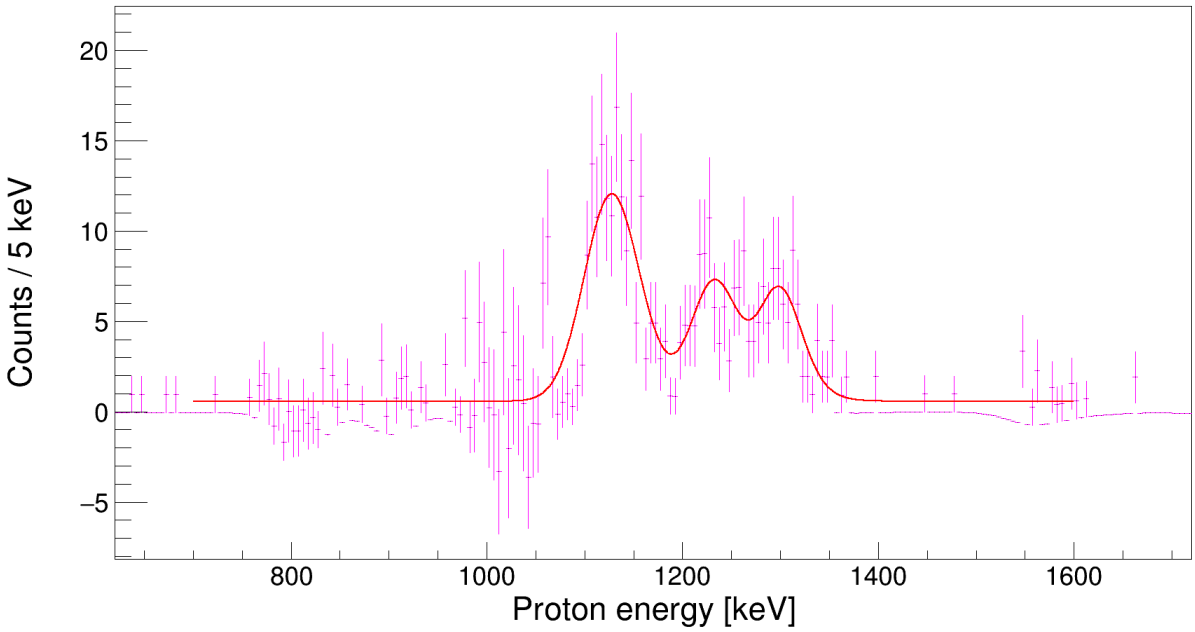

Figure 5.8: Background-subtracted energy spectrum for β-delayed protons in coincidence with 1973-keV γ decays from the fourth ^{30}P excited state to the ground state. Again, the three peaks were fit with EMG distributions, and the background is constrained to be constant.

A detailed decay scheme for ^{31}Cl($\beta\gamma$)^{31}S is provided in Ref. [120]. After correcting some minor arithmetic inconsistencies in the β-delayed γ intensities reported by Bennett *et al.*, we essentially adopted these literature values for our efficiency calibration. Using these numbers and fitting well-separated, high-statistics photopeaks across most of our SeGA spectrum, we are able to determine the relative detection probability of γ rays as a function of energy. In order to extract absolute efficiencies for arbitrary γ energies, we only need to evaluate the absolute detection efficiency at one, or ideally a few, intermediate energies. This allows us to normalize our relative efficiency curve with respect to these fixed values.

Relative Efficiency Curve

We first identified over a dozen photopeaks corresponding to strong β-delayed γ ray emissions in the proton-gated γ singles spectrum depicted in Figure 4.6. In order use the γ detection efficiency to calculate the expected number of β-delayed proton decays to ^{30}P excited states that should appear in the singles spectrum of Figure 4.2, we must ensure that we only consider γ events that originate

in the active volume of the Proton Detector when evaluating the efficiency of SeGA. This is because GADGET can only detect ^{31}Cl β-delayed proton events that occur within the Proton Detector's active region during the 200-ms time window when the gating grid is in its transparent mode. SeGA, on the other hand, can detect γ rays originating anywhere in the experimental vault at any time, including from the decays of ^{31}Cl nuclei that do not make it into the detector chamber, ^{31}Cl decays within the detector during the 300-ms beam implantation period, as well as $^{31}\mathrm{Cl}(\beta p\gamma)^{30}\mathrm{P}$ decays that result in a proton being vetoed. Thus, for the purpose of determining β-delayed proton intensities, the absolute γ detection efficiency must be evaluated for only the γ rays that are detected in coincidence with Proton Detector events that survive the veto condition.

We used a similar functional form to Equation 4.3 to fit the γ ray photopeaks in our SeGA spectrum, but instead of utilizing an EMG distribution with a high-energy tail, as we did for the proton peaks in order to account for the effect of β-summing, we used the same asymmetric Gaussian function but skewed in the opposite direction [165; 166]. This skew to the left is useful for describing the low-energy tail of the photopeak, which results from imperfect charge collection in some regions of the detector or secondary electron and *bremsstrahlung* escape from the active volume [126]. The magnitude of this skew is parameterized by the quantity λ, which should be independent of γ energy. The prominent 1248-keV photopeak in Figure 5.9 was fit using our EMG response function, where λ was allowed to be a free parameter. Since this is one of the strongest γ decays in the spectrum that is not obscured by neighboring peaks, we adopted this value of λ for all other peak fits. This yielded good fits as well as a consistent interpretation of the peak width and γ decay intensity.

Based on our knowledge of γ ray spectra acquired using HPGe detectors, we assumed the width of the photopeaks should vary smoothly with energy, such that

$$\sigma(\mu) = \sigma(\mu = 0) + m_\sigma \sqrt{\mu}. \tag{5.1}$$

First, all calibration peaks were fit in the spectrum allowing σ to be a free parameter. After plotting all χ^2-minimized values of σ as a function of μ, we fit the data using equation Equation 5.1 to

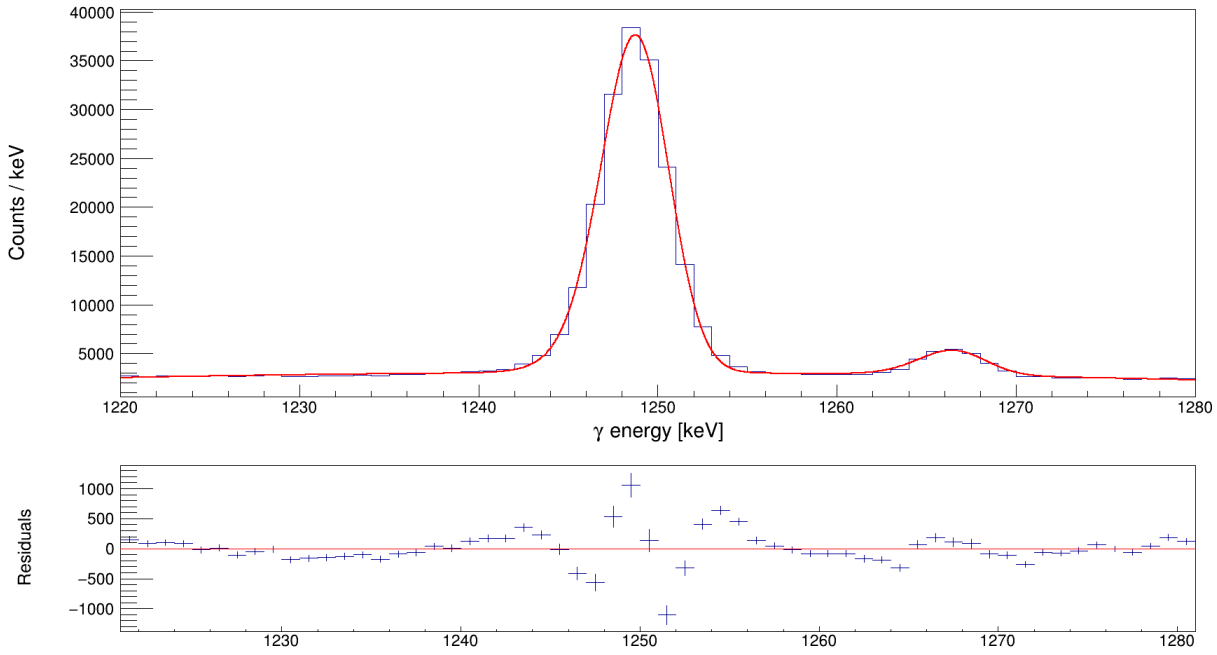

Figure 5.9: Top panel: Fit of the second-strongest photopeak in the ^{31}Cl β-delayed γ spectrum at 1248 keV. The background is modeled with a quadratic polynomial over the energy region 1220 – 1280 keV. Bottom panel: Residual plot of the difference between the histogram's bin content and the value of the fit as a function of γ energy.

find $\sigma(\mu = 0)$ and m_σ, as shown in Figure 5.10. Then, we constrained σ for each photopeak fit to conform to this energy dependence. The difference in the peak integrals between the constrained and unconstrained fits represented the largest source of systematic uncertainty associated with the total number of observed counts for a given γ ray transition, ranging from $< 1\%$ for high-statistics peaks to 14% for weaker γ transitions. The efficiencies for each photopeak were then calculated relative to the 1248-keV peak using the relationship

$$\epsilon_\gamma(\text{rel}) = \frac{I_\gamma}{N_\gamma}\frac{N_{1248}}{I_{1248}}, \tag{5.2}$$

where I_γ is the adopted β-delayed γ intensity for a given ^{31}S excited state transition, and N_γ are the total number of counts in the photopeak; I_{1248} and N_{1248} correspond to the same values but for the 1248-keV reference peak. Figure 5.11 plots the resulting efficiency curve where all values are given in arbitrary units relative to $\epsilon_{1248}(\text{rel}) = 1$. The functional form of the curve typically used to fit efficiency data can be expressed as

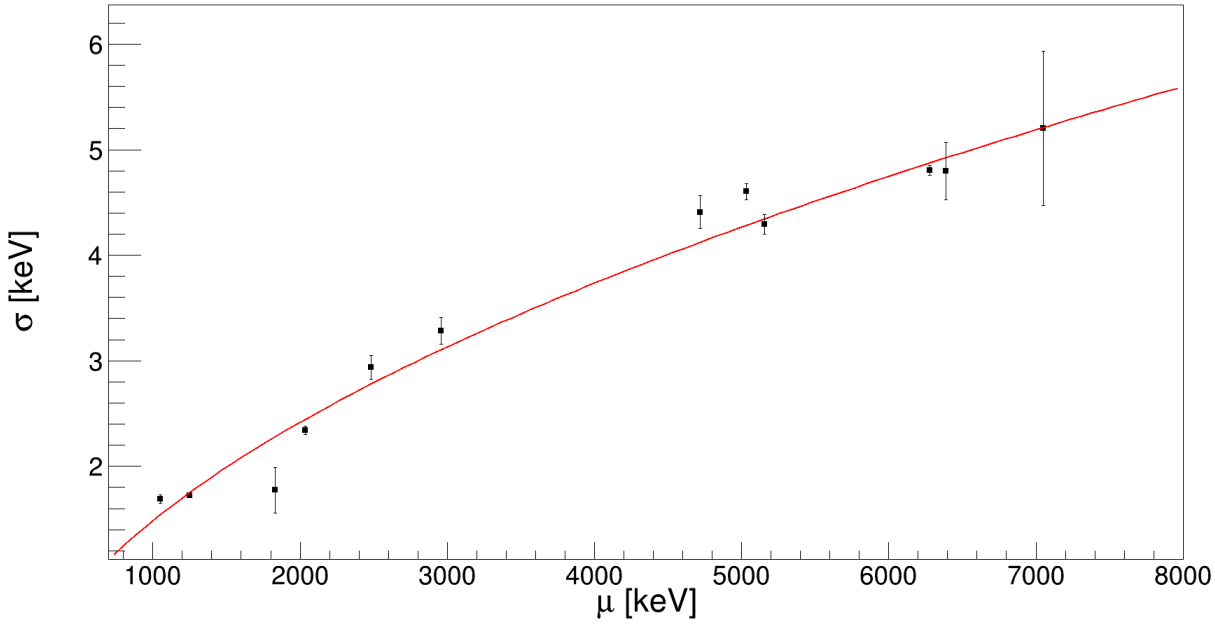

Figure 5.10: Peak width plotted with respect to peak position in the γ energy spectrum. The χ^2-minimized values of the free σ parameter are fit with a function proportional to the square root of the μ parameter.

$$\ln \epsilon = \sum_{i=0}^{i=5} C_i (\ln E_\gamma)^i. \tag{5.3}$$

Absolute Efficiency Calibration Points

In certain cases, it is relatively straightforward to determine the absolute detection efficiency at a specific γ energy. For example, in the case of ^{30}P shown in Figure 5.2, the fourth excited state decays to the second excited state via the γ_{1265} transition. The decay of the second excited state promptly follows, resulting in γ_{709} to be emitted. In this simple decay scheme, the emission of γ_{1265} is always followed by the γ_{709} transition to the ground state. Thus, if we place a coincidence gate on all γ_{1265} events, the number of γ_{709} decays in coincidence must be equal to the total number of γ_{1265} transitions, assuming perfect efficiency. If these quantities are not equal, then, the ratio between observed $\gamma_{709} - \gamma_{1265}$ coincidences and the total number of measured γ_{1265} events is simply

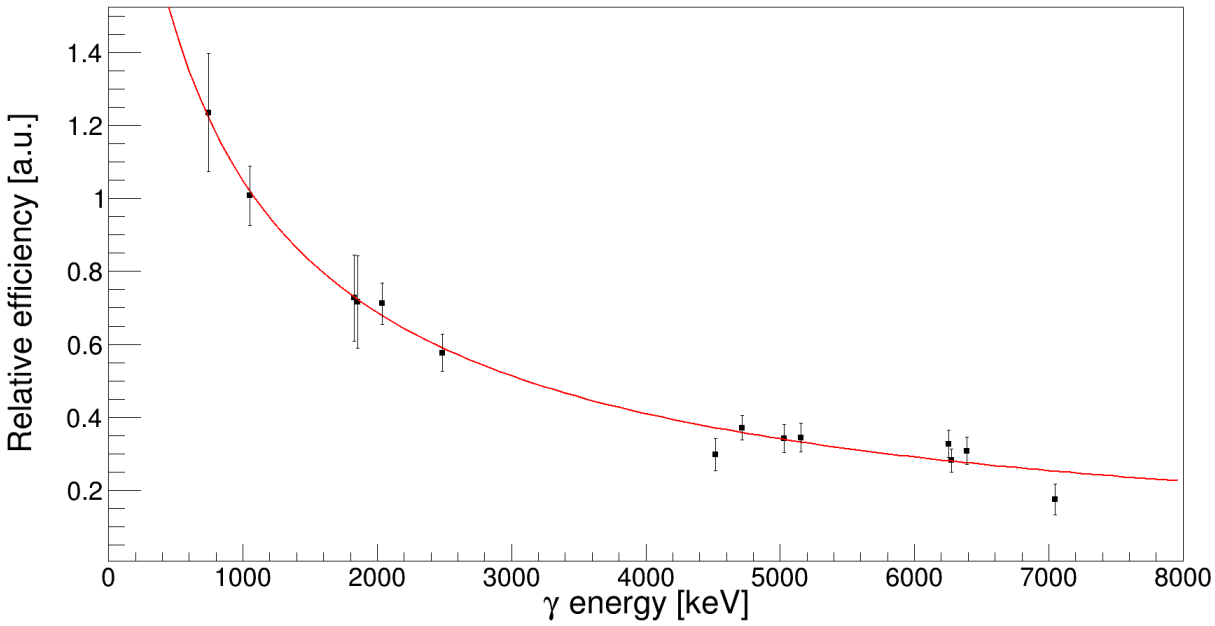

Figure 5.11: Relative detection efficiency in SeGA as a function of γ energy for events in coincidence with β-delayed proton decays.

the detection efficiency for γ_{709}. Expressed generally in terms of initial i and final f transitions, the relationship is

$$\epsilon_f = \frac{\text{Number of } \gamma_f - \gamma_i \text{ coincidences observed}}{\text{Total number of } \gamma_i \text{ events detected}}. \tag{5.4}$$

In order to determine absolute efficiencies in this way for the ^{31}Cl($\beta\gamma$)^{31}S decay scheme, we must identify analogous transition sequences where two γ rays are always emitted one after the other. Of course, the first two excited states in any level scheme will be populated by many γ transitions from higher energy levels. However, not all of these transition sequences are useful for this method. For example, the 1248-keV γ ray is emitted from the first excited state in ^{31}S. According to Ref. [120], this level is populated directly by the decay of several more highly excited states with transition energies of ranging from 946 to 5901 keV.

However, a substantial fraction of the background under lower-energy photopeaks will be contaminated by higher-energy transitions that also populate the 1248-keV level but whose γ rays have undergone Compton scattering, depositing only some of their energy in SeGA. In addition,

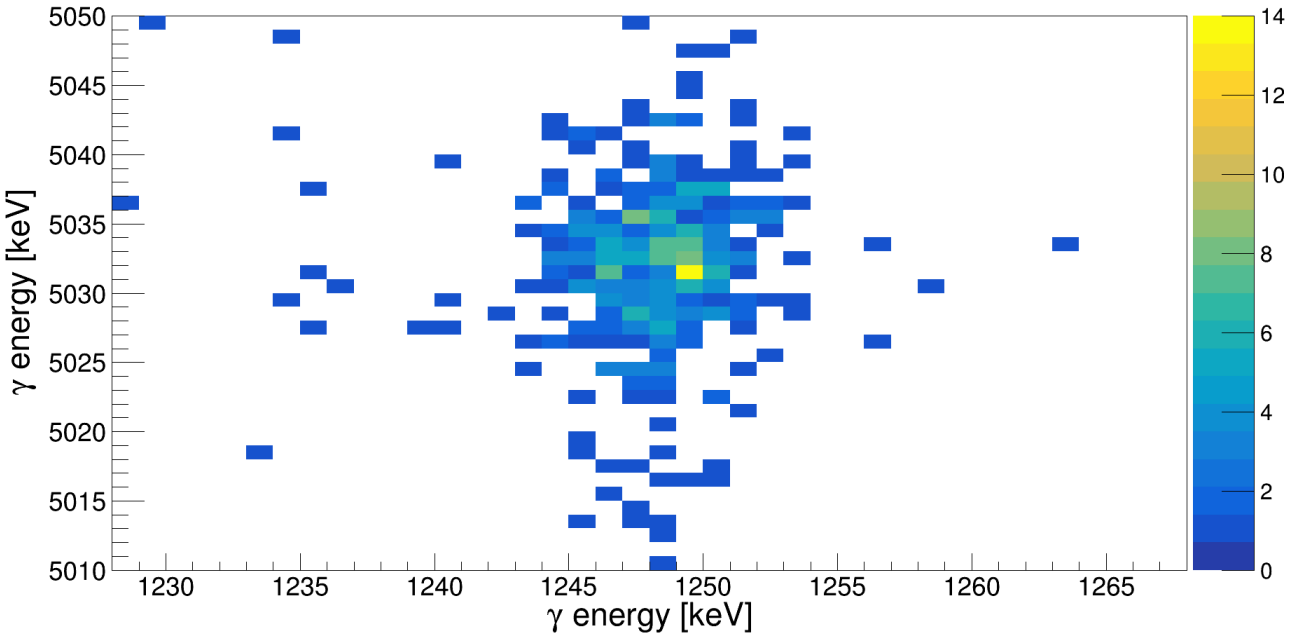

Figure 5.12: A two-dimensional histogram plotting γ-γ coincidences between the 1248- and 5030-keV transitions.

many of the higher-energy β-delayed γ decays are quite weak and had previously been unobserved. Some of the corresponding photopeaks are visible in our γ spectrum, but the probability of observing both transitions independently is reduced by the product of their detection efficiencies, which are each on the order of a few percent. This makes weak γ branches impractical for determining SeGA's absolute efficiency at 1248 keV. Furthermore, some photopeaks are obscured by other nearby γ ray peaks, making the integrals extracted from their fits unreliable. Ultimately, we were able to identify three usable γ decays to the 1248-keV level with transition energies 2035, 2959, and 5030 keV; Figure 5.12 shows one example of such γ-γ coincidences.

Fitting the photopeak shown in Figure 5.13 from the proton-gated γ spectrum yields the denominator for Equation 5.4, where in this case γ_i is the 5030-keV transition. To determine the numerator of this ratio, we need to determine the number of instances in which the 1248- and 5030-keV γ rays are detected together in coincidence. Just as we demonstrated previously with the γ-gated, background-subtracted proton spectra, we can place a coincidence gate on all 5030-keV γ ray events over several widths of the photopeak and plot the resulting coincidence γ rays. To account

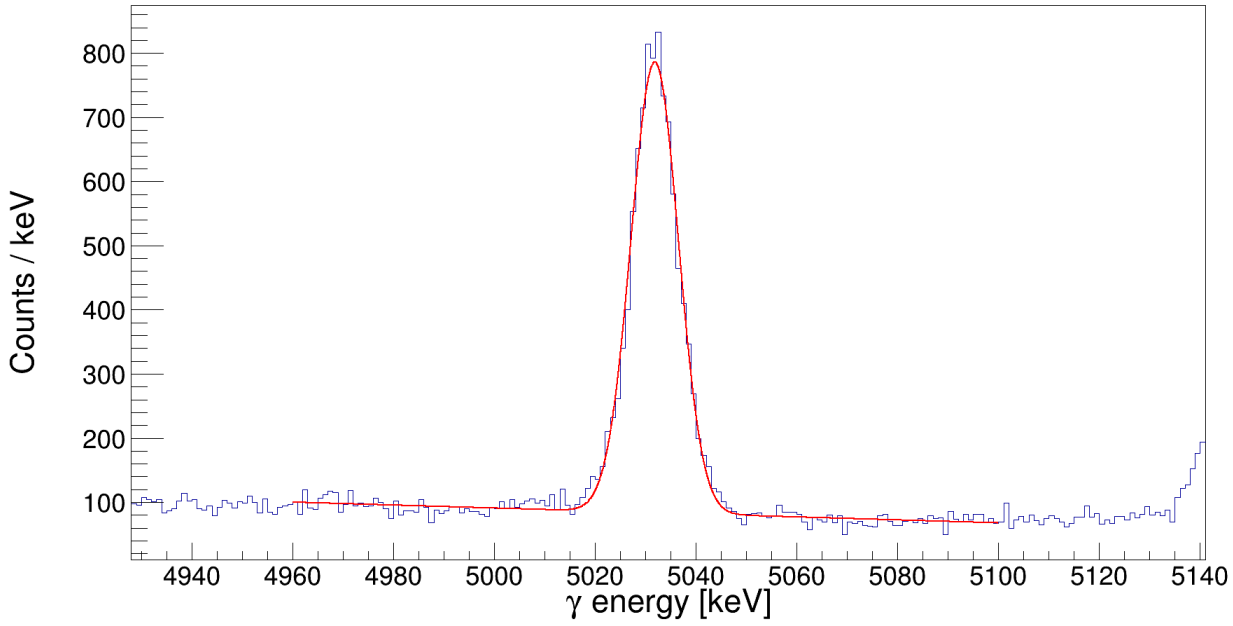

Figure 5.13: Fit of the 5030-keV photopeak. The integral of this peak is the total number of 5030-keV γ decays populating the 1248-keV first excited state of ^{31}S that are detected in coincidence with non-vetoed Proton Detector events.

for the background, we generate another γ spectrum gated on coincident γ rays with energies above the 5030-keV photopeak. To estimate the contribution of random, accidental coincidences to the 1248-keV peak, we scale the background-gated γ spectrum by the ratio between the number of γ events in the energy range of the photopeak gate and the number of counts in the background gate's range. For estimating the contribution of real, true coincidences from the Compton tails of higher-energy transitions also populating the 1248-keV state, we scale the background-gated γ spectrum by the ratio between the number of background counts under the photopeak and the number of γ events over the energy range of the background gate.

Taking the difference between the photopeak-gated and the scaled-down, background-gated γ spectra results in Figure 5.14. Lastly, fitting the 1248-keV peak in this background-subtracted coincidence spectrum allows us to calculate the absolute detection efficiency of SeGA for this γ energy. This process was repeated for both accidental and real coincidences for three different γ transitions populating the 1248-keV state in order to quantify our systematic uncertainty. Combining this with the statistical uncertainty of our median fit value results we arrive at an efficiency of

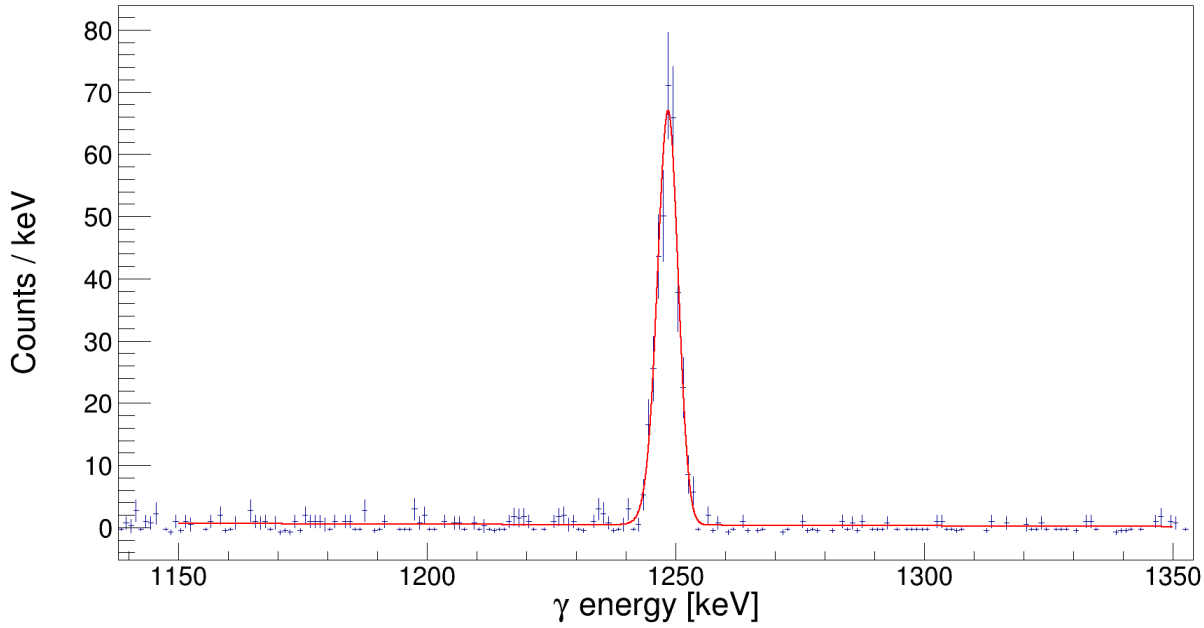

Figure 5.14: Fit of the 1248-keV photopeak after background subtraction. The integral of this peak corresponds to the number of 1248-keV γ events observed in coincidence with the 5030-keV transition that populates the first excited state.

$\epsilon_{1248} = 0.045(5)$. Similarly, we applied the same analysis procedure to determine an absolute detection efficiency at 2234 keV using transitions that feed the second excited state via the emission of 1050-, 1852-, and 2484-keV γ rays. We found that the probability to detect a 2234-keV γ in coincidence with a Proton Detector event in our experiment was $\epsilon_{2234} = 0.027(6)$. Fixing the position of these two data points in place, we normalized our relative efficiency curve from Figure 5.11 such that we are able to interpolate the proton-γ detection efficiency of the GADGET system spanning the energy range 0.7 – 7 MeV.

5.3 Analyzing the Cumulative Proton Spectrum

Having determined the detection efficiency of SeGA for γ energies spanning 0.7 – 7 MeV, we may now revisit the analysis of the cumulative spectrum for the higher-energy, β-delayed proton decays. Extracting the centroids from fits of the γ-gated, background-subtracted proton peaks allows us to determine the positions of these weak proton branches in the cumulative energy spectrum that combines all non-vetoed Proton Detector events. Dividing the peak areas obtained

from the coincidence spectra fits by SeGA's detection efficiency evaluated at the relevant γ energies, we calculated the expected number of total proton counts in the combined spectrum from these transitions. Upon fixing these parameters for the distributions of smaller proton peaks, we fit the larger proton peaks in the singles spectrum, allowing their positions and intensities to be free parameters, in order to determine their decay energies and strengths under these constraints. This process was repeated iteratively over several energy regimes, relaxing and tightening various fit parameters for the purpose of quantifying systematic uncertainties in our model of the data. However, in order to convert the peak positions within the histogram as determined by our fits into real decay energies, it was necessary for us to establish a robust energy calibration that is reliable across the entire Proton Detector spectrum.

Energy Calibration Revisited

As discussed in Chapter 4 for the calibration of the central detector pad, we relied on extrapolating from three data points within 700 – 1100 keV when reporting our measured energy of the low-energy, β-delayed proton decay through the key $J^\pi = 3/2^+$ resonance. We plotted the decay energies of the calibration peaks as evaluated in literature [119] against the means of the three Gaussian distributions used to fit the corresponding peaks for the strongest β-delayed proton decays observed in our spectrum. Fitting these three points with a first-degree polynomial provided a reasonable energy calibration function over a relatively small range of the spectrum and yielded a decay energy that was consistent with the hypothesis that we observed β-delayed proton decay through the 260-keV resonance of interest. However, this extrapolation results in large uncertainties when evaluated at energies well above or below 1 MeV. We initially hesitated to incorporate more data points from higher energies into this fit because we realized that this region of the spectrum is much more complicated than had been previously assumed. However, after careful subsequent analysis of the proton-γ coincidence data for all observable ^{30}P transitions, we have acquired a much more detailed understanding of the cumulative spectrum's underlying structure, which allowed us to produce a precise energy calibration that spans the entirety of the combined-pads spectrum.

To begin, we returned to the three largest peaks in our spectrum peaks as a starting point for our calibration. For the spectrum including data combined from all active pads, we cannot ignore the effect of β-summing, as the peaks are clearly not symmetrical. We used EMG distributions to fit these calibration peaks, also taking into account their small areal contributions from the much weaker proton decays that populate excited states. Since the response function is asymmetric, we chose to calibrate our proton energies with respect to the *mode* of each distribution: the location along the x-axis of the histogram at which the peak's fit function is at its maximum value. We determined the decay energies of all resonances in this calibration via the relation

$$E_r = E_x(^{31}\mathrm{S}) - S_p - E_x(^{30}\mathrm{P}), \tag{5.5}$$

where $E_x(^{31}\mathrm{S})$ is the excitation energy of the proton-emitting level in ^{31}S, S_p is the proton separation energy of ^{31}S, and $E_x(^{30}\mathrm{P})$ is the excitation energy of the ^{30}P level populated by β-delayed proton decay. $E_x(^{30}\mathrm{P}) = 0$ for these first three calibration points, since they correspond to proton decays to the ground state. Using the evaluated level energies and their assigned uncertainties from Nuclear Structure and Decay Data (NuDat) [167] as well as S_p from the latest mass evaluation [16], we compute $E_r = 806(2), 906(2), 1025(2)$ keV.[1] Fitting these energies as a linear function of the our distribution modes provides a well-constrained energy calibration within the region between these points. However, in order to extend this calibration to higher energies, we would like to identify protons within the energy range 806 – 1025 keV which decay from highly excited states in ^{31}S that also emit protons of several different energies.

Fortunately, we were able to identify one such proton transition populating the third excited state of ^{30}P, whose energy falls within the region over which our calibration is well-constrained; applying our local energy calibration yields a decay energy of 834 keV. After fitting all proton peaks in our γ-gated coincidence spectra, we estimated the excitation energy of their proton-emitting levels using Equation 5.5. In the case of the 834-keV transition, $E_x(^{31}\mathrm{S})$ = 834(3) + 6130.65(24) +

[1] Excitation energies used in the proton spectrum energy calibration are based on evaluated nuclear level energies as reported in NuDat [167] prior the most recent update in late June 2022. Any future changes to these preliminary values will likely reflect this.

1454.23(2) keV = 8419(3) keV. The closest level tabulated in NuDat has an excitation energy and associated uncertainty of E_x = 8424(3) keV. This level has reportedly been populated in several different experiments, including ^{31}Cl β-delayed proton decay measurements [117; 118; 168], with researchers reporting a range of excitation energies. Saastamoinen *et al.* attributes the observation of 2.3-MeV protons, which likely correspond to a visible peak of the same energy in our spectrum, to the decay of a proton-unbound ^{31}S level located at E_x = 8429(3). However, results from experiments employing a high-resolution magnetic spectrometer for the reactions ^{31}P(^{3}He,t)^{31}S and ^{32}P$(p, d)^{31}$S conclude E_x = 8418(5) [102] and E_x = 8422(2) [99], respectively. This is in good agreement with our prediction, and we can consider our result an independent measurement of this level's excitation energy. Thus, we adopt the 8419-keV level for the purpose of our energy calibration.

Gating on the proton peak near 2.3-MeV, we do not observe any evidence of coincident γ rays from ^{30}P excited states, suggesting that these events indeed correspond to ground-state proton transitions and likely originate from the 8419-keV level. Under this reasonable assumption, the transition should have decay energy of E_r = 8419(3) - 6130.65(24) keV = 2288(3) keV. We also identified two more relatively strong β-delayed proton transitions that populate the first and second excited states, calculating the predicted excitation energies of their proton-emitting level in ^{31}S. While our preliminary, three-peak energy calibration predicted excitation energies for both proton decays to be $\approx$ 10 keV less than 8419 keV, this is the only confirmed state within 20 keV. Furthermore, just as we saw for the case of the lowest-energy resonance in our spectrum, for which we reported a decay energy of E_r = 273(10) keV, when extrapolating the three-peak energy calibration > 500 keV above or below the well-constrained energy region, a 10-keV uncertainty in decay energy is to be expected. Thus, we believe it is reasonable to conclude that these protons are also emitted from the 8419-keV level, with decay energies of E_r = 8419(3) - 6130.65(24) keV - 677.01(3) keV = 1611(3) keV and E_r = 8419(3) - 6130.65(24) keV - 708.70(3) keV = 1578(3) keV. Figure 5.15 shows the combined-pads singles spectrum with the full set of proton calibration peaks labeled.

Having determined the decay energies of seven well-separated peaks across the spectrum, we

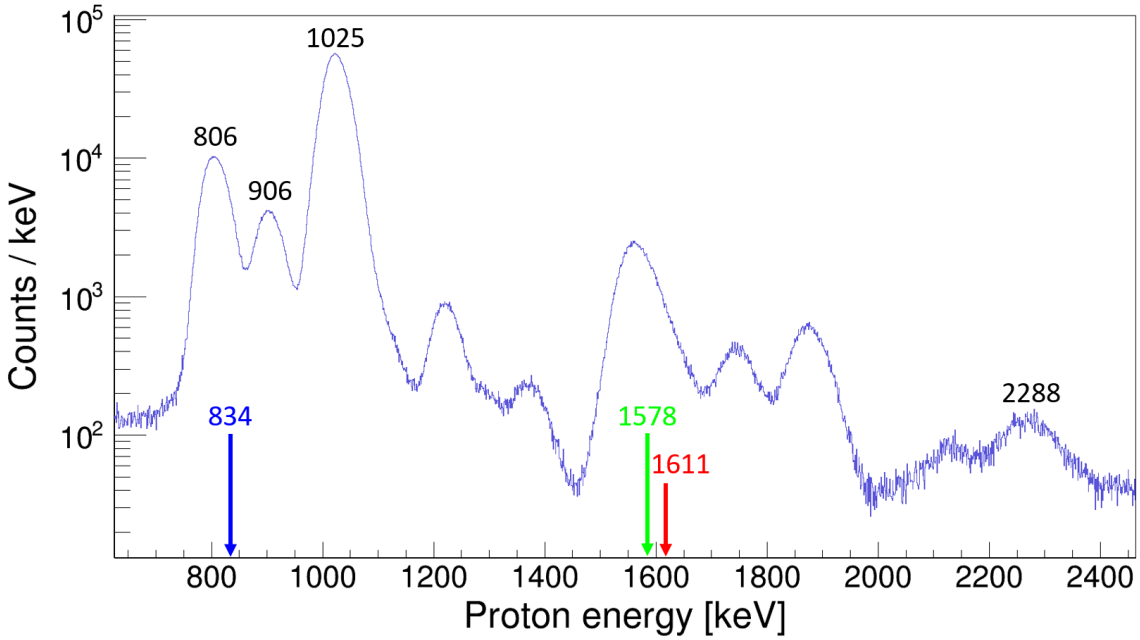

Figure 5.15: All proton peaks used in the combined-pads energy calibration are color-coded by the ^{30}P levels their transitions populate directly. Visible singles peaks corresponding to ground state transitions (black) and weaker transitions to excited states (colored) are labeled by their center-of-mass decay energies in units of keV.

applied a revised fit to the modes of the distributions modeling each of these seven peaks. Figure 5.16 shows that the Proton Detector is a good example of a proportional counter, since a linear function fits the data extremely well over the energy range 0.8 – 2.3 MeV. We utilized this function to calibrate all β-delayed proton decays observed in this experiment, and all future references to proton energies in this document reflect this calibration. This application to the combined-pads spectrum in the case of the low-energy proton peak corresponding to the astrophysically important $J^\pi = 3/2^+$ resonance results in a decay energy of $E_r = 258(3)$ keV, which brings us into near-perfect agreement with Ref. [121]. Furthermore, using Equation 5.5, we computed excitation energies for the proton-emitting levels in ^{31}S that would correspond to our observed β-delayed proton decays. In almost all cases, our expected excitation energies are consistent with the evaluated level energies of previously observed excited states, as tabulated in NuDat to within their uncertainties. In the few instances for which this is not the case, newly proposed β-delayed proton decays are very weak, and their status should be considered tentative.

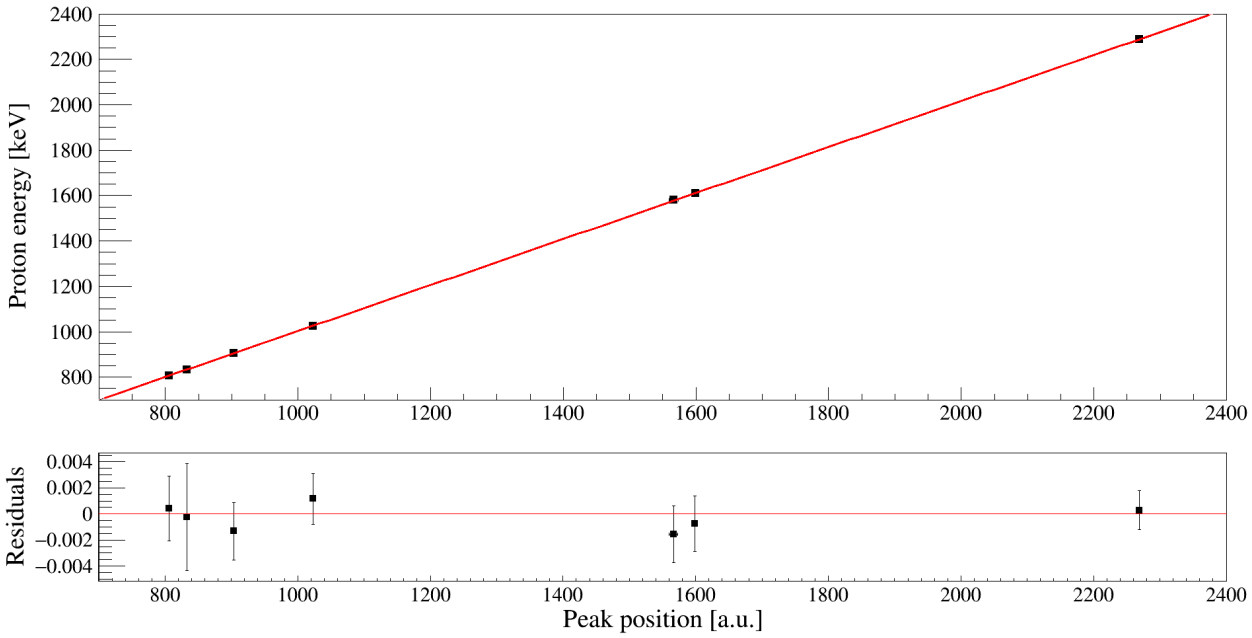

Figure 5.16: Linear energy calibration function mapping the peak position in the combined-pads spectrum to proton decay energy. The peak positions are determined by the mode of EMG distributions used to fit the data. Fixed points correspond to proton decays of ^{31}S levels with well-known excitation energies.

Constraining Fits Below 1.2 MeV

Figure 5.17 shows one such multi-peak fit over the energy region 575 – 1325 keV. What looks like only four distinct peaks, which have all been previously observed with center-of-mass decay energies 806, 906, 1026, and 1225 keV, actually contains data from over a dozen unique β-delayed proton transitions following ^{31}Cl decay. The γ-gated coincidence spectrum in Figure 5.4 reveals numerous weak proton branches to ^{30}P excited states, including decays with energies of 870, 958, 1066, 1138, 1224, and 1318 keV. We determined that of these transitions, the three highest-energy proton decays actually populated the four excited state of ^{30}P, since they can are observed in coincidence with both 1973- and 1265-keV γ rays, as shown in Figs. 5.8 and 5.7, respectively. The other three, lower-energy proton peaks, which are buried under the most prominent features in the singles spectrum, are attributed to β-delayed proton transitions to the 709-keV level of ^{30}P.

The background-subtracted proton spectra in coincidence with γ ray transitions from the third excited state of ^{30}P, as shown in Figures 5.5 and 5.6, reveal three additional β-delayed proton

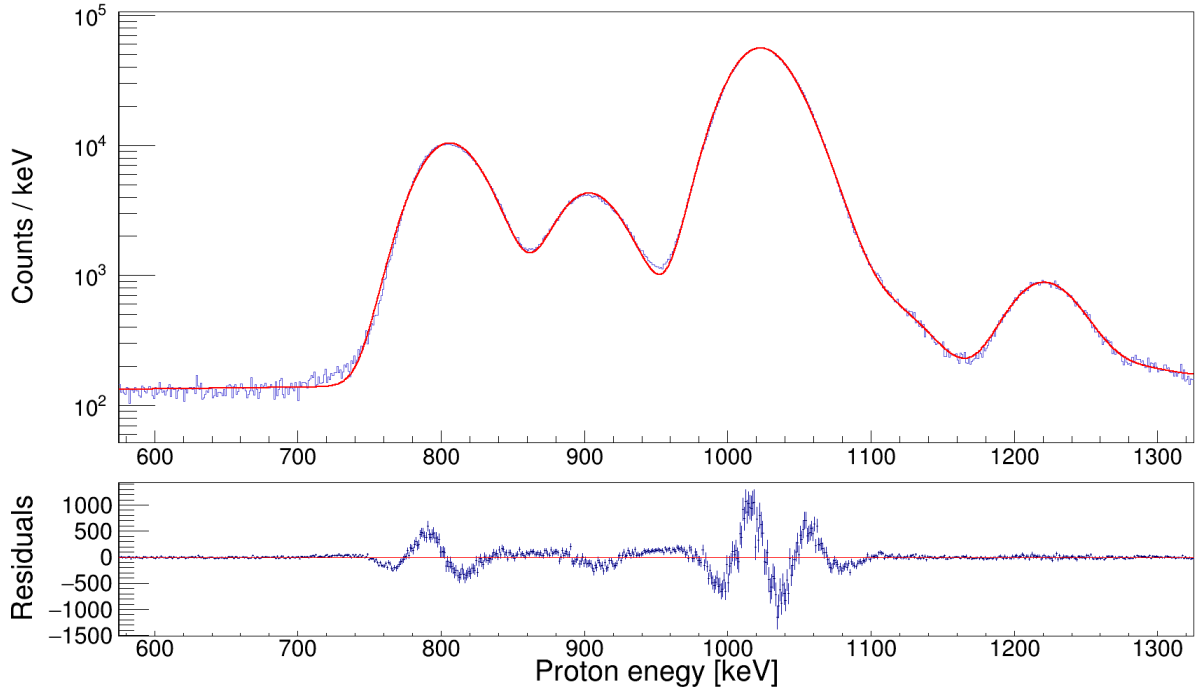

Figure 5.17: Fit of the cumulative proton spectrum over 575 – 1325 keV, including 11 EMG distributions and a linear background model. The positions of proton peaks corresponding to decay energies of 834, 869, 958, 973, and 1066 keV have all been fixed, along with their efficiency-corrected fit integrals from the background-subtracted, γ-gated coincidence spectra. The energies and intensities of the stronger proton branches are allowed to vary as free parameters, allowing us to quantify the uncertainty associated with fixing the intensities of smaller peaks.

emissions populating the 1454-keV level within the same region of the cumulative proton spectrum, which correspond to center-of-mass energies of 834, 973, and 1229 keV. Since these decays are relatively close in energy to the aforementioned weak, β-delayed protons, we considered the possibility that these were, in fact, the same transitions, populating a single ^{30}P state of relatively high excitation energy, which would result in real coincidences between these protons with γ rays of several different energies. However, we could not find any evidence of this aside from the 1138-, 1224-, and 1318-keV decays to the ^{30}P level at 1973 keV, as discussed previously. This was verified by ruling out several different potential scenarios.

First, no γ rays were observed from transitions of ^{30}P levels above excitation energies of 1973 keV. This implies that all β-delayed proton decays in our data must populate either the ground state or one of the first four excited states in ^{30}P, whose γ cascade has already been well-established

[169; 170; 171; 172]. Second, if the 834/870-keV, 958/973-keV, and 1224/1229-keV protons really correspond to the same transitions, then we should expect the number of counts observed in the coincidence spectrum to be consistent, after correcting for γ detection efficiency. The 1454-keV level in ^{30}P primarily γ decays to the ground state, but about 5% of the time, it decays to the second excited state via emission of a 746-keV γ ray. Thus, 834/870-keV and 958/973-keV protons in coincidence with 1454-keV γ rays should be 19 times more common than the same protons in coincidence with 709-keV γ rays, if they represent the same proton decays. However, the ratios between the efficiency-corrected counts are closer to ≈ 3 and ≈ 7, respectively.

If these ratios were approximately equivalent, we could not rule out the possibility that this discrepancy reflects systematic uncertainties in our background subtraction method or γ detection efficiency, but the fact that these ratios differ by more than a factor of 2 suggests they should be understood as unique transitions. Thus, in all of our cumulative spectrum over the energy range $\approx 500 - 1400$ keV, we fix both the positions and efficiency-corrected counts of these weak, β-delayed proton decays at energies 834, 869, 958, 973, and 1066 keV. Conversely, in all cases, the peak positions and amplitudes of the three strongest β-delayed proton decays in the spectrum are allowed to be free parameters, since the fitter should be able to reasonably determine this information with our newly applied constraints. As in the case of previous fits, we generally assumed a linear background model but tested other polynomials and functional forms as well. Peak widths were constrained to be a linear function of energy across the fit range.

For protons decays above 1.1 MeV in energy, we tried many fits, constraining and relaxing the positions and intensities of all peaks in various combinations. The difference between the expected number of efficiency-corrected counts in the 1138-keV peak, as determined from the coincidence spectra in Figures 5.7 and 5.8, and the integral of cumulative spectrum's best fit, for which the distribution's area and centroid are constrained as shown Figure 5.17, yields an estimate of the systematic uncertainty associated with using our γ efficiency to evaluate the weak, β-delayed proton intensities in this region. In this case, the expected number of efficiency-corrected, 1138-keV protons only account for $\approx$ 70% of the statistics in the total, combined spectrum, but fixing the

position of this peak in our cumulative spectrum fit improves our agreement to ≈ 80%. The multiple proton contributions to what visually appears to be a single peak at 1.2 MeV were neglected in Figure 5.17, and for the purposes of getting a reasonable χ^2 value for such a highly parameterized fit, the position and intensity of this feature, as well as the much smaller 1318-keV peak, were allowed to vary freely in most instances when fitting across the energy region below 1.4 MeV.

Constraining Fits Between 1.2 and 1.4 MeV

As was the case for distinguishing the 834/870- and 958/973-keV, a similar argument can be made for disentangling the multiple β-delayed proton contributions to the substantial peak at 1.2 MeV. Protons at 1138, 1224, and 1319 keV are clearly in coincidence with the 709-, 1973-, and 1265-keV γ rays. The simplest explanation for this is that these proton decays populate the 1973-keV state of ^{30}P, which promptly decays to either the 709-keV level or the ground state. There are no known γ transitions from either the fourth or third excited states to the first excited state, which means the 1218-keV protons in coincidence with the 677-keV γ rays in Figure 5.3 must be populating this ^{30}P level directly. Furthermore, only a weak, tentative, 519-keV γ branch between the fourth and third excited states has been proposed [169], and this cannot explain why there are more 1229-keV protons in coincidence with 1454-keV γ rays than with the combined statistics of 1265- and 1973-keV γ coincidences. Thus, the most reasonable conclusion is that three distinct 1.2-MeV proton transitions populate the first, third, and fourth excited states of ^{30}P.

Within the energy region that spans 1.2 – 1.4 MeV, shown in Figure 5.18, the β-delayed proton spectrum contains two more distinct features. There appears to be some visible structure near 1.3 MeV in the cumulative spectrum, but the presence of a clear proton peak at 1319 keV only becomes obvious when analyzing the coincidence spectra involving deexcitations from the fourth excited state of ^{30}P, as previously mentioned. The much more prominent peak near 1.4 MeV has been reported by Ref. [118] but was assumed to populate the ground state. However, protons in coincidence with 1454- and 746-keV γ rays reveal that at least some of this peak's amplitude must originate from 1381-keV decays that populate the third excited state of ^{30}P. Just as we analyzed

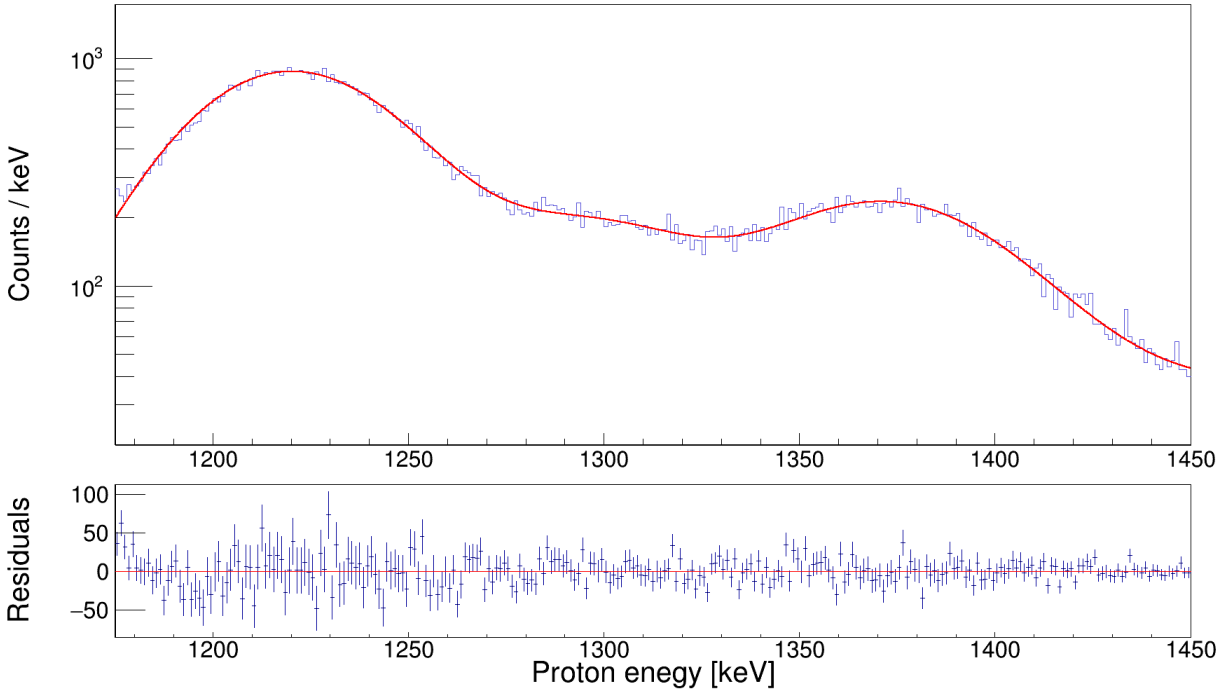

Figure 5.18: Fit of the cumulative proton spectrum over 1175 – 1450 keV, including five EMG distributions and a linear background model. The positions of proton peaks corresponding to decay energies of 1217, 1224, and 1229 keV have all been fixed, along with their efficiency-corrected fit integrals of the background-subtracted, γ-gated coincidence spectra. The positions and intensities of the 1318- and 1381-keV proton decays are allowed to vary freely and converge well with observations in the coincidence spectra.

the cumulative proton spectrum for energies below 1.2 MeV, we constrained our model of the data using the information we extracted from the proton-γ coincidence spectra in order to fit this energy region between 1.2 and 1.4 MeV.

It is possible that, in addition to decays to excited states, β-delayed protons that populate the ground state of ^{30}P could be contributing to the large peaks at 1.2 and 1.4 MeV as well. In order to estimate the possible size of this effect, we first assumed only a three-peak model, fixing only the position of a single EMG distribution for the 1.3-MeV peak, allowing the fitter to determine the energies and intensities of much larger features and assuming, just as in the previous fit range, that all decay events near 1.2 MeV can be considered part of a single proton peak. Again, we constrained the peak widths to be linear as a function of decay energy, our skew parameter to be constant, and the background beneath the peaks to be linear as well. The areas of the loosely

constrained three-peak fit could then be compared to the efficiency-corrected fit integrals of the background-subtracted, γ-gated proton peaks. In this case, the expected counts calculated using our numbers for the SeGA efficiency actually overpredicted the total number of events by factors of $\approx 1.16 - 1.26$ for the 1.2-MeV peak, $\approx 1.66 - 1.76$ for the 1.3-MeV peak, and $\approx 1.16 - 1.36$ for the 1.4-MeV peak. Fixing the position of the highest-energy peak to a 1381-keV decay energy erased the discrepancy between the two counting methods to within statistical uncertainty for 1319-keV proton decays and reduced the overcounting factors for the 1.2- and 1.4-MeV peaks to $\approx 1.09 - 1.18$ and $\approx 1.15 - 1.25$, respectively. Thus, we can reasonably say that there is no need to invoke ground-state transitions to explain the structure of this region in the proton spectrum.

Adjusting the fit range for the three-peak model, while varying which parameters were fixed or free, enabled us to assess the systematic effect of our background model on the uncertainty in our peak integrals. Furthermore, we introduced a five-peak fit, as shown in Figure 5.18, where the positions and intensities of the 1218-, 1224-, and 1229-keV peaks are fixed, to ensure that our model is able to accurately reproduce the data for the large composite peak at 1.2 MeV. This fit agrees well with the data over the region where the response function's parameters are heavily constrained, and it is able to reproduce the energy to within 1 keV, as well as the peak area to within 1% of the γ-gated, efficiency-corrected proton counts at 1381-keV. Its assignment of the peak position and integral to the more ambiguous region between the two larger features still agrees with our predictions to within 10 keV and 50%, respectively. This gives us good confidence in our response function as a reasonably accurate model of the data as well as in the quality of our efficiency calibration and our ability to use it for evaluating the weak, β-delayed protons intensities.

Constraining Fits Between 1.5 and 2 MeV

Continuing to move across the cumulative decay spectrum, we encounter a region with what appears to be three, broad proton peaks peaks between 1.5 and 2 MeV, shown in Figure 5.19. Again, upon inspection of the proton-γ coincidence spectra, we see that there are many underlying peaks that correspond to proton emissions populating excited states in ^{30}P, some of which are quite intense,

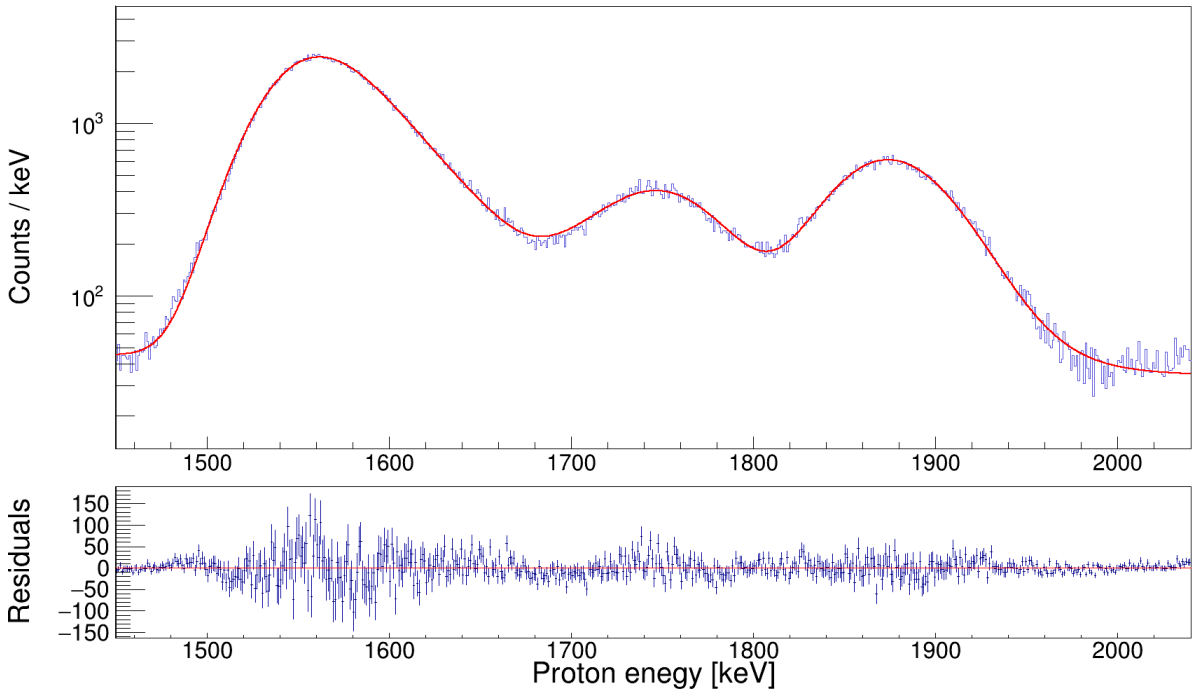

Figure 5.19: Fit of the cumulative proton spectrum over 1450 – 2050 keV, including 10 EMG distributions and a linear background model. The positions of proton peaks corresponding to decay energies of 1577, 1610, 1653, 1717, 1827, 1864, and 1872 keV have all been fixed, along with their efficiency-corrected fit integrals of the background-subtracted, γ-gated coincidence spectra. The positions and intensities of the 1574-, 1759-, and 1889-keV proton decays are allowed to vary freely, and their energies are in good agreement with previous measurements.

while others are very small. By far, the two strongest of these β-delayed proton decays populate the first and second excited states with center-of-mass energies of 1610 and 1577 keV, respectively. At first glance, it might appear that a combination of these two proton decays alone might account for the singular, massive peak visible in this region of the proton spectrum. However, after dividing the number of counts in the γ-gated proton spectra by the 677- and 709-keV γ detection efficiencies, respectively, fixing their positions in the energy spectrum along with their total peak areas, and applying the multi-peak fit as seen in Figure 5.19, we find that the combined intensity of both of these decays is still about a factor of 50 too small to account for the rest of the protons in this peak. Thus, we must conclude, that there is indeed a ground-state proton transition at 1574 keV, which agrees with the previously reported decay energy [114; 115; 116; 173; 117; 118].

In fact, contrary to the previous spectral region we considered, none of the three biggest peaks

between 1.5 and 2 MeV are primarily composed of proton decay events populating excited states. This makes fitting the spectrum over this energy range relatively straightforward. We can simply fix the energies and intensities of the weaker, excited-state transitions, add in literature values for the ground-state proton decays while letting the exact positions and integrals of their peaks remain free parameters before fitting. As always, we constrain our peak shapes to vary smoothly with energy and apply a linear model to our background, which is much more well-behaved at higher energies and, coupled with the lower statistics, makes fitting the data significantly easier. Finally, just as before, small branches close together in energy, such the 1864- and 1872-keV protons, should not be considered the same decay, as they populate different excited states with no known γ transitions between these ^{30}P levels.

Constraining Fits Above 2 MeV

With increasing excitation energy, fewer states are intensely populated by β^+ decay, as expected due to the energy dependence of the phase-space factor. This is reflected generally by decreasing intensities for ^{31}Cl β-delayed proton decays above 2 MeV, as observed in past measurements. This trend can also be seen in our data and is exacerbated by the strong energy-dependence of the Proton Detector's efficiency, as shown in Figure 4.13. However, while the statistics in this relatively high-energy regime are low, we still are able to observe some structure and evidence of a previously unobserved proton transitions. In coincidence with the 677-keV γ rays, we can clearly identify proton events at 2146 keV. This energy is consistent within the uncertainties of the evaluated literature energies that assume a ground-state transition. For the sake of simplicity, one would be inclined to think that the proton peak we observe in the cumulative spectrum is composed entirely of β-delayed proton events that populate the first excited state of ^{30}P. The fit shown in Figure 5.20 is constrained such that the integral of this peak is fixed to the intensity observed in the γ-gated coincidence spectrum, scaled by SeGA's efficiency at 677 keV. However, if we relax this parameter, the χ^2-minimizing fitter prefers a peak amplitude roughly twice the size. Thus, we cannot currently rule out the possibility of multiple nearby proton peaks, especially since Ref.

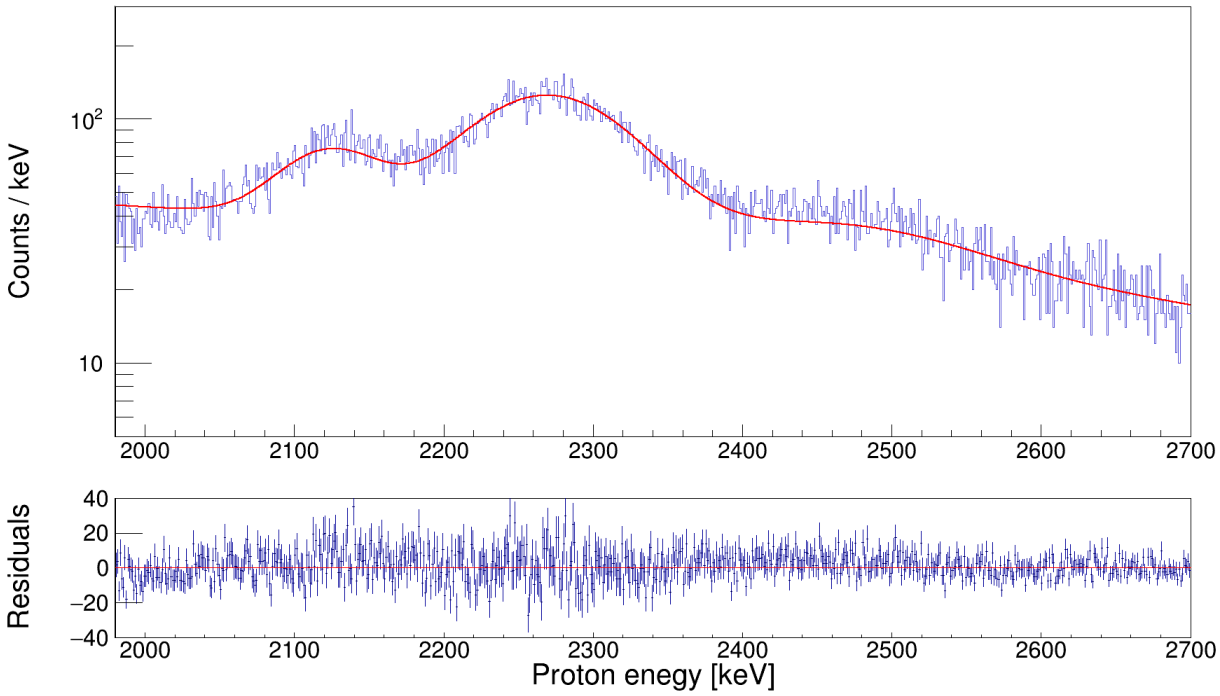

Figure 5.20: Fit of the cumulative proton spectrum over 1980 – 2700 keV, including three EMG distributions and a linear background model. The positions of proton peaks corresponding to decay energies of 2146 and 2494 keV have all been fixed, along with their efficiency-corrected fit integrals of the background-subtracted, γ-gated coincidence spectra. The positions and intensities of the 2494-keV proton decays are allowed to vary freely.

[102] reports the existence of a 8268-keV level, which is close to the excitation energy needed for a state which proton decays to the ground state of ^{30}P.

We identified the strongest β-delayed proton decay in this region to occur at 2290 keV, which is close to previously reported decay energies for this ground-state transition. When applying a variety of different constraints on the smaller peaks nearby, we allowed the peak position and area to vary as free parameters. However, despite large changes in the relative intensities of other features within the fit range, the number of counts in the 2290-keV peak varied by less than 4% over all cases. Because any proton peaks in this region will be quite broad, there is substantial overlap between nearby distributions, and relatively small changes in the amplitude of a large peak will have a disproportionately large effect on the relative intensities of smaller peaks in the vicinity.

For this reason, we are unable to conclusively identify the presence of a 2.4-MeV proton peak, reportedly observed in both Ref. [117; 118]. Based on its quoted intensity and our simulation

results for the Proton Detector efficiency at this energy, we would expect to find a distribution with an area ≈ 3.4 times smaller than that of the neighboring 2290-keV peak. When we attempt to enforce this condition on the fitter, we substantially overpredict the data within the energy range we expect to find the peak. When we relax the areal parameter of this distribution, the fitter determines that the ratio of their magnitudes should be at least $\gtrsim 9$. The relatively low statistics of this region of the spectrum and the many degrees of freedom for multi-peak distributions that are not well-constrained leads to overfitting. Therefore, a variety of models return reasonable χ^2 values, and our associated systematic uncertainties associated with with quantifying peaks above 2 MeV are substantially higher than at lower energies.

The last definitive proton peak we were able to identify in our β-delayed proton spectrum has a decay energy of 2494 keV. It was observed in coincidence with the 709-keV γ rays, implying it directly populates the second excited state of ^{30}P. In the proton-γ coincidence spectrum, it appears to be much broader than almost all other peak in our dataset. This could be a result of poor gain matching at such high energies or simply a function of degrading detector resolution with energy, but it is worth noting the relative resolution across most of the energy spectrum is reasonably stable at $4-5\%$. Another possibility is that the corresponding ^{31}S level, reported in Ref. [102], could be intrinsically broad. The peak itself in the cumulative spectrum is barely visible and was not reported in the results of previous β-delayed proton measurements.

At present, we cannot draw any quantitative conclusions about the presence of β-delayed proton decays above 2.5 MeV in our spectrum. This regime appears to consist of a continually declining background with some broad, bumpy regions of excess counts. More careful and detailed analysis is required to provide robust upper limits on β-delayed proton decays that do not constitute obviously identifiable peaks in our energy spectrum.

5.4 Preliminary Results

In the analysis discussed throughout this dissertation, we have demonstrated the capabilities of the GADGET system to measure weak, low-energy, β-delayed, charged-particles decays as well as their γ-ray coincidences with high efficiency and good energy resolution. In this chapter, we

have provided the most detailed description to date of the ^{31}Cl($\beta p\gamma$)^{30}P sequence, and a tentative decay scheme is proposed in Figure 5.21. We report definitive observations of 25 unique ^{31}Cl β-delayed proton decay channels for decay energies below 2.5 MeV, compared to the most recent literature evaluation that lists only 13 over that same energy range [119]. Furthermore, we claim that 19 of these β-delayed proton transitions populate excited states of ^{30}P, none of which have been previously reported in literature or appeared in evaluated nuclear data tables. However, it is worth mentioning the Ref. [118] did tentatively suggest that 1.2-MeV β-delayed protons could populate the third excited state of ^{30}P, and we have confirmed this observation. Preliminary values for all energies and intensities measured during NSCL experiment 17024 are tabulated in Table 5.1.[2]

[2]All excitation energies listed in Table 5.1 are computed from calibrated proton decay energies, which are subject to change. Not all unique level energies listed should be considered distinct and require further evaluation before publication.

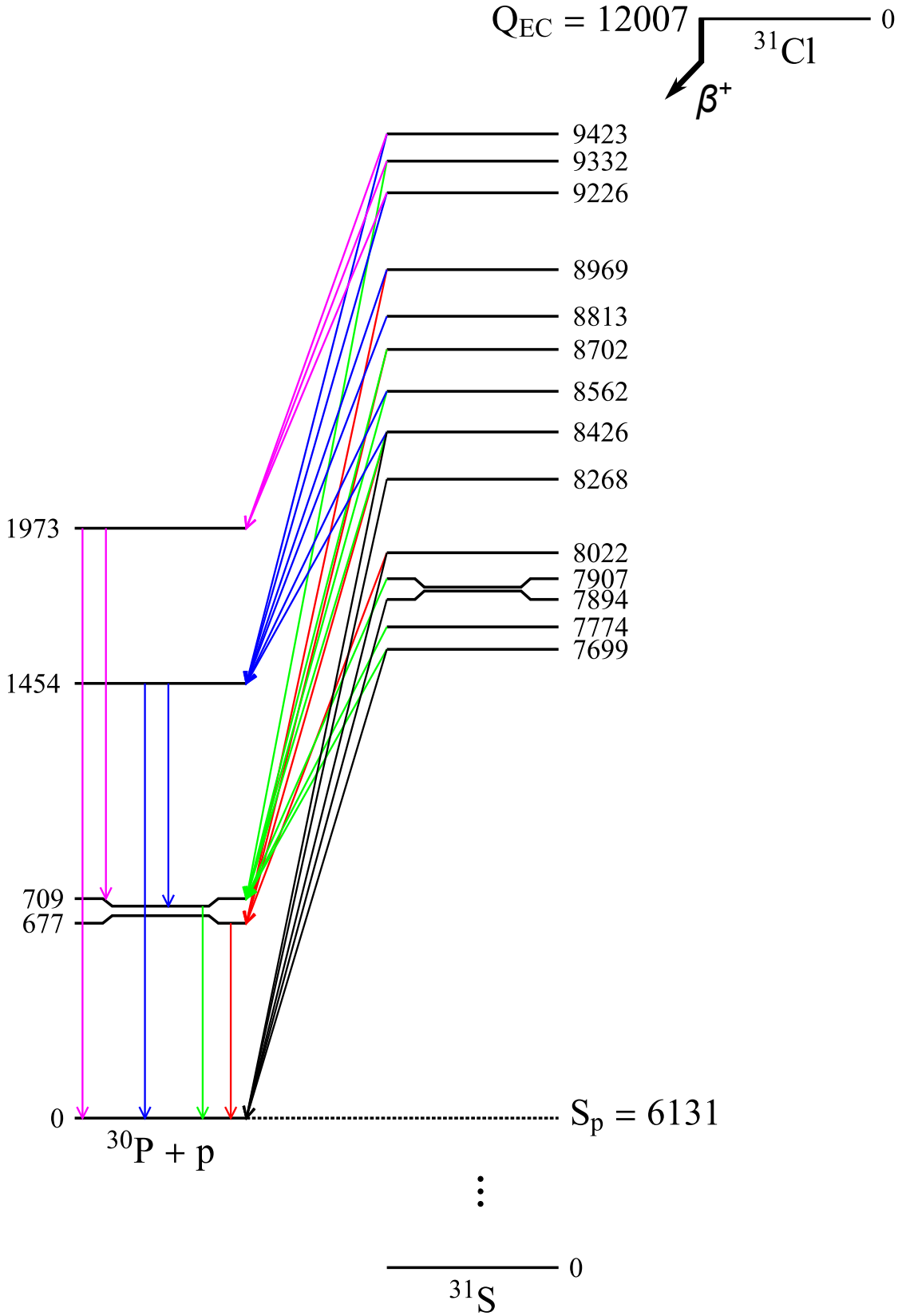

Figure 5.21: Preliminary, partial decay scheme for ^{31}Cl($\beta p\gamma$)^{30}P, including only proton-unbound levels in ^{31}S that can result in a proton decay to a ^{30}P excited state.

E_p(c.m.) [keV]	I_p(rel) [%]	$E_x(^{31}\mathrm{S})$ [keV]	$E_x(^{30}\mathrm{P})$
258(3)	0.069(5)	6389(4)	0
806(2)	15.4(8)	6937(2)	0
834(3)	0.10(1)	8419(3)	1454
870(18)	<0.05	7709(18)	709
906(2)	6.6(4)	7037(2)	0
958(12)	<0.05	7797(12)	709
973(2)	0.33(5)	8558(2)	1454
1025(2)	100(8)	7156(2)	0
1066(8)	0.20(5)	7905(8)	709
1138(4)	0.37(9)	9242(4)	1973
1218(2)	0.25(5)	8025(2)	677
1224(5)	0.31(6)	9328(5)	1973
1229(2)	1.4(3)	8814(2)	1454
1319(8)	0.61(29)	9422(8)	1973
1381(2)	0.68(18)	8966(2)	1454
1574(2)	10.8(20)	7705(2)	0
1580(3)	0.98(20)	8419(3)	709
1611(3)	2.18(45)	8419(3)	677
1653(2)	0.81(18)	9238(3)	1454
1717(3)	0.84(18)	8557(3)	709
1759(2)	2.88(55)	7889(2)	0
1822(6)	0.25(65)	9406(6)	1454
1864(8)	<0.15	8672(8)	677
1872(6)	0.22(6)	8711(6)	709
1889(2)	6.9(12)	8020(2)	0
2146(4)	0.7(6)	8954(4)	677
2148(3)	<0.62	8954(4)	677
2288(3)	4.0(7)	8419(3)	0
2494(7)	1.0(3)	9333(7)	709

Table 5.1: Preliminary energies and intensities of all ^{31}Cl β-delayed proton transitions, including the excited state of origin in the ^{31}S parent and the excited state they populate in the ^{30} daughter nucleus.

CHAPTER 6

CONCLUSIONS AND OUTLOOK

The stated goals outlined in this dissertation have been achieved over the course of this doctoral thesis project. Our primary scientific objective was to constrain the thermonuclear rate of the ^{30}P$(p,\gamma)^{31}$S reaction with the intent of reducing the nuclear physics uncertainties associated with predicting elemental and isotopic abundance ratios in ONe nova ejecta. To do this, we developed the new radiation detection system GADGET specifically to measure weak, low-energy, ^{31}Cl β-delayed proton decays through the crucial $J^\pi = 3/2^+$, 6390-keV excited state of ^{31}S. We successfully measured the proton branching ratio Γ_p/Γ of this particular resonance. Combining our experimental result with shell-model calculations for the γ decay partial width Γ_γ of this level along with past work on other resonances, we calculated the thermonuclear rate for proton capture on ^{30}P over peak nova temperatures. In agreement with our original hypothesis, we demonstrated that the contribution from this 260-keV, $\ell = 0$ resonance dominates the total rate.

Our new, recommended rate was utilized in state-of-the-art hydrodynamic simulations of classical nova explosions for a 1.35-$M_\odot$ ONe white dwarf, and we compared the results of these calculations to observed elemental abundances in the ejected shells of the V838 Herculis nova. We found our results to be in agreement with the measured O:S and S:Al ratios, and we have constrained these nuclear thermometers for ONe novae at a peak temperature of $T = 0.31$ GK. We also compared the nova model predictions to measured isotopic ratios of presolar grains hypothesized to originate in classical novae. The results of the simulations were not able to reproduce the observed isotopic ratios, but our constrained rate for the ^{30}P$(p,\gamma)^{31}$S reaction substantially reduced uncertainties in the expected ^{30}Si:^{28}Si ratio for ONe nova ejecta.

In addition, we determined that our measurement of ^{31}Cl β-delayed proton decay through the resonance of interest represents the weakest β-delayed charged-particle decay ever reported for resonances below 400 keV. Furthermore, we tentatively claim to observe a dozen new ^{31}Cl β-delayed proton decay channels and demonstrate conclusively for the first time that many of these

transitions populate excited states of ^{30}P. We have also constructed a preliminary decay scheme for $^{31}\mathrm{Cl}(\beta p\gamma)^{30}\mathrm{P}$.

Our future goals related to this work include finalizing the analysis of the decay $^{31}\mathrm{Cl}(\beta p\gamma)^{30}\mathrm{P}$. Aside from this, we would also like to constrain the lifetime of the $J^\pi = 3/2^+$, 6390-keV excited state of ^{31}S, since this is the largest remaining source of uncertainty in our resonance strength as well as the last missing piece of experimental information for this nuclear level. A Doppler shift lifetime experiment has been planned for this measurement. In addition, the GADGET system as been upgraded to Phase II and is now fully operational as a time projection chamber. We also have plans to measure the decay $^{20}\mathrm{Mg}(\beta p\alpha)^{15}\mathrm{O}$ in order to constrain the $^{15}\mathrm{O}(\alpha,\gamma)^{19}\mathrm{Ne}$ reaction in explosive He-burning for modeling type I X-ray bursts.

BIBLIOGRAPHY

[1] B. A. Brown, "Lecture Notes in Nuclear Structure Physics," 2018.

[2] A. Beiser, *Concepts of Modern Physics*. McGraw-Hill, 6 ed., 2003.

[3] W. C. Martin and W. L. Wiese, *Atomic, Molecular, and Optical Physics Handbook*. AIP Press, 1996.

[4] B. Ryden, *Introduction to Cosmology*. Cambridge University Press, 2 ed., 2017.

[5] A. T. Yue, M. S. Dewey, D. M. Gilliam, G. L. Greene, A. B. Laptev, J. S. Nico, W. M. Snow, and F. E. Wietfeldt, "Improved determination of the neutron lifetime," *Phys. Rev. Lett.*, vol. 111, p. 222501, 2013.

[6] R. W. Pattie, N. B. Callahan, C. Cude-Woods, E. R. Adamek, L. J. Broussard, S. M. Clayton, S. A. Currie, E. B. Dees, X. Ding, E. M. Engel, D. E. Fellers, W. Fox, P. Geltenbort, K. P. Hickerson, M. A. Hoffbauer, A. T. Holley, A. Komives, C.-Y. Liu, S. W. T. MacDonald, M. Makela, C. L. Morris, J. D. Ortiz, J. Ramsey, D. J. Salvat, A. Saunders, S. J. Seestrom, E. I. Sharapov, S. K. Sjue, Z. Tang, J. Vanderwerp, B. Vogelaar, P. L. Walstrom, Z. Wang, W. Wei, H. L. Weaver, J. W. Wexler, T. L. Womack, A. R. Young, and B. A. Zeck, "Measurement of the neutron lifetime using a magneto-gravitational trap and in situ detection," *Science*, vol. 360, no. 6389, pp. 627–632, 2018.

[7] M. Asplund, N. Grevesse, A. J. Sauval, and P. Scott, "The chemical composition of the sun," *Annual Review of Astronomy and Astrophysics*, vol. 47, no. 1, pp. 481–522, 2009.

[8] F. Calura and F. Matteucci, "Cosmic metal production and the mean metallicity of the universe," *Monthly Notices of the Royal Astronomical Society*, vol. 350, no. 1, pp. 351–364, 2004.

[9] J. A. Johnson, "Populating the periodic table: Nucleosynthesis of the elements," *Science*, vol. 363, no. 6426, pp. 474–478, 2019.

[10] V. T. C. J. Hansen, S. D. Kawaler, *Stellar Interiors: Physical Principles, Structure, and Evolution*. Springer, 2 ed., 2004.

[11] M. Limongi and A. Chieffi, "Presupernova evolution and explosive nucleosynthesis of zero metal massive stars," *The Astrophysical Journal Supplement Series*, vol. 199, no. 2, p. 38, 2012.

[12] H. A. Bethe, "Energy production in stars," *Phys. Rev.*, vol. 55, pp. 434–456, 1939.

[13] J. Choi, A. Dotter, C. Conroy, M. Cantiello, B. Paxton, and B. D. Johnson, "MESA Isochrones

and Stellar Tracks (MIST). I: Solar-Scaled Models," *The Astrophysical Journal*, vol. 823, no. 2, p. 102, 2016.

[14] D. D. Clayton, *Principles of stellar evolution and nucleosynthesis*. 1983.

[15] C. Iliadis, *Nuclear Physics of Stars*. Verlag, Wenheim, Germany: Wiley-VCH, 2 ed., 2007.

[16] M. Wang, W. Huang, F. Kondev, G. Audi, and S. Naimi, "The AME 2020 atomic mass evaluation (II). Tables, graphs and references*," *Chinese Physics C*, vol. 45, no. 3, p. 030003, 2021.

[17] T. Sukhbold, S. E. Woosley, and A. Heger, "A high-resolution study of presupernova core structure," *The Astrophysical Journal*, vol. 860, no. 2, p. 93, 2018.

[18] H.-T. Janka, "Explosion mechanisms of core-collapse supernovae," *Annual Review of Nuclear and Particle Science*, vol. 62, no. 1, pp. 407–451, 2012.

[19] S. M. Couch, "The mechanism(s) of core-collapse supernovae," *Philosophical Transactions of the Royal Society A: Mathematical, Physical and Engineering Sciences*, vol. 375, no. 2105, p. 20160271, 2017.

[20] D. Vartanyan, A. Burrows, D. Radice, M. A. Skinner, and J. Dolence, "A successful 3D core-collapse supernova explosion model," *Monthly Notices of the Royal Astronomical Society*, vol. 482, no. 1, pp. 351–369, 2018.

[21] S. E. Woosley and T. A. Weaver, "The Evolution and Explosion of Massive Stars. II. Explosive Hydrodynamics and Nucleosynthesis," *The Astrophysical Journal Supplement Series*, vol. 101, p. 181, 1995.

[22] D. V. A. Burrows, "Core-collapse supernova explosion theory," *Nature*, vol. 589, pp. 29–39, 2021.

[23] R. M. Wald, *General Relativity*. University of Chicago Press, 1984.

[24] T. Sukhbold, T. Ertl, S. E. Woosley, J. M. Brown, and H.-T. Janka, "Core-Collapse Supernovae from 9 to 120 Solar Masses Based on Neutrino-powered Explosions," *The Astrophysical Journal*, vol. 821, no. 1, p. 38, 2016.

[25] A. I. Karakas and J. C. Lattanzio, "The Dawes Review 2: Nucleosynthesis and Stellar Yields of Low- and Intermediate-Mass Single Stars," *Publications of the Astronomical Society of Australia*, vol. 31, p. e030, 2014.

[26] F. Käppeler, R. Gallino, S. Bisterzo, and W. Aoki, "The *s* process: Nuclear physics, stellar models, and observations," *Rev. Mod. Phys.*, vol. 83, pp. 157–193, 2011.

[27] J. S. Gallagher and S. Starrfield, "Theory and observations of classical novae," *Annual Review of Astronomy and Astrophysics*, vol. 16, no. 1, pp. 171–214, 1978.

[28] D. Prialnik and A. Kovetz, "An Extended Grid of Multicycle Nova Evolution Models," *The Astrophysical Journal*, vol. 445, p. 789, 1995.

[29] S. Starrfield, J. W. Truran, W. M. Sparks, and G. S. Kutter, "CNO Abundances and Hydrodynamic Models of the Nova Outburst," *The Astrophysical Journal*, vol. 176, p. 169, 1972.

[30] D. M. Townsley and L. Bildsten, "Theoretical modeling of the thermal state of accreting white dwarfs undergoing classical nova cycles," *The Astrophysical Journal*, vol. 600, no. 1, pp. 390–403, 2004.

[31] L. Chomiuk, B. D. Metzger, and K. J. Shen, "New insights into classical novae," *Annual Review of Astronomy and Astrophysics*, vol. 59, no. 1, pp. 391–444, 2021.

[32] C. Payne-Gaposchkin, *The Galactic Novae*. North Holland Publishing, 1957.

[33] I. Gallagher, J. S. and A. D. Code, "Ultraviolet photometry from the Orbiting Astronomical Observatory. X. Nova FH Serpentis 1970," *The Astrophysical Journal*, vol. 189, pp. 303–314, 1974.

[34] P. Kahabka and E. P. J. van den Heuvel, "Luminous Supersoft X-ray Sources," *Annual Review of Astronomy and Astrophysics*, vol. 35, no. 1, pp. 69–100, 1997.

[35] R. D. Gehrz, "The infrared temporal development of classical novae," *Annual Review of Astronomy and Astrophysics*, vol. 26, no. 1, pp. 377–412, 1988.

[36] L. A. Helton, C. E. Woodward, F. M. Walter, K. Vanlandingham, G. J. Schwarz, A. Evans, J.-U. Ness, T. R. Geballe, R. D. Gehrz, M. Greenhouse, J. Krautter, W. Liller, D. K. Lynch, R. J. Rudy, S. N. Shore, S. Starrfield, and J. Truran, "The Dusty Nova V1065 Centauri (Nova Cen 2007): a Spectroscopic Analysis of Abundances and Dust Properties," *The Astronomical Journal*, vol. 140, no. 5, pp. 1347–1369, 2010.

[37] K. Degioia-Eastwood, J. A. Hackwell, G. L. Grasdalen, and R. D. Gehrz, "A correlation between infrared excess and period for Mira variables," *The Astrophysical Journal Letters*, vol. 245, pp. L75–L78, 1981.

[38] P. Ruiz-Lapuente, "Tycho Brahe's Supernova: Light from Centuries Past," *The Astrophysical Journal*, vol. 612, no. 1, pp. 357–363, 2004.

[39] M. J. Darnley, M. F. Bode, E. Kerins, A. M. Newsam, J. An, P. Baillon, V. Belokurov, S. C. Novati, B. J. Carr, M. Crézé, N. W. Evans, Y. Giraud-Héraud, A. Gould, P. Hewett, P. Jetzer, J. Kaplan, S. Paulin-Henriksson, S. J. Smartt, Y. Tsapras, and M. Weston, "Classical novae

from the POINT–AGAPE microlensing survey of M31 – II. Rate and statistical characteristics of the nova population," *Monthly Notices of the Royal Astronomical Society*, vol. 369, no. 1, pp. 257–271, 2006.

[40] A. W. Shafter, "The Galactic Nova Rate Revisited," *The Astrophysical Journal*, vol. 834, no. 2, p. 196, 2017.

[41] P. Newman, "Koji's List of Recent Galactic Novae: Now in Reverse Chronological Order," 2022. https://asd.gsfc.nasa.gov/Koji.Mukai/novae/novae.html.

[42] A. Kawash, L. Chomiuk, J. Strader, K. V. Sokolovsky, E. Aydi, C. S. Kochanek, K. Z. Stanek, Z. Kostrzewa-Rutkowska, S. T. Hodgkin, K. Mukai, B. Shappee, T. Jayasinghe, M. R. Smith, T. W.-S. Holoien, J. L. Prieto, and T. A. Thompson, "The Galactic Nova Rate: Estimates from the ASAS-SN and Gaia Surveys," *The Astrophysical Journal*, vol. 937, no. 2, p. 64, 2022.

[43] T. M. Belloni, M. Méndez, and C. Zhang, "Timing Neutron Stars: Pulsations, Oscillations and Explosions," *Astrophysics and Space Science Library*, vol. 461, 2021.

[44] R. D. Gehrz, J. W. Truran, R. E. Williams, and S. Starrfield, "Nucleosynthesis in Classical Novae and Its Contribution to the Interstellar Medium," *Astronomical Society of the Pacific*, vol. 110, no. 743, pp. 3–26, 1998.

[45] S. Starrfield, J. W. Truran, W. M. Sparks, and M. Arnould, "On ^{7}Li production in nova explosions.," *The Astrophysical Journal*, vol. 222, pp. 600–603, 1978.

[46] M. Hernanz, J. José, A. Coc, and J. Isern, "On the Synthesis of ^{7}Li and ^{7}Be in Novae," *The Astrophysical Journal Letters*, vol. 465, p. L27, 1996.

[47] W. M. Sparks and G. S. Kutter, "Studies of Hydrodynamic Events in Stellar Evolution. II. Dynamic Instabilities in Stellar Envelopes," *The Astrophysical Journal*, vol. 175, p. 707, 1972.

[48] D. Prialnik, "The Evolution of a Classical Nova Model through a Complete Cycle," *The Astrophysical Journal*, vol. 310, p. 222, 1986.

[49] M. Politano, S. Starrfield, J. Truran, A. Weiss, and W. Sparks, "Hydrodynamic studies of accretion onto massive white dwarfs: ONeMg-enriched nova outbursts. I. Dependence on white dwarf mass," *The Astrophysical Journal*, vol. 448, p. 807, 1995.

[50] A. Kovetz and D. Prialnik, "The composition of nova ejecta from multicycle evolution models," *The Astrophysical Journal*, vol. 477, no. 1, pp. 356–367, 1997.

[51] S. Starrfield, J. Truran, M. Wiescher, and W. Sparks, "Nova nucleosynthesis," *Nuclear Physics A*, vol. 621, no. 1, pp. 495–498, 1997.

[52] J. José and M. Hernanz, "Nucleosynthesis in classical novae: CO versus ONe white dwarfs," *The Astrophysical Journal*, vol. 494, no. 2, pp. 680–690, 1998.

[53] A. Weiss and J. W. Truran, "Na-22 and Al-26 production and nucleosynthesis in novae explosions," *Astronomy & Astrophysics*, vol. 238, no. 1-2, pp. 178–186, 1990.

[54] I. Nofar, G. Shaviv, and S. Starrfield, "The Formation of ^{26}Al Nova Explosions," *The Astrophysical Journal*, vol. 369, p. 440, 1991.

[55] A. Coc, R. Mochkovitch, Y. Oberto, J. P. Thibaud, and E. Vangioni-Flam, "ONeMg novae: nuclear uncertainties on the ^{26}Al and ^{22}22Na yields," *Astronomy & Astrophysics*, vol. 299, p. 479, 1995.

[56] J. José, M. Hernanz, and A. Coc, "New Results on ^{26}Al Production in Classical Novae," *The Astrophysical Journal*, vol. 479, no. 1, pp. L55–L58, 1997.

[57] M. B. Bennett, C. Wrede, K. A. Chipps, J. José, S. N. Liddick, M. Santia, A. Bowe, A. A. Chen, N. Cooper, D. Irvine, E. McNeice, F. Montes, F. Naqvi, R. Ortez, S. D. Pain, J. Pereira, C. Prokop, J. Quaglia, S. J. Quinn, S. B. Schwartz, S. Shanab, A. Simon, A. Spyrou, and E. Thiagalingam, "Classical-Nova Contribution to the Milky Way's ^{26}Al Abundance: Exit Channel of the Key ^{25}Al$(p,\gamma)^{26}$Si Resonance," *Physical Review Letters*, vol. 111, p. 232503, 2013.

[58] M. Friedman, T. Budner, D. Pérez-Loureiro, E. Pollacco, C. Wrede, J. José, B. A. Brown, M. Cortesi, C. Fry, B. Glassman, J. Heideman, M. Janasik, M. Roosa, J. Stomps, J. Surbrook, and P. Tiwari, "Low-energy ^{23}Al β-delayed proton decay and ^{22}Na destruction in novae," *Phys. Rev. C*, vol. 101, p. 052802, 2020.

[59] J. José and C. Iliadis, "Nuclear astrophysics: the unfinished quest for the origin of the elements," *Reports on Progress in Physics*, vol. 74, no. 9, p. 096901, 2011.

[60] J. José, M. Hernanz, S. Amari, K. Lodders, and E. Zinner, "The Imprint of Nova Nucleosynthesis in Presolar Grains," *The Astrophysical Journal*, vol. 612, no. 1, pp. 414–428, 2004.

[61] C. Iliadis, A. Champagne, J. Jose, S. Starrfield, and P. Tupper, "The Effects of Thermonuclear Reaction-Rate Variations on Nova Nucleosynthesis: A Sensitivity Study," *The Astrophysical Journal Supplement Series*, vol. 142, no. 1, pp. 105–137, 2002.

[62] E. Zinner, "Stellar Nucleosynthesis and the Isotopic Composition of Presolar Grains from Primitive Meteorites," *Annual Review of Earth and Planetary Sciences*, vol. 26, pp. 147–188, 1998.

[63] D. D. Clayton and L. R. Nittler, "Astrophysics with Presolar Stardust," *Annual Review of Astronomy and Astrophysics*, vol. 42, no. 1, pp. 39–78, 2004.

[64] K. Lodders and S. Amari, "Presolar grains from meteorites: Remnants from the early times of the solar system," *Geochemistry*, vol. 65, no. 2, pp. 93–166, 2005.

[65] M. Lugaro, *Stardust from Meteorites: An Introduction to Presolar Grains*. Singapore: World Scientific Publishing, 2005.

[66] J. José and M. Hernanz, "Nucleosynthesis in classical nova explosions," *Journal of Physics G: Nuclear and Particle Physics*, vol. 34, no. 12, pp. R431–R458, 2007.

[67] P. Hoppe and U. Ott, "Mainstream silicon carbide grains from meteorites," *AIP Conference Proceedings*, vol. 402, no. 1, pp. 27–58, 1997.

[68] R. Gallino, C. M. Raiteri, and M. Busso, "Carbon Stars and Isotopic BA Anomalies in Meteoritic SiC Grains," *The Astrophysical Journal*, vol. 410, p. 400, 1993.

[69] M. Lugaro, A. M. Davis, R. Gallino, M. J. Pellin, O. Straniero, and F. Kappeler, "Isotopic Compositions of Strontium, Zirconium, Molybdenum, and Barium in Single Presolar SiC Grains and Asymptotic Giant Branch Stars," *The Astrophysical Journal*, vol. 593, no. 1, pp. 486–508, 2003.

[70] U. Ott and F. Begemann, "Discovery of s-Process Barium in the Murchison Meteorite," *The Astrophysical Journal Letters*, vol. 353, p. L57, 1990.

[71] N. Liu, T. Stephan, P. Boehnke, L. R. Nittler, C. M. O. Alexander, J. Wang, A. M. Davis, R. Trappitsch, and M. J. Pellin, "J-type Carbon Stars: A Dominant Source of ^{14}N-rich Presolar SiC Grains of Type AB," *The Astrophysical Journal*, vol. 844, no. 1, p. L12, 2017.

[72] P. Hoppe, P. Annen, R. Strebel, P. Eberhardt, R. Gallino, M. Lugaro, S. Amari, and R. S. Lewis, "Meteoritic Silicon Carbide Grains with Unusual Si Isotopic Compositions: Evidence for an Origin in Low-Mass, Low-Metallicity Asymptotic Giant Branch Stars," *The Astrophysical Journal*, vol. 487, no. 1, pp. L101–L104, 1997.

[73] S. Amari, L. R. Nittler, E. Zinner, R. Gallino, M. Lugaro, and R. S. Lewis, "Presolar SiC Grains of Type Y: Origin from Low-Metallicity Asymptotic Giant Branch Stars," *The Astrophysical Journal*, vol. 546, no. 1, pp. 248–266, 2001.

[74] N. Liu, T. Stephan, S. Cristallo, R. Gallino, P. Boehnke, L. R. Nittler, C. M. O. Alexander, A. M. Davis, R. Trappitsch, M. J. Pellin, and I. Dillmann, "Presolar silicon carbide grains of types y and z: Their molybdenum isotopic compositions and stellar origins," *The Astrophysical Journal*, vol. 881, no. 1, p. 28, 2019.

[75] S. Amari, P. Hoppe, E. Zinner, and R. S. Lewis, "Interstellar SiC with Unusual Isotopic Compositions: Grains from a Supernova?," *The Astrophysical Journal*, vol. 394, p. L43, 1992.

[76] P. Hoppe, R. Strebel, P. Eberhardt, S. Amari, and R. S. Lewis, "Isotopic properties of silicon carbide X grains from the Murchison meteorite in the size range 0.5-1.5 μm," *Meteorics & Planetary Science*, vol. 35, no. 6, pp. 1157–1176, 2000.

[77] S. Amari, X. Gao, L. R. Nittler, E. Zinner, J. Jose, M. Hernanz, and R. S. Lewis, "Presolar Grains from Novae," *The Astrophysical Journal*, vol. 551, no. 2, pp. 1065–1072, 2001.

[78] S. Amari, "Presolar grains from novae: their isotopic ratios and radioactivities," *New Astronomy Reviews*, vol. 46, no. 8-10, pp. 519–524, 2002.

[79] C. Iliadis, L. N. Downen, J. José, L. R. Nittler, and S. Starrfield, "On Presolar Stardust Grains from CO Classical Novae," *The Astrophysical Journal*, vol. 855, no. 2, p. 76, 2018.

[80] D. D. Clayton, "Extinct radioactivities: trapped residuals of presolar grains.," *The Astrophysical Journal*, vol. 199, pp. 765–769, 1975.

[81] D. D. Clayton and F. Hoyle, "Grains of Anomalous Isotopic Composition from Novae," *The Astrophysical Journal*, vol. 203, pp. 490–496, 1976.

[82] S. Amari, R. S. Lewis, and E. Anders, "Interstellar grains in meteorites: III. Graphite and its noble gases," *Geochimica et Cosmochimica Acta*, vol. 59, no. 7, pp. 1411–1426, 1995.

[83] K. M. Hynes and F. Gyngard, "The Presolar Grain Database: http://presolar.wustl.edu/p̃gd," in *40th Annual Lunar and Planetary Science Conference*, Lunar and Planetary Science Conference, p. 1198, 2009.

[84] T. Stephan, M. Bose, A. Boujibar, A. M. Davis, C. J. Dory, F. Gyngard, P. Hoppe, K. M. Hynes, N. Liu, L. R. Nittler, R. C. Ogliore, and R. Trappitsch, "The Presolar Grain Database Reloaded - Silicon Carbide," in *51st Annual Lunar and Planetary Science Conference*, Lunar and Planetary Science Conference, p. 2140, 2020.

[85] E. Zinner, "1.02 - presolar grains," in *Treatise on Geochemistry* (H. D. Holland and K. K. Turekian, eds.), pp. 1–33, Oxford: Pergamon, 2007.

[86] M. Bose and S. Starrfield, "Condensation of SiC Stardust in CO Nova Outbursts," *The Astrophysical Journal*, vol. 873, no. 1, p. 14, 2019.

[87] S. Starrfield, J. W. Truran, M. C. Wiescher, and W. M. Sparks, "Evolutionary sequences for Nova V1974 Cygni using new nuclear reaction rates and opacities," *Monthly Notices of the Royal Astronomical Society*, vol. 296, no. 3, pp. 502–522, 1998.

[88] S. Wanajo, M. aki Hashimoto, and K. Nomoto, "Nucleosynthesis in ONeMg Novae: Models versus Observations to Constrain the Masses of ONeMg White Dwarfs and Their Envelopes," *The Astrophysical Journal*, vol. 523, no. 1, pp. 409–431, 1999.

[89] S. Starrfield, W. M. Sparks, J. W. Truran, and M. C. Wiescher, "The Effects of New Nuclear Reaction Rates and Opacities on Hydrodynamic Simulations of the Nova Outburst," *The Astrophysical Journal Supplement Series*, vol. 127, no. 2, pp. 485–495, 2000.

[90] L. N. Downen, C. Iliadis, J. José, and S. Starrfield, "Nuclear Thermometers for Classical Novae," *The Astrophysical Journal*, vol. 762, no. 2, p. 105, 2013.

[91] J. Casanova, J. José, E. García-Berro, S. Shore, and A. Calder, "Kelvin-helmholtz instabilities as the source of inhomogenous mixing in nova explosions," *Nature*, vol. 478, pp. 490–492, 2011.

[92] J. Casanova, J. José, E. García-Berro, and S. Shore, "Three-dimensional simulations of turbulent convective mixing in ONe and CO classical nova explosions," *Astronomy & Astrophysics*, vol. 595, p. A28, 2016.

[93] J. Casanova, J. José, and S. N. Shore, "Two-dimensional simulations of mixing in classical novae: The effect of white dwarf composition and mass," *Astronomy & Astrophysics*, vol. 619, p. A121, 2018.

[94] K. J. Kelly, C. Iliadis, L. Downen, J. José, and A. Champagne, "Nuclear Mixing Meters for Classical Novae," *The Astrophysical Journal*, vol. 777, no. 2, p. 130, 2013.

[95] I. J. Thompson and F. M. Nunes, *Nuclear Reactions for Astrophysics: Principles, Calculation and Applications of Low-Energy Reactions*. Cambridge University Press, 2009.

[96] R. A. Wolf, "Rates of Nuclear Reactions in Solid-Like Stars*," *Physical Review*, vol. 137, pp. B1634–B1643, 1965.

[97] J. José, M. Hernanz, and C. Iliadis, "Nucleosynthesis in classical novae," *Nuclear Physics A*, vol. 777, pp. 550 – 578, 2006.

[98] Z. Ma, D. W. Bardayan, J. C. Blackmon, R. P. Fitzgerald, M. W. Guidry, W. R. Hix, K. L. Jones, R. L. Kozub, R. J. Livesay, M. S. Smith, J. S. Thomas, and D. W. Visser, "Astrophysically important ^{31}S states studied with the ^{32}S$(p, d)^{31}$S reaction," *Physical Review C*, vol. 76, p. 015803, 2007.

[99] K. Setoodehnia, A. A. Chen, J. Chen, J. A. Clark, C. M. Deibel, J. Hendriks, D. Kahl, W. N. Lennard, P. D. Parker, D. Seiler, and C. Wrede, "Level structure of ^{31}S via ^{32}S$(p, d)^{31}$S," *Physical Review C*, vol. 102, p. 045806, 2020.

[100] S. Burcher, K. A. Chipps, R. O. Hughes, C. S. Reingold, A. Saastamoinen, J. T. Harke, N. Cooper, S. Ahn, J. M. Allmond, H. Clark, J. A. Cizewski, M. R. Hall, J. Hooker, H. Jayatissa, K. L. Jones, S. Ota, S. D. Pain, K. Schmidt, A. Simon, and S. Upadhyayula, "Developing the ^{32}S$(p, d)^{31}$S$^*(p)(\gamma)$ reaction to probe the ^{30}P$(p, \gamma)^{31}$S reaction rate in classical novae," *Physical Review C*, vol. 105, p. 045805, 2022.

[101] J. Vernotte, G. Berrier-Ronsin, S. Fortier, E. Hourani, A. Khendriche, J. M. Maison, L. H. Rosier, G. Rotbard, E. Caurier, and F. Nowacki, "One-nucleon pickup reactions on ^{32}S: Experimental results and shell-model calculations," *Nuclear Physics A*, vol. 655, no. 3, pp. 415–439, 1999.

[102] C. Wrede, J. A. Caggiano, J. A. Clark, C. M. Deibel, A. Parikh, and P. D. Parker, "Measurements of ^{31}S energy levels and reevaluation of the thermonuclear resonant ^{30}P$(p,\gamma)^{31}$S reaction rate," *Physical Review C*, vol. 79, p. 045803, 2009.

[103] D. Irvine, A. A. Chen, A. Parikh, K. Setoodehnia, T. Faestermann, R. Hertenberger, H.-F. Wirth, V. Bildstein, S. Bishop, J. A. Clark, C. M. Deibel, J. Hendriks, C. Herlitzius, R. Krücken, W. N. Lennard, O. Lepyoshkina, R. Longland, G. Rugel, D. Seiler, K. Straub, and C. Wrede, "Evidence for the existence of the astrophysically important 6.40-MeV state of ^{31}S," *Physical Review C*, vol. 88, p. 055803, 2013.

[104] A. Kankainen, P. Woods, H. Schatz, T. Poxon-Pearson, D. Doherty, V. Bader, T. Baugher, D. Bazin, B. Brown, J. Browne, A. Estrade, A. Gade, J. José, A. Kontos, C. Langer, G. Lotay, Z. Meisel, F. Montes, S. Noji, F. Nunes, G. Perdikakis, J. Pereira, F. Recchia, T. Redpath, R. Stroberg, M. Scott, D. Seweryniak, J. Stevens, D. Weisshaar, K. Wimmer, and R. Zegers, "Measurement of key resonance states for the ^{30}P$(p,\gamma)^{31}$S reaction rate, and the production of intermediate-mass elements in nova explosions," *Physics Letters B*, vol. 769, pp. 549 – 553, 2017.

[105] C. Wrede, J. A. Caggiano, J. A. Clark, C. Deibel, A. Parikh, and P. D. Parker, "New ^{30}P$(p,\gamma)^{31}$S resonances and oxygen-neon nova nucleosynthesis," *Physical Review C*, vol. 76, p. 052802(R), 2007.

[106] A. Parikh, K. Wimmer, T. Faestermann, R. Hertenberger, J. José, R. Longland, H.-F. Wirth, V. Bildstein, S. Bishop, A. A. Chen, J. A. Clark, C. M. Deibel, C. Herlitzius, R. Krücken, D. Seiler, K. Straub, and C. Wrede, "Improving the ^{30}P$(p,\gamma)^{31}$S rate in oxygen-neon novae: Constraints on J^π values for proton-threshold states in ^{31}S," *Phys. Rev. C*, vol. 83, p. 045806, 2011.

[107] A. Parikh, C. Wrede, and C. Fry, "Toward concordance of E_x and J^π values for proton unbound ^{31}S states," *European Physical Journal Plus*, vol. 131, no. 9, p. 345, 2016.

[108] D. G. Jenkins, C. J. Lister, M. P. Carpenter, P. Chowdhury, N. J. Hammond, R. V. F. Janssens, T. L. Khoo, T. Lauritsen, D. Seweryniak, T. Davinson, P. J. Woods, A. Jokinen, and H. Penttila, "Mirror energy differences in the $A = 31$ mirror nuclei, ^{31}S and ^{31}P, and their significance in electromagnetic spin-orbit splitting," *Physical Review C*, vol. 72, p. 031303(R), 2005.

[109] D. G. Jenkins, A. Meadowcroft, C. J. Lister, M. P. Carpenter, P. Chowdhury, N. J. Hammond, R. V. F. Janssens, T. L. Khoo, T. Lauritsen, D. Seweryniak, T. Davinson, P. J. Woods, A. Jokinen, H. Penttila, G. Martínez-Pinedo, and J. José, "Reevaluation of the ^{30}P$(p,\gamma)^{31}$S

astrophysical reaction rate from a study of the $T = 1/2$ mirror nuclei, ^{31}S and ^{31}P," *Physical Review C*, vol. 73, p. 065802, 2006.

[110] D. T. Doherty, G. Lotay, P. J. Woods, D. Seweryniak, M. P. Carpenter, C. J. Chiara, H. M. David, R. V. F. Janssens, L. Trache, and S. Zhu, "Key Resonances in the ^{30}P$(p,\gamma)^{31}$S Gateway Reaction for the Production of Heavy Elements in ONe Novae," *Physical Review Letters*, vol. 108, p. 262502, 2012.

[111] D. T. Doherty, P. J. Woods, G. Lotay, D. Seweryniak, M. P. Carpenter, C. J. Chiara, H. M. David, R. V. F. Janssens, L. Trache, and S. Zhu, "Level structure of ^{31}S: From low excitation energies to the region of interest for hydrogen burning in novae through the ^{30}P$(p,\gamma)^{31}$S reaction," *Physical Review C*, vol. 89, p. 045804, 2014.

[112] R. P. Feynman and M. Gell-Mann, "Theory of the Fermi Interaction," *Physical Review*, vol. 109, pp. 193–198, 1958.

[113] F. Osterfeld, "Nuclear spin and isospin excitations," *Reviews of Modern Physics*, vol. 64, pp. 491–557, 1992.

[114] J. Äystö, J. Honkanen, K. Vierinen, A. Hautojärvi, K. Eskola, and S. Messelt, "Observation of beta-delayed protons in the decay of ^{31}Cl," *Physics Letters B*, vol. 110, no. 6, pp. 437–440, 1982.

[115] J. Äystö, P. Taskinen, K. Eskola, K. Vierinen, and S. Messelt, "Studies of Weak Beta-Delayed Protons Emitted in the Decay of Odd-Z, T_Z = -3/2 Nuclei," *Physica Scripta*, vol. T5, pp. 193–195, 1983.

[116] J. Äystö, X. J. Xu, D. M. Moltz, J. E. Reiff, J. Cerny, and B. H. Wildenthal, "Beta-delayed proton decays of ^{27}P and ^{31}Cl: Gamow-Teller decays with large Q values," *Physical Review C*, vol. 32, pp. 1700–1706, 1985.

[117] A. Kankainen, T. Eronen, S. P. Fox, H. O. U. Fynbo, U. Hager, J. Hakala, J. Huikari, D. G. Jenkins, A. Jokinen, S. Kopecky, I. Moore, A. Nieminen, H. Penttilä, S. Rinta-Antila, O. Tengblad, Y. Wang, and J. Äystö, "Excited states in ^{31}S studied via beta decay of ^{31}Cl," *European Physical Journal A*, vol. 27, no. 1, pp. 67–75, 2006.

[118] A. Saastamoinen, *Studies of $T_z = -3/2$ Nuclei of Astrophysical Interest*. PhD thesis, University of Jyväskylä, 2011.

[119] J. C. Batchelder, "Recommended values for β^+-delayed proton and α emission," *Atomic Data and Nuclear Data Tables*, vol. 132, p. 101323, 2020.

[120] M. B. Bennett, C. Wrede, S. N. Liddick, D. Pérez-Loureiro, D. W. Bardayan, B. A. Brown, A. A. Chen, K. A. Chipps, C. Fry, B. E. Glassman, C. Langer, N. R. Larson, E. I. McNeice, Z. Meisel, W. Ong, P. D. O'Malley, S. D. Pain, C. J. Prokop, H. Schatz, S. B. Schwartz,

S. Suchyta, P. Thompson, M. Walters, and X. Xu, "Detailed study of the decay ^{31}Cl($\beta\gamma$)^{31}S," *Physical Review C*, vol. 97, p. 065803, 2018.

[121] M. B. Bennett, C. Wrede, B. A. Brown, S. N. Liddick, D. Pérez-Loureiro, D. W. Bardayan, A. A. Chen, K. A. Chipps, C. Fry, B. E. Glassman, C. Langer, N. R. Larson, E. I. McNeice, Z. Meisel, W. Ong, P. D. O'Malley, S. D. Pain, C. J. Prokop, H. Schatz, S. B. Schwartz, S. Suchyta, P. Thompson, M. Walters, and X. Xu, "Isospin Mixing Reveals ^{30}P$(p,\gamma)^{31}$S Resonance Influencing Nova Nucleosynthesis," *Physical Review Letters*, vol. 116, p. 102502, 2016.

[122] H. Hafner and H. H. Duhm, "The ^{28}Si(^{3}He,p)^{30}P reaction at 16 and 28 MeV," *Nuclear Physics A*, vol. 227, no. 3, pp. 450–468, 1974.

[123] Y. Giomataris, P. Rebourgeard, J. Robert, and G. Charpak, "MICROMEGAS: a high-granularity position-sensitive gaseous detector for high particle-flux environments," *Nuclear Instruments and Methods in Physics Research Section A: Accelerators, Spectrometers, Detectors and Associated Equipment*, vol. 376, no. 1, pp. 29–35, 1996.

[124] J. Cockcroft, "Experimental nuclear physics," *Nature*, vol. 175, pp. 53–54.

[125] E. Pollacco, L. Trache, E. Simmons, A. Spiridon, M. McCleskey, B. Roeder, A. Saastamoinen, R. Tribble, G. Pascovici, M. Kebbiri, J. Mols, and M. Raillot, "AstroBox: A novel detection system for very low-energy protons from β-delayed proton decay," *Nuclear Instruments and Methods in Physics Research Section A: Accelerators, Spectrometers, Detectors and Associated Equipment*, vol. 723, pp. 102–108, 2013.

[126] G. F. Knoll, *Radiation Detection and Measurement*. Hoboken: John Wiley & Sons, Inc., 4 ed., 2010.

[127] F. Sauli, *Gaseous Radiation Detectors: Fundamentals and Applications*. Cambridge Monographs on Particle Physics, Nuclear Physics and Cosmology, Cambridge: Cambridge University Press, 2014.

[128] M. Friedman, D. Pérez-Loureiro, T. Budner, E. Pollacco, C. Wrede, M. Cortesi, C. Fry, B. Glassman, M. Harris, J. Heideman, M. Janasik, B. Roeder, M. Roosa, A. Saastamoinen, J. Stomps, J. Surbrook, P. Tiwari, and J. Yurkon, "GADGET: a Gaseous Detector with Germanium Tagging," *Nuclear Instruments and Methods in Physics Research Section A: Accelerators, Spectrometers, Detectors and Associated Equipment*, vol. 940, pp. 93 – 102, 2019.

[129] W. Mueller, J. Church, T. Glasmacher, D. Gutknecht, G. Hackman, P. Hansen, Z. Hu, K. Miller, and P. Quirin, "Thirty-two-fold segmented germanium detectors to identify γ-rays from intermediate-energy exotic beams," *Nuclear Instruments and Methods in Physics Research Section A: Accelerators, Spectrometers, Detectors and Associated Equipment*, vol. 466, no. 3, pp. 492–498, 2001.

[130] A. Stolz, T. Baumann, T. Ginter, D. Morrissey, M. Portillo, B. Sherrill, M. Steiner, and J. Stetson, "Production of rare isotope beams with the NSCL fragment separator," *Nuclear Instruments and Methods in Physics Research Section B: Beam Interactions with Materials and Atoms*, vol. 241, no. 1, pp. 858–861, 2005.

[131] F. Paschen, "Ueber die zum Funkenübergang in Luft, Wasserstoff und Kohlensäure bei verschiedenen Drucken erforderliche Potentialdifferenz," *Annalen der Physik*, vol. 273, no. 5, pp. 69–96, 1889.

[132] D. Bazin, J. Caggiano, B. Sherrill, J. Yurkon, and A. Zeller, "The S800 spectrograph," *Nuclear Instruments and Methods in Physics Research Section B: Beam Interactions with Materials and Atoms*, vol. 204, pp. 629–633, 2003. 14th International Conference on Electromagnetic Isotope Separators and Techniques Related to their Applications.

[133] K. Starosta, C. Vaman, D. Miller, P. Voss, D. Bazin, T. Glasmacher, H. Crawford, P. Mantica, H. Tan, W. Hennig, M. Walby, A. Fallu-Labruyere, J. Harris, D. Breus, P. Grudberg, and W. Warburton, "Digital Data Acquisition System for experiments with segmented detectors at National Superconducting Cyclotron Laboratory," *Nuclear Instruments and Methods in Physics Research Section A: Accelerators, Spectrometers, Detectors and Associated Equipment*, vol. 610, no. 3, pp. 700–709, 2009.

[134] C. Prokop, S. Liddick, B. Abromeit, A. Chemey, N. Larson, S. Suchyta, and J. Tompkins, "Digital data acquisition system implementation at the National Superconducting Cyclotron Laboratory," *Nuclear Instruments and Methods in Physics Research Section A: Accelerators, Spectrometers, Detectors and Associated Equipment*, vol. 741, pp. 163–168, 2014.

[135] R. Fox, "NSCL Data Acquisition Documentation," 2017. https://docs.nscl.msu.edu/daq/newsite/index.php.

[136] R. Brun and F. Rademakers, "ROOT: An object oriented data analysis framework," *Nuclear Instruments and Methods in Physics Research Section A: Accelerators, Spectrometers, Detectors and Associated Equipment*, vol. 389, pp. 81–86, 1997.

[137] H. Nann and B. H. Wildenthal, "(p,t) and (p,^{3}He) reactions on ^{33}S," *Physical Review C*, vol. 19, pp. 2146–2154, 1979.

[138] C. Moss, "Nuclear energy levels of ^{31}S and ^{33}C1," *Nuclear Physics A*, vol. 145, no. 2, pp. 423–448, 1970.

[139] J. F. Ziegler, M. Ziegler, and J. Biersack, "SRIM – The stopping and range of ions in matter (2010)," *Nuclear Instruments and Methods in Physics Research Section B: Beam Interactions with Materials and Atoms*, vol. 268, no. 11, pp. 1818–1823, 2010. 19th International Conference on Ion Beam Analysis.

[140] G. Gilmore, *Appendix D: Gamma-Ray Energies in the Detector Background and the Envi-*

ronment, pp. 361–364. John Wiley Sons, Ltd., 2008.

[141] E. Grushka, "Characterization of exponentially modified gaussian peaks in chromatography," *Analytical Chemistry*, vol. 44, no. 11, pp. 1733–1738, 1972. PMID: 22324584.

[142] S. Agostinelli, J. Allison, K. Amako, J. Apostolakis, H. Araujo, P. Arce, M. Asai, D. Axen, S. Banerjee, G. Barrand, F. Behner, L. Bellagamba, J. Boudreau, L. Broglia, A. Brunengo, H. Burkhardt, S. Chauvie, J. Chuma, R. Chytracek, G. Cooperman, G. Cosmo, P. Degtyarenko, A. Dell'Acqua, G. Depaola, D. Dietrich, R. Enami, A. Feliciello, C. Ferguson, H. Fesefeldt, G. Folger, F. Foppiano, A. Forti, S. Garelli, S. Giani, R. Giannitrapani, D. Gibin, J. Gómez Cadenas, I. González, G. Gracia Abril, G. Greeniaus, W. Greiner, V. Grichine, A. Grossheim, S. Guatelli, P. Gumplinger, R. Hamatsu, K. Hashimoto, H. Hasui, A. Heikkinen, A. Howard, V. Ivanchenko, A. Johnson, F. Jones, J. Kallenbach, N. Kanaya, M. Kawabata, Y. Kawabata, M. Kawaguti, S. Kelner, P. Kent, A. Kimura, T. Kodama, R. Kokoulin, M. Kossov, H. Kurashige, E. Lamanna, T. Lampén, V. Lara, V. Lefebure, F. Lei, M. Liendl, W. Lockman, F. Longo, S. Magni, M. Maire, E. Medernach, K. Minamimoto, P. Mora de Freitas, Y. Morita, K. Murakami, M. Nagamatu, R. Nartallo, P. Nieminen, T. Nishimura, K. Ohtsubo, M. Okamura, S. O'Neale, Y. Oohata, K. Paech, J. Perl, A. Pfeiffer, M. Pia, F. Ranjard, A. Rybin, S. Sadilov, E. Di Salvo, G. Santin, T. Sasaki, N. Savvas, Y. Sawada, S. Scherer, S. Sei, V. Sirotenko, D. Smith, N. Starkov, H. Stoecker, J. Sulkimo, M. Takahata, S. Tanaka, E. Tcherniaev, E. Safai Tehrani, M. Tropeano, P. Truscott, H. Uno, L. Urban, P. Urban, M. Verderi, A. Walkden, W. Wander, H. Weber, J. Wellisch, T. Wenaus, D. Williams, D. Wright, T. Yamada, H. Yoshida, and D. Zschiesche, "GEANT4-—a simulation toolkit," *Nuclear Instruments and Methods in Physics Research Section A: Accelerators, Spectrometers, Detectors and Associated Equipment*, vol. 506, no. 3, pp. 250–303, 2003.

[143] J. Allison, K. Amako, J. Apostolakis, H. Araujo, P. Arce Dubois, M. Asai, G. Barrand, R. Capra, S. Chauvie, R. Chytracek, G. Cirrone, G. Cooperman, G. Cosmo, G. Cuttone, G. Daquino, M. Donszelmann, M. Dressel, G. Folger, F. Foppiano, J. Generowicz, V. Grichine, S. Guatelli, P. Gumplinger, A. Heikkinen, I. Hrivnacova, A. Howard, S. Incerti, V. Ivanchenko, T. Johnson, F. Jones, T. Koi, R. Kokoulin, M. Kossov, H. Kurashige, V. Lara, S. Larsson, F. Lei, O. Link, F. Longo, M. Maire, A. Mantero, B. Mascialino, I. McLaren, P. Mendez Lorenzo, K. Minamimoto, K. Murakami, P. Nieminen, L. Pandola, S. Parlati, L. Peralta, J. Perl, A. Pfeiffer, M. Pia, A. Ribon, P. Rodrigues, G. Russo, S. Sadilov, G. Santin, T. Sasaki, D. Smith, N. Starkov, S. Tanaka, E. Tcherniaev, B. Tome, A. Trindade, P. Truscott, L. Urban, M. Verderi, A. Walkden, J. Wellisch, D. Williams, D. Wright, and H. Yoshida, "Geant4 developments and applications," *IEEE Transactions on Nuclear Science*, vol. 53, no. 1, pp. 270–278, 2006.

[144] J. Allison, K. Amako, J. Apostolakis, P. Arce, M. Asai, T. Aso, E. Bagli, A. Bagulya, S. Banerjee, G. Barrand, B. Beck, A. Bogdanov, D. Brandt, J. Brown, H. Burkhardt, P. Canal, D. Cano-Ott, S. Chauvie, K. Cho, G. Cirrone, G. Cooperman, M. Cortés-Giraldo, G. Cosmo, G. Cuttone, G. Depaola, L. Desorgher, X. Dong, A. Dotti, V. Elvira, G. Folger, Z. Francis, A. Galoyan, L. Garnier, M. Gayer, K. Genser, V. Grichine, S. Guatelli, P. Guèye, P. Gumplinger, A. Howard, I. Hřivnáčová, S. Hwang, S. Incerti, A. Ivanchenko,

V. Ivanchenko, F. Jones, S. Jun, P. Kaitaniemi, N. Karakatsanis, M. Karamitros, M. Kelsey, A. Kimura, T. Koi, H. Kurashige, A. Lechner, S. Lee, F. Longo, M. Maire, D. Mancusi, A. Mantero, E. Mendoza, B. Morgan, K. Murakami, T. Nikitina, L. Pandola, P. Paprocki, J. Perl, I. Petrović, M. Pia, W. Pokorski, J. Quesada, M. Raine, M. Reis, A. Ribon, A. Ristić Fira, F. Romano, G. Russo, G. Santin, T. Sasaki, D. Sawkey, J. Shin, I. Strakovsky, A. Taborda, S. Tanaka, B. Tomé, T. Toshito, H. Tran, P. Truscott, L. Urban, V. Uzhinsky, J. Verbeke, M. Verderi, B. Wendt, H. Wenzel, D. Wright, D. Wright, T. Yamashita, J. Yarba, and H. Yoshida, "Recent developments in GEANT4," *Nuclear Instruments and Methods in Physics Research Section A: Accelerators, Spectrometers, Detectors and Associated Equipment*, vol. 835, pp. 186–225, 2016.

[145] S. Biagi, "Monte Carlo simulation of electron drift and diffusion in counting gases under the influence of electric and magnetic fields," *Nuclear Instruments and Methods in Physics Research Section A: Accelerators, Spectrometers, Detectors and Associated Equipment*, vol. 421, no. 1, pp. 234–240, 1999.

[146] R. S. Wolff, "Measurement of the gas constants for various proportional-counter gas mixtures," *Nuclear Instruments and Methods*, vol. 115, no. 2, pp. 461–463, 1974.

[147] E. L. Cussler, *Diffusion: Mass Transfer in Fluid Systems*. New York: Cambridge University Press, 2 ed., 1997.

[148] J. Hirschfelder, C. F. Curtiss, and R. B. Bird, *Molecular Theory of Gases and Liquids*. New York: Wiley, 1954.

[149] R. Husted, M. Boorman, M. Trujillo, D. Hobart, and J. Smith, "Periodic Table of Elements: LANL," 2021. https://periodic.lanl.gov/index.shtml.

[150] T. Budner, M. Friedman, C. Wrede, B. A. Brown, J. José, D. Pérez-Loureiro, L. J. Sun, J. Surbrook, Y. Ayyad, D. W. Bardayan, K. Chae, A. A. Chen, K. A. Chipps, M. Cortesi, B. Glassman, M. R. Hall, M. Janasik, J. Liang, P. O'Malley, E. Pollacco, A. Psaltis, J. Stomps, and T. Wheeler, "Constraining the ^{30}P$(p,\ \gamma)^{31}$S Reaction Rate in ONe Novae via the Weak, Low-Energy, β-Delayed Proton Decay of ^{31}Cl," *Physical Review Letters*, vol. 128, p. 182701, 2022.

[151] B. A. Brown and B. H. Wildenthal, "Status of the Nuclear Shell Model," *Annual Review of Nuclear and Particle Science*, vol. 38, no. 1, pp. 29–66, 1988.

[152] B. Wildenthal, "Empirical strengths of spin operators in nuclei," *Progress in Particle and Nuclear Physics*, vol. 11, pp. 5–51, 1984.

[153] B. A. Brown and W. A. Richter, "New "USD" Hamiltonians for the *sd* shell," *Physical Review C*, vol. 74, p. 034315, 2006.

[154] W. A. Richter, S. Mkhize, and B. A. Brown, "*sd*-shell observables for the USDA and USDB

Hamiltonians," *Physical Review C*, vol. 78, p. 064302, 2008.

[155] A. Magilligan and B. A. Brown, "New isospin-breaking "USD" Hamiltonians for the *sd* shell," *Physical Review C*, vol. 101, p. 064312, 2020.

[156] C. Iliadis, "Proton single-particle reduced widths for unbound states," *Nuclear Physics A*, vol. 618, no. 1, pp. 166–175, 1997.

[157] F. C. Barker, "Comment on 'Proton single-particle reduced widths for unbound states'," *Nuclear Physics A*, vol. 637, no. 4, pp. 576–582, 1998.

[158] B. A. Brown, W. A. Richter, and C. Wrede, "Shell-model studies of the astrophysical rapid-proton-capture reaction ^{30}P$(p,\gamma)^{31}$S," *Physical Review C*, vol. 89, p. 062801(R), 2014.

[159] W. Hauser and H. Feshbach, "The Inelastic Scattering of Neutrons," *Physical Review*, vol. 87, pp. 366–373, 1952.

[160] F. Matteucci, "Stellar Evolution and Galactic Chemical Evolution," in *Frontiers of Stellar Evolution* (D. L. Lambert, ed.), vol. 20 of *Astronomical Society of the Pacific Conference Series*, p. 539, 1991.

[161] T. Rauscher and F.-K. Thielemann, "Astrophysical Reaction Rates From Statistical Model Calculations," *Atomic Data and Nuclear Data Tables*, vol. 75, no. 1, pp. 1–351, 2000.

[162] G. S. Kutter and W. M. Sparks, "Radial accretion of H-rich material onto a He white dwarf," *The Astrophysical Journal*, vol. 239, pp. 988–998, 1980.

[163] J. José, *Stellar Explosions: Hydrodynamics and Nucleosynthesis*. Boca Raton, Florida, USA: CRC Press/Francis and Taylor Group, 2016.

[164] L. R. Nittler and P. Hoppe, "Are Presolar Silicon Carbide Grains from Novae Actually from Supernovae?," *The Astrophysical Journal*, vol. 631, no. 1, pp. L89–L92, 2005.

[165] H. Jorch and J. Campbell, "On the analytic fitting of full energy peaks from Ge(Li) and Si(Li) photon detectors," *Nuclear Instruments and Methods*, vol. 143, no. 3, pp. 551–559, 1977.

[166] V. Zobel, J. Eberth, U. Eberth, and E. Eube, "^{226}Ra as calibration standard for Ge(Li) spectrometers," *Nuclear Instruments and Methods*, vol. 141, no. 2, pp. 329–336, 1977.

[167] National Nuclear Data Center (NNDC) at Brookhaven National Laboratory, "NuDat 3.0," 2022. https://www.nndc.bnl.gov/nudat3/.

[168] A. Saastamoinen, A. Kankainen, and L. Trache, "Beta-decay of ^{31}Cl: an indirect probe of the ^{30}P$(p,\gamma)^{31}$S reaction. Present status and future perspectives," *European Physical Journal*

Plus, vol. 131, no. 8, p. 272, 2016.

[169] I. Ray, M. R. Basu, R. Kshetri, M. Saha Sarkar, S. Sarkar, P. Banerjee, S. Chattopadhyay, C. C. Dey, A. Goswami, J. M. Chatterjee, A. Mukherjee, S. Bhattacharya, B. Dasmahapatra, P. Datta, H. C. Jain, R. K. Bhowmik, S. Muralithar, and R. P. Singh, "Indication of the onset of collectivity in ^{30}P," *Physical Review C*, vol. 76, p. 034315, 2007.

[170] B. Ramstein, L. H. Rosier, and R. J. De Meijer, "Investigation of states in ^{30}P via the ^{30}Si(^{3}He, t)^{30}P reaction at 30 MeV," *Nuclear Physics A*, vol. 363, no. 1, pp. 110–136, 1981.

[171] J. C. Vermeulen, C. R. Bingham, D. Dijkhuizen, R. J. De Meijer, and L. Put, "Investigation of the decay properties of high-spin two-nucleon states via the ^{28}Si(α, $d\gamma$)^{30}P reaction at E_α = 50 MeV," *Nuclear Physics A*, vol. 329, no. 1, pp. 93–108, 1979.

[172] C. E. Moss, C. Dètraz, and C. S. Zaidins, "Beta decay of ^{26}Si, ^{30}S and ^{34}Ar," *Nuclear Physics A*, vol. 174, no. 2, pp. 408–416, 1971.

[173] T. J. Ognibene, J. Powell, D. M. Moltz, M. W. Rowe, and J. Cerny, "Additional results from the β-delayed proton decays of ^{27}P and ^{31}Cl," *Physical Review C*, vol. 54, pp. 1098–1105, 1996.